SEISMOTECTONICS OF THE NORTHERN ROCKIES:
CAUSES AND EFFECTS OF THE INTRAPLATE SEISMICITY

A Dissertation
Presented in Partial Fulfillment of the Requirements for the
Degree of Doctorate of Philosophy
with a
Major in Geology
in the
College of Graduate Studies
University of Idaho
by
Daisuke Kobayashi

Major Professor: Kenneth F. Sprenke, Ph.D.

Committee Members:

Peter E. Isaacson, Ph.D.; Eric Mittelstaedt, Ph.D.; A. John Watkinson, Ph.D.

Department Administrator: Leslie Baker, Ph.D.

May 2017

AUTHORIZATION TO SUBMIT DISSERTATION

This dissertation of Daisuke Kobayashi, submitted for the degree of Doctorate of Philosophy with a Major in Geology and titled "Seismotectonics of the Northern Rockies: Causes and Effects of the Intraplate Seismicity," has been reviewed in final form. Permission, as indicated by the signatures and dates below, is now granted to submit final copies to the College of Graduate Studies for approval.

Major Professor: ______________________________ Date: ______________
Kenneth F. Sprenke, Ph.D.

Committee Members: ______________________________ Date: ______________
Peter E. Isaacson, Ph.D.

______________________________ Date: ______________
Eric Mittelstaedt, Ph.D.

______________________________ Date: ______________
A. John Watkinson, Ph.D.

Department Administrator: ______________________________ Date: ______________
Leslie Baker, Ph.D.

ABSTRACT

This dissertation presents four studies that explore potential causes and effects of the seismicity in the Northern Rockies.

The focus of Chapter 1 is on spatial correlations between the seismicity and the upper mantle structures. Tomography models suggest a strong low-velocity anomaly along the axis of the Yellowstone Tectonic Parabola. A tomography model, as well as heat flow, corrected geoid height, and shear wave splitting data, suggest a low-velocity body along the axis of another seismic parabola formed by the Centennial Tectonic Belt and Intermountain Seismic Belt (ISB). This similarity points to a common mechanism for both seismic parabolas: a passive rising of buoyant mantle overlain by a moving lithosphere.

In Chapter 2, the effects of the historical and hypothetical earthquakes on the Yellowstone magmatic system are assessed by calculating a static stress transfer from each event. The second mainshock of the 1959 Hebgen Lake sequence effectively unclamped the magma reservoir, which could have led to a magma overpressure. Among the 13 hypothetical M_W7.1-7.5 earthquakes, events at the second mainshock and largest aftershock of the Hebgen sequence, as well as the one on the Upper Yellowstone Valley fault, show the pattern of normal stress changes favorable to promote a Yellowstone eruption.

Chapter 3 presents an interpretation of the 2015 Sandpoint, Idaho earthquake sequence that occurred in the Lewis Clark Fault Zone (LCFZ). The fault plane solutions show reverse sense of oblique slips on a southeast-dipping nodal plane, which is likely to represent a reactivation of the Purcell Trench fault. The Sandpoint earthquakes, along with

the adjacent reverse-faulting events, constrain the western extent of the northeast-southwest extension of the LCFZ.

In the last chapter, I estimate the effective elastic thickness (T_e) of the Northern Rockies, using the free-air admittance method. The effect from the upper mantle density heterogeneity is taken into consideration. The result shows a T_e variation in which the relatively narrow transition zone from small to large (>10 km) T_e coincides with the ISB, as well as a limited effect from the upper mantle. The T_e estimate largely agrees with the T_e map from the Bouguer coherence method.

ACKNOWLEDGEMENTS

My deepest thanks goes to my advisor Ken Sprenke. Since the first day of my undergraduate Geophysics class in 2008, he has been continuously sharing the enjoyment of the discipline with me. I am privileged to have been taught and guided by the most creative, knowledgeable, and caring researcher I have met.

I would like to thank my committee members, Peter Isaacson, Eric Mittelstaedt, and John Watkinson, for their comments and suggestions that helped make this dissertation complete. This work would not have been possible without the generous administrative support of Mickey Gunter. I also thank Mike Stickney (Montana Bureau of Mines and Geology) for providing me with seismic data essential for all chapters, and Bill Phillips (Idaho Geological Survey) for sharing with me knowledge and insights on Idaho Geology.

Special thanks to Peter LaFemina for helping me build my foundation as a researcher, as well as Sharon Fritz, Samantha Burns, and Raymond Dixon for their invaluable help, support, and encouragement.

DEDICATION

To my dogs, Vector and Tensor,

whose support has been as essential

as the GPS and earthquake data used in my studies.

TABLE OF CONTENTS

LIST OF FIGURES

LIST OF TABLES

INTRODUCTION

Earthquakes, including large ones, occur in the Northern Rockies. In this document, the term Northern Rockies refers to the Northern Rocky Mountains in the United States, mainly north of the Snake River Plain and western Montana, and the surrounding areas, such as southern Idaho and the Middle Rocky Mountains. Although the area is in the broad zone of extension tectonics in the western U.S., the Northern Rockies is distinct because of complexities added by the following factors: the transition from the Precambrian core to the Phanerozoic terranes, long-standing repeatedly reactivated fault zones, large-scale batholith intrusions, active volcanism of Yellowstone, large upper mantle heterogeneity, and the influence of the interplate interaction along the active margin to the west.

Potential causes and effects of the seismicity and deformation in the Northern Rockies are the themes of this work. The first chapter discusses the upper mantle structures that may be responsible for the spatial distribution of the seismicity in the area. The topic in Chapter 2 is the possibility that the historical and hypothetical earthquakes in the area enhance the potential for a Yellowstone eruption through static stress transfer. Chapter 3 focuses on the 2015 Sandpoint, Idaho earthquake sequence as a manifestation of the complex deformation. In the last chapter, the effective elastic thickness of the Northern Rockies is estimated, and its spatial variation is discussed in light of the distributions of the seismicity and crustal deformation.

CHAPTER 1: SEISMICITY IN THE NORTHERN ROCKIES: IS THERE ANOTHER SEISMIC PARABOLA?

> Earthquakes within continental plates are an embarrassing stepchild of modern earthquake seismology.
>
> –S. Stein and S. Mazzotti, 2007, p. v

Abstract

Two intraplate seismic zones, namely the northern segment of the Intermountain Seismic Belt (ISB) and the Centennial Tectonic Belt (CTB), lie in the Northern Rockies, causing M~7 historical earthquakes. In search of potential factors responsible for the locations of these seismic zones, we explore the spatial correlation between the seismicity and the underlying upper mantle structures indicated by seismic tomography, gravity, and heat flow data. We focus on comparisons with the velocity perturbation anomalies and their gradients imaged by recent high-resolution tomography models which use data from the USArray networks.

The tomography models suggest an elongated, strong low-velocity (< -4%) body beneath the eastern Snake River Plain, along the axis of the Yellowstone Tectonic Parabola (YTP). The progression of Yellowstone is considered responsible for the parabolic pattern. To the north, it is possible to delineate another parabola with its vertex around Bozeman, Montana, by connecting the CTB and the northernmost segment of the ISB. An *S*-wave tomography model and heat flow data suggest an along-axis zone of relatively low velocity

and high heat flow (~1% lower and ~10 mW m^{-2} higher, respectively) in the northern parabola. Based on the similarity, we propose the mini-hotspot model for the seismicity in the Northern Rockies, where a branch of buoyant mantle overlain by the moving lithosphere is responsible for the parabolic pattern of seismicity, as in the case of the YTP.

As supporting evidence, the area's geoid height map, after removing a strong anomaly caused by Yellowstone, shows that the geoid height along the northern parabola axis is ~1 m lower than the surrounding areas, indicating a mantle-origin density deficit. A shear wave splitting analysis presents ~5-10° larger standard deviations in fast orientation along the parabola axis, which indicates an added complexity below the area.

To better study the upper mantle structures, we construct an average model from four *S*-wave tomography models by applying a technique of seismic trace stacking. The average model reveals a small low-velocity body branching out from the main body below Yellowstone/eastern Snake River Plain at ~ 200 km depths, and flowing upward around the edges of high-velocity bodies. We interpret the structure as passive rising of the buoyant mantle, the course of which is controlled by an interaction with the fragments of advancing slabs.

1.1 Introduction

There are continental intraplate seismic zones in the Unites States, despite the old age of the North American Craton. Well-known examples include the New Madrid Seismic Zone responsible for the 1811-1812 M_W7.3-8.0 earthquakes, and the Virginia Seismic Zone, in which the 2011 M_W5.8 event occurred. Among the intraplate seismic zones in the U.S., the ones in the Northern Rockies, the northern segment of the Intermountain Seismic Belt

(ISB) and the Centennial Tectonic Belt (CTB), probably draw the least attention from the public despite the concentrated seismicity including historical large earthquakes, such as the 1983 M_S7.3 Borah Peak and the 1959 M_S7.5 Hebgen Lake earthquakes.

The ISB is a zone of elevated seismicity extending from northwestern Montana to northwestern Arizona (Figure 1.1). The northernmost segment of the ISB extends northwest-southeast along the Montana-Idaho border. The CTB is a discrete seismic zone in central Idaho, lying north of the central and eastern Snake River Plain (Figure 1.1). These seismic zones meet to the north of Yellowstone around Bozeman, Montana. In another seismic zone configuration, the CTB is the northern arm of the Yellowstone Tectonic Parabola (YTP), the parabolic pattern of seismicity centered at Yellowstone (Figure 1.1). Some researchers ascribe the parabolic pattern of the YTP to the thermal effect of the advancing Yellowstone hotspot, as well as the outward migration of high seismicity along the major faults striking perpendicular to the parabola axis.

In the study area, another seismic parabola can be delineated by connecting the seismicity in western Montana and the CTB (Figure 1.1). We explore commonalities between the two parabolas through the spatial correlation between the seismicity in the Northern Rockies and the upper mantle structures, as well as other geophysical data sets, which may lead to a starting point to better understand the underlying cause of the seismicity.

1.1.1 Background

Despite its societal significance, studying continental intraplate seismicity is challenging. Continental intraplate earthquakes occur at relatively shallow depths close to the Earth's surface, often below areas unaccustomed to earthquakes, which could lead to severe damages and large fatalities. It is challenging for several reasons. It requires stretching the plate tectonics theory, which assumes rigid plate interiors. Moreover, intraplate seismic zones have unique tectonic settings and deformation mechanisms due to reworked, and often hidden, fossil structures, subtle differential stresses, and sluggish strain accumulation. The seismic Northern Rockies is made unique by the broad extension tectonics and the Yellowstone volcanism. This area is also known for the largest two historical events in the Intermountain West, the 1959 M_S7.5 Hebgen Lake and the 1983 M_S7.3 Borah Peak earthquakes.

There are two major seismic zones in the Northern Rockies. One extends from Yellowstone to northwestern Montana along the Montana-Idaho border (Figure 1.1). This zone is treated as the northern segment of the ISB, a north-south trending seismic zone extending to northwestern Arizona [*Sbar et al.*, 1972; *Smith and Sbar*, 1974; *Herrmann et al.*, 2011]. The other seismic zone is the CTB, which is located adjacent to the northern flank of the central and eastern Snake River Plain (SRP; Figure 1.1) [*Stickney and Bartholomew*, 1987]. These two seismic zones meet north of Yellowstone around Bozeman, Montana.

Studies have been made on the intraplate seismicity in the Northern Rockies to understand the underlying mechanism, which has not reached a decisive hypothesis. One model to explain the location of the ISB is a structural gradient. The ISB coincides with a transition zone from the North American Craton to the thin, deforming crust [*Lowry and Smith*, 1995; *Lowry et al.*, 2000; *Levander and Miller*, 2012]. For the underlying mechanism, *Lowry and Smith* [1995] suggested that the ISB seismogenesis was associated with the flux of low-viscosity crustal material caused by extensional stresses due to buoyancy gradients. *Becker et al.* [2015] demonstrated that vertical normal stress changes due to the underlying mantle flow are responsible for the ISB seismicity.

As for the CTB, which is undergoing extension tectonics, there are several interpretations in terms of seismic zone configuration. One classic view is that the north of the SRP, including the CTB, is the northern section of the Basin and Range province [*Pardee*,1950; *Lawrence*, 1976; *Reynolds*, 1979; *McCaffrey et al.*, 2007; *Payne et al.*, 2012], which could implicitly assume that some common underlying mechanism is responsible for the crustal extension in both Great Basin area and Northern Rockies.

In another view, which could reckon the CTB as a discrete seismic zone, the north of the SRP is not included in the Basin and Range province because of differences in post-orogeny tectonic history and extension style [e.g., *Furlong*, 1979; *Klemperer et al.*, 1986; *Stickney and Bartholomew*, 1987; *Liu and Shen*, 1998; *Hampel et al.*, 2007; *Eagar et al.*, 2010; *Stickney*, 2015]. The different tectonic history is indicated by the age of the basin fill. In the Great Basin area, the grabens are filled with Pliocene and Quaternary sediments, whereas the basin fill is predominantly Miocene in age in the Northern Rockies [*Eaton*, 1979a]. Another difference is found in the extension directions. In the Great Basin section, the extension directions are west to northwest [*Eaton*, 1979b; 1980; *Zoback and Zoback*, 1980], while in the Northern Rockies, the observed seismicity indicates the extension direction ranging from west to southwest [*Stickney and Bartholomew*, 1987; *Stickney*, 2015].

The other prevailing view is that the CTB is the northern arm of the YTP about the axis of the aseismic eastern SRP with its vertex at Yellowstone (Figure 1.1) [*Myers and Hamilton*, 1964; *Smith and Sbar*, 1974; *Smith et al.*, 1985; *Scott et al.*, 1985ab; *Anders et al.*, 1989; *Smith and Arabasz*, 1991]. The ISB segment along the Idaho-Wyoming border is the southern arm of the parabola. The tectonic parabola was first noted by *Scott et al.* [1985ab] and *Smith et al.* [1985]. They ascribed the earthquake distribution to the thermal effect of the migrating Yellowstone hotspot. It was also suggested that the hotspot migration was responsible for the temporal and spatial distribution of fault activity around the eastern SRP [*Anders and Geissman*, 1983; *Scott et al.*, 1985ab; *Smith et al.*, 1985; *Pierce and Scott*, 1986; *Pierce et al.*, 1988; *Anders and Piety*, 1988].

Anders et al. [1989] further studied the relationship between the distribution of fault activities and the hotspot progression. They investigated along-strike variations in displacement rate of the major faults striking perpendicular to the axis of the eastern SRP to find that the locus of each fault's highest displacement rate had migrated outward away from the SRP over time. Accordingly, loci of high seismicity migrated outward after the hotspot had passed over, resulting in the parabolic pattern of seismicity. This interpretation is supported by the location of the 2014 earthquake swarm near Challis, Idaho. The earthquake swarm consisting of over 100 m_b1.5-4.7 events occurred about 20-30 km northwest (i.e., away from the SRP axis) of the focus of the 1983 Borah Peak earthquake (Figure 1.1) along the Lost River fault [*Pankow et al.*, 2014]. If the earthquake swarm occurred along the northwest extension of the fault, the earthquake swarm could indicate the outward migration of fault activity.

Note that the YTP interpretation does not necessarily exclude the other interpretations. For example, there is a good chance that the original extension mechanism responsible for the CTB seismicity has been under the influence of the hotspot progression.

It is also possible that other geodynamic factors affect the spatial distribution of the regional seismicity.

1.1.2 Objectives

In the Northern Rockies, another seismic parabola appears by connecting the seismic zones in western Montana and the CTB. Does this parabola share with the YTP common characteristics that suggest a common deformation mechanism? In this study, we explore the spatial correlation between the seismicity in the Northern Rockies and geophysical data sets, such as seismic tomography, gravity, and heat flow, in search of other potential factors to affect the locations of the seismic zones. We focus on comparisons with the upper mantle structures imaged by seismic tomography models. In recent years, high-resolution tomography images have been produced as the rolling deployment of transportable seismometers in the USArray project [*Meltzer et al.*, 1999] finished carpeting the contiguous U.S. in 2013.

1.2 Tectonic Setting and Regional Seismicity

Following the Cretaceous-Eocene crustal thickening due to the Sevier and Laramide orogenies [e.g., *Armstrong and Oriel*, 1965; *Armstrong*, 1968; *Burchfiel and Davis*, 1975; *Allmendinger and Jordan*, 1981], the Intermountain West began undergoing a significant extension in the early Miocene, which formed many normal faults reactivating the Sevier and Laramide thrust faults [e.g., *Stewart*, 1971; *Royse et al.*, 1975; *Zoback and Thompson*, 1978; *Eaton*, 1982; *Dixon*, 1982]. Since ~14 Ma, the broad area of crustal extension has been overprinted by the caldera-forming eruptions of the progressing Yellowstone hotspot, resulting in the formation of the central and eastern SRP [e.g., *Morgan*, 1972; *Smith and Sbar*, 1974; *Armstrong et al.*, 1975] (Figure 1.1).

The active tectonics in the Intermountain West is reflected in Quaternary faulting and high seismicity for the intraplate setting (see Chapter 2 for details on the major faults). In this area, the boundary between active and stable tectonism is marked by the Intermountain Seismic Belt (ISB), an arcuate zone of elevated intraplate seismicity [*Smith and Sbar*, 1974]. The ISB is ~75-300 km wide and 1300 km long, extending from northwestern Montana to northwestern Arizona [*Smith and Arabasz*, 1991] (Figure 1.1). The dominant deformation style in the ISB is tectonic extension characterized by late-Quaternary normal faulting, diffuse shallow, up to ~20 km deep, seismicity, and episodic scarp-forming earthquakes (M6-7.5) [*Smith and Sbar*, 1974; *Smith and Arabasz*, 1991]. To the west of the ISB, late-Cenozoic active extensional deformation is exhibited, while stable cratons of the North American Plate lie to the east with a lower level of seismicity.

Along the northern segment of the ISB, which extends from northwestern Montana to Yellowstone, historical M>6 events have occurred [*Stickney and Bartholomew*, 1987] (Figure 1.1). In the Helena area, the Helena Valley earthquakes (M6.3 and M6.0) occurred in 1935 [*Stickney*, 1978]. Approximately 70 km southeast of Helena, the 1925 M6.8 Montana earthquake occurred in the Clarkston Valley area [*Pardee*, 1926]. The same area also experienced the 1947 M_L6.3 Virginia City earthquake [*Doser*, 1985; 1989]. The largest historical event within the ISB, the 1959 M_S7.5 Hebgen Lake sequence occurred ~50 km northwest of Yellowstone [e.g., *Witkind et al.*, 1962; *Ryall*, 1962; *Tocher*, 1962; *Doser*, 1985].

To the south of Yellowstone, the ISB trends southwest. To the immediate south of Yellowstone is the Yellowstone-Teton region characterized by the Teton fault [*Byrd et al.*, 1994] (Figure 1.1). The Teton fault is seismically active but quiescent for M>3 events [*Smith et al.*, 1990, 1993; *Smith and Arabasz*, 1991]. Geological evidence indicates a potential to produce an earthquake as large as M7.5 [*Smith et al.*, 1993]. The estimated seismic hazard in the area is the highest in the Intermountain West [*Petersen et al.*, 2008].

Along the northern flank of the Snake River Plain is the Centennial Tectonic Belt (CTB; also called Central Idaho Seismic Zone; Figure 1.1), an approximately 350 km long and 80-100 km wide seismic zone, extending from east central Idaho to Yellowstone [*Anders et al.*, 1989]. The CTB is characterized by Holocene normal faulting, which exhibits the basin-range topography similar to that to the south of the SRP [*Stickney and Bartholomew*, 1987]. The well-developed Lost River, Lemhi, and Beaverhead faults are in the western part of the CTB. In 1983, the Lost River fault ruptured in a normal sense as the M_S7.3 Borah Peak earthquake [e.g., *Doser and Smith*, 1985; *Smith et al.*, 1985; *Zollweg and Richins*, 1985; *Richins et al.*, 1987; *Barrientos et al.*, 1987] (Figure 1.1). In 2014, an earthquake swarm consisting of over 100 m_b1.5-4.7 events occurred near Challis, Idaho, about 20-30 km northwest of the focus of the 1983 event [*Pankow et al.*, 2014].

The CTB and the Idaho-Wyoming segment of the ISB together form the Yellowstone Tectonic Parabola (YTP) [*Scott et al.*, 1985ab; *Smith et al.*, 1985], which is centered about the axis of the eastern SRP and the vertex at Yellowstone (Figure 1.1). This seismic parabola is characterized by high topography and late-Cenozoic normal faults striking perpendicular to the parabola axis. Most of the major faults extend to the SRP. However, the distance from the SRP to the locus of each fault's highest slip rate increases as the distance to Yellowstone increases [*Anders et al.*, 1989], resulting in the parabolic pattern of seismicity. *Anders et al.* [1989] suggested that the geometric relationship resulted from the outward migration of the foci of active faulting associated with the progression of the hotspot.

1.3 Method

We explore the spatial correlation between the seismicity in the Northern Rockies and geophysical data sets, such as seismic tomography, gravity, and heat flow data, in search of common characteristics between the YTP and the northern parabola. We focus on comparisons with the upper mantle structures imaged by recent high-resolution seismic tomography models. The comparisons are performed by visual inspection because the regional-scale spatial distribution of the seismicity is the parameter of interest. The earthquake hypocenter data are provided by M. Stickney at the Montana Bureau of Mining and Geology [personal communication, 2013]. Plotted are $M>2$ events at <40 km depths in the year range from 2000 to 2012 (Figure 1.1). A description of each data set is given in the following section with the results. For further analyses, comparisons with the geoid anomaly and shear wave splitting measurements are introduced in Section 1.5.

1.4 Data and Results

The spatial distribution of the seismicity in the Northern Rockies is compared with the distribution of seismic velocity perturbation, gravity, and surface heat flow data. The horizontal and vertical gradients of the velocity perturbation are calculated and compared. Similarities between the YTP and the northern parabola are of particular interest. For the gravity data sets, both Bouguer and free-air anomalies are examined. The significance and implications of each data set are also discussed before each result is presented.

1.4.1 Seismic Tomography Data

We focus on comparisons between the spatial distribution of the seismicity in the Northern Rockies and the underlying upper mantle structures imaged by seismic tomography models. We compare the seismicity to the depth slices of the *S*-wave model by *James et al.* [2011], as well as the horizontal and vertical gradients in velocity perturbation.

The technique of tomography in general is a type of inverse problem to image heterogeneity of a physical property within a medium from observations of the property integrated along a number of paths of penetrating waves. The seismic tomography images Earth's subsurface heterogeneity of seismic velocity perturbation (i.e., deviation from a reference velocity model), using seismic rays [e.g., *Nolet*, 1987]. The seismic velocity perturbation is interpreted primarily as structural, thermal, or compositional variations. For Earth's mantle, thermal variation is thought to be the first-order factor of velocity anomalies, as seismic wave velocities are a function of density and elastic moduli of the medium, both of which vary with changes in temperature. A higher temperature lowers seismic velocities regardless of the type of body wave, and a lower temperature, on the other hand, raises seismic velocities. Therefore, bodies of negative velocity perturbation (i.e., seismic waves traveling slower than a reference velocity model) are interpreted as high-temperature features, such as mantle plumes. Bodies of positive perturbation in seismic imaging indicate low-temperature features, such as subducting slabs.

As another term for seismic tomography, seismic travel time tomography, suggests, this technique uses the travel time perturbations caused by perturbed slowness variations along ray paths. A large number of ray paths that sample the medium in different directions are necessary to improve resolution of tomographic imaging. The resolution of three-dimensional seismic imaging of mantle under the contiguous U.S. drastically improved as the rolling deployment of transportable seismometers in the USArray project [*Meltzer et al.*, 1999] moved across the country from 2004 through 2013. USArray is a component of the EarthScope program, whose goal is to explore the structure and evolution of the North American continent and to understand the processes controlling earthquakes and volcanoes. A major goal of USArray is to collect detailed seismic images of the North American lithosphere. Among four facilities or "observatories" of the USArray project, the most extensive one is the Transportable Array (TA), an array of 400 high-quality broadband seismometers on temporary sites, which has finished marching across the contiguous U.S. in 2013 and is operating in Alaska in 2017. The TA achieved an unprecedented network density with typical station spacing of ~70 km, which enabled a number of high-resolution tomographic models [e.g., *Obrebski et al.*, 2010; 2011; *Schmandt and Humphreys*, 2010; *James et al.*, 2011; *Porritt et al.*, 2011; 2014].

We use the *S*-wave tomography model by *James et al.* [2011], NWUS11-S, as it is one of the tomography models that fully utilizes the EarthScope data for the Western U.S. at the time of conducting this study. The *S*-wave inversion is based on 88,689 rays from 379 teleseismic events obtained primarily from multi-channel cross correlation [*VanDecar and Crosson*, 1990] of recordings at USArray TA and the High Lava Plains seismic experiment [*Eagar et al.*, 2010; *Roth et al.*, 2008], with typical bandpass filter ranges of 0.04-0.15 Hz

[*James et al.*, 2011]. The horizontal and vertical grid spacing of the publicized data are 0.25° and 25 km, respectively. Their *S*-wave model is selected over the *P*-wave model because *S*-wave models, in general, are more sensitive to the melt content, supposedly showing more contrasts between the high- and low-velocity zones at shallow depths in the study area characterized by the hotspot volcanism.

We look for map levels on which patterns of the seismic perturbation well discriminate the areas of high seismicity. We are also interested in areas of high perturbation gradient. High-temperature mantle can cause deformations in the crust through physical processes, such as thermal expansion [e.g., *Parsons and Sclater*, 1977] and increase in thermal elevation [e.g., *Lowry et al.*, 2000]. Therefore, the temperature contrast indicated by a high perturbation gradient could allow for differential stress sufficient to cause earthquakes.

Figure 1.2 shows the tomographic images in the upper mantle depth range (50 – 475 km), superimposed by the outlines of the seismic parabolas (see Appendix 1.1 for images at the greater depths up to 700 km). The most prominent feature is a zone of very strong low-velocity anomalies (< -4%) extending vertically to the ~200 km depth below the entire eastern SRP and Yellowstone. This low-velocity zone (LVZ) coincides with the axis of the YTP, being sandwiched by high-velocity zones (up to +3%; Figure 1.2a-f). This low-velocity body, interpreted as high-temperature buoyant mantle, is consistently imaged by other seismic tomography models [e.g., *Waite et al.*, 2006; *Xue and Allen*, 2007; *James et al.*, 2011; *Obrebski et al.*, 2011; *Schmandt et al.*, 2012; *Porritt et al.*, 2014]. Because this low-velocity anomaly is spatially constrained by the high-velocity zones and does not extend vertically deeper than ~200 km depth (Figure 1.2g-r), some researchers suggest this structure represents passive rising of mantle through a Farallon slab gap and/or around edges of the advancing Farallon slab, rather than an intermittent upwelling [e.g., *Sigloch et al.*, 2008; *James et al.*, 2011; *Porritt et al.*, 2014].

As for the YTP, the LVZ lies along the parabola axis, being bracketed by the high-velocity zones at <200 km depths (Figure1.2a-f). The same pattern is recognized in the northern parabola, although the temperature contrast is small. A zone of relatively low velocity extends from central Idaho to western Montana, with high-velocity zones to its north and south (Figure 1.2a-f). If the velocity contrast in the northern parabola is not a noise, this observation suggests the possibility of the same configuration of upper mantle structures, including a virtual hotspot at the vertex of the northern parabola. This mini-hotspot model is tested with additional geophysical data sets and discussed in Section 1.5.

The horizontal gradients in the velocity perturbation are obtained as follows. For each depth slice, perturbation data within 0.5° from each data point are found. Then, the slope of the best fit plane to the selected data points is adopted as the horizontal gradient of the center point. The plots of the horizontal gradient at shallow depth slices (50–250 km) are shown in Figure 1.3 (see Appendix 1.2 for images at the greater depths up to 700 km). Almost the only prominent pattern is the area of high gradients surrounding the eastern SRP and Yellowstone because of the strong negative anomaly along the SRP. In the depth range where the negative SRP anomaly is not present (200 km and deeper), there is no clear pattern of gradient. The high gradient zone surrounding the eastern SRP is weakly correlated with the YTP although it is not widening southwestward to parallel the parabola pattern (Figure 1.3a-d). The map patterns of the horizontal gradient do not have any notable correlation with the northern parabola.

The vertical gradients represent changes of velocity perturbation in the vertical direction. The gradient is given simply by the division of a difference in data value between two data points of the same horizontal coordinate and two adjacent depth slices over the depth step (25 km). The calculated results are viewed and plotted as values at the average depth between the two depth slices. Figure 1.4 shows the results in the depth range from 62.5 to 487.5 km (see Appendix 1.3 for images at the greater depths up to 700 km). The sign convention is that a value is positive when the perturbation value approaches the positive infinity when the depth decreases (i.e., shallowing). In other words, when a temperature decreases upward, which is expected in the regular geotherm profile, the value of the vertical gradient is positive, which is indicated by the blue spectrum in the figure.

In the plots of the vertical gradients (Figure 1.4), most zones of high vertical gradients appear associated with the strong low-velocity anomaly along the eastern SRP. Below the eastern SRP and Yellowstone, the polarity changes from negative to positive at ~100 km depth (Figure 1.4b-d), and positive to negative at ~400 km depth (Figure 1.4n-o). The temperature drop at <100 km depths is probably due to the transition from asthenosphere to lithosphere. The deeper polarity change at ~400 km from the cooling to warming trends, which could indicate an interruption from course-changing buoyant mantle, is consistent with the idea that the Yellowstone hotspot is not a chimney-like structure [e.g., *Ritsema et al.*, 1999; *Christiansen et al.*, 2002]. No direct correlation is found between the parabolic patterns of the seismicity and the vertical gradient. As for the comparison between the two parabolas, there is a weak warming trend below the northern parabola axis from ~300 km to ~150 km depths (Figure 1.4d-k), which is similar to the YTP axis. This trend also suggests the body of relatively low velocity below the northern parabola axis.

1.4.2 Gravity Data

Gravity anomalies are closely associated with subsurface structures and deformation mechanisms. We also compare the seismicity distribution in the Northern Rockies with the Bouguer and free-air anomalies. The Bouguer anomaly signifies subsurface density contrasts. Simply stated, positive Bouguer anomalies indicate relatively high-density materials at depths, with a large-scale example being uplifted lithospheric mantle as a result of crustal thinning. Conversely, negative Bouguer anomalies represent low-density materials, such as crustal roots, in the context of crustal deformation. The free-air gravity anomaly shows deviations from the isostatic equilibrium. Positive free-air anomalies indicate undercompensation (i.e., floating higher than the equilibrium depth), and negative anomalies overcompensation.

We plot complete Bouguer anomaly and free-air anomaly data compiled by *Pan American Center for Earth & Environmental Studies* (PACES) at University of Texas at El Paso [2015]. The terrain corrections were calculated using a digital elevation model in a method by *Plouff* [1966; see also *Godson and Plouff*, 1988]. For the reduction of the data, latitude and longitude values were referenced to NAD83 (horizontal datum), and elevation values to NGVD88 (vertical datum).

Figure 1.5 shows the complete Bouguer gravity anomaly in the study area. The most distinct pattern is a zone of relatively small (~ -130– -180 mGal) negative anomaly along the eastern SRP surrounded by zones of large negative anomalies, which roughly coincide with the YTP. The highest anomaly values (~-60 mGal) are found in the western part of the study area. The SRP Bouguer gravity high was first reported by *Bonini and Lavin* [1957] and has been studied. The gravity contrast to the surrounding areas has been attributed to a positive mass anomaly within the upper crust probably caused by the volcanics, as well as the crustal thinning along the SRP indicated by seismic refraction data [*Mabey*, 1982]. Yellowstone does not affect the distribution of Bouguer anomaly in the surrounding area (Figure 1.5). A small zone of strong negative anomaly (~-235 mGal) exists at the youngest caldera (Figure 1.5), which may represent Yellowstone's crustal magma sources (see Chapter 2 for detailed description of the magma reservoir). The northern arm of the YTP extends in the area of strong negative anomaly, while the southern arm marks the area of high gradient (Figure 1.5). For the northern parabola, there is little correlation between the pattern of the Bouguer anomaly and the seismicity distribution (Figure 1.5).

The free-air anomaly in the study area is presented in Figure 1.6. This map shows the SRP as a zone of weak anomaly, which indicates the area is in the approximate isostatic equilibrium. In contrast, the map shows a long-wavelength positive anomaly around Yellowstone, suggesting a mass deficit due to an uncompensated topographic swell [*Richards et al.*, 1988; *Waschbusch and McNutt*, 1994; *Smith et al.*, 2009]. In central Idaho and southwestern Montana, basin-range topography is expressed by the free-air anomalies, which alludes to a certain level of lithospheric strength (see Chapter 4 for discussion on the effective elastic thickness of the study area). A notable spatial correlation is not found between the parabolic patterns of seismicity and the free-air anomalies (Figure 1.6).

1.4.3 Surface Heat Flow Data

Studies on seismicity and surface heat flow have found correlations and proposed various potential mechanisms connecting the heat flow and seismicity. For example, relationships between heat flow and the regional frictional strength along the southern segments of the San Andreas fault have been suggested [e.g., *Zhu*, 2016]. For the same region, areas of high heat flow are characterized by swarm-type seismic activities whereas the typical foreshock-mainshock-aftershock sequences occur more in areas with normal or low surface heat flow [*Enescu et al.*, 2009]. *Mogi* [1963] analyzed Japanese earthquake data to find faster aftershock decays in regions of higher crustal temperature. Most studies on this topic discuss cases in specific areas, which indicates a difficulty to propose a universal relationship because additional factors, such as lithology and presence of fluid, also control affect both surface heal flow and seismogenesis.

We plot and compare the surface heat flow data with the seismicity in the Northern Rockies. We use data compiled by the SMU Geothermal Lab [*Blackwell et al.*, 2011], which is shown in Figure 1.7. As predicted by the distribution of the low seismic velocity zone, very high heat flow is observed in Yellowstone and the eastern SRP. Relatively high heat flow is observed in southern Idaho, northwestern Utah, and northeastern Nevada, which probably corresponds to the Basin and Range extension. Perhaps most interesting in this study is the finger of relatively high (~ +10 mW m^{-2}) heat flow extending from north central Idaho to western Montana, coinciding with the zone of relatively low seismic velocity imaged in the tomographic model (Figure 1.2a-f). This feature also suggests the similarity between the northern and southern seismic parabolas.

1.5 The Mini-Hotspot Model

The notable similarity between the YTP and the proposed northern parabola is an elongated zone of relatively low seismic velocities along the axis of each seismic parabola.

The low-velocity (i.e., high-temperature) parabola axes are suggested in the tomography images, vertical gradients of the velocity perturbation, and the heat flow data. If these along-axis anomalies are due to a common upper mantle structure, then the eastern end of the northern parabola axis is the location of a branch of rising mantle underlying the moving North American Plate, as in the case of Yellowstone. However, the signature of the northern parabola axis is weak and therefore may be a mere noise. To test the presence of the LVZ and the miniature hotspot*, we examine the geoid anomaly and shear wave splitting data in this section. We also construct a reference tomography model by applying a technique of seismic trace stacking to the 3-D tomography data sets to study the upper mantle structures that the published tomography models agree on.

1.5.1 Corrected Geoid Height Data

Variations in geoid height are associated with the subsurface density anomalies. With other conditions being equal, a subsurface density deficit causes a negative geoid height, while a high-density subsurface body raises the geoidal surface. If the low-velocity body along the northern parabola axis is substantial, it is indicated as an area of relatively low geoid height.

We use the geoid data of the GEOID12 model in the NAD83 ellipsoid reference frame presented by the *National Geodetic Survey* [2014]. The geoidal surface in the study area is strongly overprinted by the effect of Yellowstone, which needs to be removed to interpret the low-amplitude geoid signatures [cf. *Zuber and Smith*, 1997; *Sprenke et al.*, 2005]. The Yellowstone effect is manifested as an 800 km wide, conical-shaped anomaly of

---

* The name is coined for convenience and may be misnomered because of the potential passive rising of buoyant mantle beneath the Yellowstone area.

up to +15 m, compared to the surrounding area (Figure1.8ab). The anomaly is thought to be resulted from the isostatically uncompensated Yellowstone topographic swell, which surpasses the counter effect of the buoyant low-density mantle causing the topographic swell [*Crough*, 1978, 1983; *Burov et al.*, 2007]. To observe low-amplitude geoid signatures, the best fit axisymmetric Yellowstone anomaly is subtracted from the raw data in the following manner. The area centered at Yellowstone is divided into multiple annuli with the radius increment of the 0.08° angular distance. Larger annular widths would cause discontinuous seams between the annuli. Then, the average geoid value (Figure 1.8c) in each annulus is subtracted from the data to find the residual geoid height.

The corrected geoid map is shown in Figure 1.9. There is a geoid low trending from north central Idaho to western Montana, coinciding with the northern parabola axis. The geoid height in the area is ~1 m lower than the surrounding area. The largest part of the low-geoid area is in the high-elevation Bitterroot Mountains and in the area of moderate- to high-density bedrocks and basement [*Lewis et al.*, 2012]. These factors never act to decrease the geoid height. Therefore, we can conclude that the geoid low results from a density contrast at the mantle depths, which is probably caused by the buoyant low-seismic velocity body along the parabola axis.

1.5.2 Teleseismic Shear Wave Splitting Data

In the context of mantle dynamics, shear wave splitting is a technique for testing the mantle anisotropy due to an olivine crystal alignment associated with the mantle flow and stress state [e.g., *Fuchs*, 1977; *Ando et al.*, 1980; 1983; *Silver and Chan*, 1991; *Vinnik et al.*, 1992; *Silver*, 1996; *Wolfe and Solomon*, 1998]. When an incident shear wave enters an anisotropic medium, the shear wave splits into two polarized shear waves propagating at different speeds. The transverse direction of the faster wave is parallel to the mineral alignment, while the trailing wave oscillates at a different angle, oftentimes near perpendicular to the alignment. This velocity difference together with the traveled distance results in an arrival time delay recorded in the seismogram, indicating the degree of anisotropy in the medium.

The split teleseismic shear-wave analysis reveals the homogeneity of the column below the receiver. When teleseismic data are used for the analyses, it is safe to assume that the result indicates the state of the vertical column in the upper mantle beneath the receiver because of the small (i.e., steep to near vertical) incoming ray path angle. In the vertical column, shear waves can split multiple times causing multiple fast axes if the waves pass through more than two anisotropic layers. Therefore, a large azimuthal variation in fast orientation indicates an inhomogeneity caused by multiple mantle flow regimes and middle- to small-scale mantle structures, such as buoyant mantle meandering up through fragments of a subducting slab. However, it is impossible to determine at what depth each resultant fast axis is caused because the shear wave splitting technique has virtually no vertical resolution by the nature of the method.

We use data from the comprehensive shear wave splitting database for the western and central U.S. presented by *Liu et al.* [2014]. The database contains 16,105 pairs of splitting parameters from teleseismic (84°-180°) events that occurred between 1989 and 2012, and recorded by 1774 broadband seismic stations of the networks, including the USArray TA, IRIS/USGS Global Seismographic Network, US National Seismic Network, GEOSCOPE, and PASSCAL portable seismic arrays.

Figure 1.10 shows the distribution of the circular standard deviation of spatially averaged fast orientations [*Liu et al.*, 2014]. This parameter indicates the degree of complex anisotropy. The standard deviation is ~10° higher in north central Idaho and western Montana along the northern parabola axis than the surrounding areas. This result suggests a structural complexity beneath the area, which may include the upper mantle disturbance due to the elongated LVZ.

1.5.3 Average *S*-Wave Tomography Model from the *N*th-Root Stack

If the mini-hotspot exists in western Montana, there must be a body of high-temperature mantle branching to the location. Although recent tomography models using the USArray data agree on the distribution of large-scale anomaly bodies, discrepancies arise for relatively small features because of differences in method, model parameters, and the data used. For this reason, it is difficult to confidently locate small flows branching out from the main buoyant mantle body. To handle this problem, we construct an average tomography model by applying a technique of seismic trace stacking, the *n*th-root stack [*Muirhead*, 1968; *McFadden et al.*, 1987], to the 3-D tomography data sets.

The *n*th-root stack [*Muirhead*, 1968; *McFadden et al.*, 1987] is a noise reduction technique in multichannel seismic data processing. The linear stack, which is the arithmetic mean of the observations, is a simple, commonly used method low in computational cost. As a downside, it is not very effective when noises are not in the normal distribution. In such cases, the *n*th-root stack, which is the *n*th-power of mean *n*th-root, is effective and yet relatively low in cost. If there are m observations of data t, the *n*th-root stack R of the observations is defined by:

$$R_n = \left[\frac{1}{m}\sum_{i=1}^{m}\sqrt[n]{t_i}\right]^n \qquad (1.1)$$

Signs must be retained in taking both *n*th-power and *n*th-root. Figure 1.11 shows that the *n*th-root stack attains higher signal-to-noise ratios than the linear stack. As a trade-off, very small signals tend to be destructed, as exemplified by the destruction of some side lobes of the wavelets (Figure 1.11de).

We apply the *n*th-root stack to 3-D seismic tomography data to construct an average model. We select *S*-wave models that: (1) use the USArray data as the main data source, (2) are not a joint inversion with surface waves, and (3) have a <0.5° horizontal grid spacing. These criteria select the *S*-wave model by *James et al.* [2011], the *SH*-wave model by *Tian et al.* [2011], and the *SH*- and *SV*-models by *Porritt et al.* [2014]. These data sets are normalized by interpolating them on a common grid (0.2° × 0.2° horizontal × 20 km vertical) and calculating the standard scores (i.e., *z*-scores). Then, the 4th-root stack is applied. The resultant velocity anomalies simply indicate zones that all or most of the used tomographic models agree on, and must be interpreted as strongly smoothed 3-D geometries because of the destruction of very small signals due to the nature of the *n*th-root stack technique.

Figure 1.12 shows the stacking result on horizontal slices at shallow (70-230 km) depths. The zones of strong negative anomalies below the eastern SRP and Yellowstone are predicted as in the *S*-wave models used in the stacking. The LVZ along the northern parabola axis is also well predicted (Figure 1.12a-f). The cross sections of the 4th-root stack model are shown in Figure 1.13. The section A-A′-A″ transects both parabolas, showing a striking similarity between the two parabolas, a central low-velocity body sandwiched by high-velocity bodies (Figure 1.13a). The section B-B′ shows that the low-velocity body branches out at ~200 km depth from the main, high-temperature mantle body, and flows upward around a low-temperature body (Figure 1.13b). Figure 1.14 shows an isosurface (z = 0.09) of the 4th-root stack model. This 3-D render shows the main high-temperature body below the Yellowstone/eastern SRP area branch out at ~200 km depth toward the vertex of the northern seismic parabola. This branching in the average tomography model provides a further evidence for the LVZ along the northern parabola axis as a similarity between the two parabolas.

1.6 Discussion

Through this study, we explore the spatial correlation between the seismicity in the Northern Rockies and seismic tomography data, as well as various geophysical data sets, with a focus on the YTP and proposed northern parabola formed by the northern ISB and CTB. The *S*-wave tomography model by *James et al.* [2011] indicates a weak LVZ along the axis of the northern parabola, which is geometrically identical to the distribution of LVZ in the YTP (Figure 1.2). The surface heat flow data agree with the low-velocity parabola axis by presenting a relatively high heat flow anomaly along the axis (Figure 1.7). Based on these results, we propose the mini-hotspot model to explain the similarity between the two parabolas. This model is supported by: (1) the geoid low along the northern parabola axis after removing the conical-shaped Yellowstone effect (Figure 1.9), (2) the large standard deviation of fast orientations of the splitting shear wave analysis (Figure 1.10), and (3) the low-velocity branch to the northern parabola vertex, flowing along the parabola axis, which is indicated in the average *S*-wave tomography models (Figures 1.12-14).

If the mini-hotspot model is probable, then why is the northern parabola axis not parallel to the motion of the North American plate? Around the vertex, the trend of the LVZ of the northern parabola is nearly parallel to the YTP's low-velocity axis, as well as the North American Plate motion (Figure 1.12a). The source of the low-velocity axis may result from passive rising of the mantle controlled by an interaction with the remnant slabs. As for the origin of Yellowstone, some researchers attribute it to interactions between local conditions in the lithosphere and upper mantle, as opposed to the conventional view of the vertical-column hotspot model [e.g., *Wilson*, 1963; *Burke and Wilson*, 1976; *Crough and Jurdy*, 1980; *Richards et al.*, 1988; *Duncan and Richards*, 1991]. *Christiansen et al.* [2002] propose that Yellowstone's upper mantle origin is affected by preexisting structures, such as the subducting Farallon slab, based on the lack of plume-like structure indicated in an early tomographic model [*Ritsema et al.*, 1999]. Presenting tomographic images using the USArray data, *James et al.*, [2011] suggest a subduction-related process where the LVZ beneath the eastern SRP and Yellowstone results from the flows around the fragmented Farallon slab. These observations suggest that the trend of the low-velocity feature below the northern parabola can be easily controlled by the configuration of lithospheric structures. The result of the 4th-root stack indicates that both branching out from the main high-temperature body and flowing westward along the northern parabola axis are around low-temperature bodies interpreted as the fragmented Farallon slab [e.g., *James et al.*, 2011] (Figures 1.12 and 1.13b). Therefore, the course of the branching low-velocity body is likely to be determined by an advancing slab pushing the mantle to flow around the edges, and a fragmented slab forcing it to flow through the gaps.

For the YTP, *Anders et al.* [1989] suggest that the loci of high slip rate along the major faults migrated away from the YTP axis after Yellowstone passed by. This model can be tested for the northern parabola through geological studies on the development history of the major faults since Miocene time.

Conclusions

The comparisons between the seismicity distribution and the upper mantle structures revealed a common geometrical pattern between the two seismic parabolas: an LVZ along each seismic parabola in the depth range up to 200 km. This commonality may suggest the same mechanism responsible for the parabolic distribution of the seismicity. Although the signal of the northern parabola LVZ is weak, the following finding directly or indirectly suggest the presence of a low-velocity body.

1. A zone of relatively high (~ +10 mW m^{-2}) heat flow extends from north central Idaho to western Montana along the northern parabola axis.
2. The corrected geoid height of the study area shows an along-axis geoid low, which is ~1 m lower than the surrounding area, in the northern parabola. Being in a mountainous area, the negative geoidal anomaly suggests a mantle origin.
3. A shear wave splitting analysis presents the spatial distribution of the standard deviation of fast orientations, which indicates that the values are ~10° higher along the norther parabola axis than the surrounding areas. This result suggests a structural complexity beneath the area, which may include the disturbance due to the elongated LVZ.

4. The average *S*-wave model shows the low-velocity body below Yellowstone branch out at ~200 km depth and passively rise around high-velocity bodies, which may represent fragments of an advancing slab, toward the northern parabola axis.

References

Allmendinger, R. W., and T. E. Jordan (1981), Mesozoic evolution, hinterland of the Sevier orogenic belt, *Geology*, *9*(7), 308–313, doi:10.1130/0091-7613(1981)9<308:MEHOTS>2.0.CO;2.

Anders, M. H., and J. W. Geissman (1983), Late Cenozoic evolution of Swan Valley, Idaho, *Eos Trans. AGU*, *64*(45), 858, doi:10.1029/EO064i045p00657.

Anders, M. H., and L. A. Piety (1988), Late Cenozoic displacement history of the Grand Valley, Snake River and Star Valley faults, southeastern Idaho, *Geol. Soc. Am. Abstr. Programs*, *20*(4), 44.

Anders, M. H., J. W. Geissman, L. A. Piety, and J. T. Sullivan (1989), Parabolic distribution of circumeastern Snake River Plain seismicity and latest Quaternary faulting: Migratory pattern and association with the Yellowstone hotspot, *J. Geophys. Res.*, *94*(B2), 1589–1621, doi:10.1029/JB094iB02p01589.

Ando, M., Y. Ishikawa, and H. Wada (1980), S-wave anisotropy in the upper mantle under a volcanic area in Japan, *Nature*, 286, 43–46, doi:10.1038/286043a0.

Ando, M., Y. Ishikawa, and F. Yamazaki (1983), Shear wave polarization anisotropy in the upper mantle beneath Honshu, Japan, *J. Geophys. Res.*, 88(B7), 5850–5864, doi:10.1029/JB088iB07p05850.

Armstrong, F. C., and S. S. Oriel (1965), Tectonic development of Idaho-Wyoming thrust belt, *AAPG Bull.*, *49*(11), 1847–1866.

Armstrong, R. L. (1968), Sevier orogenic belt in Nevada and Utah, *Geol. Soc. Am. Bull.*, *79*(4), 429–458, doi:10.1130/0016-7606(1968)79[429:SOBINA]2.0.CO;2.

Armstrong, R. L., W. P. Leeman, and H. E. Malde (1975), K-Ar dating, Quaternary and Neogene volcanic rocks of the Snake River Plain, Idaho, *Am. J. Sci.*, *275*(3), 225–251, doi:10.2475/ajs.275.3.225.

Barrientos, S. E., R. S. Stein, and S. N. Ward (1987), Comparison of the 1959 Hebgen Lake, Montana and the 1983 Borah Peak, Idaho, earthquakes from geodetic observations, *Bull. Seism. Soc. Am.*, *77*(3), 784–808.

Becker, T. W., A. R. Lowry, C. Faccenna, B. Schmandt, A. Borsa, and C. Yu (2015), Western US intermountain seismicity caused by changes in upper mantle flow, *Nature*, *524*, 458–461, doi:10.1038/nature14867.

Blackwell, D., M. Richards, Z. Frone, J. Batir, A. Ruzo, R. Dingwall, and M. Williams (2011), Temperature-at-depth maps for the conterminous US and geothermal resource estimates, *GRC Trans.*, *35*, 1545–1550.

Bonini, W. E., and P. M. Lavin (1975), Gravity anomalies in southern Idaho and southwestern Montana, *Geol. Soc. Am. Bull.*, 68(12), 1702.

Burchfiel, B. C., and G. S. Davis (1975), Nature and controls of Cordilleran orogenesis, Western United States: Extensions of an earlier synthesis, *Am. J. Sci.*, *275-A*, 363–396.

Burke, K., and J. T. Wilson (1976), Hotspots on the Earth's surface, *Sci. Am.*, *235*(2), 46–57.

Burov, E., L. Guillou-Frottier, E. d'Acremont, L. Le Pourhiet, and S. Cloetingh (2007), Plume head–lithosphere interactions near intra-continental plate boundaries, *Tectonophysics*, *434*(1–4), 15–38, doi:10.1016/j.tecto.2007.01.002.

Byrd, J. O. D., R. B. Smith, and J. W. Geissman (1994), The Teton fault, Wyoming: Topographic signature, neotectonics, and mechanisms of deformation, *J. Geophys. Res.*, *99*(B10), 20095–20122, doi:10.1029/94JB00281.

Christiansen, R. L., G. R. Foulger, and J. R. Evans (2002), Upper-mantle origin of the Yellowstone hotspot, *Geol. Soc. Am. Bull.*, *114*(10), 1245–1256, doi:10.1130/0016-7606(2002)114<1245:UMOOTY>2.0.CO;2.

Crough, S. T. (1978), Thermal origin of mid-plate hot-spot swells, *Geophys. J. R. Astr. Soc.*, 55(2), 451–469, doi:10.1111/j.1365-246X.1978.tb04282.x.

Crough, S. T. (1983), Hotspot swells, *Ann. Rev. Earth Planet. Sci.*, *11*, 165–193, doi:10.1146/annurev.ea.11.050183.001121.

Crough, S. T., and D. M. Jurdy (1980), Subducted lithosphere, hotspots, and the geoid, *Earth Planet. Sci. Lett.*, *48*(1),15–22, doi:10.1016/0012-821X(80)90165-X.

Dixon, J. S. (1982), Regional Structural Synthesis, Wyoming Salient of Western Overthrust Belt, *AAPG Bull*., 66(10), 1560–1580.

Doser, D. I. (1985), Source parameters and faulting processes of the 1959 Hebgen Lake, Montana, earthquake sequence, *J. Geophys. Res.*, *90*(B6), 4537–4555, doi:10.1029/JB090iB06p04537.

Doser, D. I. (1989), Source parameters of Montana earthquakes (1925-1964) and tectonic deformation in the northern Intermountain Seismic Belt, *Bull. Seism. Soc. Am.*, *79*(1), 31–51.

Doser, D. I., and R. B. Smith (1985), Source parameters of the 28 October 1983 Borah Peak, Idaho, Earthquake from body wave analysis, *Bull. Seism. Soc. Am.*, *75*(4), 1041–1051.

Duncan, R. A., and M. A. Richards (1991), Hotspots, mantle plumes, flood basalts, and true polar wander, *Rev. Geophys.*, *29*(1), 31–50, doi:10.1029/90RG02372.

Eagar, K. C., M. J. Fouch, and D. E. James (2010), Receiver function imaging of upper mantle complexity beneath the Pacific Northwest, United States, *Earth Planet. Sci. Lett.*, *297*(1-2), 141–153, doi:10.1016/j.epsl.2010.06.015.

Eaton, G. P. (1979a), A plate-tectonic model for late Cenozoic crustal spreading in the western United States, in *Rio Grande Rift: Tectonics and Magmatism*, edited by R. E. Riecker, pp. 7–32, AGU, Washington, D. C.

Eaton, G. P. (1979b), Regional geophysics, Cenozoic tectonics, and geologic resources of the Basin and Range Province and adjoining regions, in *1979 Basin and Range Symposium*, edited by G. W. Newman, and H. D. Goode, pp. 11–39, Rocky Mtn. Assoc. Geol. and Utah Geol. Assoc., Denver, CO.

Eaton, G. P. (1980), Geophysical and geological characteristics of the crust of the Basin and Range province, in *Continental Tectonics, studies in geophysics*, pp. 96-113, National Academy of Sciences, Washington, D.C.

Eaton, G. P. (1982), THE BASIN AND RANGE PROVINCE: Origin and Tectonic Significance, *Ann. Rev. Earth Planet. Sci*., *10*, 409–440, doi:10.1146/annurev.ea.10.050182.002205.

Enescu, B., S. Hainzl, and Y. Ben-Zion (2009), Correlations of Seismicity Patterns in Southern California with Surface Heat Flow Data, *Bull. Seism. Soc. Am.*, *99*(6), 3114–3123, doi:10.1785/0120080038.

Fuchs, K. (1977), Seismic anisotropy of the subcrustal lithosphere as evidence for dynamical processes in the upper mantle, *Geophys. J. R. Astr. Soc*, *49*, 167–179, doi:10.1111/j.1365-246X.1977.tb03707.x

Furlong, K. P. (1979), An analytic stress model applied to the Snake River Plain (northern Basin and Range province, U.S.A.), *Tectonophysics*, *58*(3-4), T1 l–T15, doi:10.1016/0040-1951(79)90308-1.

Godson, R., and D. Plouff (1988), BOUGUER version 1.0—A microcomputer gravity-terrain-correction program, *U.S. Geol. Surv. Open File Rep.*, *88-644-A-C*.

Hampel, A., R. Hetzel, and A. L. Densmore (2007), Postglacial slip-rate increase on the Teton normal fault, northern Basin and Range Province, caused by melting of the Yellowstone ice cap and deglaciation of the Teton Range?, *Geology*, *35*(12), 1107–1110, doi:10.1130/G24093A.1.

Herrmann, R. B., H. Benz, and C. J. Ammon (2011), Monitoring the Earthquake Source Process in North America, *Bull. Seism. Soc. Am.*, *101*(6), 2609–2625, doi:10.1785/0120110095.

James, D. E., M. J. Fouch, R. W. Carlson, and J. B. Roth (2011), Slab fragmentation, edge flow and the origin of the Yellowstone hotspot track, *Earth Planet. Sci. Lett.*, *311*(1–2), 124–135, doi:10.1016/j.epsl.2011.09.007.

Lawrence, R. D. (1976), Strike-slip faulting terminates the Basin and Range province in Oregon, *Geol. Soc. Am. Bull.*, *87*(6), 846–850, doi:10.1130/0016-7606(1976)87<846: SFTTBA>2.0.CO;2.

Levander, A., and M. S. Miller (2012), Evolutionary aspects of lithosphere discontinuity structure in the western U.S., *Geochem. Geophys. Geosyst.*, *13*(7), Q0AK07, doi:10.1029/2012GC004056.

Lewis, R. S., P. K. Link, L. R. Stanford, and S. P. Long (2012), Geologic Map of Idaho, Idaho Geol. Surv.

Liu, M., and Y. Shen (1998), Crustal collapse, mantle upwelling, and Cenozoic extension in the North American Cordillera, *Tectonics*, *17*(2), 311–321, doi:10.1029/98TC00313.

Liu, K. H., A. Elsheikh, A. Lemnifi, U. Purevsuren, M. Ray, H. Refayee, B. Yang, Y. Yu, and S. S. Gao (2014), A uniform database of teleseismic shear wave splitting measurements for the western and central United States, *Geochem. Geophys. Geosyst.*, *15*, 2075–2085, doi:10.1002/2014GC005267.

Lowry, A. R., and R. B. Smith (1995), Strength and rheology of the western U.S. Cordillera, *J. Geophys. Res.*, *100*(B9), 17947–17963, doi:10.1029/95JB00747.

Lowry, A. R., N. M. Ribe, and R. B. Smith (2000), Dynamic elevation of the Cordillera, western United States, *J. Geophys. Res.*, *105*(B10), 23371–23390, doi:10.1029/2000JB900182.

Mabey, D. R. (1982), Geophysics and tectonics of the Snake River Plain, Idaho, in *Cenozoic Geology of Idaho*, edited by B. Bonnichsen and R. M. Breckenridge, pp. 139–153, Idaho Bureau of Mines and Geology Bulletin.

McCaffrey, R., A. I. Qamar, R. W. King, R. Wells, G. Khazaradze, C. A. Williams, C. W. Stevens, J. J. Vollick, and P. C. Zwick (2007), Fault locking, block rotation and crustal deformation in the Pacific Northwest, *Geophys. J. Int.*, *169*(3), 1315–1340, doi:10.1111/j.1365-246X.2007.03371.x.

McFadden, P. L., B. J. Drummond, and S. Kravis (1987), The *N*th-root stack: A cheap and effective processing technique, *Explor. Geophys.*, *18*(1/2), 135–137, doi:10.1071/EG987135.

Meltzer, A. et al. (1999), USArray Initiative, *GSA Today*, *9*(11), 8–10.

Mogi, K. (1963), Some discussions on aftershocks, foreshocks, and earthquake swarms–the fracture of a semi-infinite body caused by an inner stress origin and its relation to the earthquake phenomena, *Bull. Earthquake. Res. Inst.*, *41*, 615–658.

Morgan, W. J. (1972), Deep mantle convection plume and plate motions, *AAPG Bull.*, *56*(2), 203–213.

Muirhead, K. J. (1968), Eliminating false alarms when detecting seismic events automatically, *Nature*, 217, 533–534, doi:10.1038/217533a0.

Myers, W. B., and W. Hamilton (1964), Deformation accompanying the Hebgen Lake earthquake of August 17, 1959, *U.S. Geol. Surv. Prof. Pap. 435-I*, U.S. Gov. Print. Off., Washington, D. C.

National Geodetic Survey (2012), GEOID12. Available at: https://www.ngs.noaa.gov/GEOID/GEOID12/ (accessed 1 January 2017).

Nolet, G. (1987), Seismic wave propagation and seismic tomography, in *Seismic Tomography with Applications in Global Seismology and Exploration Geophysics*, edited by G. Nolet, pp. 1–23, Reidel Publishing Company, Netherlands.

Obrebski, M., R. M. Allen, F. Pollitz, and S.-H. Hung (2011), Lithosphere-asthenosphere interaction beneath the western United States from the joint inversion of body-wave traveltimes and surface-wave phase velocities, *Geophys. J. Int.*, *185*(2), 1003–1021, doi:10.1111/j.1365-246X.2011.04990.x.

Pan American Center for Earth & Environmental Studies (2015), Gravity Database of the US - Office of Research and Sponsored Projects. Available at: http://research.utep.edu/default.aspx?tabid=37229 (accessed 1 October 2015).

Pankow, K. L., M. Stickney, K. D. Koper, and K. M. Whidden (2014), The 2014 Challis, Idaho Earthquake Swarm, in 2014 AGU Fall Meeting, 2014 Dec 15–19, San Francisco, California.

Pardee, J. T. (1926), The Montana earthquake of June 27, 1925, *U.S. Geol. Surv. Prof. Pap. 147*, U.S. Gov. Print. Off., Washington, D. C.

Pardee, J. T. (1950), Late Cenozoic block faulting in western Montana, *Geol. Soc. Am. Bull.*, *61*(4), 359–406, doi:10.1130/0016-7606(1950)61[359:LCBFIW]2.0.CO;2.

Parsons, B., and J. G. Sclater (1977), An analysis of the variation of ocean floor bathymetry and heat flow with age, *J. Geophys. Res.*, *82*(5), 803–827, doi:10.1029/JB082i005p00803.

Payne, S. J., R. McCaffrey, R. W. King, and S. A. Kattenhorn (2012), A new interpretation of deformation rates in the Snake River Plain and adjacent basin and range regions based on GPS measurements, *Geophys. J. Int.*, *189*(1), 101–122. doi:10.1111/j.1365-246X.2012.05370.x.

Petersen, M. D., A. D. Frankel, S. C. Harmsen, C. S. Mueller, K. M. Haller, R. L. Wheeler, R. L. Wesson, Y. Zeng, O. S. Boyd, D. M. Perkins, N. Luco, E. H. Field, C. J. Wills, and K. S. Rukstales (2008), Documentation for the 2008 update of the United States National Seismic Hazard Maps, *U.S. Geol. Surv. Open File Rep., 2008-1128*.

Pierce, K. L., and W. E. Scott (1986), Migration of faulting along and outward from the track of thermo-volcanic activity in the eastern Snake River Plain region during the last 15 m.y., *Eos Trans. AGU*, *67*(44), 1225.

Pierce, K. L., W. E. Scott, and L. A. Morgan (1988), Eastern Snake River Plain neotectonics: Faulting in last 15 Ma migrates along and outward from the Yellowstone "hotspot" track, *Geol. Soc. Am. Abstr. Programs*, *20*(4), 463.

Plouff, D. (1966), Digital terrain corrections based on geographic coordinates (abs.), *Geophysics*., *31*(6), 1208.

Porritt, R. W., R. M. Allen, D. C. Boyarko, and M. R. Brudzinski (2011), Investigation of Cascadia segmentation with ambient noise tomography, *Earth Planet. Sci. Lett.*, *309*(1–2), 67–76, doi:10.1016/j.epsl.2011.06.026.

Porritt, R. W., R. M. Allen, and F. F. Pollitz (2014), Seismic imaging east of the Rocky Mountains with USArray, *Earth Planet. Sci. Lett.*, *402*, 16–25, doi:10.1016/j.epsl.2013.10.034.

Reynolds, M. W. (1979), Character and extent of Basin-Range faulting, western Montana and east-central Idaho, in *1979 Basin and Range Symposium*, edited by G. W. Newman, and H. D. Goode, pp. 185–193, Rocky Mtn. Assoc. Geol. and Utah Geol. Assoc., Denver, CO.

Richards, M. A., B. H. Hager, and N. H. Sleep (1988), Dynamically supported geoid highs over hotspots: Observation and theory, *J. Geophys. Res.*, *93*(B7), 7690–7708, doi:10.1029/JB093iB07p07690.

Richins, W. D., J. C. Pechmann, R. B. Smith, C. J. Langer, S. K. Goter, J. E. Zollweg, and J. J. King (1987), The 1983 Borah Peak, Idaho, earthquake and its aftershocks, *Bull. Seism. Soc. Am.*, *77*(3), 694–723.

Ritsema, J., H. J. van Heijst, J. H. Woodhouse (1999), Complex shear wave velocity structure imaged beneath Africa and Iceland, *Science*, *286*(5446), 1925–1928, doi:10.1126/science.286.5446.1925.

Roth, J. B., M. J. Fouch, D. E. James, and R. W. Carlson (2008), Three-dimensional seismic velocity structure of the northwestern United States, *Geophys. Res. Lett.*, *35*, L15304, doi:10.1029/2008GL034669.

Royse, F., Jr., M. A. Warner, and D. L. Reese (1975), Thrust belt structural geometry and related stratigraphic problems, Wyoming-Idaho-northern Utah, in *Deep Drilling Frontiers of the Central Rocky Mountains*, edited by D. W. Bolyard, pp. 41–54, Rocky Mountain Association of Geologists, Denver, CO.

Ryall, A. (1962), The Hebgen Lake, Montana, earthquake of August 18, 1959: *P* waves, *Bull. Seism. Soc. Am.*, *52*(2), 235–271.

Sbar, M. L., M. Barazangi, J. Dorman, C. H. Scholz, and R. B. Smith (1972), Tectonics of the Intermountain Seismic Belt, Western United States: Microearthquake Seismicity and Composite Fault Plane Solutions, *Geol. Soc. Am. Bull.*, *83*, 13–28, doi:10.1130/0016-7606(1972)83[13:TOTISB]2.0.CO;2.

Schmandt, B., and E. Humphreys (2010), Complex subduction and small-scale convection revealed by body-wave tomography of the western United States upper mantle, *Earth Planet. Sci. Lett.*, *297*(3–4), 435–445, doi:10.1016/j.epsl.2010.06.047.

Schmandt, B., K. Dueker, E. Humphreys, S. Hansen (2012), Hot mantle upwelling across the 660 beneath Yellowstone, *Earth Planet. Sci. Lett.*, 331–332, 224–236, doi:10.1016/j.epsl.2012.03.025.

Scott, W. E., K. L. Pierce, and M. H. Hait Jr. (1985a), Quaternary tectonic setting of the 1983 Borah Peak earthquake, central Idaho. in *Proceedings of Conference XXVIII - The Borah Peak earthquake*, edited by R. S. Stein and R. C. Bucknam, pp. 1–26.

Scott, W. E., K. L. Pierce, and M. H. Hait Jr. (1985b), Quaternary tectonic setting of the 1983 Borah Peak earthquake, central Idaho, *Bull. Seism. Soc. Am.*, *75*, 1053–1066.

Sigloch, K., N. McQuarrie, and G. Nolet (2008), Two-stage subduction history under North America inferred from multiple-frequency tomography, *Nat. Geosci.*, *1*, 458–462, doi:10.1038/ngeo231.

Silver, P. G., and W. W. Chan (1991), Shear wave splitting and subcontinental mantle deformation, *J. Geophys. Res.*, *96*(B10), 16429–16454, doi:10.1029/91JB00899.

Smith, R. B., and W. J. Arabasz (1991), Seismicity of the Intermountain seismic belt, in *GSA Decade Map Vol. 1*, edited by D. B. Slemmons, E. R. Engdahl, M. D. Zoback, and D. D. Blackwell, pp. 185–228.

Smith, R. B., and M. L. Sbar (1974), Contemporary tectonics and seismicity of the western United States with emphasis on the Intermountain Seismic Belt, *Geol. Soc. Am. Bull.*, *85*(8), 1205–1218, doi:10.1130/ 0016–7606(1974)85<1205:CTASOT>2.0.CO;2.

Smith, R. B. W. D., Richins, and D. I. Doser (1985), The 1983 Borah Peak, Idaho earthquake: regional seismicity, kinematics of faulting, and tectonic mechanism, *U.S. Geol. Surv. Open File Rep*. *85-290*, 236–263.

Smith, R. B., J. O. D. Byrd, and D. D. Susong (1990), Neotectonics and structural evolution of the Teton fault, in *Geologic field tours of western Wyoming and parts of adjacent Idaho, Montana, and Utah*, edited by S. Roberts, *Geological Survey of Wyoming Public Information Circular*, *29*, 126–138.

Smith, R. B., J. O. D. Byrd, and D. D. Susong (1993), The Teton fault, Wyoming: Seismotectonics, Quaternary history, and earthquake hazards, in *Geology of Wyoming*, edited by A. W. Snoke, J. R. Steidtmann, and S. M. Roberts, *Geological Survey of Wyoming Memoir*, *5*, 628–667.

Smith, R. B., M. Jordan, B. Steinberger, C. M. Puskas, J. Farrell, G. P. Waite, S. Husen, W. L. Chang, and R. O'Connell (2009), Geodynamics of the Yellowstone hotspot and mantle plume: Seismic and GPS imaging, kinematics, and mantle flow, *J. Volcanol. Geotherm. Res.*, *188*(1), 26–56, doi:10.1016/j.jvolgeores.2009.08.020.

Sprenke, K. F., L. L. Baker, A. F. Williams (2005), Polar wander on Mars: Evidence in the geoid, *Icarus*, *174*(2), 486–489, doi:10.1016/j.icarus.2004.11.009.

Silver, P. G. (1996), Seismic anisotropy beneath the continents: Probing the depths of geology, *Ann. Rev. Earth Planet. Sci.*, 24, 385–432, doi:10.1146/annurev.earth.24.1.385.

Stewart, J. H. (1971). Basin and Range structure: A system of horsts and grabens produced by deep-seated extension, *Geol. Soc. Am. Bull.*, *82*(4), 1019–1044, doi:10.1130/0016-7606(1971)82[1019:BARSAS]2.0.CO;2.

Stickney, M. C. (1978), Seismicity and faulting of central western Montana, *Northwest Geology*, *7*, 1–9.

Stickney, M.C. (2015), Seismicity within and adjacent to the eastern Lewis and Clark Line, west-central Montana, *Northwest Geology*, *44*, 19–36.

Stickney, M. C., and M. J. Bartholomew (1987), Seismicity and late Quaternary faulting of the northern Basin and Range Province, Montana and Idaho, *Bull. Seism. Soc. Am.*, *77*(5), 1602–1625.

Tian, Y., Y. Zhou, K. Sigloch, G. Nolet, and G. Laske (2011), Structure of North American mantle constrained by simultaneous inversion of multiple-frequency *SH*, *SS*, and Love waves, *J. Geophys. Res.*, *116*, B02307, doi:10.1029/2010JB007704.

Tocher, D. (1962), The Hebgen Lake, Montana, earthquake of August 17, 1959, MST, *Bull. Seism. Soc. Am.*, *52*(2), 153–162.

VanDecar, J. C., and R. S. Crosson (1990), Determination of teleseismic relative phase arrival times using multi-channel cross-correlation and least squares, *Bull. Seism. Soc. Am.*, *80*(1), 150–159.

Vinnik, L. P., L. I. Makeyeva, A. Milev, and A. Y. Usenko (1992), Global patterns of azimuthal anisotropy and deformations in the continental mantle, *Geophys. J. Int.*, *111*(3), 433–447, doi:10.1111/j.1365-246X.1992.tb02102.x

Waite, G. P., R. B. Smith, and R. M. Allen (2006), V_P and V_S structure of the Yellowstone hot spot from teleseismic tomography: Evidence for an upper mantle plume, *J. Geophys. Res.*, *111*, B04303, doi:10.1029/2005JB003867.

Waschbusch, P. J., M. K. McNutt (1994), Yellowstone: A continental midplate (hot spot) swell, *Geophys. Res. Lett.*, *21*(16), 1703–1706, doi:10.1029/94GL00429.

Wilson, J. T. (1963), A possible origin of the Hawaiian Islands, *Can. J. Phys.*, 41,863–870.

Witkind, I. J., W. B. Myers, J. B. Hadley, W. Hamilton, and G. D. Fraser (1962), Geologic Features of the Earthquake at Hebgen Lake, Montana, August 17, 1959, *Bull. Seism. Soc. Am.*, *52*(2), 163–180.

Wolfe, C. J., and S. C. Solomon (1998), Shear-wave splitting and implications for mantle flow beneath the MELT region of the East Pacific Rise, *Science*, *280*(5367), 1230–1232, doi:10.1126/science.280.5367.1230.

Xue, M., and R. M. Allen (2007), The fate of the Juan de Fuca plate: Implications for a Yellowstone plume head, Earth Planet. Sci. Lett., 264(1–2), 266–276, doi:10.1016/j.epsl.2007.09.047.

Zhu, P. P. (2016), Frictional strength and heat flow of southern San Andreas Fault, *J. Seism.*, *20*(1), 291-304, doi:10.1007/s10950-015-9527-7.

Zoback, M. L., and G. A. Thompson (1978), Basin and Range rifting in northern Nevada: Clues from a mid-Miocene rift and its subsequent offsets, *Geology*, *6*(2), 111–116, doi:10.1130/0091-7613(1978)6<111:BARRIN>2.0.CO;2.

Zoback, M. L., and M. Zoback (1980), State of stress in the conterminous United States, *J. Geophys. Res.*, *85*(B11), 6113–6156, doi:10.1029/JB085iB11p06113.

Zollweg, J. E., and W. D. Richins (1985), Later aftershocks of the 1983 Borah Peak, Idaho, earthquake and related activity in central Idaho, *U.S. Geol. Surv. Open File Rep.*, *85-290*, 345–367.

Zuber, M. T., and D. E. Smith (1997), Mars without Tharsis, *J. Geophys. Res.*, *102*(E12), 28673–28685, doi:10.1029/97JE02527.

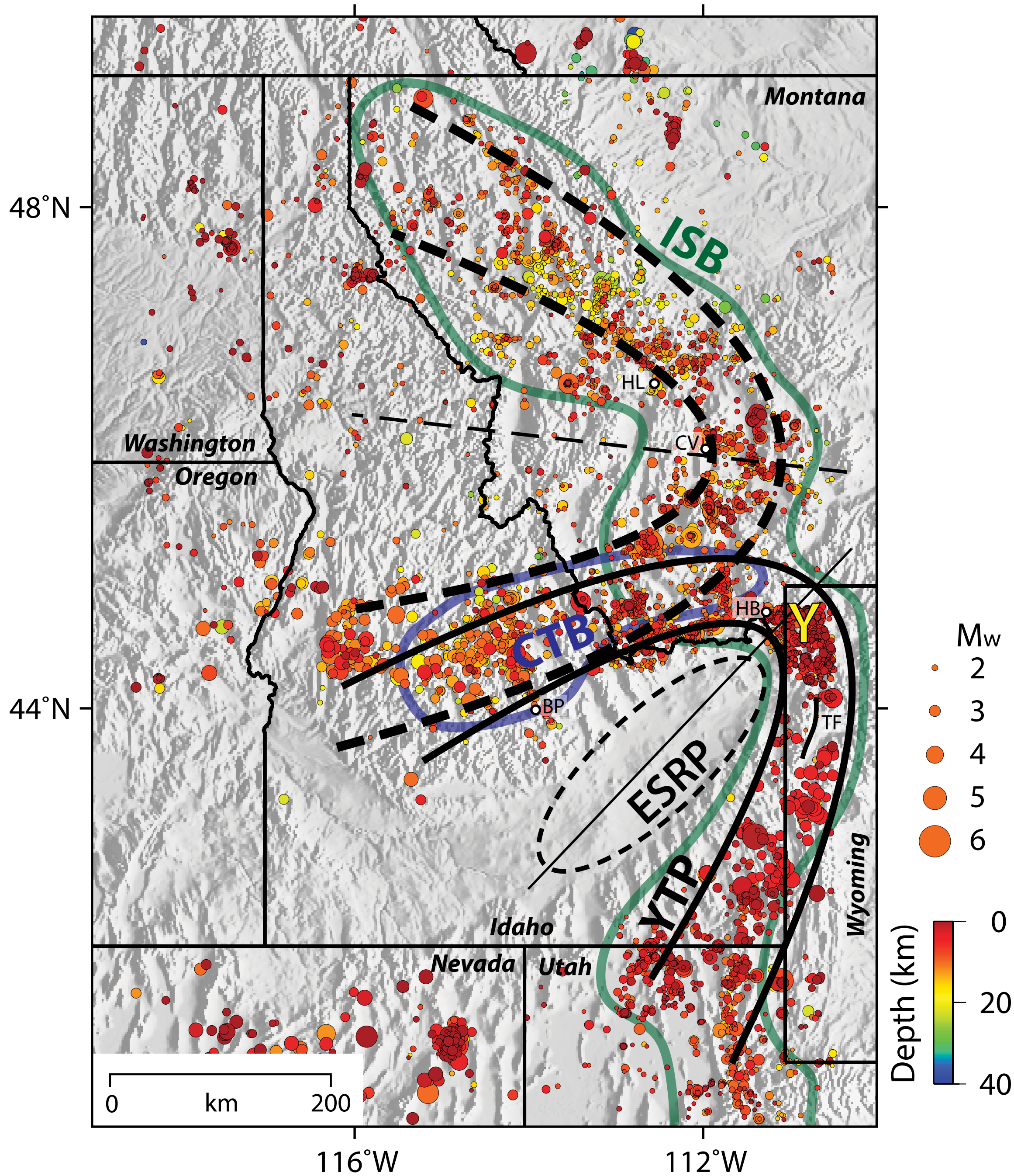

Figure 1.1. Regional seismicity and seismic zones. Earthquake epicenters (dots; M>1.5; 2000-2012) [M.C. Stickney, personal communication, 2013] are scaled by magnitude and color-coded by focal depth. White dots represent the epicenters of the historical events mentioned in text (HL: Helena, CV: Clarkston Valley, HB: Hebgen Lake, BP: Borah Peak). Major seismic zones in the map area are the Intermountain Seismic Belt (ISB; green outline), Centennial Tectonic Belt (CTB; blue outline), and Yellowstone Tectonic Parabola (black outline). The proposed northern seismic parabola is outlined by thick black dashed lines. The axis of each parabola is also shown. Annotations are given for the eastern Snake River Plain (ESRP; thin dashed outline), Yellowstone (Y), and Teton fault (TF).

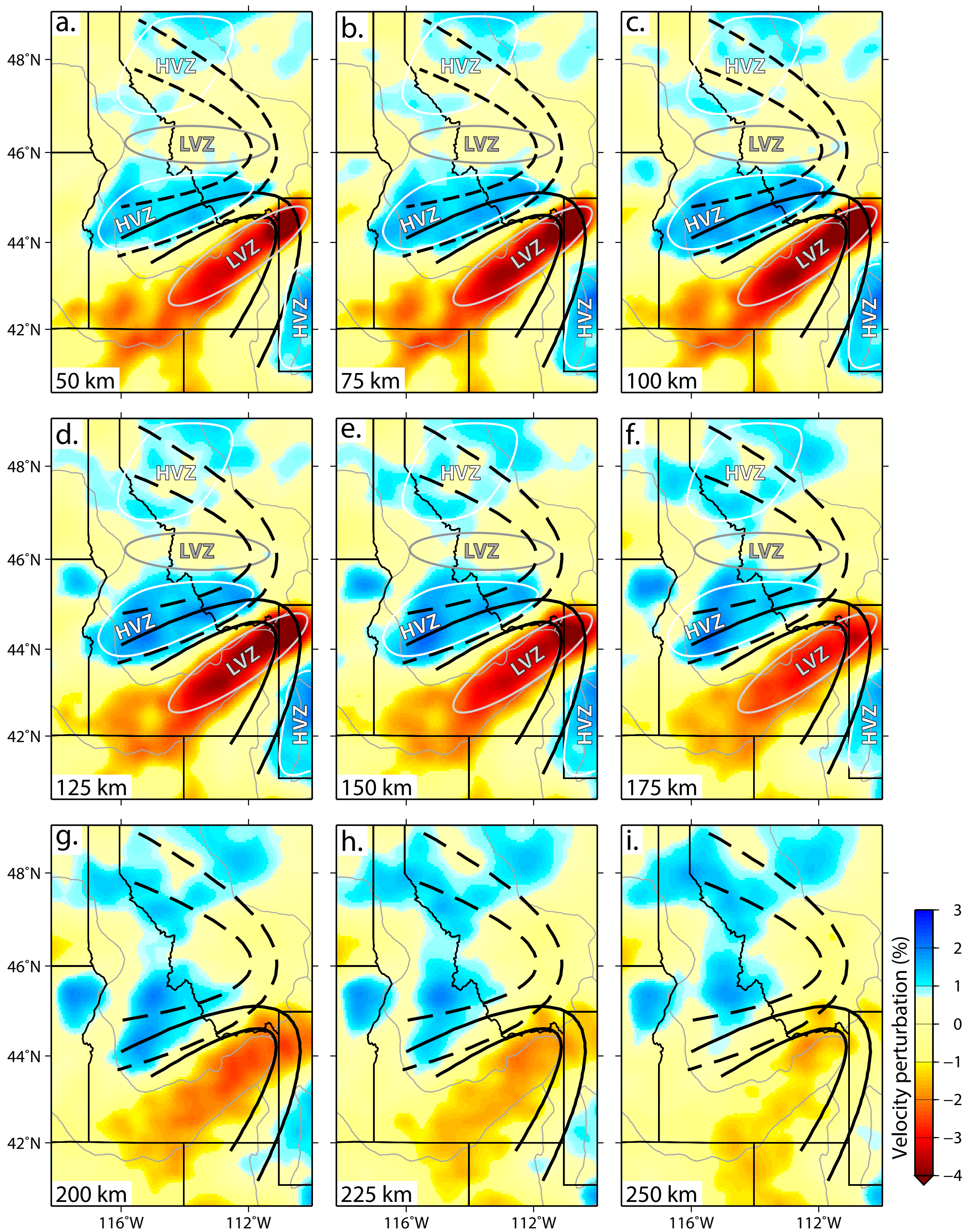

Figure 1.2. Horizontal sections of the *S*-wave tomography model of *James et al.* [2011]. Depths for (a–r) are given in lower left-hand corner. The Yellowstone Tectonic Parabola and proposed northern parabola are outlined by solid and dashed lines, respectively. High- and low-velocity zones (HVZ; LVZ) at shallow depths are delineated.

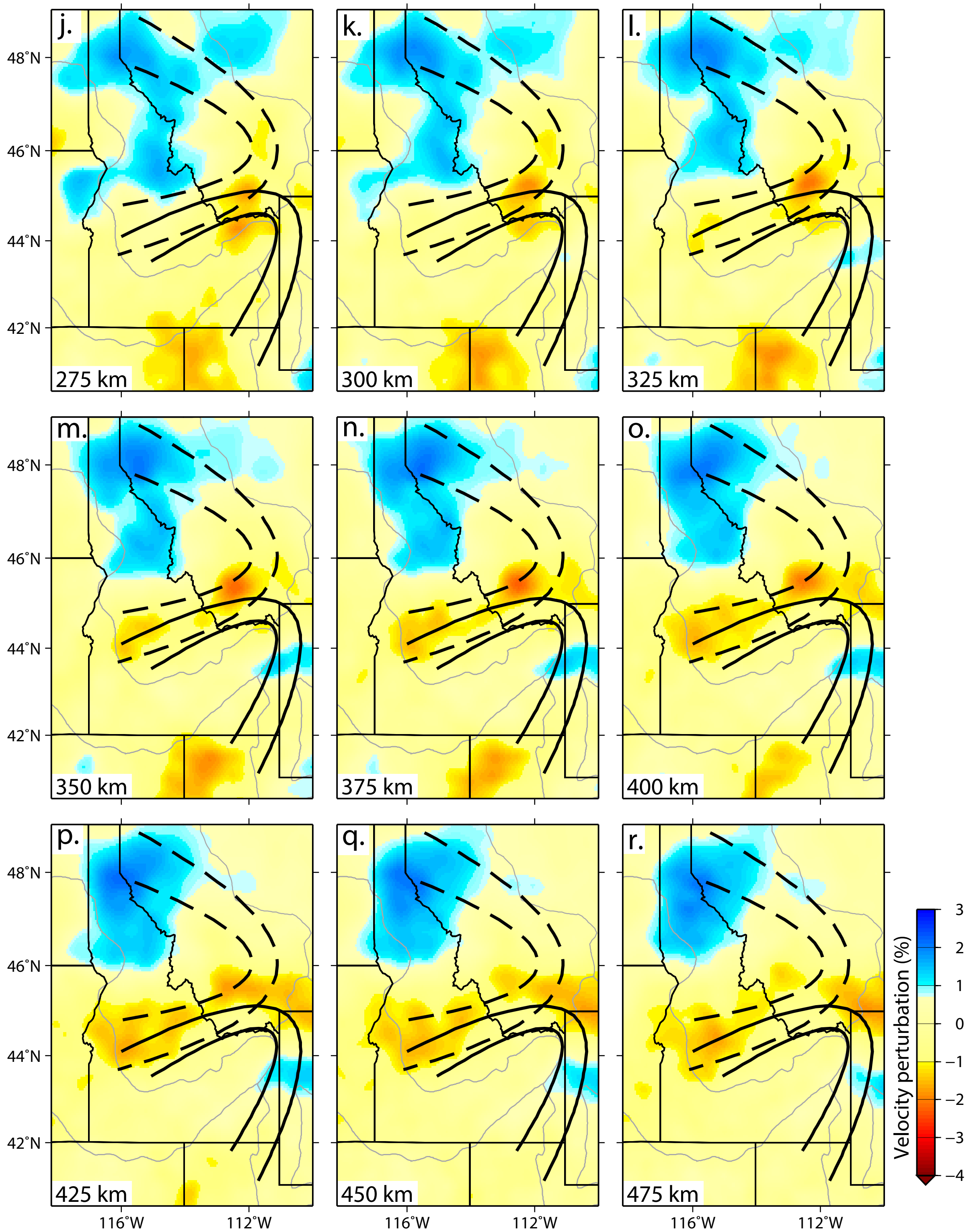

Figure 1.2. (continued)

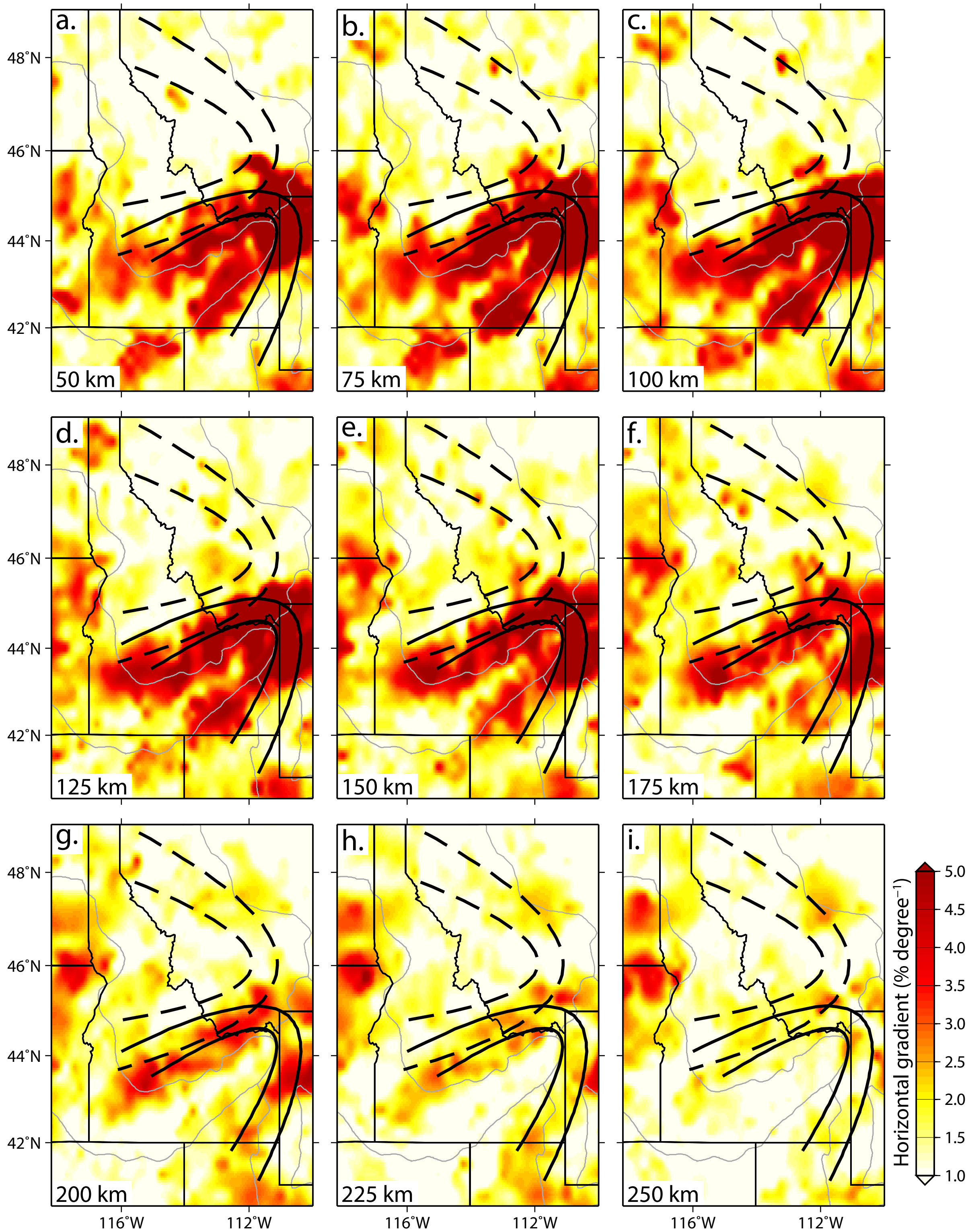

Figure 1.3. Horizontal gradients of the *S*-wave velocity perturbations from *James et al.* [2011]. Depths for (a–i) are given in lower left-hand corner. See Figure 1.2 for explanation.

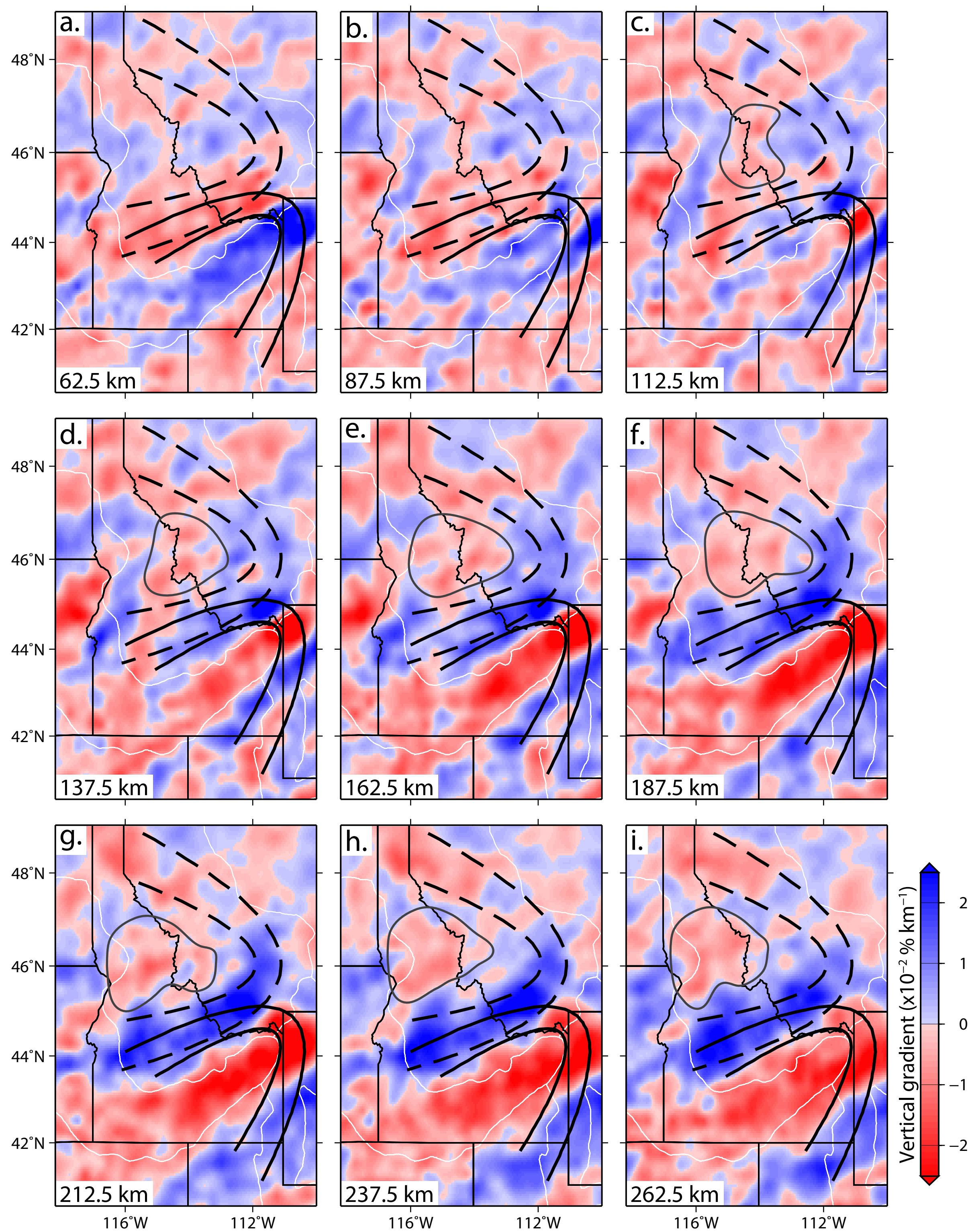

Figure 1.4. Vertical gradients of the *S*-wave velocity perturbations from *James et al.* [2011]. Depths for (a–r) are given in lower left-hand corner. Zones of negative gradient are delineated by gray line. See Figure 1.2 for explanation.

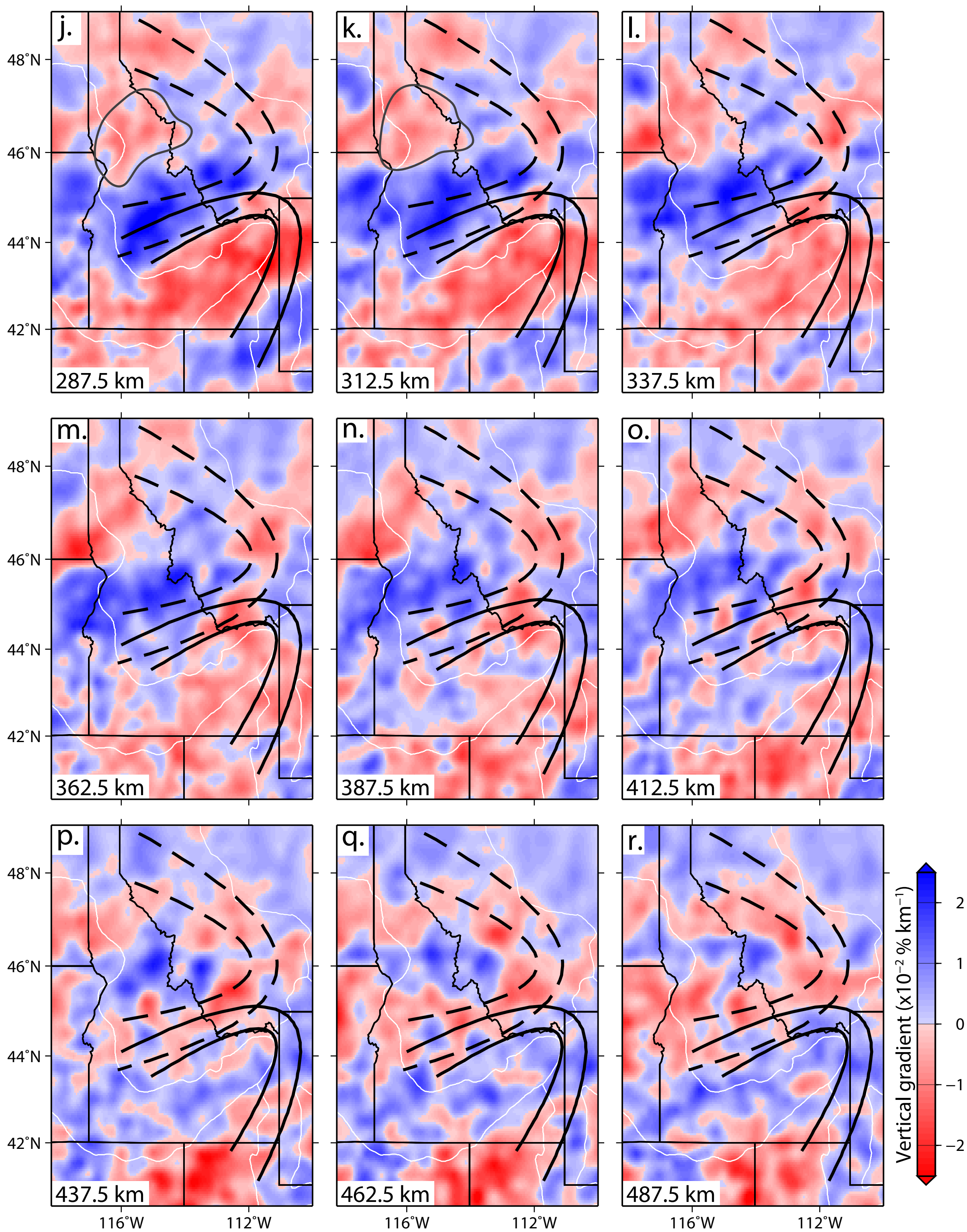

Figure 1.4. (continued)

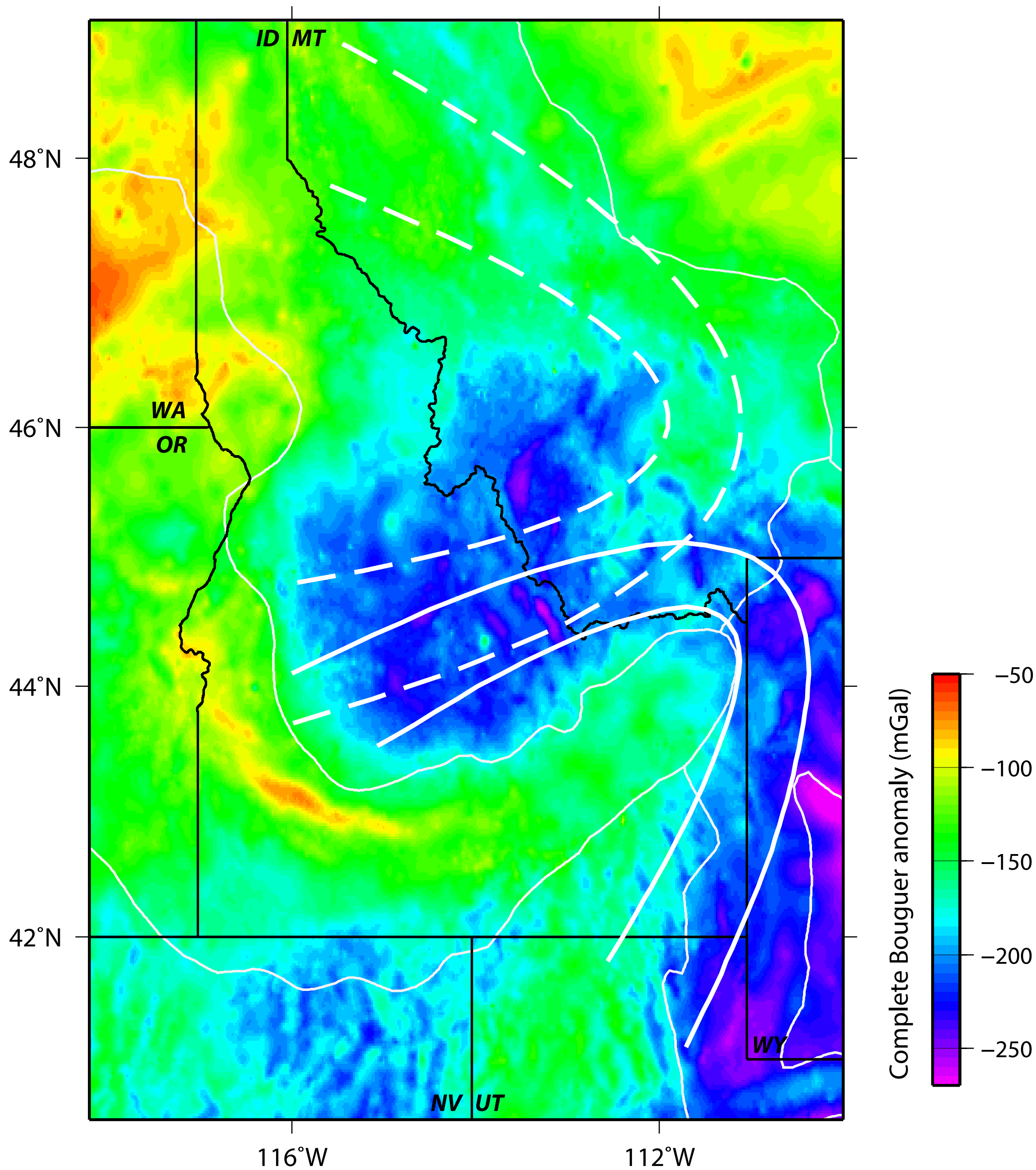

Figure 1.5. Complete Bouguer gravity anomaly of the study area. Data from *Pan American Center for Earth & Environmental Studies* [2015]. The Yellowstone Tectonic Parabola and proposed northern seismic parabola are outlined by solid and dashed lines, respectively. Bouguer anomaly is relatively high in the Snake River Plain, which is surrounded by the area of very low anomaly.

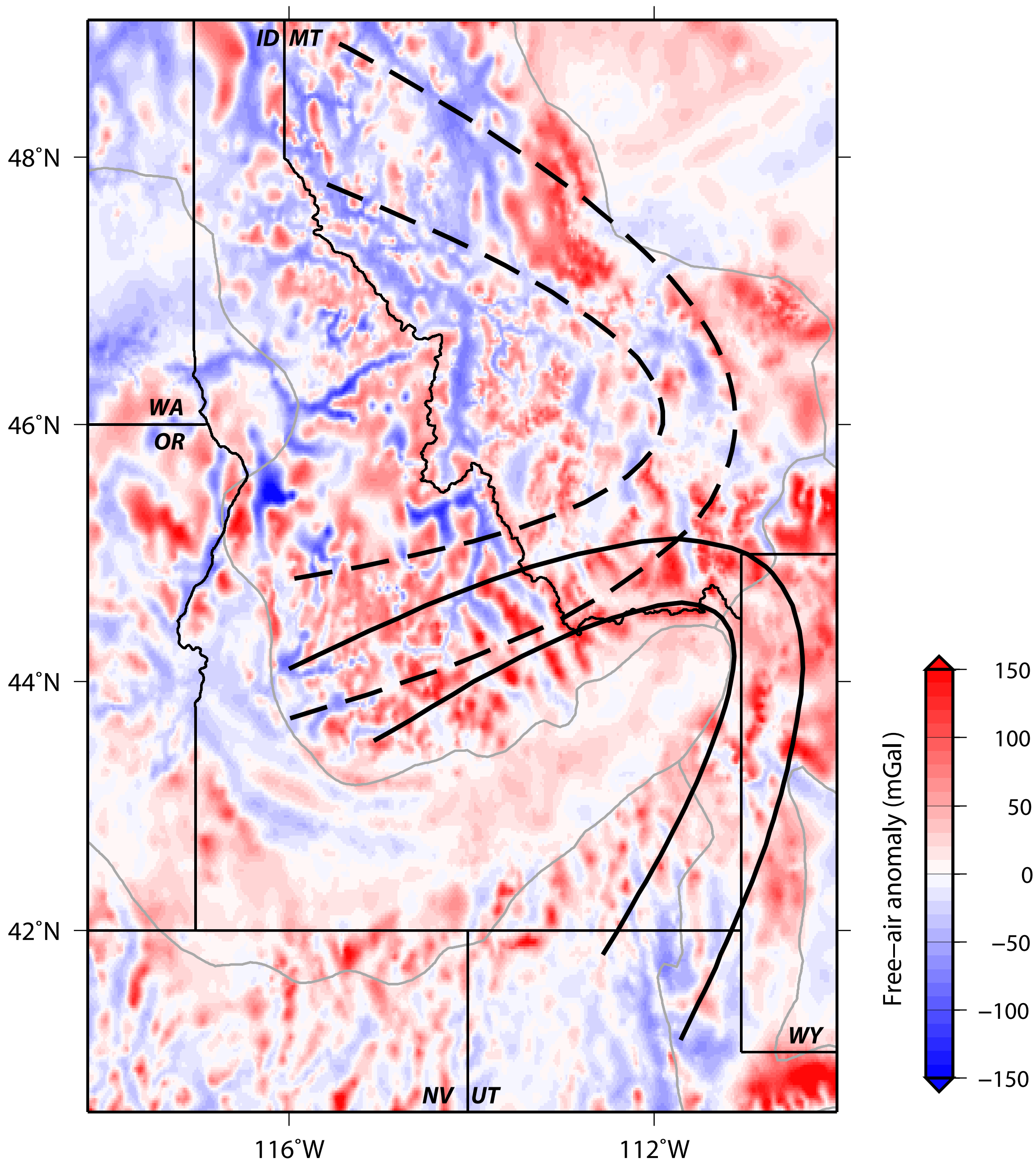

Figure 1.6. Free-air gravity anomaly of the study area. Data from *Pan American Center for Earth & Environmental Studies* [2015]. The Yellowstone Tectonic Parabola and proposed northern seismic parabola are outlined by solid and dashed lines, respectively. The basin-range style topography is indicated in the Northern Rockies.

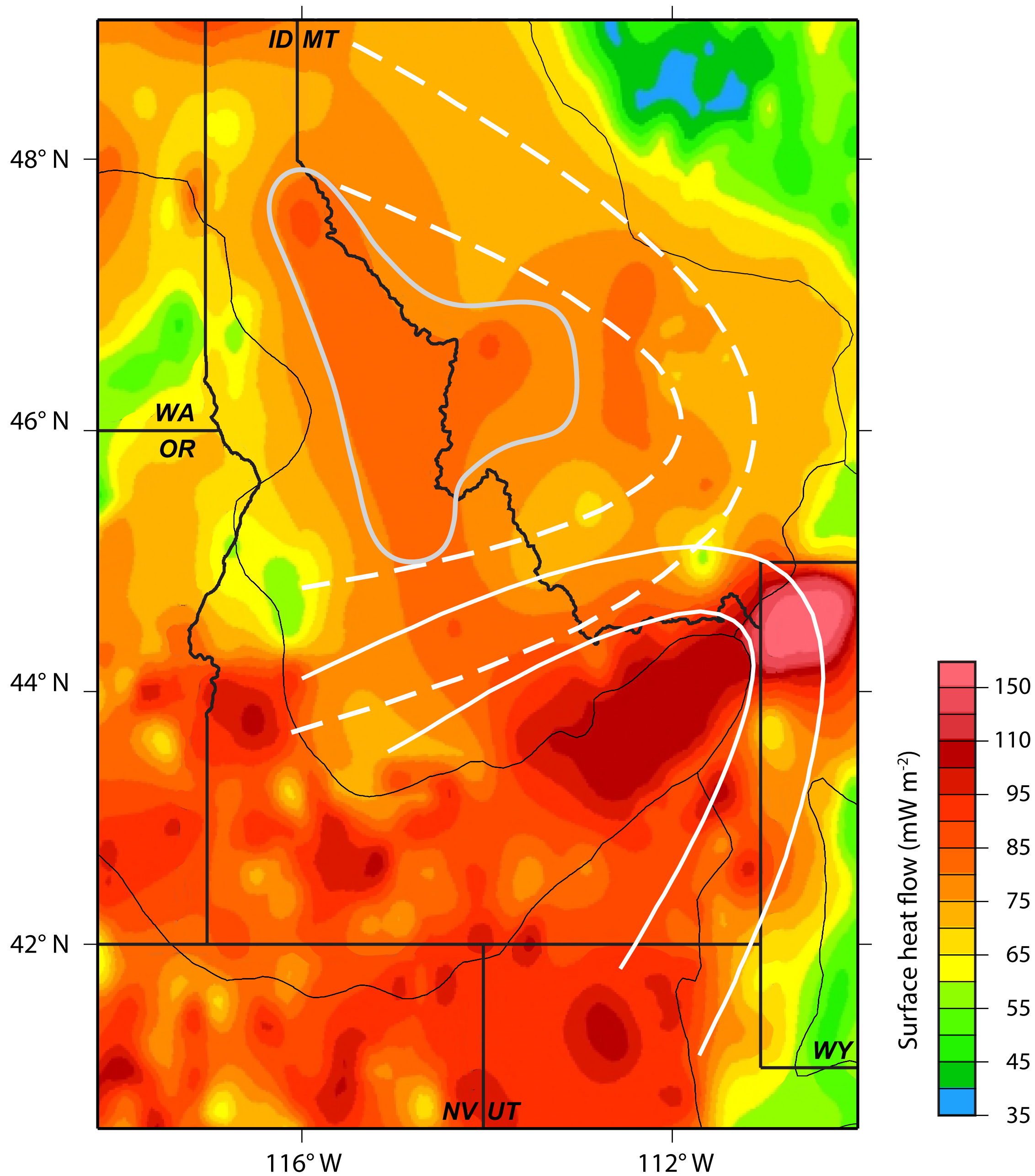

Figure 1.7. Surface heat flow of the study area modified from *Blackwell et al.* [2011]. Very strong (>90 mW m^{-2}) heat flow anomaly is found in Yellowstone and the eastern Snake River Plain. A zone of relatively high (~80 mW m^{-2}) heat flow (gray outline) is found in the northern parabola.

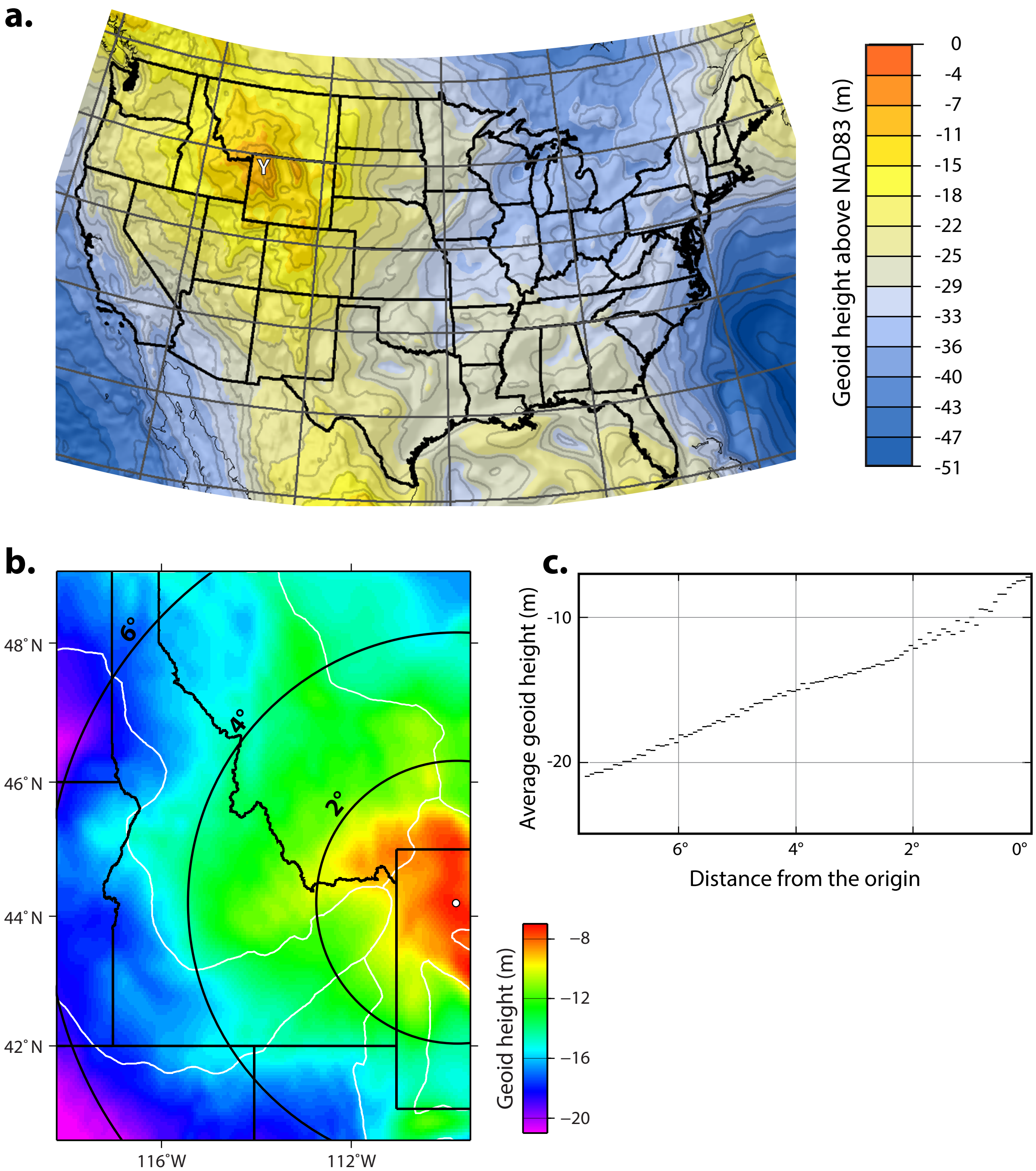

Figure 1.8. Geoid height in (a) North America and (b) the study area. Data from *National Geodetic Survey* [2014]. The geoid maps show the Yellowstone geoid anomaly. Angular distances from the origin for removing the Yellowstone effect are shown. The origin is at 109.8°W, 44.2N (white dot), the location of the highest geoid anomaly. (c) The average geoid height of each 0.08° wide annulus defines the best fit Yellowstone anomaly. Data in all directions from the origin are used to find the average geoid heights.

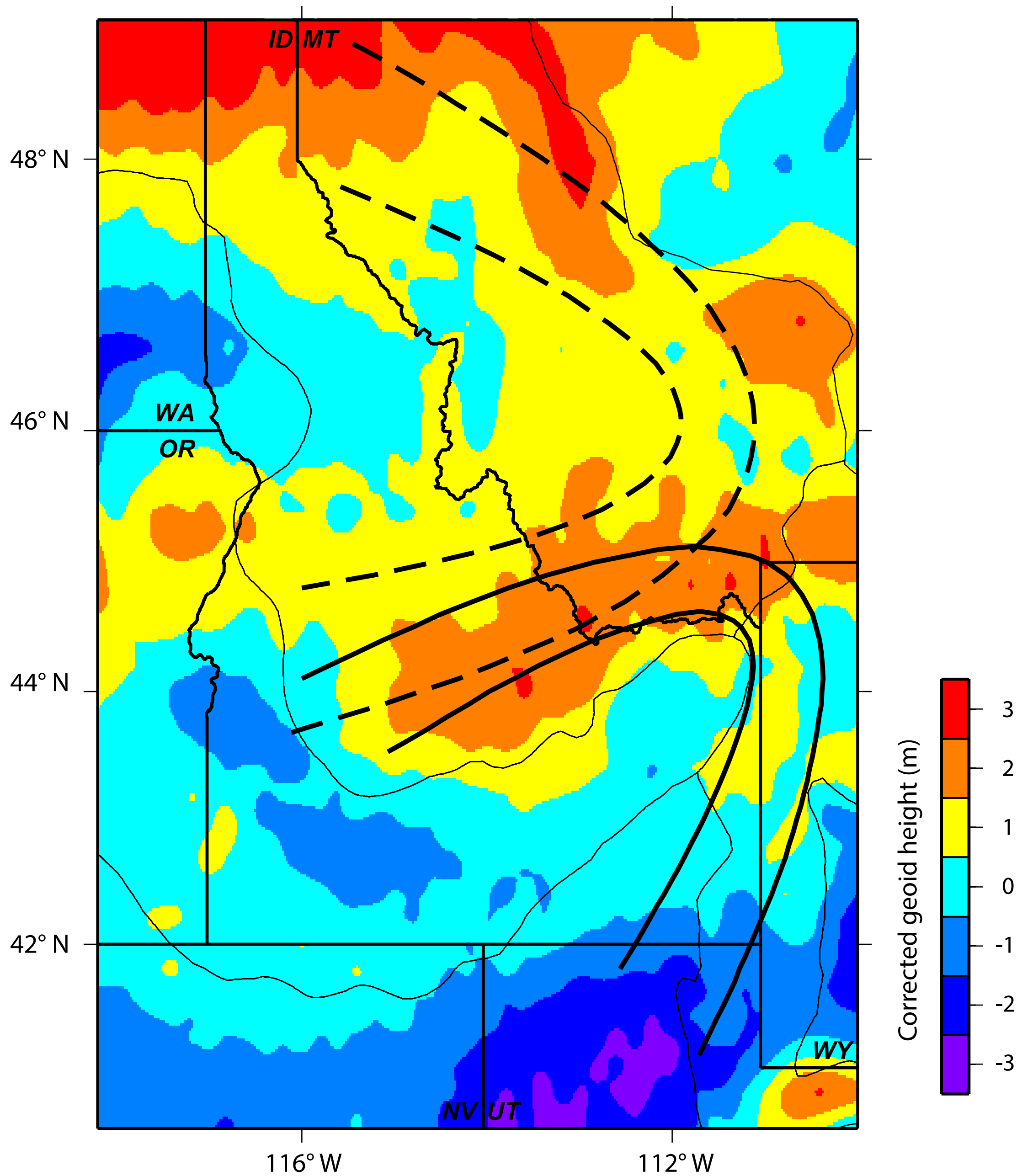

Figure 1.9. Geoid height map after removing the best fit Yellowstone effect. In northcentral Idaho is a geoidal low potentially caused by a density deficit in the upper mantle.

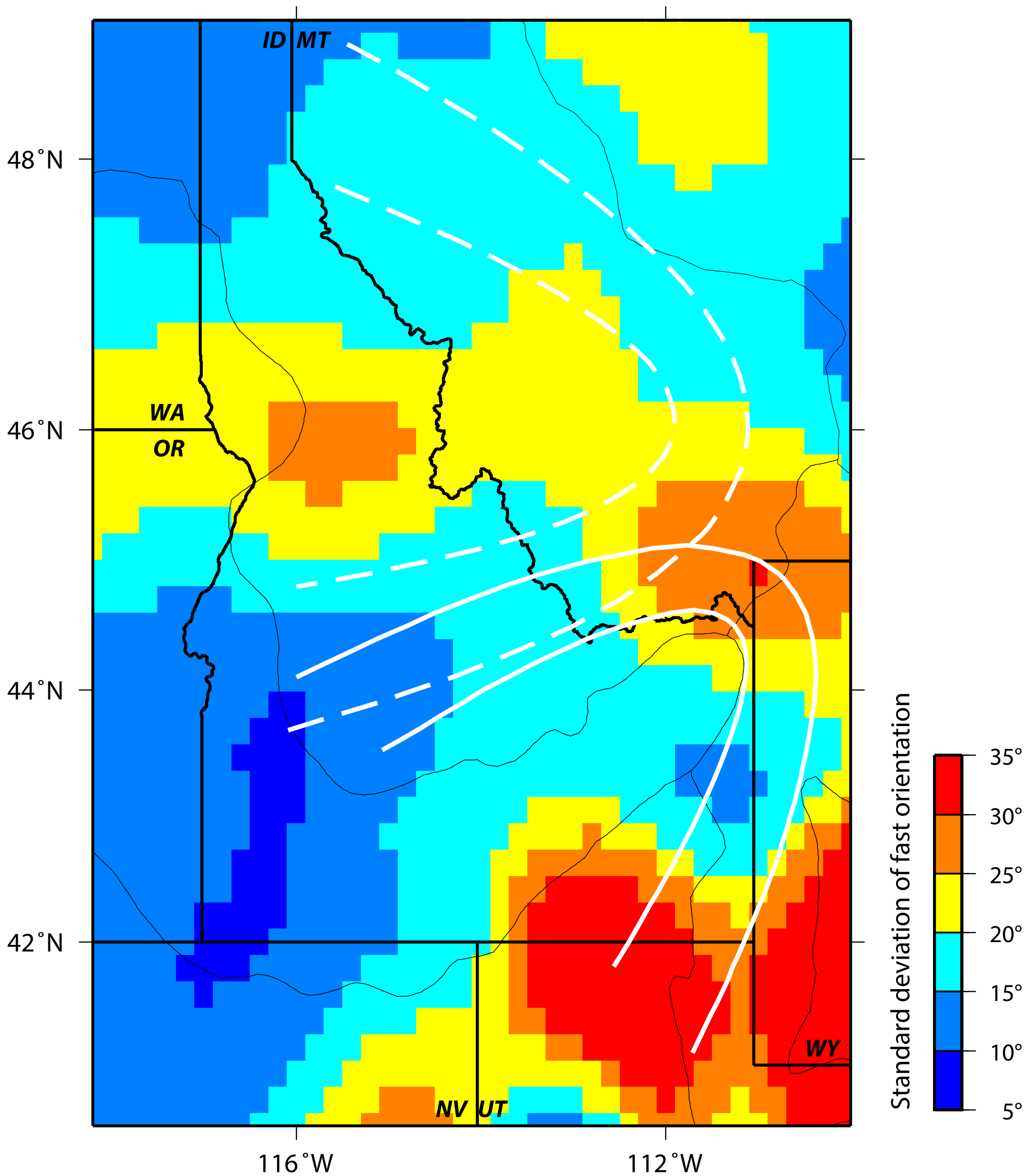

Figure 1.10. Distribution of the standard deviation of spatially averaged fast orientations from a shear wave splitting analysis. Data from *Liu et al.* [2014]. The standard deviation is ~10° higher in northcentral Idaho and western Montana than the surrounding areas. A large standard deviation suggests a structural complexity beneath the area.

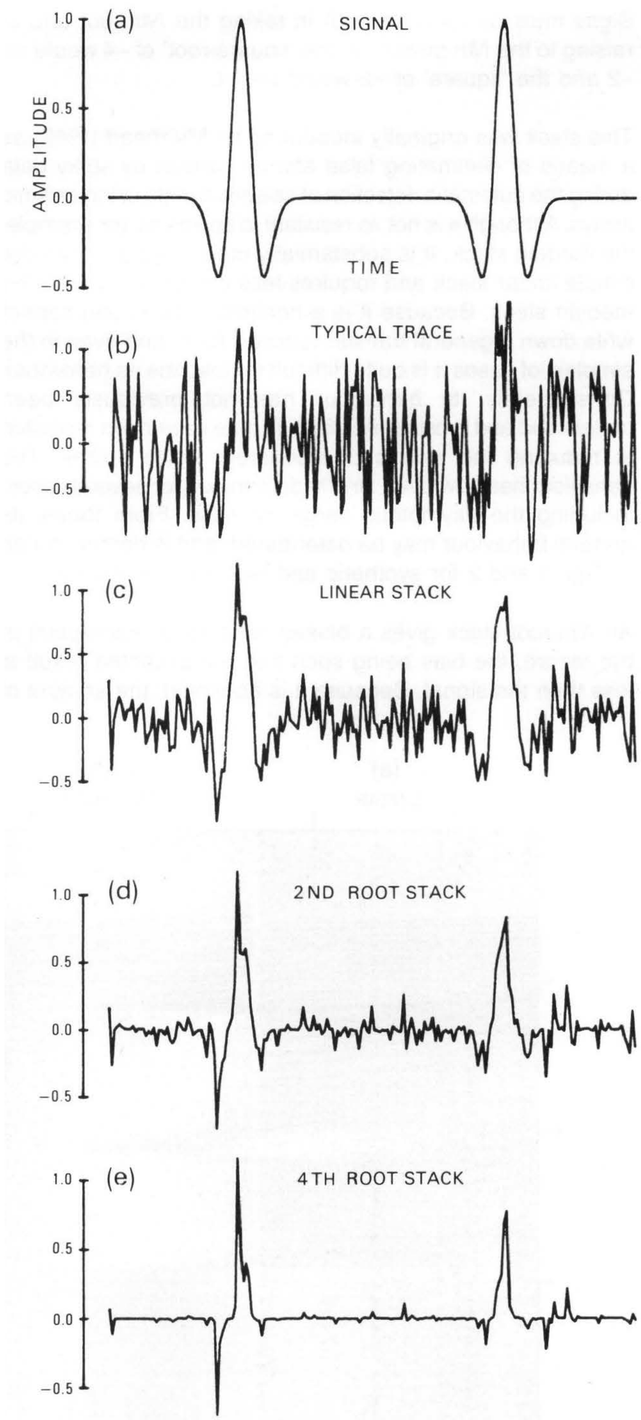

Figure 1.11. Noise reduction effect of the *n*th-root stack [*McFadden et al.*, 1987]. (a) the original trace with two wavelets. (b) a trace after noise in the random distribution is added. The results of (c) linear, (d) 2nd-root, and (e) 4th-root stacks of 12 traces are shown. The method of *n*th-root stack attains higher signal-to-noise ratios than the linear stack, but very small signals tend to be destructed, as exemplified by the destruction of some side lobes of the original wavelets.

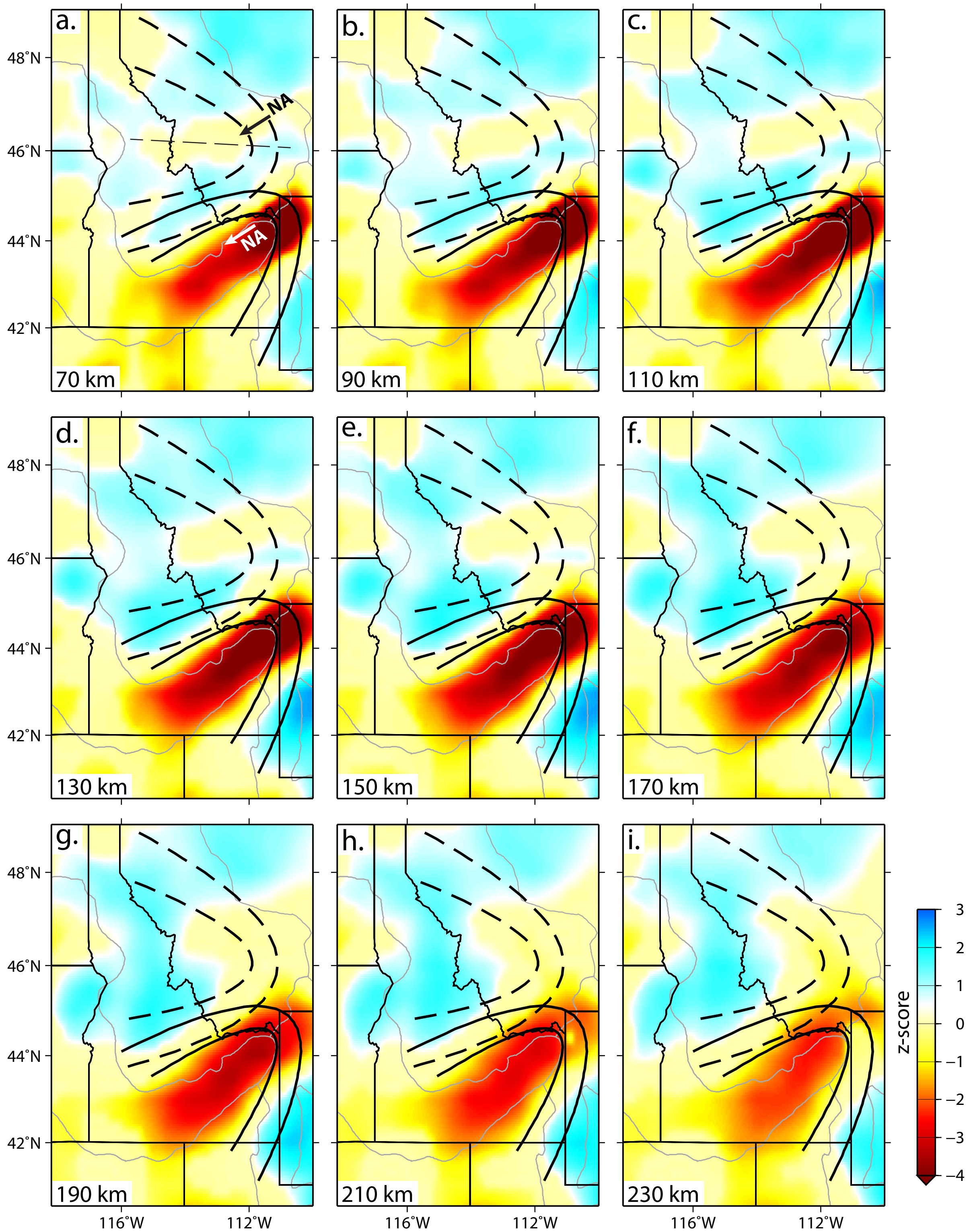

Figure 1.12. Result of the 4th-root stack on horizontal sections. Depths for (a–i) are given in lower left-hand corner. Arrows indicate the motion of North American Plate (NA). Elongated low-velocity zones lie along the axes of both parabolas at shallow depths.

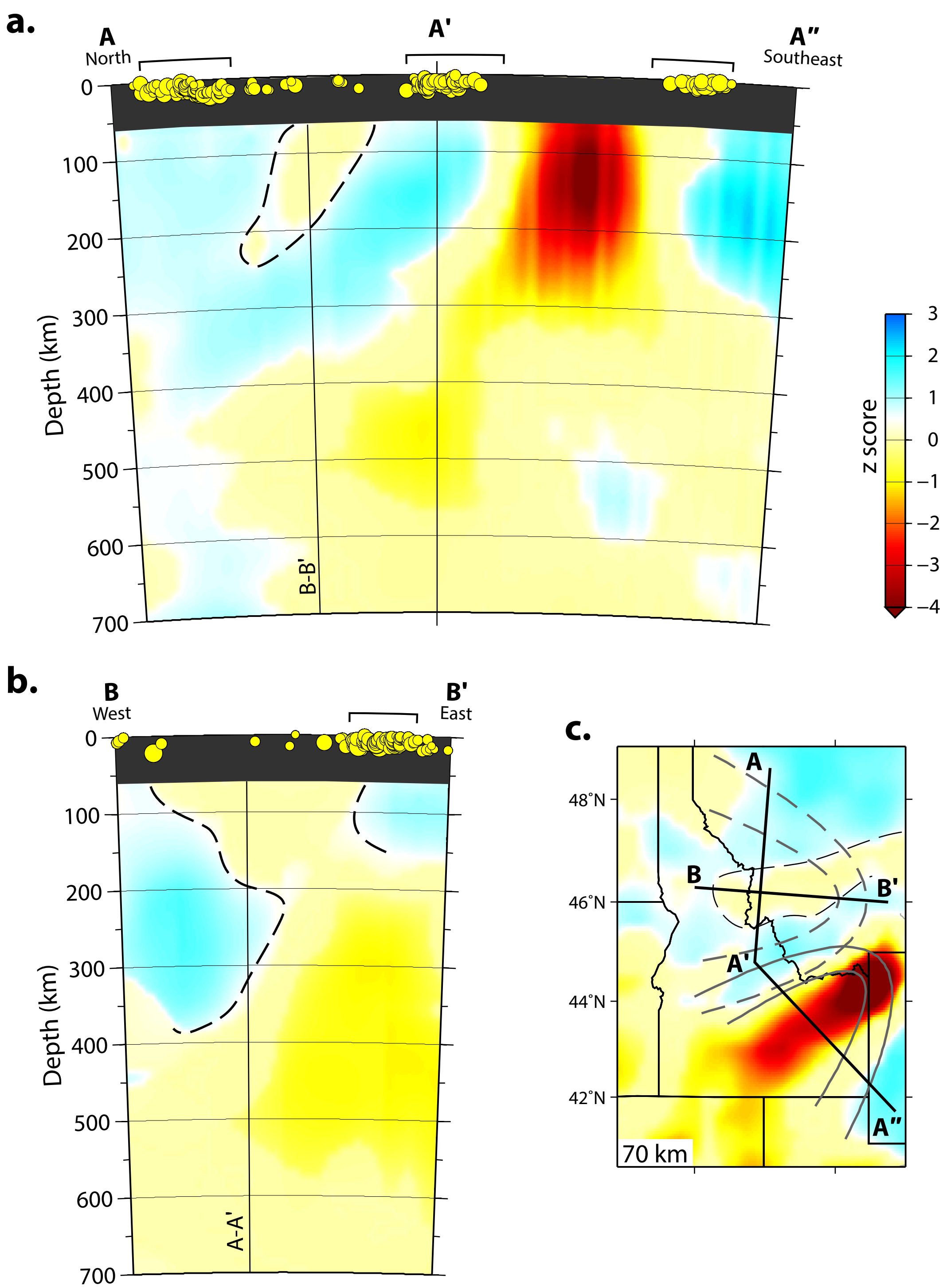

Figure 1.13. Vertical sections of the 4th-root stack model. (a) N–S–SE cross-section, which transects both parabolas perpendicular to each axis, shows the common geometric pattern, a low-velocity zone at the axis sandwiched by high-velocity zones. (b) Cross-section along the northern parabola axis shows the low-velocity zone branch out at ~200 km depth. Brackets show the locations of the parabolas. Yellow dots represent M>2 events within 15 km from the profiles. (C) Map showing the locations of the profiles.

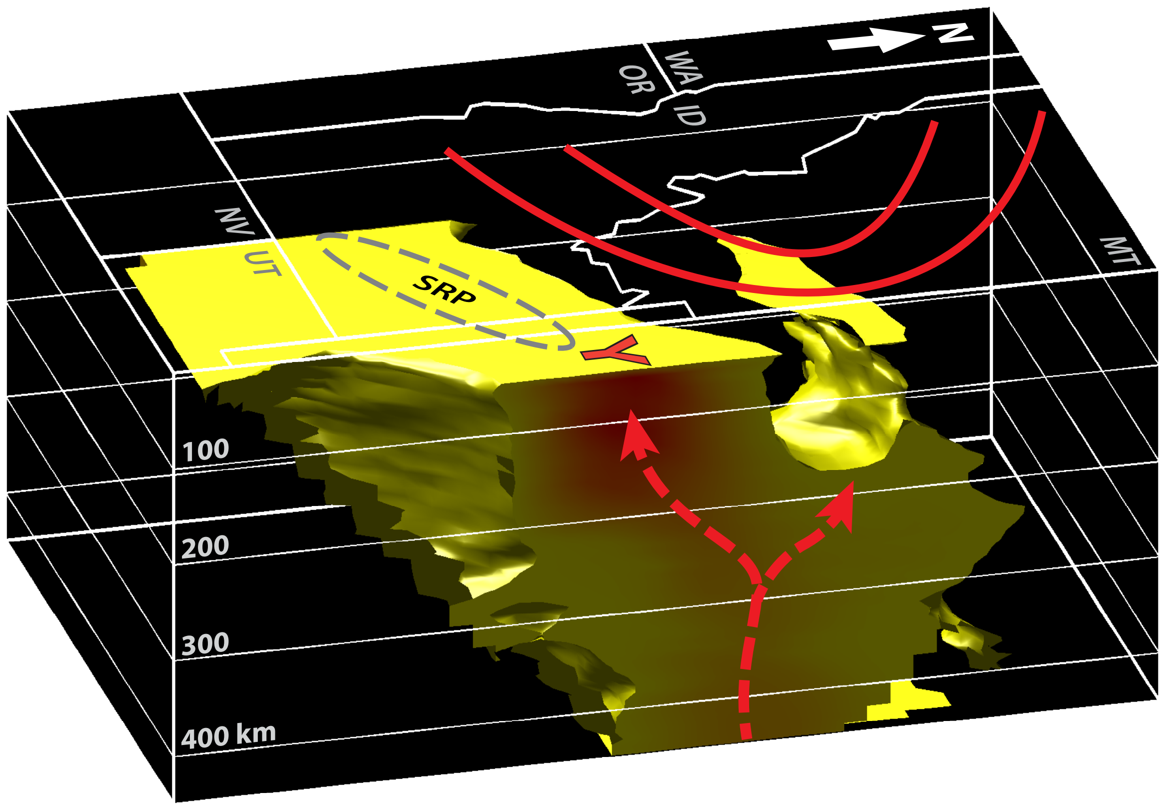

Figure 1.14. Isosurface (z = 0.09) of the 4th-root stack model. The isosurface is trimmed at 115.5°W and 50 km depth for visivility. Labels of Yellowstone and the SRP are at 50 km depth (i.e., on the top surface of the isosurface. Parabolas are at 0 km depth (i.e, on the 3-D model surface). The main high-temperature body below the Yellowstone/eastern SRP area branches out at ~200 km depth toward the vertex of the northern seismic parabola.

CHAPTER 2: STATIC STRESS TRANSFER FROM HISTORICAL AND HYPOTHETICAL EARTHQUAKES IN THE NORTHERN ROCKIES TO THE YELLOWSTONE MAGMATIC SYSTEM

> [T]he eruptions of volcanos, which happen at the same time with earthquakes, may, with more probability, be ascribed to those earthquakes . . . whenever, at least, the earthquakes are of any considerable extent.
>
> –J. Michell, 1760, p. 579

Abstract

The Yellowstone volcanic field is surrounded by several seismic zones in the Northern Rockies. We assess the effects of the historical and hypothetical earthquakes in the area on the Yellowstone magmatic system by calculating a static stress transfer from each event. A recent tomographic model revealed a Yellowstone magma reservoir at 5-17 km depths and a potential magma pathway to the surface for an eruption. These magmatic features are approximated as vertical rectangular planes, on which normal stress changes are estimated using an elastic dislocation model, as well as the location, and rupture parameters of each event. We examine effects of four large historical earthquakes around Yellowstone, the two mainshocks (M_W6.3 and M_W7.3) and the largest aftershock (M_W6.1) of the 1959 Hebgen Lake sequence, and the 1983 Borah Peak (M_W6.8) event. Their origin details and source parameters are from published studies. We also simulate 13 hypothetical M_W7.1-7.5 earthquakes along the major faults.

Among the four historical events, the second Hebgen Lake mainshock caused the largest normal stress change on the model planes. In the results, the reservoir plane is unclamped in a large area, with the maximum value of 1.4 bars, which may facilitate bubble nucleation of volatiles in the magma, leading to an overpressure in the reservoir. The effects from the other historical events appear very limited. Among the hypothetical earthquakes, the events at the second Hebgen mainshock and aftershock, as well as the one at the Upper Yellowstone Valley fault, show stress change patterns favorable to induce an eruption. The hypothetical M_W7.5 event at the second Hebgen mainshock unclamps the reservoir plane by up to 2.4 bars. The hypothetical event at the Habgen aftershock strongly clamps the reservoir plane by up to 11.1 bars while unclamping the pathway plane by up to 4.9 bars. The event at the Upper Yellowstone Valley fault causes areas of both clamping and unclamping on the reservoir plane at the same time, which could initiate magma circulation. Geologic evidence indicates that the Upper Yellowstone Valley fault has been active throughout the late Quaternary without any recorded historical earthquake.

2.1 Introduction

Static stress transfer from a tectonic earthquake to a volcanic system could promote a volcanic eruption. Here static stress transfer refers to a stress change due to permanent deformation in crust caused by the offset of a remote fault. There are numerous cases where elevated volcanic activities, including eruptions, were preceded by a large earthquake [e.g., *Linde and Sacks*, 1998]. One example is volcanically active Mt. Fuji, whose last explosive (VEI 5) eruption in 1707 started 49 days after the largest (M_w8.7) historical earthquake in Japan prior to the 2011 Tohoku-Oki earthquake. *Chesley et al.* [2012] demonstrated that the change in normal stress due to the 1707 earthquake compressed a magma chamber and at the same time unclamped the dike immediately above the chamber, triggering magma mixing and the subsequent eruption.

Yellowstone is one of the largest continental volcanoes surrounded by multiple seismic zones in which M>7 earthquakes have occurred. Recent tomographic models clearly image the magma reservoirs of Yellowstone [*Farrell et al.*, 2014; *Huang et al.*, 2015]. In this study, we investigate the effects of the historical and hypothetical earthquakes on the Yellowstone magmatic system by calculating stress changes caused by each earthquake.

2.1.1 Background

Although the spatiotemporal correlation between volcanic eruptions and the preceding earthquakes was suggested as early as the 18^{th} century [*Michell*, 1760], few studies on the potential relationship had been conducted until the 1960s [*Yokoyama*, 1971, and references therein]. In 1835, the M8.2 Concepción earthquake in middle Chile was followed, within a couple of days, by three volcanic eruptions, Michinmahuida and Corcovado in southern Chile, and the Isabela island of the Galápagos. Having experienced the earthquake and the Isabela eruption, *Charles Darwin* [1839] suggested a common cause or subsurface connections between the earthquake and the volcano. *Blot* [1965] discussed the potential relationship between the 1960 offshore Vladivostok earthquake, Russia, and the 1962 Mount Tokachi, Japan, eruption at hundreds of kilometers to the east from the epicenter. Blot speculated that an unknown seismic energy that traveled at a low speed (1-2 km day^{-1}) induced the eruption. *Minakami* [1968] pointed out a temporal correlation between the three M>7 earthquakes that occurred in southwestern Japan over 808 months and the elevated volcanic activities, such as the earthquake swarms in the calderas and eruptions of the Kirishima volcanic group that happened within three months after each earthquake. For one of the three series of the events, because the loci of the volcanic activities migrated over time, *Minakami et al.* [1970] suggested that a release of crustal strain was associated with the earthquake-volcano relationship.

Further studies on the earthquake-volcano relationship pointed to a change in the stress field as the connecting mechanism. Researchers noticed the historical two-way coupling, both eruptions following earthquakes and ones preceding, of Mt. Vesuvius and the Apennine earthquakes in Italy [*Bonasia et al.*, 1985; *Marzocchi et al.*, 1993]. Earthquakes following volcanic activities were also found in other areas. Studies on such cases in Iceland [*Stefánsson et al.*, 1993], Hawaii [*Dvorak*, 1994], and the Asal rift, Djibouti [*Jacques et al.*, 1996] revealed that those earthquakes were normal-faulting events following episodes of volcanic inflation or dike intrusion. The 1974 M6.7 and 1978 M7.0 Izu earthquakes, Japan, followed volcanic inflation on the Izu peninsula [*Thatcher and Savage*, 1982]. *Thatcher and Savage* [1982] attributed the events to a change in stress field due to the volcanic inflation. In May 1980, a sequence of four M~6 earthquakes occurred within 10 km from the Long Valley caldera, California, which may have been preceded by a volcanic inflation episode [*Savage and Clark*, 1982; *Cockerham and Corbett*, 1987]. *Savage and Clark* [1982] demonstrated that the inferred inflation could have brought the stress state 0.1-1.0 MPa closer to the Coulomb failure at three of the four faults that ruptured when the 1980 event occurred.

These observations and analyses lead to a consensus that static stress transfer was responsible for volcano-induced earthquakes. In turn, the concept was applied to cases where volcanic activities followed the earthquakes. In 1991, Mt. Pinatubo, Philippine, erupted (VEI 6) 11 months after the 1990 M7.8 Luzon earthquake that occurred ~100 km away from the volcano. *Bautista et al.* [1996] found that the earthquake increased the stress on a magma conduit beneath Pinatubo by ~0.1 MPa, potentially promoting the eruption. For the cases of the Mt. Vesuvius eruptions and Apennine earthquakes, *Nostro et al.* [1998] demonstrated through the calculation of stress change that the eruptions were promoted by earthquakes most effectively when the magma reservoir was clamped at depth and the near-surface conduit was unclamped.

In the 1990s, such calculations of static stress change were facilitated by the establishment of an elastic dislocation model. *Okada* [1985] presented a complete set of analytical solutions for surface deformation due to shear and tensile faults. Later, he extended the dislocation model to calculate internal displacements and strains in an elastic medium, which made it possible to find stress changes around subsurface magmatic features [*Okada*, 1992]. Coupled with the advancement of high-precision geodetic instruments, such as GPS and InSAR, the elastic dislocation model, known as the Okada model, has been widely used for modeling fault geometry [e.g., *Nahm et al.*, 2013; *Wicks et al.*, 2013] and magma chamber geometry [e.g., *Geirsson*, 2014] from surface deformation, as well as stress changes on earthquake nodal planes [e.g., *Toda et al.*, 2011; *Ma et al.*, 2005] and on magmatic features [e.g., *Nostro et al.*, 1998; *Chesley et al.*, 2012].

2.1.2 Objectives

A volcanic system on which effects from seismicity can be tested is Yellowstone, one of the largest continental volcanoes on the earth. A variety and concentration of hydrothermal features [*Christiansen*, 2001], as well as anomalously high heat flow [*Farrell et al.*, 2014], indicate active magmatism beneath Yellowstone. The volcanic field lies within the Intermountain Seismic Belt [*Sbar et al.*, 1972; *Smith and Sbar*, 1974] and near the Centennial Tectonic Belt [*Stickney and Bartholomew*, 1987], in which the 1983 M_W6.9 Borah Peak earthquake occurred ~270 km away from Yellowstone [e.g., *Doser and Smith*, 1985]. The 1959 M_W~7.5 Hebgen Lake earthquake occurred only ~45 km northwest of the rim of the youngest Yellowstone caldera [*Tocher*, 1962; *Ryall*, 1962; *Witkind et al.*, 1962]. The drastic coseismic and postseismic uplift episodes occurred in the Yellowstone caldera and the surrounding area, indicating an inflation of the magmatic system [*Reilinger*, 1986; *Holdahl and Dzurisin*, 1991]. A recent tomographic model by *Farrell et al.* [2014] revealed a Yellowstone magma reservoir at 5-17 km depths and a potential pathway to the surface for an eruption. This tomographic image allows for a reliable geometric approximation of the magmatic system, on which stress changes due to earthquakes can be calculated.

Here we examine effects of four large historical earthquakes around Yellowstone, the two mainshocks (m_b6.3 and m_b7.0) and the largest aftershock (m_b6.5) of the 1959 Hebgen Lake sequence, and the 1983 Borah Peak (M_W6.9) event. We model the normal stress change imparted on the Yellowstone magmatic system due to the historical events, using Okada's elastic dislocation model. We also simulate 13 hypothetical M_W~7.5 earthquakes along major faults around Yellowstone to determine if those events enhance the potential for an eruption.

2.2 Tectonic Setting

Yellowstone is the largest active volcanic system in North America. Tomographic models show two large magma reservoirs beneath the Yellowstone caldera. Yellowstone is surrounded by three major seismic zones, the Intermountain Seismic Belt, Centennial Tectonic Belt, and Centennial shear zone. The 1959 Hebgen Lake earthquake sequence occurred in the immediate northwest of Yellowstone. The 1983 Borah Peak earthquake occurred in the Centennial Tectonic Belt.

2.2.1 Yellowstone Volcanic System

Yellowstone is one of the world's largest continental hotspot volcanoes. It is responsible for the hotspot track extending from the eastern Oregon-Nevada border to the current Yellowstone location. Yellowstone's caldera-forming eruptions in the last 12 Ma formed the central and eastern Snake River Plain (Figure 2.1). The last three caldera-forming eruptions occurred at 2.1, 1.3, and 0.64 Ma. The most recent event formed the 60 km long caldera, commonly known as the Yellowstone caldera [*Christiansen*, 2001]. Since then, ~60 smaller eruptions, with the most recent at 70,000 years ago, occurred to date [*Christiansen and Blank*, 1972]. Tomographic studies image Yellowstone's mantle plume extending from the mid-mantle to ~50 km depths (Figure 2.2) [e.g., *Porritt et al.*, 2014; *Schmandt and Humphreys*, 2010; *Smith et al.*, 2009], which feeds the magmatic system in the crust. *P*-wave tomographic models have revealed two magma reservoirs beneath the Yellowstone calderas: a lower basaltic magma body and an upper rhyolitic one (Figure 2.3) [*Farrell et al.*, 2014; *Huang et al.*, 2015]. The basaltic magma body resides at ~25-50 km depths with the volume of ~46,000 km^3 [*Huang et al.*, 2015]. The upper rhyolitic magma reservoir is 90 km long and 5-17 km deep, running SW-NE along the long axis of the

Yellowstone caldera [*Farrell et al.*, 2014] (Figure 2.4). Farrell et al.'s tomographic model also reveals that the low-velocity body continues upward to the surface, extending ~15 km northeast of the Yellowstone caldera (Figure 2.4). The shallowest portion is also suggested by a gravity model as a low-density body [*DeNosaquo et al.*, 2009] which lies below the largest area of hydrothermal alteration in the Yellowstone volcanic field [*Werner et al.*, 2008; *DeNosaquo et al.*, 2009; *Farrell et al.*, 2014]. The shallow northeastern portion is interpreted as a body of magmatic fluids (i.e., gas, hydrothermal fluids, and melt) [*Farrell et al.*, 2014].

2.2.2 Seismic Zones and Historical Earthquakes around Yellowstone

Yellowstone is located in the middle of the Intermountain Seismic Belt (ISB), an arcuate zone of elevated intraplate seismicity extending from northwestern Montana to northwestern Arizona [*Smith and Sbar*, 1974; *Smith and Arabasz*, 1991] (Figure 2.1). The ISB is characterized by relatively shallow (up to ~20 km) normal-faulting earthquakes, which include episodic scarp-forming (M6-7.5) events [*Smith and Sbar*, 1974; *Smith and Arabasz*, 1991]. Yellowstone is also located at the eastern end of an east-west trending seismic zones, the Centennial Tectonic Belt and the Centennial shear zone (Figure 2.1).

To the north of Yellowstone, historical M>6 events have occurred in the ISB along the segment from the Helena area, Montana, to Yellowstone [*Stickney and Bartholomew*, 1987] (Figure 4.1). In the Helena area, the Helena Valley earthquakes (M6.3 and M6.0) occurred in 1935 [*Stickney*, 1978]. Approximately 70 km southeast of Helena, the 1925 M6.8 Montana earthquake occurred in the Clarkston Valley area [*Pardee*, 1926]. The same area also experienced the 1947 M_L6.3 Virginia City earthquake [*Doser*, 1985; 1989]. The largest historical event within the ISB, the 1959 Hebgen Lake sequence occurred on August

17^{th} only ~50 km northwest of the Yellowstone's youngest caldera. The two mainshocks occurred at 10-15 km depths, possibly reactivating one or more Laramide thrust faults in a dextral normal sense [e.g., *Witkind et al.*, 1962; *Ryall*, 1962; *Tocher*, 1962; *Doser*, 1985]. The largest aftershock of the sequence is a normal-faulting event that occurred ~30 km north of the center of the caldera at ~10 km depth [*Tocher*, 1962; *Witkind et al.*, 1962; *Doser*, 1985]. The Hebgen sequence caused a large landslide which resulted in 28 fatalities.

To the south of Yellowstone, the ISB trends southwest (Figure 2.1). To the immediate south of Yellowstone is the Yellowstone-Teton region known for a high level of seismicity. A major active fault in the area is the Teton fault marked by a 3-52 m high, 55 km long fault scarp [*Byrd et al.*, 1994]. The Teton fault appears to be seismically quiescent for M>3 events [*Smith et al.*, 1990, 1993; *Smith and Arabasz*, 1991]. However, geological evidence indicates a potential to produce an earthquake as large as M7.5 [*Smith et al.*, 1993]. The estimated seismic hazard in the area is the highest in the Intermountain West [*Petersen et al.*, 2008].

Along the northern flank of the Snake River Plain is a seismic zone, the Centennial Tectonic Belt (CTB; also called Central Idaho Seismic Zone; Figure 2.1), which is characterized by Holocene normal faulting and high seismicity [*Stickney and Bartholomew*, 1987]. The CTB is an approximately 350 km long and 80-100 km wide zone, extending from east central Idaho to Yellowstone [*Anders et al.*, 1989]. The basin-range topography in the CTB is similar to that to the south of the SRP [*Stickney and Bartholomew*, 1987]. The well-developed Lost River, Lemhi, and Beaverhead faults are in the western part of the CTB. In 1983, 280 km east of the Yellowstone caldera, the Lost River fault ruptured in a normal sense as the $M_S7.3$ Borah Peak earthquake [e.g., *Doser and Smith*, 1985; *Smith et al.*, 1985; *Zollweg and Richins*, 1985; *Richins et al.*, 1987; *Barrientos et al.*, 1987]. The earthquake caused a 36 km long fault scarp with the maximum displacement of 2.7 m [*Crone et al.*, 1985] as well as two deaths and ~$12.5 million in damages [*Stover*, 1985]. In 2014, an earthquake swarm consisting of over 100 m_b1.5-4.7 events occurred near Challis, Idaho, about 20-30 km northwest of the focus of the 1983 event [*Pankow et al.*, 2014].

The narrow area between the CTB and the eastern SRP is referred to as the Centennial shear zone (CSZ), in which extension-driven dextral shear is accommodated [*Payne et al.*, 2008; 2012; 2013]. Kinematic block models by *Payne et al.* [2008; 2012; 2013] revealed that the contrast between the rapid extension in the CTB and the scarcely deforming eastern SRP caused the dextral shear at 0.3-1.5 mm a^{-1} in the CSZ. In line with the modeling result, dextral strike-slip earthquakes in the shear zone have been documented [*Stickney*, 1997; 2007].

2.3 Theories

Both dynamic and static stress changes can induce a volcanic eruption. There are various eruption triggering mechanisms, some of which require specific patterns of stress change. The effect of static stress transfer on the Yellowstone magmatic system is the focus of this study. The stress changes are calculated using an elastic dislocation model.

2.3.1 Dynamic and Static Stress Changes

Remote earthquakes can affect a magmatic system through either dynamic or static stresses [e.g., *Nostro et al.*, 1998; *Linde and Sacks*, 1998; *Manga and Brodsky*, 2006]. Dynamic stress changes are caused by transient and oscillatory deformation from propagation of seismic waves. Static stress changes are a result of instantaneous and permanent deformation due to a slip on the rupture plane, which therefore is time-independent. When a hypocenter is relatively close to the volcano, it is difficult to distinguish between effects from dynamic and static stress changes, either observationally or theoretically, with current knowledge. When the volcano is many hundreds of kilometers away from the earthquake source, it is likely that only dynamic stress changes affect the volcanism [*Manga and Brodsky*, 2006]. The reason for above lies in the difference in decay rate between dynamic and static stresses. Although both stresses attenuate as the distance from the source r increases, dynamic stresses decay more gradually than static stresses. The empirical relationship between surface waves and dynamic stresses indicates that the attenuation is in inverse proportion to $r^{1.66}$, whereas static stresses fall off as $1/r^3$ [e.g., *Lay and Wallace*, 1995]. For historical earthquakes which were not recorded as seismograms, it is impractical to estimate dynamic stress transfers because the amplitude and frequency of the seismic waves depend a great deal on the heterogeneities of the source fault. In this study, we focus on volcanism induced by static stress changes.

2.3.2 Eruption Triggers Due to Stress Transfers

There are a variety of eruption-triggering mechanisms. Listing the mechanisms, *Schmincke* [2004] separates them into three groups: intrinsic factors, composites of intrinsic and extrinsic factors, and extrinsic factors. The intrinsic factors include the buoyancy of magma (especially for effusive eruptions; e.g., Hawaii), overpressure due to volatile differentiation and vesiculation (for explosive eruptions), and an injection of mafic magma into a silicic magma chamber (e.g., Mt. Fuji [*Chesley et al.*, 2012]). Examples of the composite factors are decompression by sector collapse (e.g., Mt. St. Helens [e.g., *Voight et al.*, 1983]) and magma-water interaction (e.g., Helgafjell, Iceland [e.g., *Zimanowski et al.*, 1997]). The earthquake is listed as an extrinsic factor along with atmospheric and climatic influences, tides, and meteorite impacts.

Various mechanisms in which stress transfers from an earthquake induce a volcanic eruption have been proposed. In models involving dynamic stress changes, bubbles of volatiles in magma play a key role [e.g., *Brodsky et al.*, 1998; *Hill et al.*, 2002; *Schmincke*, 2004]. For example, seismic waves could initiate bubble nucleation and ascent of volatiles in a magma reservoir, which leads to an overpressure at the top of the reservoir. Seismic waves may also be able to let the existing bubbles loose from the surface of the crystals or the reservoir wall, which in turn leads to the rise of the bubbles. In another model, pressure oscillations from *P*-wave propagation causes alternating expansion and contraction of the bubbles, which promotes bubble growth. As an indirect mechanism, seismic waves trigger or drive magma convection and circulation by dislodging crystal mushes accumulated at the top of a magma chamber.

Static stress transfers also disturb magmatic systems. Studies have introduced cases where an eruption was possibly triggered, whether directly or indirectly, by a static stress change due to an earthquake [e.g., *Nostro et al.*, 1998; *Chesley et al.*, 2012; *Diez et al.*, 2005; *De la Cruz-Reyna et al.*, 2010]. Two basic mechanisms are compression and decompression around a magma reservoir. Compression on a magma reservoir causes an overpressure, which can trigger an eruption if the magma reservoir is close to the critical state. *Nostro et al.* [1998] demonstrated that earthquakes in the Apennines could promote the nearby Vesuvius eruptions by compressing the magma body. Decompression around a magma reservoir facilitates bubble nucleation and magma ascent, which eventually leads to magma overpressure. *Walter and Amelung* [2007] presented evidence that the 2004 M9.3 Sumatra earthquake caused an abrupt decompression of the magmatic system of the Sumatra-Andaman volcanic arc, which resulted in a series of eruptions. In the case of the 1707 Mt. Fuji eruption, decompression due to the preceding earthquake initiated the process for the eruption. The decompression unclamped the dike immediately above the mafic magma chamber at ~20 km depth, allowing the basaltic magma to ascend and mingle with felsic magma in the shallower magma chambers, which triggered the eruption [*Chesley et al.*, 2012; *Sparks et al.*, 1977].

Every earthquake generates quadrants of compression and decompression in the double-couple theory. A coordination of compression and decompression sometimes becomes a mechanism favorable for triggering an eruption. The Vesuvius eruptions were most effectively promoted when a stress change compresses the magma body and unclamps near-surface magma conduits at the same time [*Nostro et al.*, 1998]. When a part of a magma chamber is compressed and another part is decompressed, magma circulation or convection may be initiated or intensified in the magma chamber [e.g., *Cardoso and Woods*, 1999].

2.3.3 Static Stress Change Calculation

Figure 2.5 shows a simple example of static stress changes at the surface caused by a strike-slip motion along a vertical, rectangular fault plane. A stress change at an arbitrary point *p*, which is away from a rupture plane in a homogeneous elastic medium, is a function of the rupture parameters, the elastic properties of the medium, and the position of the point *p* relative to the fault. The rupture parameters consist of the attitude (i.e., strike and dip) and geometry (i.e., width, length, and depth) of the fault, as well as the direction (i.e., rake) and amount of the slip. The elastic properties are described by the elastic moduli of the crust. The calculation of static stresses is based on the elastic dislocation formulae by *Okada* [1992], that use Green's function to find displacements within a half-space with uniform elastic properties.

2.4 Method

We use the Coulomb 3.3 program to model normal stress changes caused by the historical and hypothetical earthquakes. The hypothetical events are either at the locations of the notable historical events or at well-developed faults that have been active through the Holocene. As receivers of the stress changes, the Yellowstone magma reservoir and the potential magma pathway are modeled as vertical planes.

2.4.1 Stress Change Modeling with Coulomb

We employ the Coulomb 3.3 program [*Lin and Stein*, 2004; *Toda et al.*, 2005; 2011] to model static stress changes imparted on the Yellowstone magmatic system by the historical and hypothetical earthquakes. Coulomb is designed to calculate static displacements, strains, and stresses in an elastic half-space caused by deformations, such as earthquakes and magmatic intrusions, following the Okada dislocation model [*Okada*, 1992].

In this study, the source of deformation is earthquakes, and the receiver of the stress change is the Yellowstone magmatic system. We model each source earthquake as a uniform slip on a flat rectangle rupture plane. The source is described by the location, depth, dimension (i.e., length l and width w), and attitude (i.e., strike θ and dip δ) of the fault, as well as the rake λ and displacement d of the slip. The elastic property of the medium is specified by Young's modulus and Poisson's ratio, for which we assume typical values, 8×10^5 bars and 0.25, respectively. We resolve normal stress changes onto the modeled Yellowstone magma reservoir and potential main magma pathway. These magmatic features are approximated as vertical rectangular planes. The vertical attitude is optimal for the receivers because lateral stress transfers are significant in this study; we test near-field earthquakes which are in the same depth range (~10 km) as the magmatic features.

2.4.2 Modeled Historical Earthquakes

We test effects of the two mainshocks and the largest aftershock of the 1959 Hebgen Lake sequence, as well as the 1983 Borah Peak earthquake. Their origin details and source parameters are from published studies.

2.4.2.1 The 1959 Hebgen Lake Sequence

The 18 August 1959 Hebgen Lake sequence consists of two mainshocks (m_B6.3 and m_B7.0), which occurred five seconds apart from each other (at 06:37:18 and 06:37:23 UTC, respectively), and aftershocks including two M_L>6 events at 15:26 on the 18th and at 04:04 on the 19th UTC [*Doser*, 1985]. The epicentral area is characterized by Quaternary normal faults superimposing on preexisting Laramide folds and thrusts [*Smith and Sbar*, 1974]. The fault-plane and moment tensor solutions indicate that the mainshocks are normal-faulting events that reactivated Laramide thrust faults [*Doser*, 1985].

Doser [1985] presented the focal mechanisms of the major events in the sequence (Table 2.1). We test the events that have well constrained mechanisms, the two mainshocks and the largest aftershock (m_B6.5 at 15:26) (Figure 2.6). The moment tensor solution of each event from the long-period body wave data is used to find the strike, dip, and rake of each event. *Doser* [1985] also presented the other parameters, the length and width of the rupture plane, as well as the average displacement of the slip, of each event from the body wave modeling.

Table 2.1. Origin details and source parameters of the historical earthquakes tested in this study.

Event		Origin time, UTC	Epicenter	Depth (km)	M_W
The 1959 Hebgen Lake	The first mainshock	Aug. 18 06:37:18	111.113W, 44.880N	10	6.3
	The second mainshock	Aug. 18 06:37:23	111.026W, 44.838N	15	7.3
	The largest aftershock	Aug. 18 15:26:07	110.720W, 44.850N	10	6.1
The 1983 Borah Peak		Oct. 28 14:06:22	113.87W, 43.98N	15.4	6.8

Table 2.1. (continued)

Event		θ	δ	λ	l (km)	w (km)	d (m)	Reference
The 1959 Hebgen Lake	The first mainshock	95±5°	42±5°	-112°	6.0	14.9	1.0	
	The second mainshock	93±5°	48±5°	-131°	21.0	19.6	6.6	*Doser*, 1985
	The largest aftershock	83±5°	50±5°	-86°	9.0	13.0	0.5	
The 1983 Borah Peak		138±3°	45±3°	-60±5°	21.0	22.6	1.4	*Doser and Smith*, 1985

The first mainshock is a normal-faulting event at ~10 km depth on a fault plane striking at 95 ± 5° and dipping at 42 ± 5° to the southwest [*Doser*, 1985]. (Table 2.1; Figure 2.6; Hereafter, the attitude descriptions of non-vertical fault planes obey the right-hand rule, where the strike is 90° away counter-clockwise from the dip direction [*Aki and Richards*, 1980].) The length and width of the rupture plane are 6.0 km and 14.9 km, respectively, and the average displacement is 1.0 m at -112° of rake. (Hereafter, rake angles follow the sign convention by *Aki and Richards* [1980], where positive values indicate a reverse motion, and 0° rake indicates the sinistral motion.)

The second mainshock probably ruptured a deeper part of the same fault plane as the first one, releasing a larger seismic moment in a very similar mechanism [*Doser*, 1985] (Table 2.1; Figure 2.6). The source is at ~15 km depth. The fault plane strikes at 93 ± 5° and dips at 48 ± 5°. The rupture plane dimension is 21.0 km length by 19.6 km width. The average displacement is 6.6 m at the rake of -131°.

The largest aftershock is also a normal-faulting event that occurred ~29 km east of the mainshocks [*Doser*, 1985] (Table 2.1; Figure 2.6). The strike of the fault plane is 83 ± 5°, and the dip is 50 ± 5°. The motion is almost pure dip-slip (λ = -86°). The slip of 0.5 m occurred on a rupture plane of 9 km length and 13 km width. The source depth is ~10 km.

2.4.2.2 The 1983 Borah Peak Earthquake

The 28 October 1983 Borah Peak earthquake (M_S 7.3) occurred in east central Idaho along a segment of the Lost River fault, a major southeast-striking normal fault in the area active through the Holocene [*Smith et al.*, 1985; *Richins et al.*, 1987]. The event was followed by 421 M_C>2.0 aftershocks [*Richins et al.*, 1987].

The source parameters were determined from various seismologic and geodetic methods, which consistently indicate an oblique slip with a normal and sinistral sense [*Doser and Smith*, 1985; *Barrientos et al.*, 1985; *Nábělek et al.*, 1985; *Ekström and Dziewonski*, 1985; *Ward and Barrientos,* 1986; *Stein and Barrientos*, 1985]. We adopt the source parameters from short-period first motion data [*Doser and Smith*, 1985] (Table 2.1). In the mechanism, the fault plane strikes at 138 ± 3° and dips at 43 ± 3°. The average slip is 1.4 m at the rake of -60±5°. The rupture plane dimension is 21.0 km length by 22.6 km width, and the source is at ~15.4 km depth.

2.4.3 Modeled Hypothetical Earthquakes

In addition to the effects of the historical earthquakes, we investigate static stress changes from 13 hypothetical M_W7.1-7.5 earthquakes around Yellowstone. The list of the hypothetical events is presented in Table 2.2. The locations and focal mechanisms of the events are shown in Figure 2.7. Each event and its location will be discussed in Section 2.4.3.2.

Table 2.2. Source locations and rupture parameters of the hypothetical earthquakes.*

ID	Fault	Long.	Lat.	θ	δ	λ
1	Lost River	-113.870	43.980	138°	45°	-60°
2	Lemhi	-113.511	44.249	138°	45°	-60°
3	Beaverhead	-113.198	44.536	138°	45°	-60°
4	Hebgen Lake 1	-111.113	44.880	95°	42°	-112°
5	Hebgen Lake 2	-111.026	44.838	93°	48°	-131°
6	Hebgen Lake 3	-110.720	44.850	83°	50°	-86°
7	Madison	-111.561	44.778	158°	60°	-90°
8	Centennial	-111.709	44.594	282°	80°	180°
9	Upper Yellowstone Valley	-110.209	44.237	171°	60°	-90°
10	Teton (normal)	-110.671	43.807	19°	70°	-90°
11	Teton (strike-slip)	-110.671	43.807	19°	70°	0°
12	Grand Valley	-111.281	43.413	139°	60°	-90°
13	Emigrant	-110.715	45.391	226°	60°	-90°

* Focal depth is 9.0 km for all events.

Table 2.2. (continued)

ID	Fault	M_W	l (km)	w (km)	d (m)
1	Lost River	7.5	35.0	25.5	7.5
2	Lemhi	7.5	35.0	25.5	7.5
3	Beaverhead	7.5	35.0	25.5	7.5
4	Hebgen Lake 1	7.5	35.0	26.9	7.5
5	Hebgen Lake 2	7.5	35.0	24.2	7.5
6	Hebgen Lake 3	7.5	35.0	23.5	7.5
7	Madison	7.5	35.0	20.8	7.5
8	Centennial	7.1	68.0	18.1	1.2
9	Upper Yellowstone Valley	7.5	35.0	20.8	7.5
10	Teton (normal)	7.5	35.0	19.2	7.5
11	Teton (strike-slip)	7.1	68.0	18.1	1.2
12	Grand Valley	7.5	35.0	20.8	7.5
13	Emigrant	7.5	35.0	20.8	7.5

Four of the 13 hypothetical events are located where the notable historical events occurred. The remaining nine hypothetical events are along well-developed faults active through the Holocene that have not caused a major historical earthquake. We test those nine events because in the study area, having no record of a large earthquake does not necessarily indicate a continuing aseismic nature. The study area is characterized by active tectonics despite the intraplate setting. Therefore, it is probable that strain is accumulating along those faults. In continental intraplate settings, strain rates are generally very small (in the order of 10^{-6}-10^{-9} a^{-1} [e.g., *Li et al.*, 2007]), which often results in recurrence intervals larger than the human timescale. For example, paleoseismic studies estimate the average slip rate of the Lost River fault to be 0.2-0.3 mm a^{-1} [*Hanks and Schwartz*, 1987; *Scott et al.*, 1985ab], and an estimate of the displacement of the fault by the 1983 event is ~1.4 m [*Doser and Smith*, 1985]. This corresponds to the average recurrence interval of 4700-7000 years. Considering the potential sluggish strain accumulation around the ostensibly aseismic faults, we test the hypothetical events along well-developed Holocene faults with no major earthquake record, in addition to those events located at the notable historical events.

2.4.3.1 Determination of the Magnitude, Focal Mechanisms, and Fault Geometries

In order to explore the potential, however small, for earthquake-induced Yellowstone volcanism, we hypothesize earthquakes of M_W~7.5, which is extraordinarily large for the intracontinental setting. In the study area, a M_W7.5 event is highly unlikely but theoretically possible. A seismic moment corresponding to the moment magnitude of 7.5 is achieved if, for example, a 35 km long and 20.8 km wide rupture plane slips by 7.5 m, assuming the shear modulus of 32 GPa. As for the well-developed faults in the area, one or two fault segments together make the total length of ~30-40 km. If the whole brittle layer of continental crust (~18 km thick) is ruptured along a 60° dipping plane, the width of the rupture plane is ~20.8 km. Note that the width of the 1983 Borah Peak rupture plane is estimated to be 22.6 km [*Doser and Smith*, 1985]. The slip of 7.5 m is extremely large. However, the 6.6 m slip of the second Hebgen mainshock indicates the potential for the area's crust to accumulate a sufficient strain. The calculation above is based on the basic equation for the moment magnitude scale [*Kanamori*, 1977],

$$M_W = \frac{2}{3}\log_{10} M_0 - 10.7 \tag{2.1}$$

where M_0 is the seismic moment in dyne·cm. The seismic moment is given by

$$M_0 = \mu A d \tag{2.2}$$

where μ is shear modulus, and A (= $l \times w$) is rupture area [*Kanamori*, 1977].

When a hypothetical event is at the location of a major historical event of known mechanism, we adopt the mechanism and increase the rupture area and displacement to correspond to the moment magnitude of 7.1-7.5, assuming that the whole brittle layer is ruptured. If no major earthquake has been recorded along a fault, or if no focal mechanism solution for a historical event is available, we adopt the attitude of the fault suggested by geological studies to hypothesize an event. Otherwise, we assume a pure dip slip (λ = -90°) on a 60° dipping plane for normal faults, and a pure strike slip (λ = 0° or 180°) along the vertical plane for strike-slip faults. The list of the hypothetical events does not include any reverse or thrust fault; Yellowstone is surrounded by large areas of tectonic extension (i.e., the ISB, CTB, and the Basin and Range province) and the CSZ. For the rupture plane dimension and average displacement of strike-slip faulting events, we follow the empirical relationships between those parameters, moment magnitude, and fault type by *Wells and Coppersmith* [1994]. Each regression between those parameters in the study is based on a large number of data points, providing a statistical significance, which suggests that the relationships are unlikely to be affected by other factors.

2.4.3.2 Geologic Descriptions and Fault Geometries

The descriptions of the 13 hypothetical earthquakes are presented in this section (Table 2.2; Figure 2.7). Events 1, 2, and 3 mimic the focal mechanism of the 1983 Borah Peak earthquake in a larger scale along the three major basin-range style normal faults in east central Idaho. Events 4, 5, and 6 have the focal mechanisms of the two mainshocks and the largest aftershock of the 1959 Hebgen Lake sequence, respectively, at each location. Events 7 and 8 are normal-faulting and strike-slip-faulting events, respectively, located ~50 km west of Yellowstone. Event 9 is a normal-faulting event located to the immediate southeast of Yellowstone at the position line-symmetrical to the Hebgen Lake events about the long axis of the Yellowstone caldera, which runs northeast-southwest. Events 10 and 11 are normal-faulting and strike-slip-faulting events at the Teton fault. The reason for testing both normal and strike-slip faulting on the normal Teton fault is also discussed below. Event 12 is a normal-faulting event located ~100 km south-southwest of Yellowstone. Event 13 is a normal-faulting event ~60 km north of Yellowstone. For all the hypothetical events, we set the source depth at 9 km as the failure of the whole brittle layer of 18 km thick is assumed.

Event 1, The Lost River fault. The Lost River, Lemhi, and Beaverhead faults are the most prominent southwest-dipping basin-range style normal faults in east central Idaho. Of the three, the Lost River fault is farthest from Yellowstone, located ~240 km to west-southwest, and the most seismically active [e.g., *Stickney*, 2007]. The fault dips at high angles at the surface, which forms a fault-block mountain, the Lost River range [e.g., *Haller and Wheeler*, 1992]. Seismologic and geologic studies suggest that the fault has a minor sinistral component [*Doser and Smith*, 1985; *Crone*, 1985; *Crone et al.*, 1987]. The fault has the ~130 km long surface trace which exhibits Quaternary surface ruptures [e.g., *Cochran*, 1985; *Hanks and Schwartz*, 1987]. The fault consists of six or seven segments. The 1983 Borah Peak earthquake ruptured the northern section [e.g., *Doser and Smith*, 1985; *Scott et al.*, 1985a; *Crone*, 1985; *Crone et al.*, 1987; *Susong et al.*, 1990]. The earthquake swarm occurred in 2014 about 20-30 km northwest of the focus of the 1983 event, which suggests a larger fault length than the surface trace [*Pankow et al.*, 2014]. The recurrence interval of large earthquakes is estimated to be 6-15 Ka [*Vincent*, 1995; *Haller and Wheeler*, 2010a]. The estimate of slip rate is small (~0.2-0.3 mm a^{-1}) [*Scott et al.*, 1985b; *Hanks and Schwartz*, 1987].

Event 1 mimics the focal mechanism of the 1983 Borah Peak earthquake, where the strike is 138°, dip is 45°, and rake is -60° (normal faulting in a sinistral sense; Table 2.2; Figure 2.7). The hypothetical rupture plane has the length of 35 km, width of 25.5 km, and displacement of 7.5 m.

Event 2, The Lemhi fault. The Lemhi fault is another major range-forming high-angle normal fault located ~210 km west-southwest of Yellowstone, between the Lost River and Beaverhead faults [e.g., *Anderson*, 1934; *Baldwin*, 1951]. The fault is divided into five to nine segments, depending on the methodology, which add up to ~140 km long [*Stickney and Bartholomew*, 1987; *Haller*, 1988; *Baltzer*, 1990; *Turko*, 1988; *Turko and Knuepfer*, 1991; *Crone and Haller*, 1991]. All but the two end segments show Holocene surface ruptures [*Haller*, 1988]. Paleoseismologic observations suggest the recurrence interval of 15-25 Ka [*Haller*, 1988; *Baltzer*, 1990]. The slip rate estimate is ~0.3 mm a^{-1} [*Scott et al.*, 1985b; *Haller and Wheeler*, 2010b]. The same rupture parameters as Event 1 are given to Event 2 (Table 2.2; Figure 2.7).

Event 3, The Beaverhead fault. The Beaverhead fault is the easternmost among the three major faults in east central Idaho [*Witkind*, 1975]. The fault exhibits a 200 km long fault scarp which offsets Holocene deposits, forming the Beaverhead Mountains [*Haller*, 1988]. The fault has four major segments [*Haller*, 1988]. The recurrence interval is estimated to be smaller than 25 Ka with a potential large uncertainty [*Haller*, 1988]. The slip rate estimate is <0.3 mm a^{-1} based on an analogy of the Lost River fault [*Scott et al.*, 1985b; *Haller et al.*, 2010]. The same rupture parameters as Event 1 are given to Event 3 on the Beaverhead fault (Table 2.2; Figure 2.7).

Event 4, The Hebgen Lake 1. The two mainshocks of the 1959 Hebgen Lake earthquake caused surface rupture of the Hebgen fault [*Myers and Hamilton*, 1961; 1964; *Witkind*, 1964; 1969; *Witkind et al.*, 1962; 1964]. The Hebgen fault is a high-angle (60°-80°) southwest-dipping normal fault that bounds the northeastern side of the Hebgen Lake to the immediate west of Yellowstone [*Witkind*, 1975; *Johns et al.*, 1982; *Witkind et al.*, 1962; 1964]. The surface trace of the fault is approximately 15 km long, and the fault scarp is 3 m high on average [*Witkind*, 1964]. The fault generally parallels the Laramide-age thrust faults [*Witkind*, 1964; *Myers and Hamilton*, 1964]. Paleoseismic investigations revealed multiple terraces indicating recurrent seismicity [*Pierce et al.*, 2000ab]. A majority of investigators suggest the recurrence interval of <15 Ka [*van der Woerd et al.*, 2000; *Wheeler and Krystinik*, 1992; *Ostenaa and Wood*, 1990; *Haller*, 2010a]. In a seismologic study, the slip rate of this fault is estimated to be 0.8-2.5 mm a^{-1} [*Doser*, 1985]. Through a geological slip analysis, *Wheeler and Krystinik* [1992] estimate a long-term (up to 2 Ma) slip rate to be 0.2-1.0 mm a^{-1}. A slip rate estimate by *Stickney et al.* [2000] is 1.0-5.0 mm a^{-1}.

Event 4 mimics the focal mechanism of the first mainshock of the 1959 Hebgen Lake event, which has the strike of 95°, dip of 42°, and the rake of -112° (normal faulting in a dextral sense; Table 2.2; Figure 2.7). The rupture parameters extended for the hypothetical event are the fault length of 35 km, width of 26.9 km, and displacement of 7.5 m.

Event 5, The Hebgen Lake 2. Event 5 is also located at the Hebgen fault (see the preceding paragraphs on the Hebgen fault) with the fault parameters adopted from the second mainshock of the 1959 Hebgen Lake event: 93° strike, 48° dip, and -131° rake (normal faulting in a high sinistral sense; Table 2.2; Figure 2.7). The rupture plane parameters are the same as Event 4 (see above).

Event 6, The Hebgen Lake 3. The location of Event 6 is at the 1959 Hebgen Lake largest aftershock, which is ~30 km east of the mainshocks [*Doser*, 1985]. There is no known fault in the epicentral area whose attitude is consistent with the nodal planes of the aftershock. For the hypothetical event, we adopt the fault plane solution for the aftershock suggested by *Doser* [1985], 83° strike, 50° dip, and -86° rake (nearly pure normal faulting; Table 2.2; Figure 2.7). The rupture parameters are the same as Event 4 (see above).

Event 7, The Madison fault. The Madison fault, also referred to as the Madison Range fault and Madison Valley fault [*Pardee*, 1950], is a seismically active, high-angle, southwest-dipping normal fault located ~30 km west of Yellowstone. The footwall forms the Madison Range to the northeast of the fault. The Hebgen fault is located ~15-20 km northeast of the Madison fault. The 1959 Hebgen Lake earthquake caused <1 m slips of the multiple short parts of the Madison fault [*Witkind*, 1964; *Myers and Hamilton*, 1964]. Researchers define three [*Pardee*, 1950; *Shelden*, 1960; *Johns et al.*, 1982; *Schneider*, 1985] or more [*Young*, 1985; *Ruleman and Lageson*, 2002] sections of the fault forming rightstepping en echelon. The total fault length is ~98 km. The average strike is ~158°, and the dip at the surface is ~60° [*Mathieson*, 1983]. The Madison fault is well expressed by nearly continuous fault scarps that indicate recurrent seismicity in the late Quaternary [*Gary*, 1980; *Schneider*, 1985; *Lundstrom*, 1986; *Ruleman*, 2002; *Ruleman and Lageson*, 2002]. *Lundstrom* [1986] estimates the average recurrence interval in the last 2 Ma to be 10-25 Ka based on the tilting rate of the graben. Researchers estimate slip rates of the fault in a range from ~0.2 to 1.0 mm a^{-1} [*Ruleman and Lageson*, 2002; *Lundstrom*, 1986; *Mathieson*, 1983; *Haller*, 2010b].

Event 7 is located at the Madison fault. The strike and dip of 158° and 60°, respectively, are adopted from the geological observations [*Mathieson*, 1983] (Table 2.2; Figure 2.7). The pure dip slip in the normal sense (λ = -90°) is assumed. The rupture length and width of the hypothetical event is 35 km and 20.8 km, respectively, and the displacement is 7.5 m.

Event 8, The Centennial fault. The Centennial fault is a north-dipping normal fault system located only ~50 km west of Yellowstone. The fault bounds the north side of the Centennial range [*Bond*, 1978; *Pardee*, 1950; *Witkind*, 1975]. The largest escarpment of the fault is ~600 m [*Witkind*, 1975]. The fault system appears to be active from the mid Pleistocene through the Holocene [*Bartholomew et al.*, 2002; *Majerowicz*, 2008; *Petrik*, 2008; *Anastasio et al.*, 2010]. Slip rate estimates for this fault range from 0.3 to 1.3 mm a^{-1} [*Pierce and Morgan*, 1992; *Petrik*, 2008; *Sonderegger et al.*, 1982; *Reilinger et al.*, 1977; *Haller*, 2010c]. The Centennial fault is comprised of a series of nowthwest-trending left-stepping en echelon faults, which makes the overall eastward trend [*Petrik*, 2008]. The western end of the Centennial fault overlaps with the eastern end of the opposite-dipping

Lima Reservoir fault. Together they accommodate dextral transtension [*Majerowicz et al.*, 2007; *Majerowicz*, 2008; *Anastasio et al.*, 2010]. The Centennial fault system is located in the CSZ, in which the dextral shear caused by the differential motion between the SRP and CTB is accommodated in a broad area [*Payne et al.*, 2008; 2013]. In the CSZ, only a fraction of events are normal faulting along a north-dipping nodal plane [*Stickney*, 2007]. The majority of the fault-plane solutions indicate dextral motion [*Payne et al.*, 2013]. Slip analyses also suggest accommodation of dextral shear during the middle to late Pleistocene and Holocene [*Majerowicz et al.*, 2007; *Majerowicz*, 2008; *Anastasio et al.*, 2010].

Event 8 is modeled as a pure dextral-slip event (λ = 180°) along the Centennial fault, assuming the shear strain in the area is accommodated by the Centennial and Lima Reservoir faults (Table 2.2; Figure 2.7). The strike of 282° and dip of 80° are assumed based on the geological investigations [e.g., *Witkind*, 1975; *Petrik*, 2008]. Based on the empirical relationship between magnitude and rupture parameters [*Wells and Coppersmith*, 1994], the rupture length, width, and displacement are set to be 68 km, 18.1 km, and 1.2 m, respectively.

Event 9, The Upper Yellowstone Valley fault. Event 9 is a slip along the Upper Yellowstone Valley fault, which is located to the immediate southeast of Yellowstone (Figure). Even though there is no record of a large event along this fault, we test the hypothetical event because this normal fault is at the position line-symmetrical to the Hebgen fault about the NE-SW-running long axis of the Yellowstone caldera. The area around the fault is likely to be accumulating extensional strain that could potentially cause an event of a magnitude comparable to that of the Hebgen Lake earthquakes.

The Upper Yellowstone Valley fault is a group of en echelon faults along the Upper Yellowstone valley [*Richmond and Pierce*, 1971; 1972]. The fault system is also referred to as the Yellowstone River faults [*Case*, 1997; *Wong et al.*, 2000]. The total length of the fault system at the surface is ~25 km. The en echelon geometry trending north-south (θ = 171°) forms a full graben, the Upper Yellowstone valley, which indicates a conjugate set of normal faults [*Richmond and Pierce*, 1971; 1972; *Smedes et al.*, 1989]. The fault scarp offsets the Pleistocene glacial deposit by up to 5 m [*Richmond and Pierce*, 1971]. There is insufficient geological information to suggest a recurrence interval or slip rate of the fault with some certainty.

Event 9 is a pure normal-faulting event along the Upper Yellowstone Valley fault, whose average strike is ~171° (Table 2.2; Figure 2.7). We assume a 35 km long 20.8 km wide rupture plane dipping at 60° to the west. The amount of slip is 7.5 m.

Event 10, normal faulting of the Teton fault. The Teton fault is located ~25 km south of Yellowstone in an area of high seismicity [*Love and Reed*, 1968; *Smith et al.*, 1993]. It is a normal fault that exhibits a 3-52 m high Holocene fault scarp [*Byrd et al.*, 1994], which bounds the eastern margin of the Teton range. The Teton fault has six segments adding up to 59 km in total [*Susong et al.*, 1987]. The overall average strike is 19°, and the nearly linear strike suggests a steep dip. Kinematic models suggest a dip of 45°-70° [*Byrd et al.*, 1994]. Even though the Teton fault appears to be seismically quiescent for M>3 events [*Smith et al.*, 1990, 1993; *Smith and Arabasz*, 1991], geological evidence indicates a potential to produce an earthquake as large as M7.5, and recurrence intervals of 1500-6000 years for scarp-forming events [*Gilbert et al.*, 1983; *Doser and Smith*, 1983; *Smith et al.*, 1993].

Event 10 is a pure normal-faulting slip (λ = 180°) along a hypothetically extended Teton fault (Table 2.2; Figure 2.7). The attitude of the rupture plane is adopted from the actual Teton fault, which strikes at 19° and dips at 70° [*Byrd et al.*, 1994]. The rupture area is 35 km length by 19.2 km width, and the slip is 7.5 m.

Event 11, sinistral faulting of the Teton fault. We also test a sinistral slip on the Teton fault. Although there is no record of a historical strike-slip event along the Teton fault, a paleoseismic investigation at a trenching site found an indication of lateral slips. In fact, the motion of the SRP tectonic block suggests shear strain accumulation around the fault. The Teton area is located on the opposite side of the CSZ with respect to the SRP, which is rotating clockwise about the pole in the central Idaho [*Payne et al.*, 2013; *McCaffrey et al.*, 2007; 2013]. If the rate of the rotational motion is higher than the terrane to the southeast of the SRP, as it is higher than the CTB causing the CSZ, sinistral strain can accumulate along the southern flank of the SRP including the Teton area.

To find strain rate patterns in the Teton area, we analyze GPS surface velocity data. Researchers have proposed several methods to identify strain patterns from GPS data [*Wdowinski et al.*, 2001; *Allmendinger et al.*, 2007; *Kahle et al.*, 2000; *Hackl et al.*, 2009]. The main difference among these methods is the interpolation scheme of GPS data to obtain a continuous and uniform velocity field. We adopt the method by *Hackl et al.* [2009], who use the splines in tension algorithm [*Wessel and Bercovici*, 1998] for the east and north velocity components separately. The method is relatively simple and therefore low in computational cost compared to the other method. This method as well as the others cited above require only geodetic velocity data as input. Hence, the result is free from influences of knowledge and assumption in the geologic setting.

Following the method by *Hackl et al.* [2009], we find dilatation and shear strain patterns, which are shown in Figure 2.8. The resultant strain patterns show that both dilatation (~40×10^{-9} a^{-1}; Figure 2.8a) and shear (~30×10^{-9} a^{-1}; Figure 2.8b) strains are accumulating in the Teton area. On this basis, a hypothetical event of sinistral faulting on the Teton fault is also tested as Event 11.

Event 11 is a sinistral-slip (λ = 0°) event along an extended Teton fault (Table 2.2; Figure 2.7). As in the case of Event 10, the attitude of the hypothetical rupture plane is adopted from the actual Teton fault (θ = 19° and δ = 70°). The study by *Wells and Coppersmith* [1994] suggests the rupture length of 68 km and the displacement of 1.2 m for a strike-slip rupture with the width of 18.1 km.

Event 12, The Swan Valley section of The Grand Valley fault. The Grand Valley fault is a major normal fault located ~120 km south-southwest of Yellowstone, extending from the southern margin of the SRP southward along the Idaho-Wyoming border. It is a high-angle southwest-dipping fault that forms a full graben, the Swan valley, together with the antithetic Snake River fault [*Piety et al.*, 1992]. Four segments, totaling to ~136 km long, are defined based on the difference in slip rate [*Piety et al.*, 1992]. The average strike of the whole fault is 158°. Although there is no record of a large historical earthquake, paleoseismic evidence indicates that the fault has been active though the Quaternary [*Piety et al.*, 1992]. Seismic reflection data suggest 2-3 km thick basin fill [*Royse et al.*, 1975; *Dixon*, 1982].

The Swan Valley section [*Piety et al.*, 1986; 1992; *McCalpin et al.*, 1994] is the 49 km long, northernmost section of the Grand Valley fault, extending from the SRP to the Idaho-Wyoming border. The fault trace is inferred for this section because of the absence of fault scarps. The average strike of the section is 139°. The recurrence interval of the segment is estimated to be ~100 Ka [*Piety et al.*, 1992]. Slip rates as small as ~0.02 mm a^{-1} have been suggested for this section [*Piety et al.*, 1986; *Anders*, 1990].

Event 12 simulates a pure normal-faulting slip (λ = -90°) of the Swan Valley section of the Grand Valley fault (Table 2.2; Figure 2.7). The strike of the hypothetical event is 139°, and a 60° dip is assumed. The rupture area is 35 km length by 20.8 km width, and the amount of slip is 7.5 m.

Event 13, The Emigrant fault. The Emigrant fault [*Pardee*, 1950] is located ~50 km north of Yellowstone [*Lopez and Reiten*, 2003]. The fault is also referred to as the Deep Creek fault [*Bonini et al.*, 1972; *Personius*, 1982ab; 1986] and the Emigrant Valley fault [*U.S. Coast and Geodetic Survey*, 1959]. The Emigrant fault is a range-front normal fault dipping to the northwest [*Bonini et al.*, 1972]. The total length of the fault trace is 43 km. The average strike of the whole fault is 226°. The dip estimates are 50°-60° [*Personius*, 1982ab; *Pardee*, 1950] although a model based on gravity anomaly data suggests a vertical dip [*Bonini et al.*, 1972]. The fault has been active since at least 15 Ma [*Pierce and Morgan*, 1992] with the recurrence interval estimate of 10-15 Ka [*Mason*, 1992]. The slip rate is estimated to be <1.0 mm a^{-1} [*Pierce and Morgan*, 1992; *Ruleman et al.*, 2000; *Ruleman*, 2002].

Event 13 is a pure normal-faulting event along the extended Emigrant fault (Table 2.2; Figure 2.7). The strike and dip are 226° and 60°, respectively. The rupture plane is 35 km length by 20.8 km width. The displacement of the event is 7.5 m.

2.4.4 Modeled Yellowstone Magmatic System

The tomographic model by *Farrell et al.* [2014] images a low-velocity body interpreted as the Yellowstone magma reservoir and its northeastward shallowing extension (Figure 2.4). Figure 2.5 shows the 3-D isosurface of the low-velocity body [*Farrell et al.*, 2014; Farrell, personal communication, 2015]. For the normal stress change calculations, the magma reservoir and potential main magma pathway are approximated by vertical rectangle planes. The model plane of the magma reservoir (hereafter "the reservoir plane") is indicated by red rectangles or red lines in the figures in this chapter. The model plane of the potential magma pathway (hereafter "the pathway plane") is indicated by navy rectangles or navy lines.

2.4.4.1 Magma Reservoir

We calculate earthquake-caused normal stress changes on a vertical model plane that approximates the location and size of the Yellowstone magma reservoir imaged by a seismic tomographic model by *Farrell et al.* [2014] (Figure 2.4). Their model attained an unprecedentedly high resolution by using earthquake data collected by the Yellowstone Seismic Network over 26 years from 1984 to 2011. The model shows a low V_p body interpreted as a crustal magma reservoir below the youngest (0.64 Ma) caldera. The magma reservoir has an elongated shape, ~60 km long and ~20 km wide, running NE-SW. Its long axis coincides with that of the Yellowstone caldera. The top and bottom of the low-velocity body are at ~5 km and ~17 km, respectively.

The magma reservoir is modeled as a vertical rectangular plane of 60 km long located at the long axis of the magma reservoir (Figures 2.4 and 2.9). The width in the vertical direction is 12 km, mimicking the depth extent of the magma reservoir, from 5 km to 17 km. In this study, the NW-SE running short axis of the magma reservoir is not tested. The normal stresses on the model plane along the short axis is effectively changed by earthquakes located in the direction perpendicular to the plane (i.e., to the northeast or southwest of Yellowstone), in which neither historical nor hypothetical events are located.

2.4.4.2 Magma Pathway

The tomographic images by *Farrell et al.* [2014] show that the low-velocity body shallows extending ~15 km northeast of the caldera (Figure 2.4). The shallowing part is interpreted as a body of magmatic fluids (i.e., gas, hydrothermal fluids, and melt) because it lies below the most thermally and hydrothermally active basin in the volcanic field [*Farrell et al.*, 2014]. Based on the interpretation, we assume that the northeastward extension becomes the initial main magma pathway when an eruption occurs. In order to find normal stress changes, the potential magma pathway is modeled as a vertical rectangular plane perpendicular to the long axis of the magma reservoir (Figures 2.4 and 2.9). The model plane approximates a vertical slice of the pathway, extending from 1 km to 6 km depths. The length is 34 km.

2.5. Results

Normal stress changes on the Yellowstone magmatic system caused by the four historical and 13 hypothetical events were estimated using the elastic dislocation model. The second mainshock of the 1959 Hebgen lake earthquakes as well as three hypothetical events (Events 5, 6, and 9) show stress change patterns favorable to facilitate or trigger an eruption.

Figure 2.10 shows the maximum clamping and unclamping on the reservoir plane caused by each hypothetical event. Similarly, Figure 2.11 shows the maximum unclamping on the pathway plane. Overall, M_W7.1-7.5 events more than 200 km away from the magmatic system cannot cause a significant stress change around the receivers, regardless of fault geometry or source mechanism (Figures 2.10 and 2.11). Even if an event is in a proximal area, the fault attitude and position relative to the magmatic system must be optimal to affect the stress field around the receiver. For example, the hypothetical event on the Centennial fault (i.e., Event 8) cause small stress changes on the model planes despite a short distance (~60 km) (Figures 2.10 and 2.11).

The result of each tested event is shown in Figures 2.12 through 2.28. Each figure shows the resultant stress changes caused by each event, either historical or hypothetical, with the same set of plots, two maps and two cross sections. All the plots show normal stress changes. The first map of each figure (labeled "a") shows the stress change at the depth of 3.5 km, which is the mid-depth of the pathway plane extending from 1 km to 6 km depths. The second map (labeled "b") shows the 11 km depth, the mid-depth of the reservoir plane. The normal stress change on the reservoir plane is shown in the red rectangle in the first cross section (labeled "c") of each figure. The navy rectangle in the second cross section (labeled "d") represents the pathway plane. In these figures, the blue spectrum (i.e., positive values) indicates unclamping (i.e., decrease in normal stress). Conversely, clamping (i.e., increase in normal stress) is represented by the red spectrum (i.e., negative values). The values of stress change are in bars (1 bar = 0.1 MPa).

We tested the sensitivity of our results to variation in the model parameters and found that for realistic strike, dip, and rake for the earthquakes, the models returned very similar results.

2.5.1 Effects of the Historical Earthquakes

We tested four historical earthquakes in the area: the two mainshocks and the largest aftershock of the 1959 Hebgen Lake earthquakes, as well as the 1983 Borah Peak earthquake. Among them, the second Hebgen Lake mainshock caused the largest normal stress change on the model planes of the magma reservoir and potential pathway. The effects from the other events appear limited.

2.5.1.1 The 1959 Hebgen Lake Sequence

Figure 2.12 shows the normal stress changes due to the M_W6.3 first mainshock of the Hebgen Lake sequence. This is a normal-faulting event with a small dextral-slip component. In the figure, none of the lobes of large stress change reach Yellowstone’s magmatic system (Figure 2.12ab). The cross sections show virtually no effect on the model planes (Figure 2.12cd). The maps show that the lobes of stress change extend farther in the direction perpendicular to the strike than the parallel direction, which is predictable when the strike-slip component is small or none.

The M_W7.3 second mainshock ruptured a larger area than the first mainshock (Table 2.2), which is obviously shown in the extent of the stress changes (Figure 2.13). The maps show that a lobe of decreased normal stress (i.e., unclamping) hits the modeled magma reservoir (Figure 2.13ab). As a result, the reservoir plane is unclamped in a large area, with the maximum value of 1.4 bars at the center of the top edge of the model plane. This unclamping may facilitate bubble nucleation of volatiles in the magma, which in turn leads to an increase in magma volume and therefore an overpressure in the magma reservoir. The normal stress moderately increases in the southwestern end of the magma reservoir (Figure 2.12c). This contrast between the areas of increased and decreased stresses may promote magma circulation in the reservoir. The effect on the model plane for the magma pathway is limited; the earthquake decreases the normal stress as high as 0.15 bars (Figure 2.13d).

The largest aftershock of the Hebgen Lake sequence (M_W6.1) was smaller but took place closer to Yellowstone. The effects from this event on the Yellowstone magmatic system are small (Figure 2.14). The normal stress on the reservoir plane is slightly increased (i.e., clamping) as much as 0.10 bars (Figure 2.14c). On the pathway plane, the normal stress decreased by up to 0.12 bars (Figure 2.14d).

2.5.1.2 The 1983 Borah Peak Earthquake

In contrast to the Hebgen Lake sequence which took place ~50 km from Yellowstone, the 1983 M_W6.8 Borah Peak earthquake occurred ~250 km away. Although the event changed the normal stress in a large area around the epicenter, the distance was too far to affect the Yellowstone magmatic system (Figure 2.15).

2.5.2 Effects of the Hypothetical Earthquakes

We also simulated normal stress changes due to 13 hypothetical events, 11 M_W7.5 normal-faulting and two M_W7.1 strike-slip-faulting events (Figures 2.10 and 2.11). The hypothetical events located on the prominent normal faults in south central Idaho (i.e., the

Lost River, Lemhi, and Beaverhead faults) have little effect on the Yellowstone magmatic system. Among the others, Events 5 at the Hebgen second mainshock, Event 6 at the Hebgen aftershock, and Event 9 at the Upper Yellowstone Valley fault show stress change patterns favorable to induce an eruption.

Event 1, The Lost River fault. The first hypothetical event is placed on the Lost River fault, which the 1983 Borah Peak earthquake ruptured (Table 2.2; Figure 2.7). Since the moment magnitude of the hypothetical event (M_W7.5) is larger than the 1983 Borah Peak earthquake (M_W6.8), the lobes of significant stress change are larger (Figure 2.16ab). However, the distance to Yellowstone is still too large to affect the stress field around the receiver (Figure 2.16cd).

Event 2, The Lemhi fault. Event 2 is on the Lemhi fault, another major normal fault in the area that strikes parallel to the Lost River fault (Table 2.2; Figure 2.7). Although the epicenter is ~60 km closer to Yellowstone than Event 1, the effects of this event do not reach Yellowstone (Figure 2.17ab). The cross sections indicate near-zero values of stress change (Figure 2.17cd).

Event 3, The Beaverhead fault. Event 3 is on the other basin-range normal fault in south central Idaho, the Beaverhead fault (Table 2.2; Figure 2.7). This fault is closest (~200 km) to Yellowstone among the three prominent normal faults. Still, the distance is too large for Event 3 to significantly change the stress field around Yellowstone (Figure 2.18).

Event 4, The Hebgen Lake 1. Event 4 is a normal-faulting event which adopts the location and fault parameters of the 1959 Hebgen Lake first mainshock (Table 2.2; Figure 2.7). This hypothetical event weakly changes the normal stress on the model planes (Figure 2.19). A large area on the reservoir model plane is unclamped by up to 0.87 bars while the southwestern end of the model plane is slightly clamped at around -1 bar (Figure 2.19c). The pathway plane is also weakly unclamped with the maximum value of 1.1 bars.

Event 5, The Hebgen Lake 2. Event 5 adopts the location and fault parameters of the second mainshock of the Hebgen Lake sequence (Table 2.2; Figure 2.7). Our result shows that the second mainshock effectively decreased the normal stress on the reservoir plane. The result for this hypothetical event shows the same pattern of stress change (Figure 2.20) as the actual second mainshock of the Hebgen sequence (Figure 2.13). The normal stress moderately decreases on the largest part of the reservoir model plane by up to 2.4 bars (Figure 2.20c). The maximum unclamping is found at the center of the top edge. The southwestern end of the model plane is clamped by up to 1.2 bars (Figure 2.20c). The whole pathway plane is weakly unclamped by ~1-1.7 bars (Figure 2.20d). As in the case of the Hebgen Lake second mainshock, this unclamping on a large area of the reservoir plane is favorable to initiate bubble nucleation. Also, the contrast between clamping and unclamping can cause magma circulation.

Event 6, The Hebgen Lake 3. Event 6 is at the location of the largest aftershock of the Hebgen Lake sequence (Table 2.2; Figure 2.7). According to our result, the actual aftershock was too small to affect the stress field around Yellowstone even though its epicenter was closer to the model planes than the mainshocks (Figure 2.14). On the other hand, this hypothetical event strongly affects the stress field (Figure 2.21). Moreover, the pattern of normal stress change is very favorable to trigger an eruption. The largest area on the reservoir plane is strongly clamped (Figure 2.21c). The northeastern part is most strongly clamped with the absolute maximum value of 11.1 bars. In addition, the upper part of the pathway model plane is moderately unclamped by up to 4.9 bars (Figure 2.21d). If a large earthquake that were to occur at the largest aftershock, it would squeeze the magma reservoir while opening up the potential magma pathway.

Event 7, The Madison fault. Event 7 is a normal-faulting event located on the Madison fault (Table 2.2; Figure 2.7). Although the epicenter is not too far away from Yellowstone (~60 km), the event does not cause a large normal stress change on the reservoir plane mainly because the model plane is located in the transition zone between lobes of positive and negative stress changes (Figure 2.22ab). As a result, the northeastern half of the reservoir model plane is weakly clamped by up to 1.0 bar (the absolute maximum value) while the other half is weakly unclamped by up to 0.79 bars (Figure 2.22c). This contrast may facilitate magma circulation. The pathway model plane is moderately clamped with the absolute maximum value of 0.44 bars (Figure2.22d).

Event 8, The Centennial fault. Event 8 is a strike-slip event along the Centennial fault located only ~70 km west of Yellowstone (Table 2.2; Figure 2.7). This event does not cause a significant change in normal stress on either model planes because Yellowstone is located in the transition zone between areas of positive and negative stress changes (Figure 2.23ab). Accordingly, both cross sections show virtually no effects from the event (Figure 2.23cd).

Event 9, The Upper Yellowstone Valley fault. Event 9 is a normal-faulting event located to the immediate south of Yellowstone (Table 2.2; Figure 2.7). The resultant pattern of stress change is preferable to initiate magma circulation. The southwestern half of the reservoir plane is moderately clamped by up to 2.3 bars (the absolute maximum value) while the other half is moderately unclamped by up to 1.9 bars (Figure 2.24c). In addition, the normal stress change unclamps the pathway plane by decreasing the stress by up to 5.0 bars (Figure 2.24d).

Event 10, normal faulting of the Teton fault. Event 10 is a normal faulting of the Teton fault (Table 2.2; Figure 2.7). The fault is located only ~50 km south of the southwestern end of the magma reservoir. However, the effects on the model planes appear scarce (Figure 2.25). Both model planes undergo very small decreases in normal stress (up to ~0.5 bars) (Figure 2.25cd).

Event 11, sinistral faulting of the Teton fault. Event 11 is a strike-slip faulting of the Teton fault (Table 2.2; Figure 2.7). This event also causes little effect on the model planes (Figure 2.26). On the reservoir plane, only the southwestern end is weakly unclamped by up to 1.0 bar (Figure 2.26c). The cross section for the pathway plane shows no effect from the strike-slip event (Figure 2.26d).

Event 12, The Swan Valley section of The Grand Valley fault. Event 12 is a normal-faulting event located ~100 km south-southwest of Yellowstone (Table 2.2; Figure 2.7). The normal stress change around Yellowstone due to this event is small (Figure 2.27). The normal stress is slightly increased by up to 0.56 bars on the reservoir plane and by ~0.25 bars on the pathway model plane (the absolute maximum values) (Figure 2.27cd).

Event 13, The Emigrant fault. Event 13 is a normal-faulting event on the Emigrant fault ~70 km north of Yellowstone (Table 2.2; Figure 2.7). A lobe of stress increase reaches the pathway model plane (Figure 2.28). The reservoir model plane is moderately clamped in the northeastern end with the absolute maximum value of 2.0 bars (Figure 2.28c). The whole pathway plane is moderately clamped by up to 1.3 bars (the absolute maximum value) (Figure 2.28d). The clamping on the reservoir model plane may slightly increase the pressure in the magma reservoir. However, the clamping on the pathway plane does not facilitate the release of the pressure.

2.6 Discussion

The aim of this study is to estimate static stress changes around the Yellowstone magmatic system caused by the historical and hypothetical earthquakes in the area. The second mainshock of the 1959 Hebgen lake earthquakes, as well as three hypothetical events (Events 5, 6, and 9), show stress change patterns favorable to facilitate or trigger an eruption. Whether stress changes from those earthquakes are great enough to induce an eruption depends on the state of magma in the magma reservoir. Several future directions of this study are also discussed in this section.

Could the stress changes caused by the tested earthquakes actually trigger a Yellowstone eruption? It largely depends on the pressure and fluid state of the magma in the magma reservoir. According to our result, the second Hebgen mainshock decreased the normal stress (i.e., unclamping) on the reservoir plane by up to 1.4 bars (Figure 2.13c). In comparison, a decrease in normal stress of 0.1-1.0 bars caused by four local M_W5.1 earthquakes is considered responsible for the 1999 eruption of Cerro Negro volcano, Nicaragua [*Diez et al.*, 2005]. *De la Cruz-Reyna et al.* [2010] note that decreases in normal stress of only 0.01 and 0.03 bars due to preceding earthquakes induced the eruptions of the 1999 Popocatépetl, Mexico, and the 2003 Tungurahua, Ecuador, respectively. This suggests that even a small normal stress change can trigger an eruption if the pressure in a magma chamber is close to the critical point. Although there is no direct way to measure the pressure in a magma chamber, it is possible to construct working models to estimate the shape and inflation rate of a magma chamber from the pattern of surface deformation [e.g., *Mogi*, 1958; *Geirsson*, 2014]. Such information aids estimating the magma chamber pressure with many assumed parameters, ranging from the temperature, composition, and compressibility of the magma to the temperature and lithology of the country rock [e.g., *Huppert and Woods*, 2002].

Both the second Hebgen mainshock in 1959 and Event 5, which mimics the mainshock, indicate decreases in normal stress (i.e., unclamping) on the reservoir plane (Figures 2.13 and 2.20), potentially causing bubble nucleation. How long does it take to accumulate elastic strain along the fault comparable to those events'? The estimates of the long-term slip rate of the Hebgen fault are in the range from ~0.2 to 5.0 mm a^{-1} [*Wheeler and Krystinik*, 1992; *Stickney et al.*, 2000]. The displacement by the second Hebgen mainshock is estimated to be 6.6 m [*Doser*, 1985]. For the M_W7.5 hypothetical event at the same location (Event 5), a slip displacement of 7.5 m is assumed (Table 2.2). Assuming: (1) that the 1959 events fully released the accumulated elastic strain at the time, (2) that the full slip deficit is accommodated as elastic strain (i.e., no plastic deformation), and (3) that the accumulated strain is not partially released as a small event, it takes ~1320-33,000 years to accumulate the slip deficit of 6.6 m. Under the same assumptions, the slip deficit of 7.5 m requires ~1500-37,500 years. Note that if the first assumption is false, the necessary amount of time is shortened. If the second and/or third assumptions are false, the duration is prolonged.

Because of the limited geologic information, the earthquake cycle analysis cannot be applied to Event 6, which mimics the Hebgen aftershock (Table 2.2). This hypothetical event imparts a considerable negative normal stress change (i.e., clamping) on the reservoir plane while unclamping the modeled pathway (Figure 2.21). There is no known fault in the epicentral area whose attitude is consistent with the nodal planes of the aftershock. Therefore, neither slip rate nor the last occurrence of a large earthquake along the fault is clear.

Event 9 on the Upper Yellowstone Valley fault is the other hypothetical event that shows a stress change pattern favorable to induce an eruption (Figures 2.7 and 2.24). A good contrast between clamping and unclamping is found on the reservoir plane (Figure 2.24c), which could initiate magma circulation. An estimate of the fault slip rate is 0.4-1.4 mm a^{-1}, although the values are model-dependent [*Wong et al.*, 2000]. Under the same assumptions described above, it requires ~5400-18,700 years to accumulate the slip deficit of 7.5 m. Considering that the fault has been active throughout the late Quaternary (<15 Ka) [*Pierce*, 1998], and that no historical large earthquake on this fault is recorded, the Upper Yellowstone Valley fault may be ready to slip if the actual slip rate is in the higher end of the estimated range.

Because this study is preliminary on the Yellowstone-earthquake relationship, several future directions of this study can be proposed. With a 3-D model of the magma reservoir and an assumed compressibility, volume changes of the magma reservoir due to the earthquakes can be estimated. For the hypothetical events that show potential for inducing an eruption, it is worth testing more realistic fault and slip geometries by tapering the source slips, which removes unrealistic stress concentrations at the edges of the fault. Static stress effects of earthquakes on the lower magma reservoir can also be estimated. Seismic tomographic model by *Huang et al.* [2015] revealed a larger basaltic magma reservoir residing in 20-45 km depths, deeper than the one we modeled. This magma reservoir can initiate an eruption process by feeding magma to the upper magma reservoir, causing magma mingling as in the case of the 1707 Mt. Fuji eruption [*Chesley et al.*, 2012]. *Nostro et al.* [1998] analyzed the two-way coupling between Vesuvius eruptions and Apennine earthquakes. Because of the incomparable size of Yellowstone's magma reservoir, its deflation after a large eruption could drastically change the stress field in a large area. As a result, the stress states around the nearby faults could be brought closer to the Coulomb failure. It is of interest to determine what faults would be affected by the magma reservoir deflation.

Conclusions

We investigate the effects of the four historical and 13 M_W~7.5 hypothetical earthquakes in the Northern Rockies on the Yellowstone magmatic system imaged in a seismic tomography model. Normal stress changes on the modeled magma reservoir and pathway are calculated using the elastic dislocation model. The following is a summary of the notable results and their implications.

1. Despite the proximity to Yellowstone (~50 km), the result shows virtually no effect from the first mainshock (M_W6.3) and the largest aftershock (M_W6.1) of the 1959 Hebgen Lake sequence because of the attitudes and slip directions of the events.
2. The M_W7.3 second Hebgen mainshock unclamps the reservoir plane in a large area, with the maximum value of 1.4 bars at the center of the top edge of the model plane, which could facilitate bubble nucleation. The normal stress moderately increases in the southwestern end of the reservoir plane. This contrast

between the areas of increased and decreased normal stresses may promote magma circulation. The effect on the pathway plane is limited.

3. None of the historical or hypothetical events in south central Idaho, namely the 1983 M_W6.8 Borah Peak and the M_W7.5 hypothetical events on the Lost River, Lemhi, and Beaverhead faults, affects the stress field around the Yellowstone magmatic system because of the large distances.
4. Hypothetical Event 5, which adopts the location and fault parameters of the second Hebgen mainshock, decreases the normal stress on the largest part of the reservoir plane by up to 2.4 bars, which could initiate bubble nucleation. The event also clamps the southwestern part of the reservoir plane by up to 1.2 bars. This contrast between the positive and negative stress changes could promote magma circulation. Based on the estimated slip rates of the fault, it takes ~1320-33,000 years to accumulate the slip deficit of 6.6 m, the amount of the slip in the 1959 Hebgen Lake event.
5. The hypothetical event at the Hebgen Lake aftershock (Event 6) shows the pattern of normal stress change very favorable to trigger an eruption. The largest area on the reservoir plane is strongly clamped by up to 11.1 bars, while the pathway plane is moderately unclamped by up to 4.9 bars. If a large earthquake comparable to this hypothetical event occurs at the location, it would squeeze the magma reservoir while opening the potential magma pathway.
6. Event 9 on the Upper Yellowstone Valley fault causes a contrast of normal stress change (+1.9 and -2.3 bars) on the reservoir plane, promoting magma circulation. At the same time, this event unclamps the pathway plane by up to 5.0 bars.

Considering that the fault has been active throughout the late Quaternary (<15 Ka) [*Pierce*, 1998], and that no historical large earthquake on this fault is recorded, the Upper Yellowstone Valley fault might be ready to slip.

7. Our strain analysis indicates that both dilatational and shear strains are accumulating around the Teton fault. However, neither normal nor strike-slip faulting on the fault causes very small stress changes (1.0 bar at largest) on the receiver planes.

References

Aki, K. and P. G. Richards (1980), *Elementary Seismology: Theory and Methods*, Vol. 1, W. H. Freeman and Co., San Francisco, Calif.

Allmendinger, R. W., R. Reilinger, and J. Loveless (2007), Strain and rotation rate from GPS in Tibet, Anatolia, and the Altiplano, *Tectonics*, *26*, TC3013, doi:10.1029/2006TC002030.

Anastasio, D. J., C. N. Majerowicz, F. J. Pazzaglia, and C. A. Regalla (2010), Late Pleistocene– Holocene ruptures of the Lima Reservoir fault, SW Montana: *J. Struct. Geol.*, *32*, 1996–2008, doi:10.1016/j.jsg.2010.08.012.

Anders, M. H. (1990), Late Cenozoic evolution of Grand and Swan Valleys, Idaho, in Roberts, S., ed., Geologic field tours of western Wyoming, Geological Survey of Wyoming Public Information Circular 29, p. 15-25.

Anders, M. H., J. W. Geissman, L. A. Piety, and J. T. Sullivan (1989), Parabolic distribution of circumeastern Snake River Plain seismicity and latest Quaternary faulting: Migratory pattern and association with the Yellowstone hotspot, *J. Geophys. Res.*, *94*(B2), 1589–1621, doi:10.1029/JB094iB02p01589.

Anderson, A. L. (1934), A preliminary report on recent block faulting in Idaho, *Northwest Science*, *8*, 17–28.

Baldwin, E. M. (1951), Faulting in the Lost River Range area of Idaho, *Am. J. Sci.*, *249*, 884–902.

Baltzer, E. M. (1990), Quaternary surface displacement and segmentation of the northern Lemhi fault, Idaho: Binghamton, State University of New York, M.S. thesis, 88 p., 2 pl., scale 1:62,500.

Barrientos, S. E., S. N. Ward, J. González-Ruiz, and R. S. Stein (1985), Inversion for moment as a function of depth from geodetic observations and long period body waves of the 1983 Borah Peak, Idaho, earthquake, *U.S. Geol. Surv. Open File Rep.*, *85-290*, 485–518.

Barrientos, S. E., R. S. Stein, and S. N. Ward (1987), Comparison of the 1959 Hebgen Lake, Montana and the 1983 Borah Peak, Idaho, earthquakes from geodetic observations, *Bull. Seism. Soc. Am.*, *77*(3), 784–808.

Bartholomew, M. J., M. C. Stickney, E. M. Wilde, and R. G. Dundas (2002), Late Quaternary paleoseismites: Syndepositional features and section restoration used to indicate paleoseismicity and stress-field orientations during faulting along the main Lima Reservoir fault, southwestern Montana, *Geol. Soc. Am. Spec. Pap.*, *359*, p. 29–47

Bautista, B. C., M. L. P. Bautista, R. S. Stein, E. S. Barcelona, R. S. Punongbayan, E. P. Laguerta, A. R. Rasdas, G. Ambubuyog, and E. Q. Amin (1996), Relationship of regional and local structures to Mount Pinatubo activity, in *The 1991-1992 Eruptions of Mount Pinatubo, Philippines*, edited by C. G. Newhall and R. S. Punongbayan, pp. 351–370, Univ. of Wash. Press, Seattle.

Blot, C. (1965), Relations entre les séismes profonds et les éruptions volcaniques au Japon, *Bull. Volcanol.*, *28*(1), 25–63, doi:10.1007/BF02596913.

Bonasia, V., E. Del Pezzo, F. Pinque, R. Scandone, and R. Scarpa (1985), Eruptive history, seismic activity and ground deformations at Mt. Vesuvius, Italy, *Ann. Geophys.*, *3*, 395–406.

Bond, J. G., compiler (1978), Geologic map of Idaho. Idaho Department of Lands, Idaho Bureau of Mines and Geology, scale 1:500,000.

Bonini, W. E., W. N. Kelley, Jr., and D. W. Hughes (1972), Gravity studies of the Crazy Mountains and the west flank of the Beartooth Mountains, Montana, in Lynn, J., Balster, C., and Warne, J., eds., Crazy Mountains Basin, Montana Geological Society, 21st Annual Geological Conference, September 22-24, 1972, Guidebook, p. 119-127.

Brodsky, E. E., B. Sturtevant, and H. Kanamori (1998), Earthquakes, volcanoes, and rectified diffusion, *J. Geophys. Res.*, *103*(B10), 23827–23838, doi:10.1029/98JB02130.

Byrd, J. O. D., R. B. Smith, and J. W. Geissman (1994), The Teton fault, Wyoming: Topographic signature, neotectonics, and mechanisms of deformation, *J. Geophys. Res.*, *99*(B10), 20095–20122, doi:10.1029/94JB00281.

Cardoso, S. S. S., and A. W. Woods (1999), On convection in a volatile-saturated magma, *Earth Planet. Sci. Lett.*, *168*(3-4), 301–310, doi:10.1016/S0012-821X(99)00057-6.

Case, J. C. (1997), Earthquakes and active faults in Wyoming, Geological Survey of Wyoming Preliminary Hazard Report 97-2, 58 p.

Chesley, C., P. C. LaFemina, C. Puskas, and D. Kobayashi (2012), The 1707 M_w8.7 Hoei earthquake triggered the largest historical eruption of Mt. Fuji, *Geophys. Res. Lett.*, *39*(24), L24309, doi:10.1029/2012GL053868.

Christiansen, R. L. (2001), *The Quaternary and Pliocene Yellowstone Plateau Volcanic Field of Wyoming, Idaho, and Montana*, *U.S. Geol. Surv. Prof. Pap.*, *729-G*, 145 pp.

Christiansen, R. L., and H. R. Blank Jr. (1972), Volcanic stratigraphy of the Quaternary rhyolite plateau in Yellowstone National Park, Wyoming, *U.S. Geol. Surv. Prof. Pap.*, *729-B*, 18 pp.

Cochran, B. D. (1985), Age of late Quaternary surface ruptures along the Thousand Springs-Mackay segment of the Lost River Range fault system, in *National Earthquake Hazards Reduction Program, Summaries of technical reports, Volume XXI* edited by M. L. Jacobson, T. R. Rodriguez, U.S. Geol. Surv. Open File Rep. 86-31, 113–121.

Cockerham, R. S., and E. J. Corbett (1987), The July 1986 Chalfant Valley, California, earthquake sequence: Preliminary results, *Bull. Seism. Soc. Am.*, *77*(1), 280–289.

Crone, A. J. (1985), Fault scarps, landslides, and other features associated with the Borah Peak earthquake of October 28, 1983, central Idaho: a field trip guide, *U.S. Geol. Surv. Open File Rep. 85-290*.

Crone, A. J., and K. M. Haller (1991), Segmentation and the coseismic behavior of Basin and Range normal faults—Examples from east-central Idaho and southwestern Montana, in Hancock, P.L., Yeats, R.S., and Sanderson, D.J., eds., Characteristics of active faults: Journal of Structural Geology, v. 13, p. 151-164.

Crone, A. J., M. N. Machette, M. G. Bonilla, J. J. Lienkaemper, R. C. Bucknam, K. L. Pierce, and W. E. Scott (1985), Characteristics of surface faulting accompanying the Borah Peak earthquake, central Idaho, in Workshop XXVIII on the Borah Peak earthquake, *U.S. Geol. Surv.*, *Open File Rept*. *85-290*, 43–58.

Crone, A. J., M. N. Machette, M. G. Bonilla, J. J. Lienkaemper, K. L. Pierce, W. E. Scott, and R. C. Bucknam (1987), Surface faulting accompanying the Borah Peak earthquake and segmentation of the Lost River fault, central Idaho, *Bull. Seism. Soc. Am.*, *77*, 739–770.

Darwin, C. (1839), *Journal of researches into the natural history and geology of the countries visited during the voyage of H.M.S. Beagle round the world, under the command of Capt. Fitz Roy, R.N*, John Murray, London.

De la Cruz-Reyna, S., M. Tarraga, R. Ortiz, and A. Martinez-Bringas (2010), Tectonic earthquakes triggering volcanic seismicity and eruptions: Case studies at Tungurahua and Popocatépetl volcanoes, *J. Volcanol. Geotherm. Res.*, *193*(1–2), 37–48, doi:10.1016/j.jvolgeores.2010.03.005.

DeNosaquo, K. R., R. B. Smith, and A. R. Lowry (2009), Density and lithospheric strength models of the Yellowstone–Snake River Plain volcanic system from gravity and heat flow data, *J. Volcanol. Geotherm. Res.*, *188*(1), 108–127, doi:10.1016/j.jvolgeores.2009.08.006.

Díez, M., P. C. La Femina, C. B. Connor, W. Strauch, and V. Tenorio (2005), Evidence for static stress changes triggering the 1999 eruption of Cerro Negro Volcano, Nicaragua and regional aftershock sequences, *Geophys. Res. Lett.*, *32*, L04309, doi:10.1029/2004GL021788.

Dixon, J. S. (1982), Regional structural synthesis, Wyoming salient of Western Overthrust belt, *AAPG Bull.*, 66, 1560–1580.

Doser, D. I. (1985), Source parameters and faulting processes of the 1959 Hebgen Lake, Montana, earthquake sequence, *J. Geophys. Res.*, *90*(B6), 4537–4555, doi:10.1029/JB090iB06p04537.

Doser, D. I. (1989), Source parameters of Montana earthquakes (1925-1964) and tectonic deformation in the northern Intermountain Seismic Belt, *Bull. Seism. Soc. Am.*, *79*(1), 31–50.

Doser, D. I., and R. B. Smith (1983), Seismicity of the Teton-Southern Yellowstone region, Wyoming, *Bull. Seism. Soc. Am.*, *73*, 1369–1394.

Doser, D. I., and R. B. Smith (1985), Source parameters of the 28 October 1983 Borah Peak, Idaho, Earthquake from body wave analysis, *Bull. Seism. Soc. Am.*, *75*(4), 1041–1051.

Dvorak, J. (1994), An earthquake cycle along the south flank of Kilauea Volcano, Hawaii, *J. Geophys. Res.*, *99*(B5), 9533–9541, doi:10.1029/94JB00040.

Ekström, G., and A. M. Dziewonski (1985), Centroid-moment tensor solutions for 35 earthquakes in Western North America (1977-1983), *Bull. Seism. Soc. Am.*, *75*(1), 23–39.

Farrell, J., R. B. Smith, S. Husen, and T. Diehl (2014), Tomography from 26 years of seismicity revealing that the spatial extent of the Yellowstone crustal magma reservoir extends well beyond the Yellowstone caldera, *Geophys. Res. Lett.*, *41*, 3068–3073, doi:10.1002/2014GL059588.

Gary, S. D. (1980), Quaternary geology and geophysics of the upper Madison Valley, Madison County, Montana, Missoula, University of Montana, M.S. thesis, 76 p., 2 pls.

Geirsson, H. (2014), Crustal deformation and volcanism at active plate boundaries, Ph.D. dissertation, Dep. of Geosci, Penn State, University Park, PA.

Gilbert, J. D., D. Ostenaa, and C. Wood (1983), Seismotectonic study of Jackson Lake Dam and Reservoir, Minidoka Project, Idaho-Wyoming, U.S. Bureau of Reclamation Seismotectonic Report 83-8, 123 p., 11 pl.

Hackl, M., R. Malservisi, and S. Wdowinski (2009), Strain rate patterns from dense GPS networks, *Nat. Hazards Earth Syst. Sci.*, *9*, 1177–1187, doi:10.5194/nhess-9-1177-2009.

Haller, K. M. (1988), Segmentation of the Lemhi and Beaverhead faults, east-central Idaho, and Red Rock fault, southwest Montana, during the late Quaternary, Boulder, University of Colorado, M.S. thesis, 141 p., 10 pls.

Haller, K. M., compiler (2010a), Fault number 656, Hebgen fault, in Quaternary fault and fold database of the United States, U.S. Geological Survey website, https://earthquakes.usgs.gov/hazards/qfaults, accessed 01/02/2017 01:23 PM.

Haller, K. M., compiler (2010b), Fault number 655b, Madison fault, Madison Canyon section, in Quaternary fault and fold database of the United States, U.S. Geological Survey website, https://earthquakes.usgs.gov/hazards/qfaults, accessed 01/02/2017 02:05 PM.

Haller, K. M., compiler (2010c), Fault number 643b, Centennial fault, Red Rock Lakes section, in Quaternary fault and fold database of the United States: U.S. Geological Survey website, https://earthquakes.usgs.gov/hazards/qfaults, accessed 01/02/2017 02:28 PM.

Haller, K. M., and R. L. Wheeler (1992), Quaternary fault and fold database of the United States, *U.S. Geol. Surv. Open File Rep. 03-417*.

Haller, K. M., and R. L. Wheeler (2010a), Fault number 601c, Lost River fault, Thousand Springs section, in Quaternary fault and fold database of the United States: U.S. Geological Survey website, https://earthquakes.usgs.gov/hazards/qfaults, accessed 01/02/2017 12:28 PM.

Haller, K. M., and R. L. Wheeler (2010b), Fault number 602d, Lemhi fault, Warm Creek section, in Quaternary fault and fold database of the United States: U.S. Geological Survey website, https://earthquakes.usgs.gov/hazards/qfaults, accessed 01/02/2017 12:48 PM.

Haller, K.M., Wheeler, R.L., and Adema, G.W., compilers (2010), Fault number 603e, Beaverhead fault, Nicholia section, in Quaternary fault and fold database of the United States: U.S. Geological Survey website, https://earthquakes.usgs.gov/hazards/qfaults, accessed 01/02/2017 01:09 PM.

Hanks, T. C., and D. P. Schwartz (1987), Morphologic dating of the pre-1983 fault scarp on the Lost River fault at Doublespring Pass Road, Custer County, Idaho, *Bull. Seism. Soc. Am.*, *77*(3), 837–846.

Hill, D. P., F. Pollitz, and C. Newhall (2002), Earthquake-Volcano Interactions, *Physics Today*, *55*(11), 41–47, doi:10.1063/1.1535006.

Holdahl, S. R., and D. Dzurisin (1991), Time-dependent models of vertical deformation for the Yellowstone–Hebgen Lake region, 1923–1987, *J. Geophys. Res.*, *96*(B2), 2465–2483, doi:10.1029/90JB02011.

Huang, H.-H., F.-C. Lin, B. Schmandt, J. Farrell, R. B. Smith, and V. C. Tsai (2015), The Yellowstone magmatic system from the mantle plume to the upper crust, *Science*, *348*, 773–776, doi:10.1126/science.aaa5648.

Huppert, H. E., and A. W. Woods (2002), The role of volatiles in magma chamber dynamics, *Nature*, *420*, 493495, doi:10.1038/nature01211.

Jacques, E., G. C. P. King, P. Tapponnier, J. C. Ruegg, and I. Manighetti (1996), Seismic activity triggered by stress changes after the 1978 events in the Asal Rift, Djibouti, *Geophys. Res. Lett.*, *23*(18), 2481–2484, doi:10.1029/96GL02261.

Johns, W. M., W. T. Straw, R. N. Bergantino, H. W. Dresser, T. E. Hendrix, H. G. McClernan, J. C. Palmquist, and C. J. Schmidt (1982), Neotectonic features of southern Montana east of 112°30' west longitude: Montana Bureau of Mines and Geology Open-File Report 91, 79 p., 2 sheets.

Kahle, H.-G., M. Cocard, Y. Peter, A. Geiger, R. Reilinger, A. Barka, and G. Veis (2000), GPS-derived strain rate field within the boundary zones of the Eurasian, African, and Arabian Plates, *J. Geophys. Res.*, *105*(B10), 23353–23370, doi:10.1029/2000JB900238.

Kanamori, H. (1977), The energy release in great earthquakes, *J. Geophys. Res.*, *82*(20), 2981–2987, doi:10.1029/JB082i020p02981.

Lay, T., and T. C. Wallace (1995), *Modern Global Seismology*, Academic Press, San Diego, CA, 521 pp.

Li, Q., M. Liu, Q. Zhang, and E. Sandvol (2007), Stress evolution and seismicity in the central-eastern United States: Insight from geodynamic modeling, in *Continental Intraplate Earthquakes: Science, Hazard, and Policy Issues*, edited by S. Stein and S. Mazzotti, Spec. Pap. Geol. Soc. Am., 425, 149–166.

Lin, J. and R. S. Stein (2004), Stress triggering in thrust and subduction earthquakes, and stress interaction between the southern San Andreas and nearby thrust and strike-slip faults, *J. Geophys. Res.*, *109*, B02303, doi:10.1029/2003JB002607.

Linde, A. T., and I. S. Sacks (1998), Triggering of volcanic eruptions, *Nature*, *395*, 888–490, doi:10.1038/27650.

Lopez, D. A., and J. C. Reiten (2003), Preliminary geologic map of Paradise Valley, south-central Montana, Montana Bureau of Mines and Geology Open-File Report 480, 22 p., 1 sheet, 1:50,000 scale.

Love, J. D., and J. R. Reed, Jr. (1968), Creation of the Teton landscape—The geologic story of Grand Teton National Park, Grand Teton Natural History Association, 120 p.

Lundstrom, S.C. (1986), Soil stratigraphy and scarp morphology studies applied to the Quaternary geology of the southern Madison Valley, Montana: Arcata, California, Humboldt State University, M.S. thesis, 53 p., 1 pl., scale 1:24,000.

Ma, K.-F., C.-H. Chan, and R. S. Stein (2005), Response of seismicity to Coulomb stress triggers and shadows of the 1999 M_w = 7.6 Chi-Chi, Taiwan, earthquake, *J. Geophys. Res.*, *110*, B05S19, doi:10.1029/2004JB003389.

Majerowicz, C. N. (2008), Quaternary Rupture History of the Lima Reservoir Fault System, SW Montana, M.S. thesis, Bethlehem, Pennsylvania, Lehigh University, 49 p., 1 plate.

Majerowicz, C. N., N. W. Harkins, C. A. Regalla, J. K. Troy, F. J. Pazzaglia, and D. J. Anastasio (2007), Transtension along the northeastern boundary of the Snake River Plain, *Geol. Soc. Am. Abstr. Programs*, *39*(6), 292.

Manga, M., and E. Brodsky (2006), Seismic Triggering of Eruptions in the Far Field: Volcanoes and Geysers, *Annu. Rev. Earth Planet. Sci.*, *34*, 263–291, doi:10.1146/annurev.earth.34.031405.125125.

Marzocchi, W., R. Scandone, and F. Mulargia (1993), The tectonic setting of Mount Vesuvius and the correlation between its eruptions and earthquakes of the Southern

Apennines, *J. Volcanol. Geotherm. Res.*, *58*, 27–41, doi:10.1016/0377-0273(93)90100-6.

Mason, D. B. (1992), Earthquake magnitude potential of active faults in the Intermountain seismic belt from surface parameter scaling: Salt Lake City, University of Utah, M.S. thesis, 110 p.

Mathieson, E. L. (1983), Late Quaternary activity of the Madison Range fault along its 1959 rupture trace, Madison County, Montana, Stanford, California, Stanford University, M.S. thesis, 169 p., 4 pls.

McCaffrey, R., A. I. Qamar, R. W. King, R.Wells, G. Khazaradze, C. A. Williams, C. W. Stevens, J. J. Vollick, and P. C. Zwick (2007), Fault locking, block rotation and crustal deformation in the Pacific Northwest, *Geophys. J. Int.*, *169*(3), 1315–1340, doi:10.1111/j.1365-246X.2007.03371.x.

McCaffrey, R., R. W. King, S. J. Payne, and M. Lancaster (2013), Active tectonics of northwestern U.S. inferred from GPS-derived surface velocities, *J. Geophys. Res. Solid Earth*, *118*, 709–723, doi:10.1029/2012JB009473.

McCalpin, J. P., M. N. Machette, and K. M. Haller, compilers (1994), Fault number 726a, Grand Valley fault, Swan Valley section, in Quaternary fault and fold database of the United States: U.S. Geological Survey website, https://earthquakes.usgs.gov/hazards/qfaults, accessed 01/02/2017 06:30 PM.

Michell, J. (1760), Conjectures concerning the cause, and observations upon the phaenomena of earthquakes; particularly of that great earthquake of the first of November, 1755, which proved so fatal to the city of Lisbon, and whose effects were felt as far as Africa, and more or less throughout almost all Europe, *Phil. Trans. R. Soc. Lond.*, *51*, 566–634.

Minakami, T. (1968), Is there any mutual relationship among occurrence of Hyuganada earthquake, earthquake-swarm in the Kakuto-caldera area and volcanic activity of Kirishima?, *Bull. Volcanol. Soc. Japan*, *13*(1), 48.

Minakami, T., M. Hagiwara, M. Yamaguchi, E. Koyama, and K. Hirai (1970), The Ebino Earthquake Swarm and the Seismic Activity in the Kirishima Volcanoes, in 1968-1969, Part 4. Shifts of Seismic Activity from the Kakuto Caldera to Simmoe-dake, Nakadake and Takatiho-mine, *Bull. Earthquake Res. Inst.*, *48*(2), 205–233.

Mogi, K. (1958), Relations between the eruptions of various volcanoes and the deformations of the ground surface around them, *Bull. Earthquake Res. Inst. Univ. Tokyo*, *36*, 99–134.

Myers, W.B., and W. Hamilton (1961), Deformation accompanying the Hebgen Lake, Montana, earthquake of August 17, 1959—Single-basin concept, *U.S. Geol, Surv. Prof. Pap.*, *424*, p. D-168-D-170.

Myers, W.B., and W. Hamilton (1964), Deformation accompanying the Hebgen Lake earthquake of August 17, 1959, in The Hebgen Lake, Montana, earthquake of August 17, 1959, *U.S. Geol, Surv. Prof. Pap.*, *435-I*, 55–98.

Nábělek, J. L., H. Eyidogan, and M. N. Tiksoz (1985), Source parameters of the Borah Peak, Idaho, earthquake of October 28, 1983 from body-wave inversion, *EOS Trans. AGU 66*, 308.

Nahm, A. L., T. Öhman, and D. A. Kring (2013), Normal faulting origin for the Cordillera and Outer Rook Rings of Orientale Basin, the Moon, *J. Geophys. Res. Planets*, *118*, 190–205, doi:10.1002/jgre.20045.

Nostro, C., R. S. Stein, M. Cocco, M. E. Belardinelli, and W. Marzocchi (1998), Two-way coupling between Vesuvius eruptions and southern Apennine earthquakes, Italy, by elastic stress transfer, *J. Geophys. Res.*, *103*(B10), 24487–24504, doi:10.1029/98JB00902.

Okada, Y. (1985), Surface deformation due to shear and tensile faults in a half-space, *Bull. Seism. Soc. Am.*, *75*, 1135–1154.

Okada, Y. (1992), Internal deformation due to shear and tensile faults in a half-space, *Bull. Seism. Soc. Am.*, *82*(2), 1018–1040.

Ostenaa, D., and C. Wood (1990), Seismotectonic study for Clark Canyon Dam, Pick-Sloan Missouri Basin Program, Montana, *U.S. Bureau of Reclamation Seismotectonic Report*, *90-4*.

Pankow, K. L., M. Stickney, K. D. Koper, and K. M. Whidden (2014), The 2014 Challis, Idaho Earthquake Swarm, in 2014 AGU Fall Meeting, 2014 Dec 15–19, San Francisco, California.

Pardee, J. T. (1926), The Montana earthquake of June 27, 1925, *U.S. Geol. Surv. Prof. Pap.*, *147*, 7–23.

Pardee, J. T. (1950), Late Cenozoic block faulting in western Montana, *Geol. Soc. Am. Bull*, *61*, 359–406.

Payne, S. J., R. McCaffrey, and R. W. King (2008), Strain rates and contemporary deformation in the Snake River Plain and surrounding Basin and Range from GPS and seismicity, *Geology*, *36*(8), 647–650, doi:10.1130/G25039A.1.

Payne, S. J., R. McCaffrey, R. W. King, and S. A. Kattenhorn (2012), A new interpretation of deformation rates in the Snake River Plain and adjacent basin and range regions based on GPS measurements, *Geophys. J. Int.*, *189*, 101–122. doi:10.1111/j.1365-246X.2012.05370.x.

Payne, S. J., R. McCaffrey, and S. A. Kattenhorn (2013), Extension-driven right-lateral shear in the Centennial shear zone adjacent to the eastern Snake River Plain, Idaho, *Lithosphere*, *5*(4), 407–419, doi:10.1130/L200.1.

Personius, S. F. (1982a), Geologic setting and geomorphic analysis of Quaternary fault scarps along the Deep Creek fault, upper Yellowstone valley, south-central Montana: Bozeman, Montana State University, M.S. thesis, 77 p., 1 sheet, scale 1:125,000.

Personius, S. F. (1982b), Geomorphic analysis of the Deep Creek fault, upper Yellowstone valley, south-central Montana, in Reid, S.G., and Foote, D.J., eds., Geology of Yellowstone Park area: Wyoming Geological Association, 33rd Annual Field Conference, Mammoth Hot Springs, Wyoming, September 15-18, 1982, Guidebook, p. 203-212.

Personius, S. F. (1986), Quaternary faulting along the Deep Creek fault upper Yellowstone valley, southwestern Montana, in Locke, W.W., ed., Quaternary geomorphic evolution of the Yellowstone region: Rocky Mountain Cell, Friends of the Pleistocene, September 6-8, 1986, Guidebook, p. 3-30.

Petersen, M. D., A. D. Frankel, S. C. Harmsen, C. S. Mueller, K. M. Haller, R. L. Wheeler, R. L. Wesson, Y. Zeng, O. S. Boyd, D. M. Perkins, N. Luco, E. H. Field, C. J. Wills, and K. S. Rukstales (2008), Documentation for the 2008 update of the United States National Seismic Hazard Maps: *U.S. Geol. Surv. Open File Rep. 2008-1128*, 61 p.

Petrik, F. E. (2008), Scarp analysis of the Centennial normal fault, Beaverhead County, Montana and Fremont County, Idaho, Bozeman, Montana State University, M.S. thesis, 287 p.

Pierce, K. L., compiler (1998), Fault number 761, Upper Yellowstone Valley faults, in Quaternary fault and fold database of the United States, U.S. Geological Survey website, https://earthquakes.usgs.gov/hazards/qfaults, accessed 04/26/2017 10:59 AM.

Pierce, K. L., and L. A. Morgan (1992), The track of the Yellowstone hot spot—Volcanism, faulting, and uplift, *Geol. Soc. Am. Mem.*, *179*, 1–53.

Pierce, K. L., D. R. Lageson, C. A. Ruleman, and R. G. Hintz (2000a), Holocene paleoseismology of Hebgen Lake normal fault, MT—The Cabin Creek site of the Hebgen Lake paleoseismology working group, *Eos Trans. AGU*, *81*(48), 1170.

Pierce, K. L., D. R. Lageson, C. A. Ruleman, and R. G. Hintz (2000b), Paleoseismology of Hebgen Lake normal fault at Cabin Creek, MT Preliminary report of the Hebgen Lake Paleoseismology Working Group, *Geol. Soc. Am. Abstr. Programs*, *32*(7), 442.

Piety, L. A., J. T. Sullivan, and M. H. Anders (1992), Segmentation and paleoseismicity of the Grand Valley fault, southeastern Idaho and western Wyoming, *Geol. Soc. Am. Mem.*, *179*, 155–182.

Piety, L. A., C. K. Wood, J. D. Gilbert, J. T. Sullivan, and M. H. Anders (1986), Seismotectonic study for Palisades Dam and Reservoir, Palisades Project, Bureau of Reclamation Seismotectonic Report 86-3, 198 p., 2 pls.

Porritt, R. W., R. M. Allen, and F. F. Pollitz (2014), Seismic imaging east of the Rocky Mountains with USArray, *Earth Planet. Sci. Lett.*, *402*, 16–25, doi:10.1016/j.epsl.2013.10.034.

Reilinger, R. (1986), Evidence for postseismic viscoelastic relaxation following the 1959 $M = 7.5$ Hebgen Lake, Montana, Earthquake, *J. Geophys. Res.*, *91*(B9), 9488–9494, doi:10.1029/JB091iB09p09488.

Reilinger, R. E., G. P. Citron, and L. D. Brown (1977), Recent vertical crustal movements from precise leveling data in southwestern Montana, western Yellowstone National Park, and the Snake River Plain, *J. Geophys. Res.*, *82*(33), 5349–5359, doi:10.1029/JB082i033p05349.

Richins, W. D., J. C. Pechmann, R. B. Smith, C. J. Langer, S. K. Goter, J. E. Zollweg, and J. J. King (1987), The 1983 Borah Peak, Idaho, earthquake and its aftershocks, *Bull. Seism. Soc. Am.*, *77*(3), 694–723.

Richmond, G. M., and K. L. Pierce (1971), Surficial geologic map of the Two Ocean Pass quadrangle, Yellowstone National Park and adjoining area, Wyoming: U.S. Geological Survey Miscellaneous Geologic Investigations I-635, scale 1:62,500.

Richmond, G. M., and K. L. Pierce (1972), Surficial geologic map of the Eagle Peak quadrangle, U.S. Geological Survey Miscellaneous Geologic Investigations I-637, scale 1:62,500.

Royse, F. J., M. A. Warner, and D. L. Reese (1975), Thrust belt structural geometry and related stratigraphic problems Wyoming-Idaho-northern Utah, in Bolyard, D.W., ed., Deep drilling frontiers of the central Rocky Mountains: Denver, Colorado, Rocky Mountain Association of Geologists—1975 Symposium, p. 41-54.

Ruleman, C. A. (2002), Quaternary tectonic activity within the northern arm of the Yellowstone tectonic parabola and associated seismic hazards, southwest Montana: Bozeman, Montana State University, M.S. thesis, 158 p.

Ruleman, C. A., and D. R. Lageson (2002), Late Quaternary tectonic activity along the Madison fault zone, Southwest Montana, *Geol. Soc. Am. Abstr. Programs*, *34*(4), 12.

Ruleman, C., D. R. Lageson, and M. C. Stickney (2000), Paradise Valley seismic gap, Southwest Montana, *Geol. Soc. Am. Abstr. Programs*, *32*(5), p. 37.

Ryall, A. (1962), The Hebgen Lake, Montana, earthquake of August 18, 1959: *P* waves, *Bull. Seism. Soc. Am.*, *52*(2), 235–271.

Savage, J. C., and M. M. Clark (1982), Magmatic resurgence in Long Valley caldera, California: Possible cause of the 1980 Mammoth Lakes earthquakes, *Science*, *217*, 531–533, doi:10.1126/science.217.4559.531.

Sbar, M. L., M. Barazangi, J. Dorman, C. H. Scholz, and R. B. Smith (1972), Tectonics of the Intermountain Seismic Belt, Western United States: Microearthquake Seismicity and Composite Fault Plane Solutions, *Geol. Soc. Am. Bull.*, *83*, 13–28, doi:10.1130/0016-7606(1972)83[13:TOTISB]2.0.CO;2.

Schmandt, B., and E. Humphreys (2010), Complex subduction and small-scale convection revealed by body-wave tomography of the western United States upper mantle, *Earth Planet. Sci. Lett.*, *297*(3–4), 435–445, doi:10.1016/j.epsl.2010.06.047.

Schmincke, H-U (2004), *Volcanism*, Springer, Heidelberg, Germany.

Schneider, N. P. (1985), Morphology of the Madison Range fault scarp, southwest Montana—Implications for fault history and segmentation, Oxford, Ohio, Miami University, M.S. thesis, 131 p.

Scott, W. E., K. L. Pierce, and M. H. Hait Jr. (1985a), Quaternary tectonic setting of the 1983 Borah Peak earthquake, central Idaho. in Stein, R.S., and Bucknam, R.C., eds., Proceedings of Conference XXVIII - The Borah Peak earthquake p. 1–26.

Scott, W. E., K. L. Pierce, and M. H. Hait Jr. (1985b), Quaternary tectonic setting of the 1983 Borah Peak earthquake, central Idaho, *Bull. Seism. Soc. Am.*, *75*, 1053–1066.

Shelden, A. W. (1960), Cenozoic faults and related geomorphic features in the Madison Valley, Montana, in *West Yellowstone—Earthquake area*, edited by D.E. Campau, and H. W. Anisgard, Billings Geological Society, 11th Annual Field Conference, September 7-10, p. 178–184.

Smedes, H. W., J. W. M'Gonigle, and J. J. Prostka (1989), Geologic map of the Two Ocean Pass quadrangle, Yellowstone National Park and vicinity, Wyoming, U.S. Geological Survey Geologic quadrangle Map GQ-1667, scale 1:62,500.

Smith, R. B., and W. J. Arabasz (1991) Seismicity of the Intermountain seismic belt, in D. B. Slemmons, E. R. Engdahl, M. D. Zoback, and D. D. Blackwell, eds., GSA Decade Map Vol. 1, 185–228.

Smith, R. B., and M. L. Sbar (1974), Contemporary tectonics and seismicity of the western United States with emphasis on the Intermountain Seismic Belt, *Geol. Soc. Am. Bull.*, *85*(8), 1205–1218, doi:10.1130/ 0016–7606(1974)85<1205:CTASOT>2.0.CO;2.

Smith, R. B. W. D., Richins, and D. I. Doser (1985), The 1983 Borah Peak, Idaho earthquake: regional seismicity, kinematics of faulting, and tectonic mechanism, in Proceedings of Conference XXVIII on the Borah Peak, Idaho Earthquake, *U.S. Geol. Surv. Open File Rept*. *85-290*, 236–263.

Smith, R. B., J. O. D. Byrd, and D. D. Susong (1990), Neotectonics and structural evolution of the Teton fault, in Geologic field tours of western Wyoming and parts of adjacent Idaho, Montana, and Utah edited by S. Roberts, *Goological Survey of Wyoming Public Information Circular*, *29*, 126–138.

Smith, R. B., J. O. D. Byrd, and D. D. Susong (1993), The Teton fault, Wyoming: Seismotectonics, Quaternary history, and earthquake hazards, in Geology of Wyoming edited by A. W. Snoke, J. R. Steidtmann, S. M. Roberts, *Geological Survey of Wyoming Memoir*, *5*, 628–667.

Smith, R. B., M. Jordan, B. Steinberger, C. M. Puskas, J. Farrell, G. P. Waite, S. Husen, W. L. Chang, and R. O'Connell (2009), Geodynamics of the Yellowstone hotspot and mantle plume: Seismic and GPS imaging, kinematics, and mantle flow, *J. Volcanol. Geotherm. Res.*, *188*(1), 26–56, doi:10.1016/j.jvolgeores.2009.08.020.

Sonderegger, J. L., J. D. Schofield, R. B. Berg, and M. L. Mannick (1982), The upper Centennial Valley, Beaverhead and Madison Counties, Montana, *Montana Bureau of Mines and Geology Memoir*, *50*, 53.

Sparks, S. R. J., H. Sigurdsson, and L. Wilson (1977), Magma mixing: A mechanism for triggering acid explosive eruptions, *Nature*, *267*, 315–318, doi:10.1038/267315a0.

Stefánsson, R., R. Böđvarsson, R. Slunga, P. Einarsson, S. Jakobsdóttir, H. Bungum, S. Gregersen, J. Havskov, J. Hjelme, and H. Korhonen (1993), Earthquake prediction research in the South Iceland seismic zone and the SIL project, *Bull. Seism. Soc. Am.*, *83*(3), 696–716.

Stein, R. S., and S. E. Barrientos (1985), Planar high-angle faulting in the basin and range: Geodetic analysis of the 1983 Borah Peak, Idaho, earthquake, *J. Geophys. Res.*, *90*(B13), 11355–11366, doi:10.1029/JB090iB13p11355.

Stickney, M. C. (1978), Seismicity and faulting of central western Montana, *Northwest Geology*, *7*, 1–9.

Stickney, M. C. (1997), Seismic Source Zones in Southwest Montana, *Montana Bureau of Mines and Geology Open-File Report*, *366*, 52 p.

Stickney, M. C. (2007), Historic earthquakes and seismicity in southwestern Montana, *Northwest Geology*, *36*, 167–186.

Stickney, M. C., and M. J. Bartholomew (1987), Seismicity and late Quaternary faulting of the northern Basin and Range Province, Montana and Idaho, *Bull. Seism. Soc. Am.*, *77*(5), 1602–1625.

Stickney, M. C., K. M. Haller, and M. N. Machette (2000), Quaternary Faults and Seismicity in Western Montana, *Montana Bureau of Mines and Geology Spec. Pub.*, *114*.

Stover, C. W. (1985), The Borah Peak, Idaho earthquake of October 28, 1983–Isoseismal map and intensity distribution, *Earthquake Spectra*, *2*(1), 11–16, doi:10.1193/1.1585299.

Susong, D. D., R. B. Smith, and R. L. Bruhn (1987), Quaternary faulting and segmentation of the Teton fault zone, Grand Teton National Park, Wyoming, *Eos Trans. AGU*, *68*, 1952.

Susong, D. D., S. U. Janecke, and R. L. Bruhn (1990), Structure of a fault segment boundary in the Lost River fault zone, Idaho, and possible effect on the 1983 Borah Peak earthquake rupture, *Bull. Seism. Soc. Am.*, *80*(1), 57–68.

Thatcher, W., and J. C. Savage (1982), Triggering of large earthquakes by magma-chamber inflation, Izu Peninsula, Japan, *Geology*, *10*(12), 637–640, doi:10.1130/0091-7613(1982)10<637:TOLEBM>2.0.CO;2.

Tocher, D. (1962), The Hebgen Lake, Montana, earthquake of August 17, 1959, MST, *Bull. Seism. Soc. Am.*, *52*(2), 153–162.

Toda, S., R. S. Stein, K. Richards-Dinger, and S. B. Bozkurt (2005), Forecasting the evolution of seismicity in southern California: Animations built on earthquake stress transfer, *J. Geophys. Res.*, *110*, B05S16, doi:10.1029/2004JB003415.

Toda, S., J. Lin, and R. S. Stein (2011), Using the 2011 M_w 9.0 off the Pacific coast of Tohoku Earthquake to test the Coulomb stress triggering hypothesis and to calculate faults brought closer to failure, *Earth Planets Space*, *63*, 725–730, doi:10.5047/eps.2011.05.010.

Toda, S., R. S. Stein, V. Sevilgen, and J. Lin (2011), Coulomb 3.3 Graphic-Rich Deformation and Stress-Change Software for Earthquake, Tectonic, and Volcano Research and Teaching— User Guide, *U.S. Geol. Surv. Open File Rep. 2011-1060*.

Turko, J. M. (1988), Quaternary segmentation history of the Lemhi Fault, Idaho: Binghamton, State University of New York, M.A. thesis, 91 p.

Turko, J. M., and P. L. K. Knuepfer (1991), Late Quaternary fault segmentation from analysis of scarp morphology, *Geology*, *19*(7), 718–721, doi:10.1130/0091-7613(1991)019<0718:LQFSFA>2.3.CO;2.

U.S. Coast and Geodetic Survey (1959), Preliminary report—Hebgen Lake, Montana earthquakes, August 1959, U.S. Department of Commerce, 15 p.

van der Woerd, J., L. Benedetti, M. W. Caffee, and R. Finkel (2000), Slip-rate and earthquake recurrence time on the Hebgen Lake fault (Montana)—Constraints from surface exposure dating of alluvial terraces and bedrock fault scarp, *Eos Trans. AGU*, *81*(48), 1160.

Vincent, K. R. (1995), Implications for models of fault behavior from earthquake surface-displacement along adjacent segments of the Lost River fault, Idaho: Tucson, University of Arizona, Ph.D. dissertation, 152 p.

Voight, B., R. J. Janda, H. Glicken, and P. M. Douglass (1983), Nature and mechanics of the Mount St Helens rockslide-avalanche of 18 May 1980, *Géotechnique*, *33*(3), 243–273, doi:10.1680/geot.1983.33.3.243.

Walter, T. R., and F. Amelung (2007), Volcanic eruptions following $M \geq 9$ megathrust earthquakes: Implications for the Sumatra-Andaman volcanoes, *Geology*, *35*(6), 539–542, doi:10.1130/G23429A.1.

Ward, S. N., and S. E. Barrientos (1986), An inversion for slip distribution and fault shape from geodetic observations of the 1983, Borah Peak, Idaho, Earthquake, *J. Geophys. Res.*, *91*(B5), 4909–4919, doi:10.1029/JB091iB05p04909.

Wdowinski, S., Y. Bock, Y. Forrai, Y. Melzer, and G. Baer (2001), The GIL network of continuous GPS monitoring in Israel for geodetic and geophysical applications, *Israel J. Earth Sci.*, *50*, 39–47.

Wells, D. L., and K. J. Coppersmith (1994), New Empirical Relationships among Magnitude, Rupture Length, Rupture Width, Rupture Area, and Surface Displacement, *Bull. Seism. Soc. Am.*, *84*(4), 974–1002.

Werner, C., S. Hurwitz, W. C. Evans, J. B. Lowenstern, D. Bergfeld, H. Heasler, C. Jaworowski, and A. Hunt (2008), Volatile emissions and gas geochemistry of Hot

Springs Basin, Yellowstone National Park, USA, *J. Volcanol. Geotherm. Res., 178*, 751–762.

Wessel, P., and D. Bercovici (1998), Interpolation with Splines in Tension: A Green's Function Approach, *Math. Geol.*, *30*(1), 77–93, doi:10.1023/A:1021713421882.

Wheeler, R. L., and K. B. Krystinik (1992), Persistent and nonpersistent segmentation of the Wasatch fault zone, Utah—Statistical analysis for evaluation of seismic hazard, *U.S. Geol. Surv. Prof. Pap.*, *B1-B47*.

Wicks, C., C. Weaver, P. Bodin, and B. Sherrod (2013), InSAR Evidence for an active shallow thrust fault beneath the city of Spokane Washington, USA, *J. Geophys. Res. Solid Earth*, *118*, 1268–1276, doi:10.1002/jgrb.50118.

Witkind, I. J. (1964), Reactivated faults north of Hebgen Lake, in The Hebgen Lake, Montana, earthquake of August 17, 1959, *U.S. Geol. Surv. Prof. Pap.*, *435-G*, p. 37-50.

Witkind, I. J. (1969), Geology of the Tepee Creek quadrangle, Montana-Wyoming, *U.S. Geol. Surv. Prof. Pap.*, *609*.

Witkind, I. J. (1975), Preliminary map showing known and suspected active faults in Idaho: U.S. Geological Survey Open-File Report 75-278, 71 p. pamphlet, 1 sheet, scale 1:500,000.

Witkind, I. J., W. B. Myers, J. B. Hadley, W. Hamilton, and G. D. Fraser (1962), Geologic features of the earthquake at Hebgen Lake, Montana, August 17, 1959, *Bull. Seism. Soc. Am.*, *52*(2), 163–180.

Witkind, I. J., J. B. Hadley, and W. H. Nelson (1964), Pre-Tertiary stratigraphy and structure of the Hebgen Lake area, in The Hebgen Lake, Montana, earthquake of August 17, 1959, *U.S. Geol. Surv. Prof. Pap.*, *435-R*, p.199–207.

Wong, I., S. Olig, and M. Dober (2000), Preliminary probabilistic seismic hazard analyses—Island Park, Grassy Lake, Jackson Lake, Palisades, and Ririe Dams, U.S. Department of the Interior, Bureau of Reclamation Technical Memorandum D8330-2000-17.

Yokoyama, I. (1971) Volcanic eruptions triggered by tectonic earthquakes, *Geophys. Bull. Hokkaido Univ.*, *25*, 129–139.

Young, S.L.-W. (1985), Structural history of the Jordan Creek area northern Madison Range, Madison County, Montana, Austin, University of Texas at Austin, M.S. thesis, 113 p., 2 pls.

Zollweg, J. E., and W. D. Richins (1985), Later aftershocks of the 1983 Borah Peak, Idaho, earthquake and related activity in central Idaho, *U.S. Geol. Surv. Open File Rep.*, *85-290*, 345–367.

Zimanowski, B., R. Büttner, V. Lorenz, and H.-G. Häfele (1997), Fragmentation of basaltic melt in the course of explosive volcanism, *J. Geophys. Res.*, *102*(B1), 803–814, doi:10.1029/96JB02935.

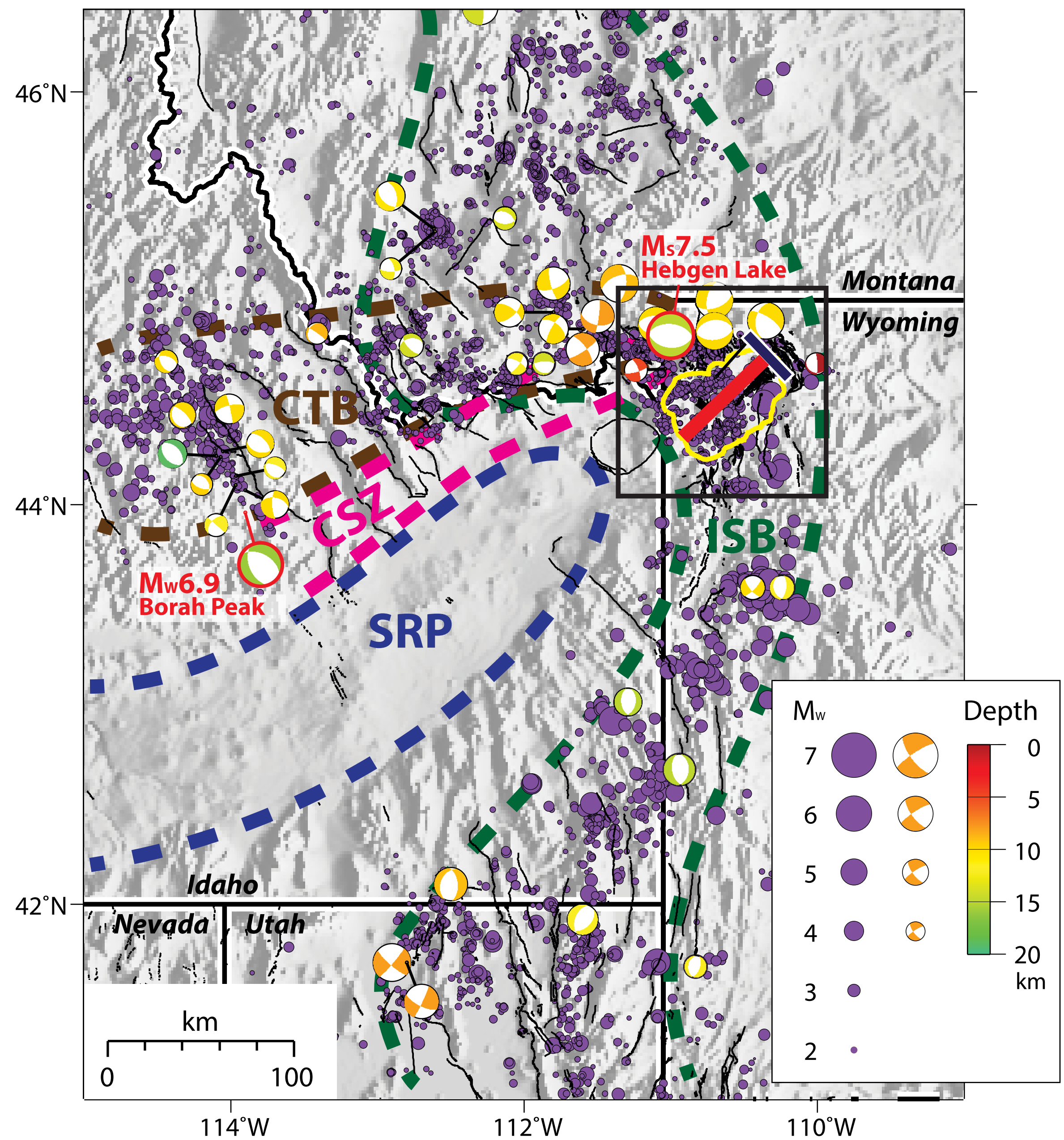

Figure 2.1. Regional tectonic setting and seismicity. Earthquake epicenters (purple dots; M>1.5; 2000-2012) [M.C. Stickney, personal communication, 2013] are scaled by magnitude. Fault plane solutions are color-coded by focal depth. Major seismic zones in the map area are the Intermountain Seismic Belt (ISB; green outline), Centennial Tectonic Belt (CTB; blue outline), and Centennial shear zone (CSZ: pink outline). The Snake River Plain (SRP) is delineated by blue line. The youngest caldera of Yellowstone is outlined by yellow line. Surface traces of the modeled reservoir plane and pathway plane (see text for details) are represented by thick red line and navy line, respectively. Thin black lines represent Quaternary faults. Box in map outlines area of Figure 2.9.

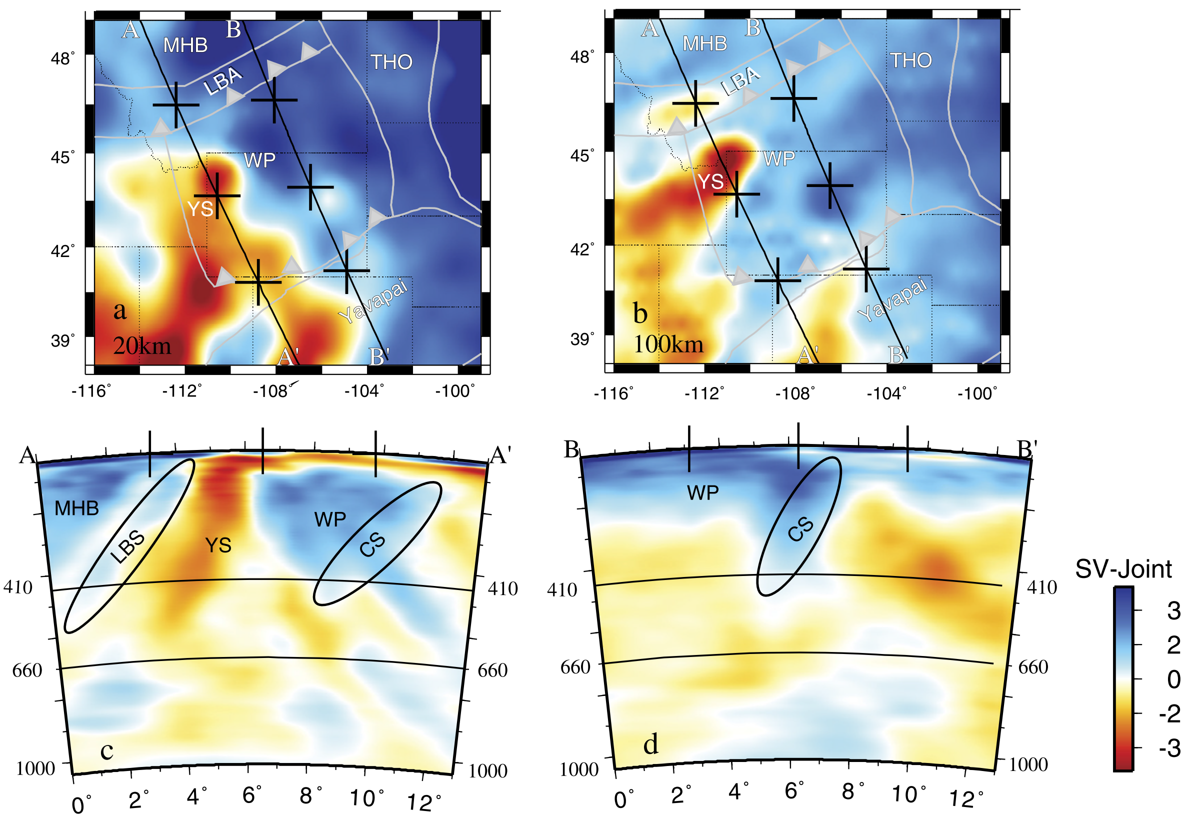

Figure 2.2. Horizontal and cross sections of the *SV*-joint tomographic model [*Porritt et al.*, 2014]. Maps are given at (a) 20 km and (b) 100 km. Locations of profiles (c) A–A′ and (d) B–B′ are shown on the maps. Yellowstone's mantle plume extends from the mid-mantle to ~50 km depths. MHB: Medicine Hat Block; LBA: Little Belt Arc; LBS: Little Belt Slab; YS: Yellowstone; WP: Wyoming Province; CS: Cheyenne Slab; THO: Trans-Hudson Orogen; LC: Laurentia Craton.

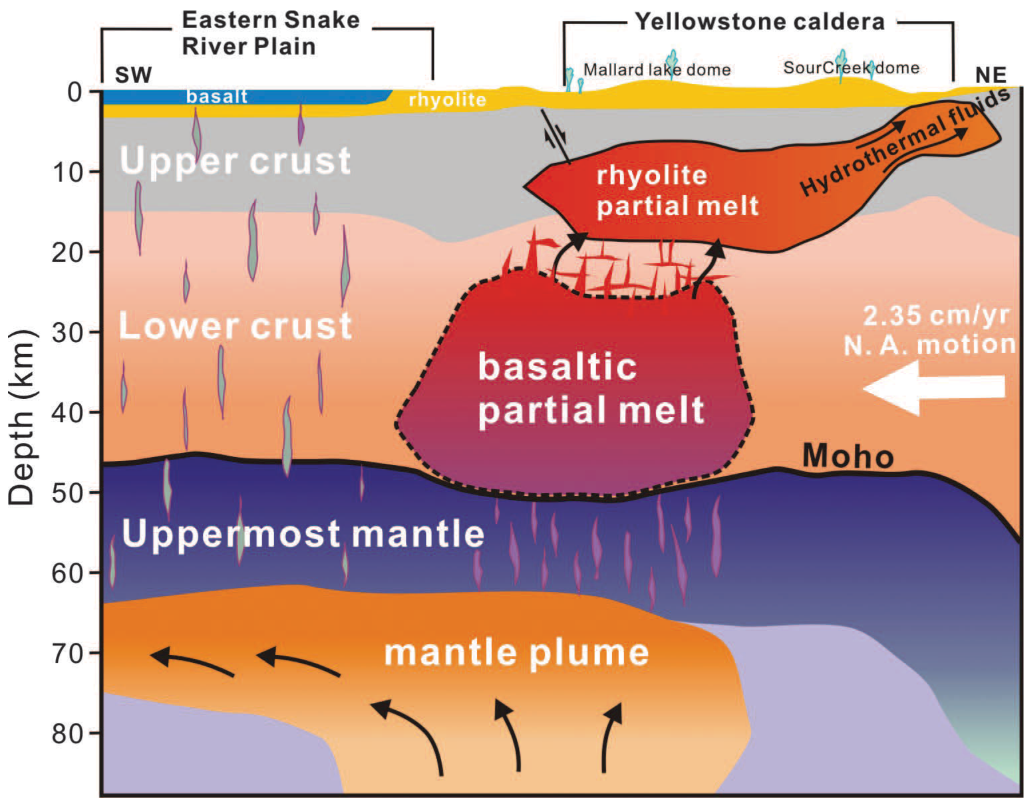

Figure 2.3. Schematic model for the Yellowstone magmatic system [*Huang et al.*, 2015]. The geometry of the upper- and lower-crustal magma reservoirs is based on the 5% V_P reduction in the tomographic model. The white arrow indicates the North American plate motion.

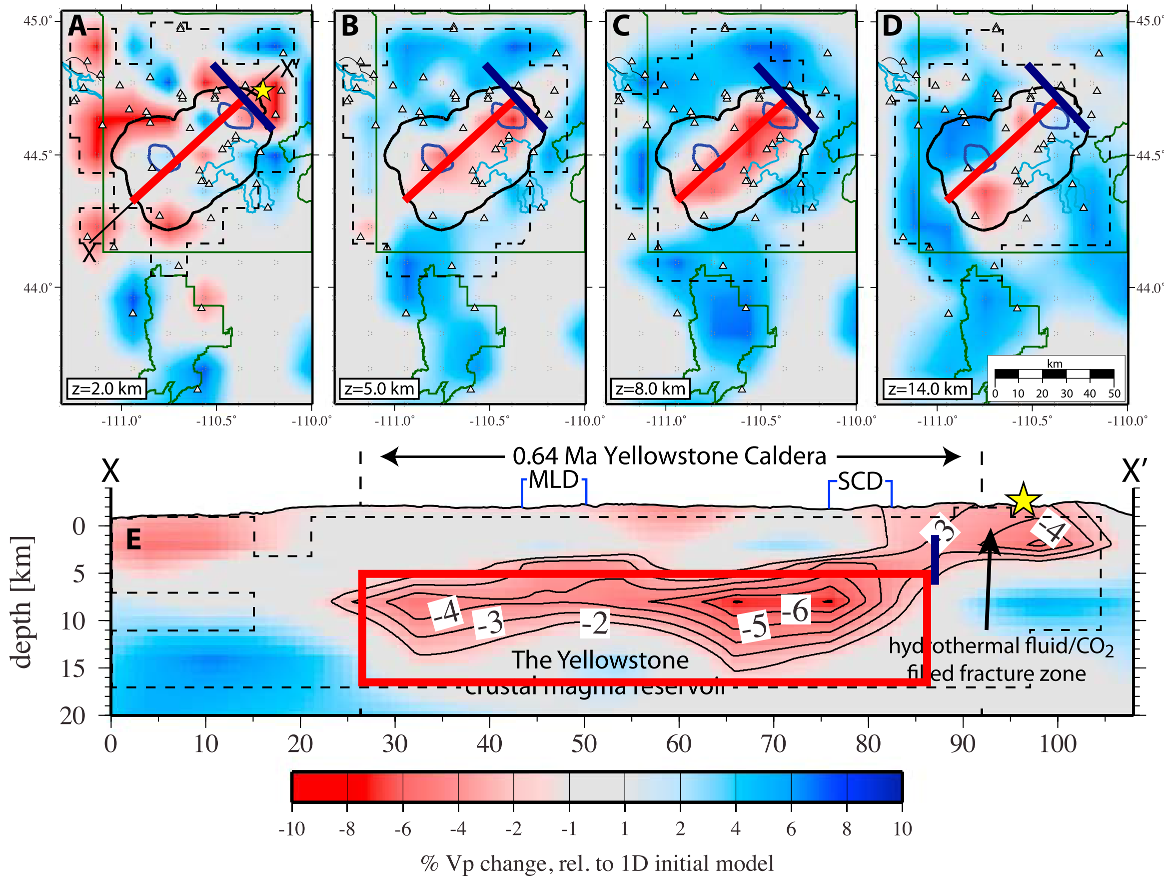

Figure 2.4. Horizontal and cross sections of the *P*-wave velocity model for the Yellowstone volcanic system [*Farrell et al.*, 2014]. Maps are given at (a) 2 km, (b) 5 km, (c) 8 km, and (d) 14 km. Profiles X–X′ (e) is along the long axis of the Yellowstone caldera. Location of the profile is shown on the map (a). Modeled reservoir plane and pathway plane (see text for details) are represented by thick red lines/box and navy lines, respectively. White triangles are seismic stations used in the tomographic inversion. Yellow star is the location of the Hot Springs Basin Group. MLD: Mallard Lake dome; SCD: Sour Creek dome.

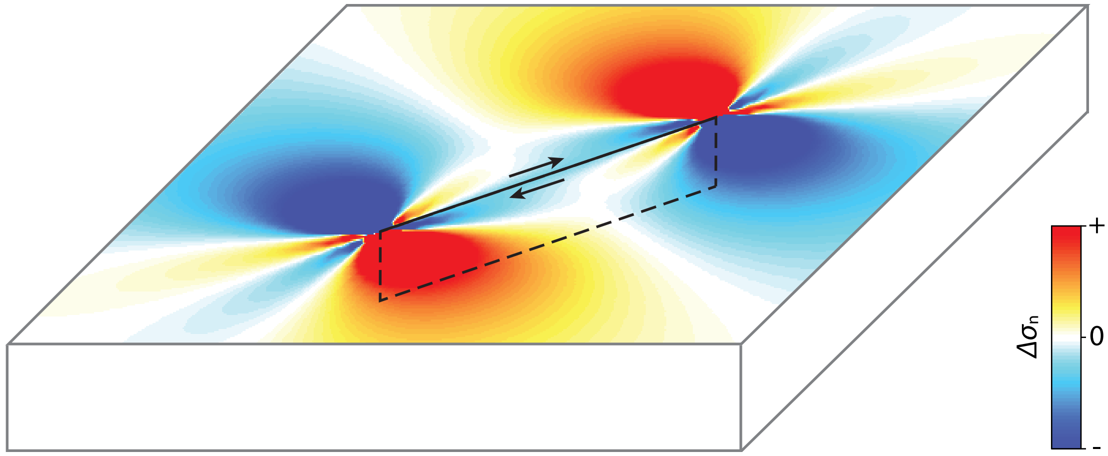

Figure 2.5. Simple example of static stress changes at the surface caused by a strike-slip motion along a vertical, rectangular fault plane. A stress change at an arbitrary point *p* in a homogeneous elastic medium is a function of the rupture parameters, the elastic properties of the medium, and the position of the point *p* relative to the fault.

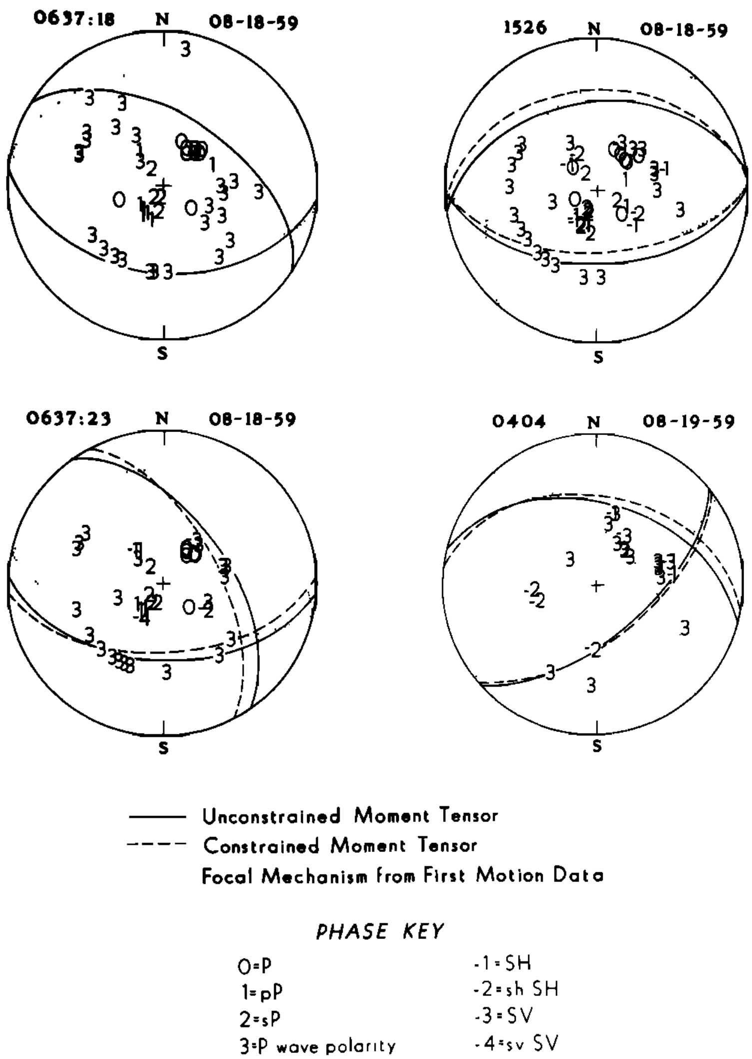

Figure 2.6. Focal mechanisms and seismic moment tensors of the 06:37:18, 06:37:23, 15:26, and 04:04 events of the Hebgen Lake sequence [*Doser*, 1985].

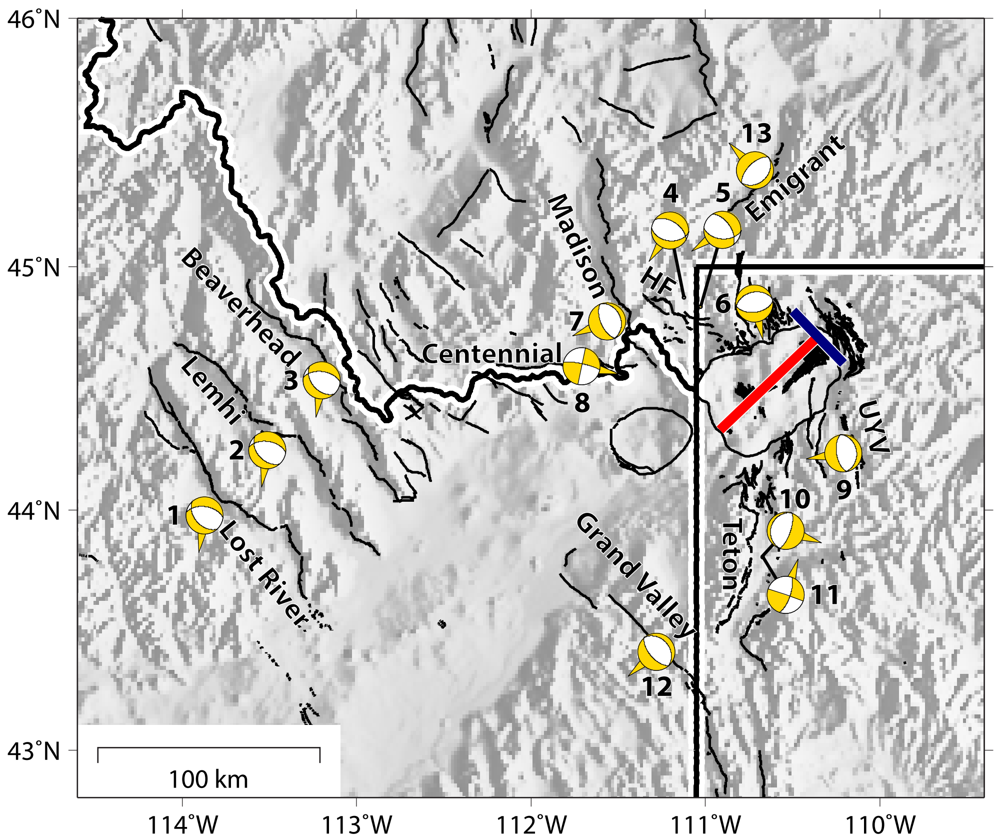

Figure 2.7. Locations and focal mechanisms of the 13 hypothetical M_W7.1-7.5 earthquakes around Yellowstone. Focal depth is 9.0 km for all events. HF: Hebgen Fault; UYV: Upper Yellowstone Valley Fault. Surface traces of the modeled reservoir plane and pathway plane are represented by thick red line and navy line, respectively. Thin black lines represent Quaternary faults.

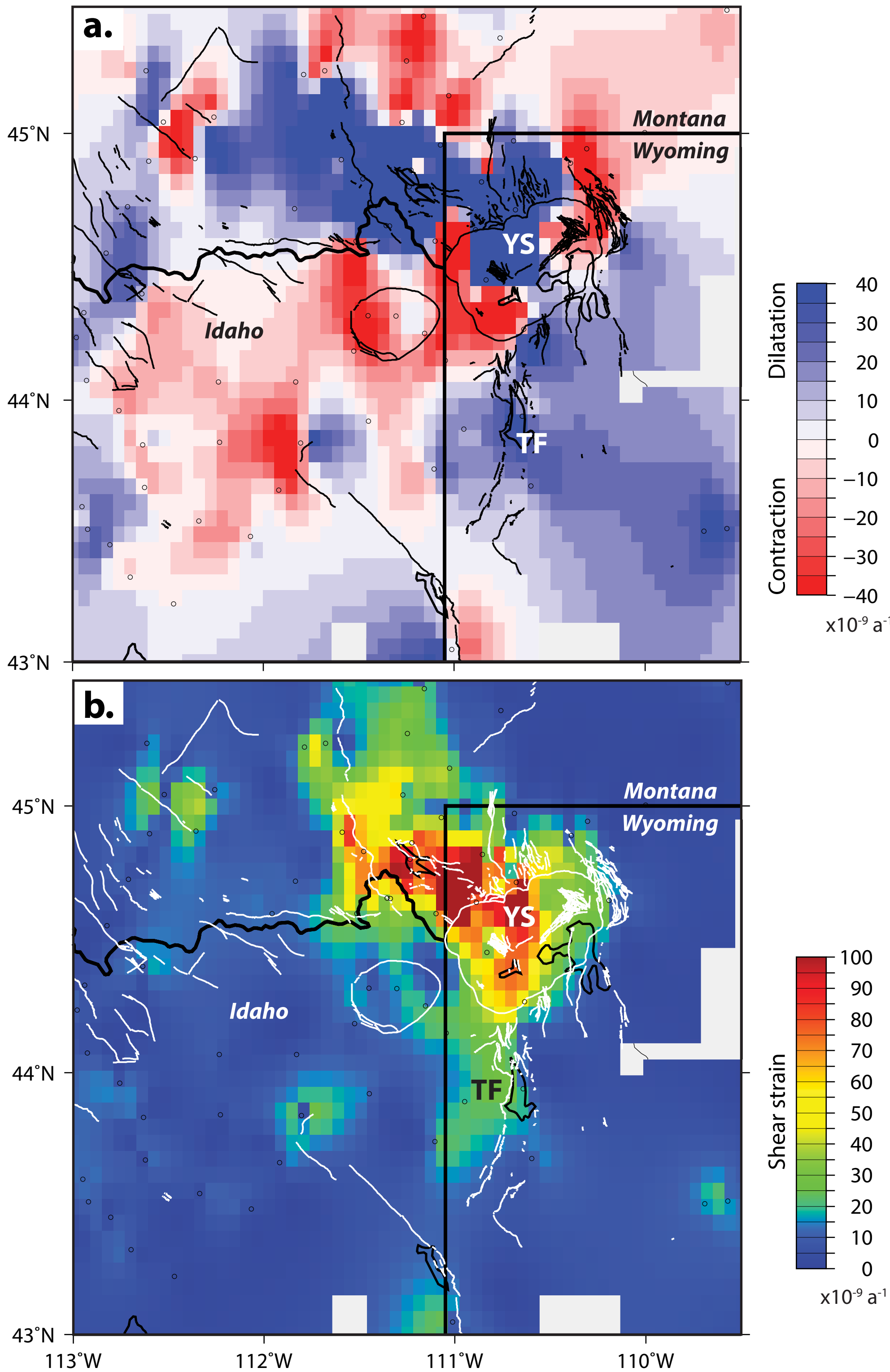

Figure 2.8. Patterns of (a) dilatation and (b) shear strain from GPS surface velocity data. Both dilatation and shear strains are accumulating in the Teton area. YS: Yellowstone; TF: Teton Fault. Thin black/white lines represent Quaternary faults.

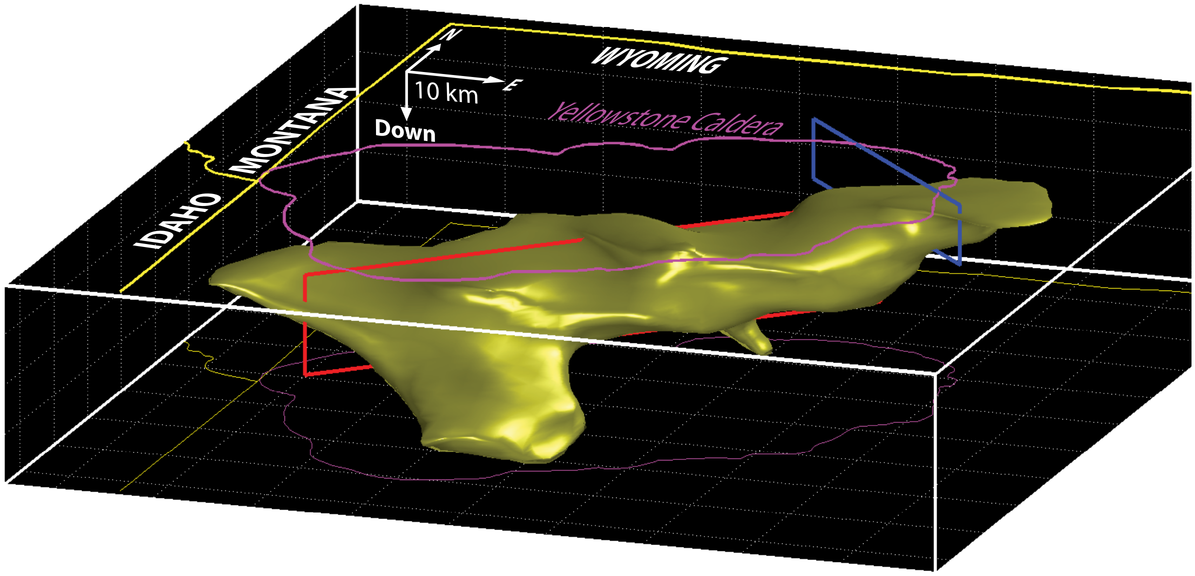

Figure 2.9. Isosurface (-2%) of the *P*-wave tomography model [*Farrell et al.*, 2014] showing the Yellowstone magmatic system. Data from Farrell [personal communication, 2015]. Modeled reservoir plane and pathway plane are outlined by red and blue lines, respectively. The magma reservoir is modeled as a vertical rectangular plane of 60 km long located at the long axis of the magma reservoir. The width in the vertical direction is 12 km, mimicking the depth extent of the magma reservoir, from 5 km to 17 km. The northeastward extension of the low-velocity body possibly becomes the initial main magma pathway when an eruption occurs. The potential magma pathway is modeled as a vertical rectangular plane perpendicular to the long axis of the magma reservoir. The model plane approximates a vertical slice of the pathway, extending from 1 km to 6 km depths. The length is 34 km.

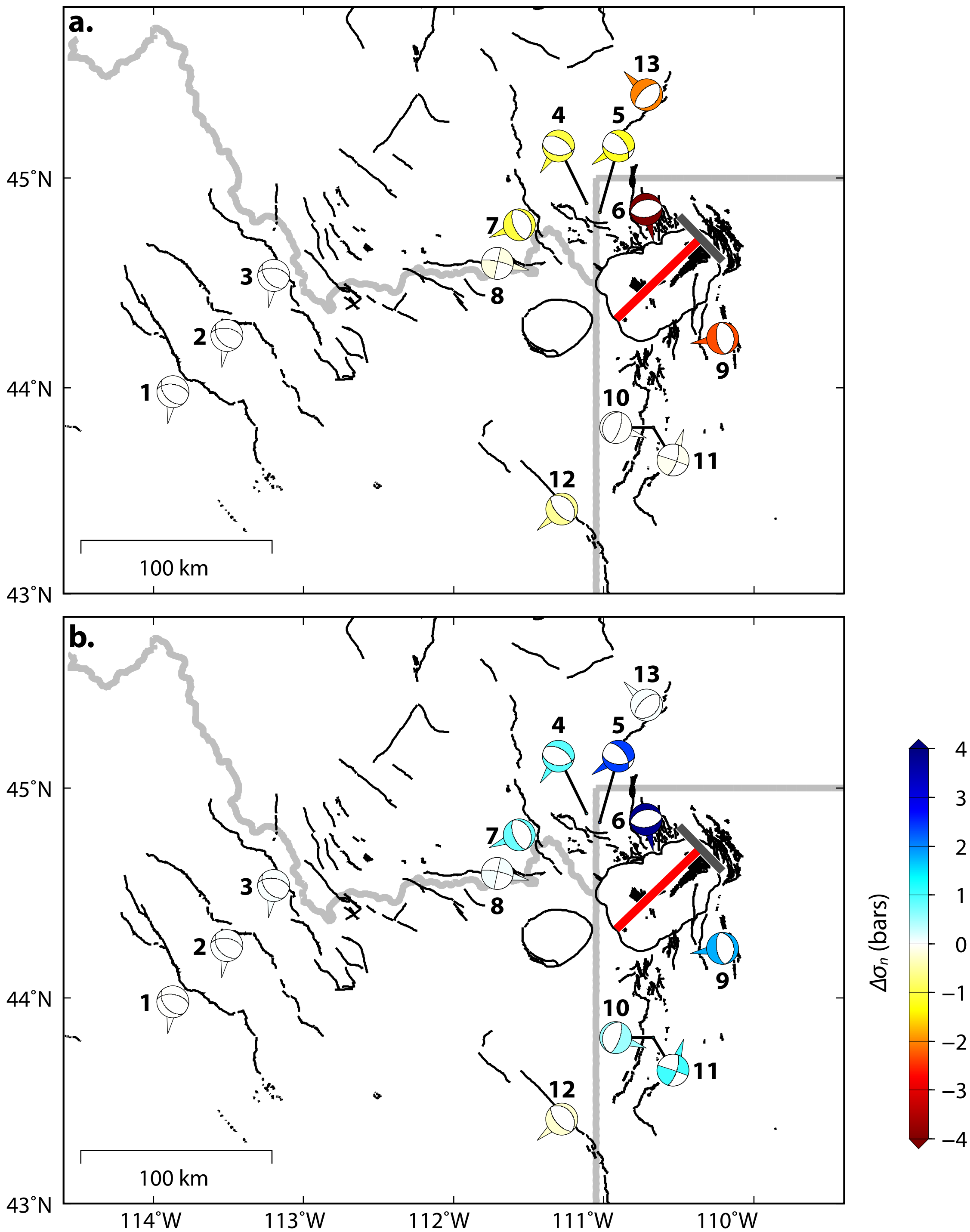

Figure 2.10. Maximum (a) clamping and (b) unclamping on the reservoir plane caused by each hypothetical event. Values of stress change are indicated by the color of the compressional quadrants. Blue spectrum indicates unclamping (i.e., decrease in normal stress), and red spectrum indicates clamping. 1 bar = 0.1 MPa. M_W7.1-7.5 events more than 200 km away from the magmatic system cannot cause a significant stress change around the receivers, regardless of fault geometry or source mechanism.

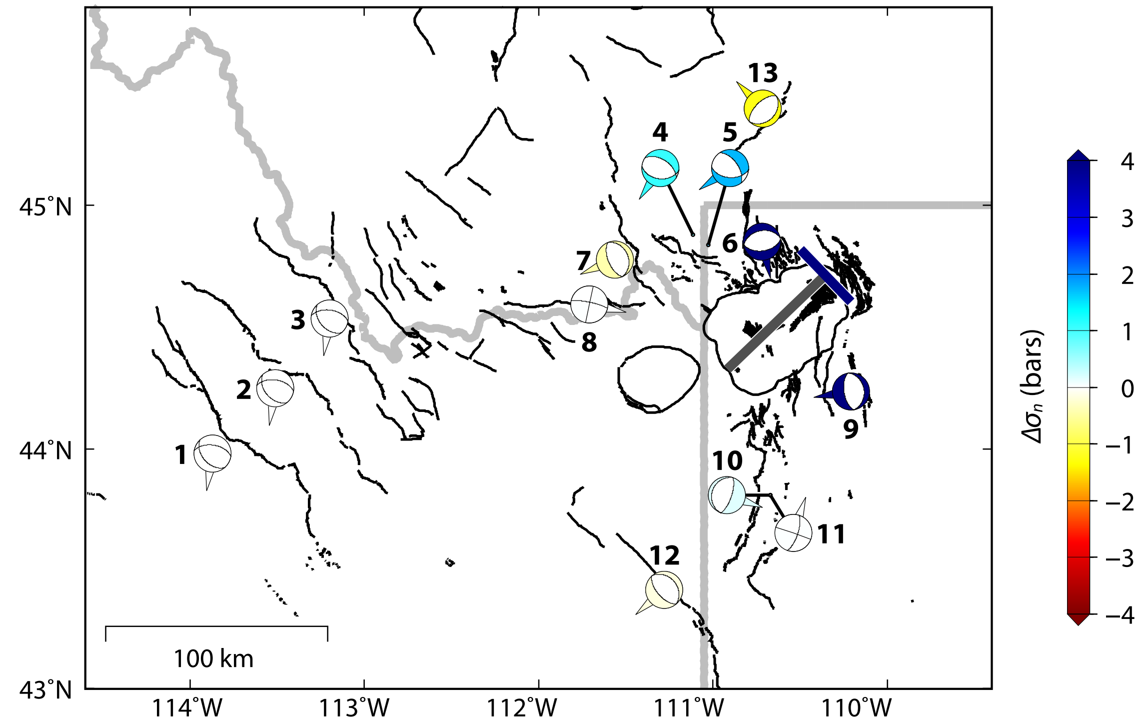

Figure 2.11. Maximum unclamping on the pathway plane caused by each hypothetical event. See Figure 2.10 for explanation.

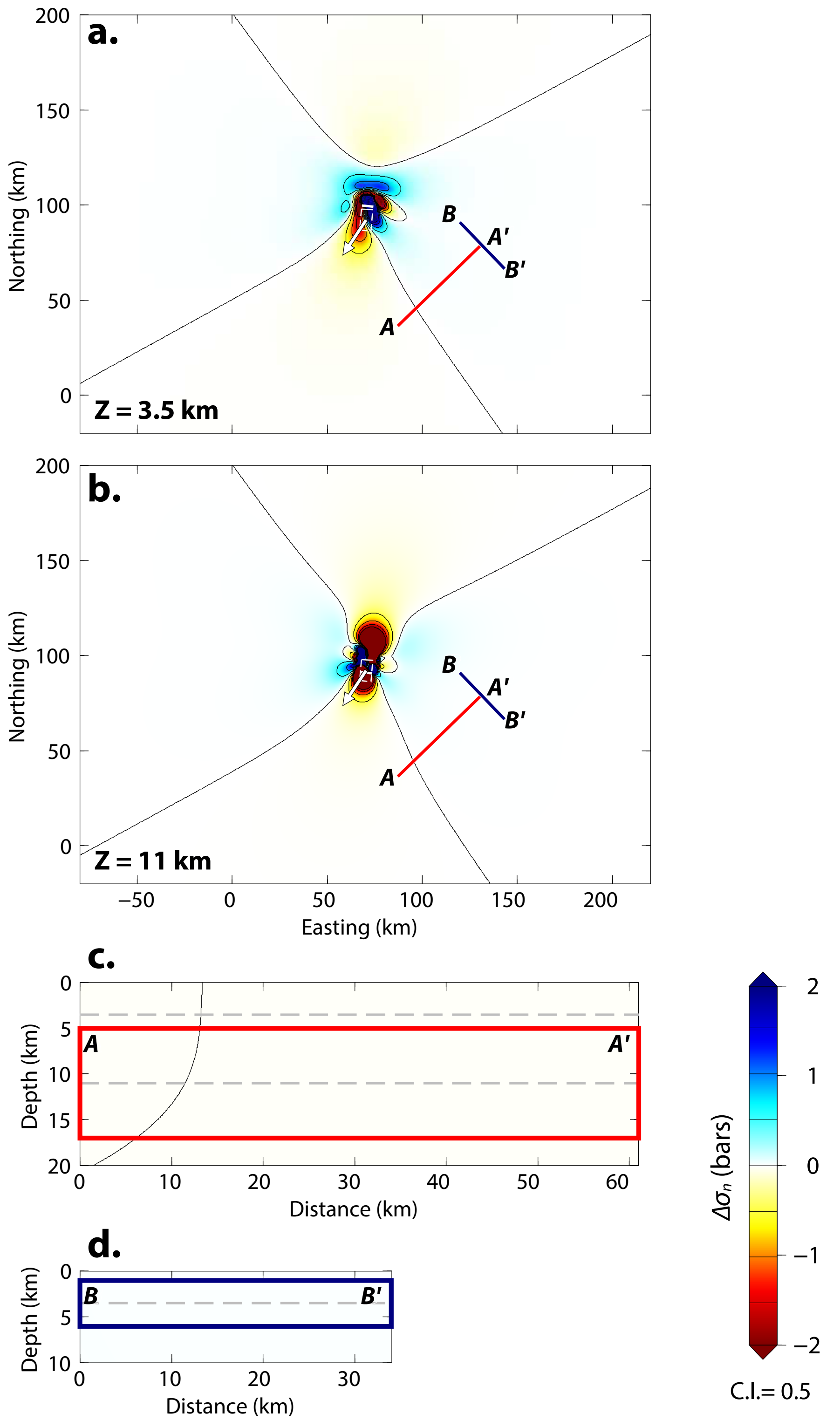
a.
Z = 3.5 km
Northing (km)
B
A′
B′
A
b.
Z = 11 km
Easting (km)
c.
Depth (km)
Distance (km)
d.
Δσ$_n$ (bars)
C.I.= 0.5

Figure 2.12

Figure 2.12. Normal stress changes due to the first mainshock of the Hebgen Lake sequence. Horizontal sections at (a) 3.5 km and (b) 11 km depths, as well as cross sections for the reservoir plane (c; red rectangle) and pathway plane (d; navy rectangle) are presented. Blue spectrum indicates unclamping, and red spectrum clamping. 1 bar = 0.1 MPa. White dashed rectangle, thick bar, and arrow on each map indicate the rupture plane projected on the horizontal section, intersection line between the rupture plane or its extension and the horizontal section, and slip vector azimuth, respectively. The arrow does not indicate the amount of slip. Gray dashed lines on the cross sections indicate the depths of horizontal sections.

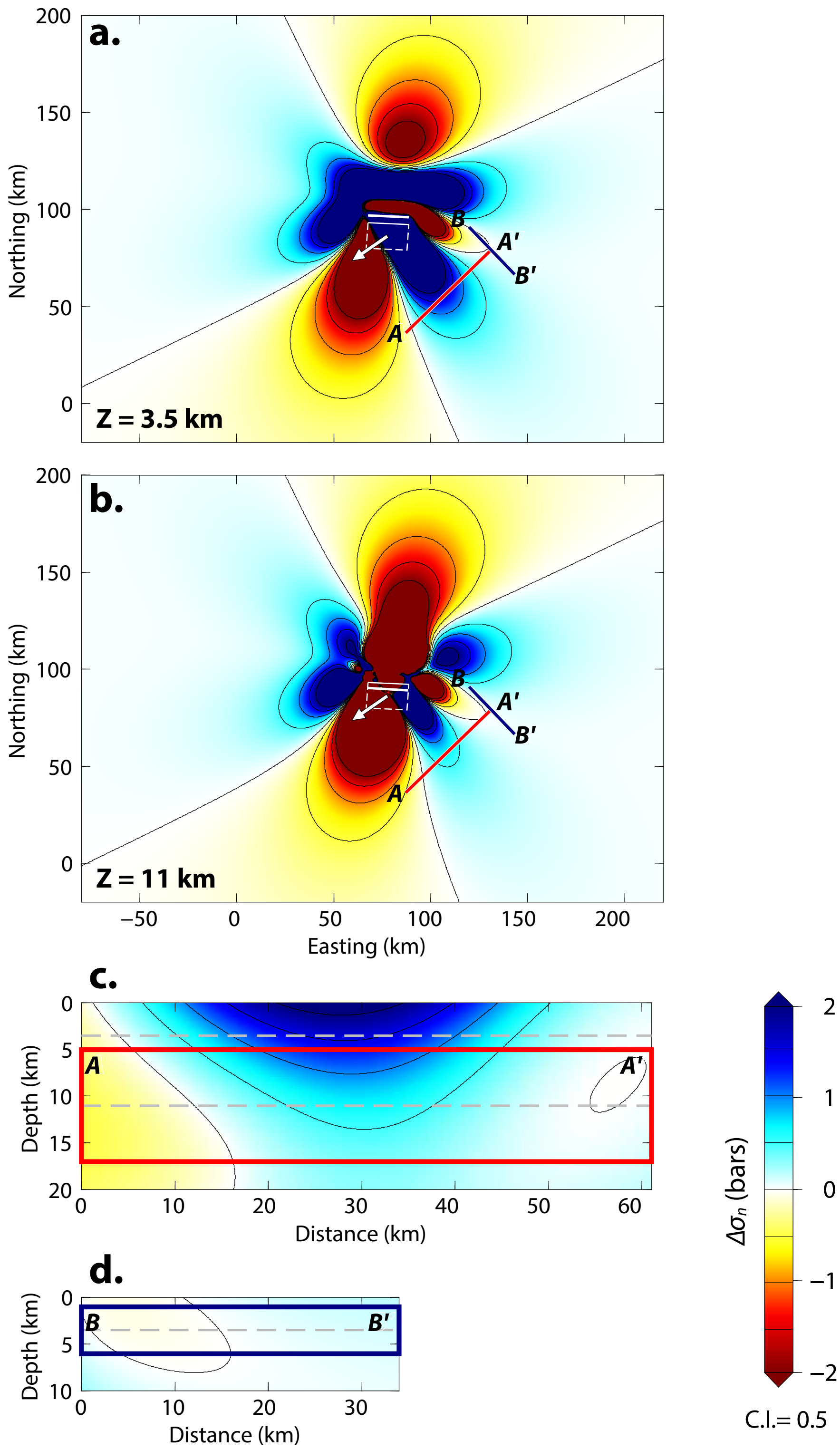

Figure 2.13. Normal stress changes due to the second mainshock of the Hebgen Lake sequence. See Figure 2.12 for explanation.

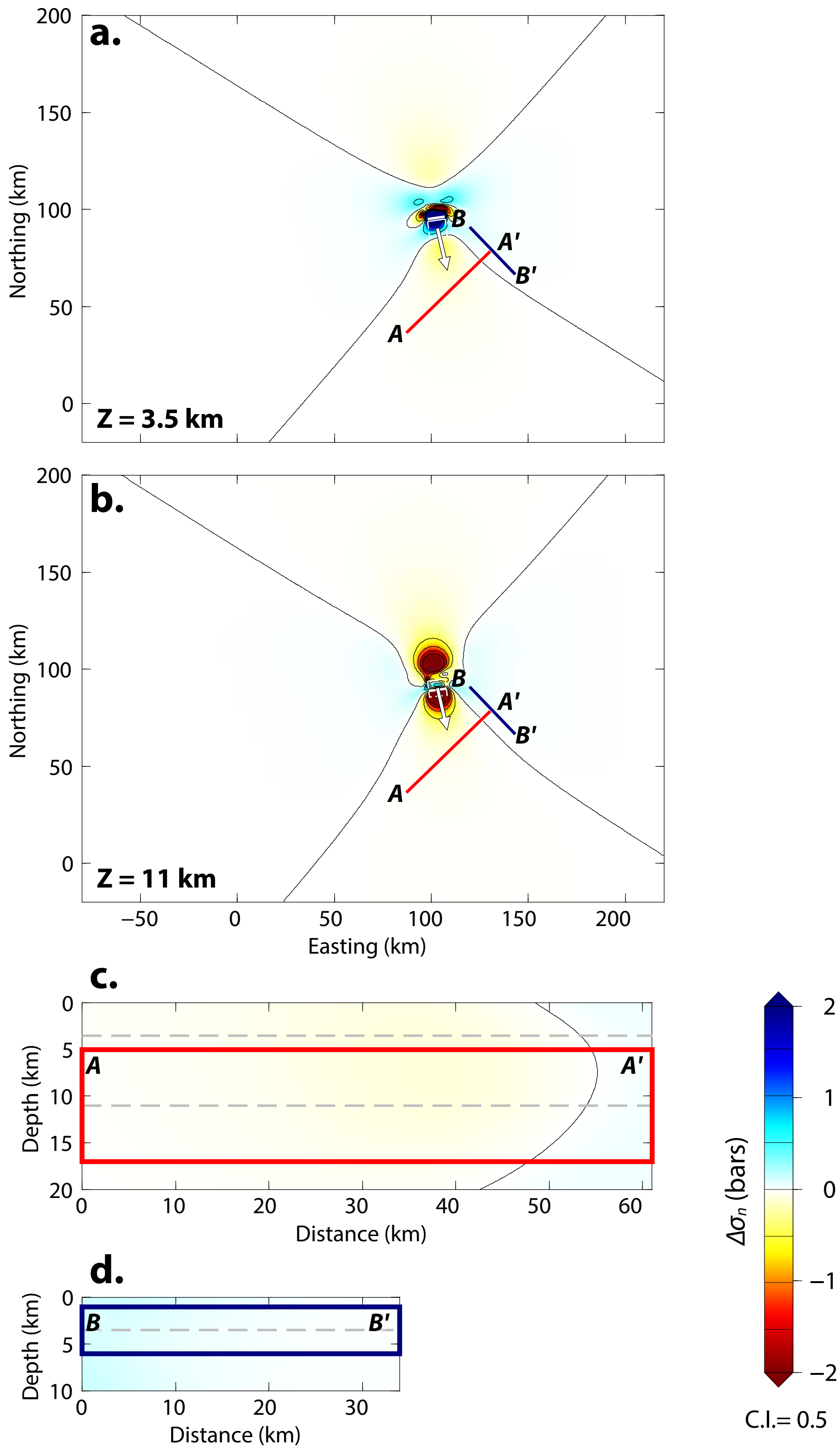

Figure 2.14. Normal stress changes due to the largest aftershock of the Hebgen Lake sequence. See Figure 2.12 for explanation.

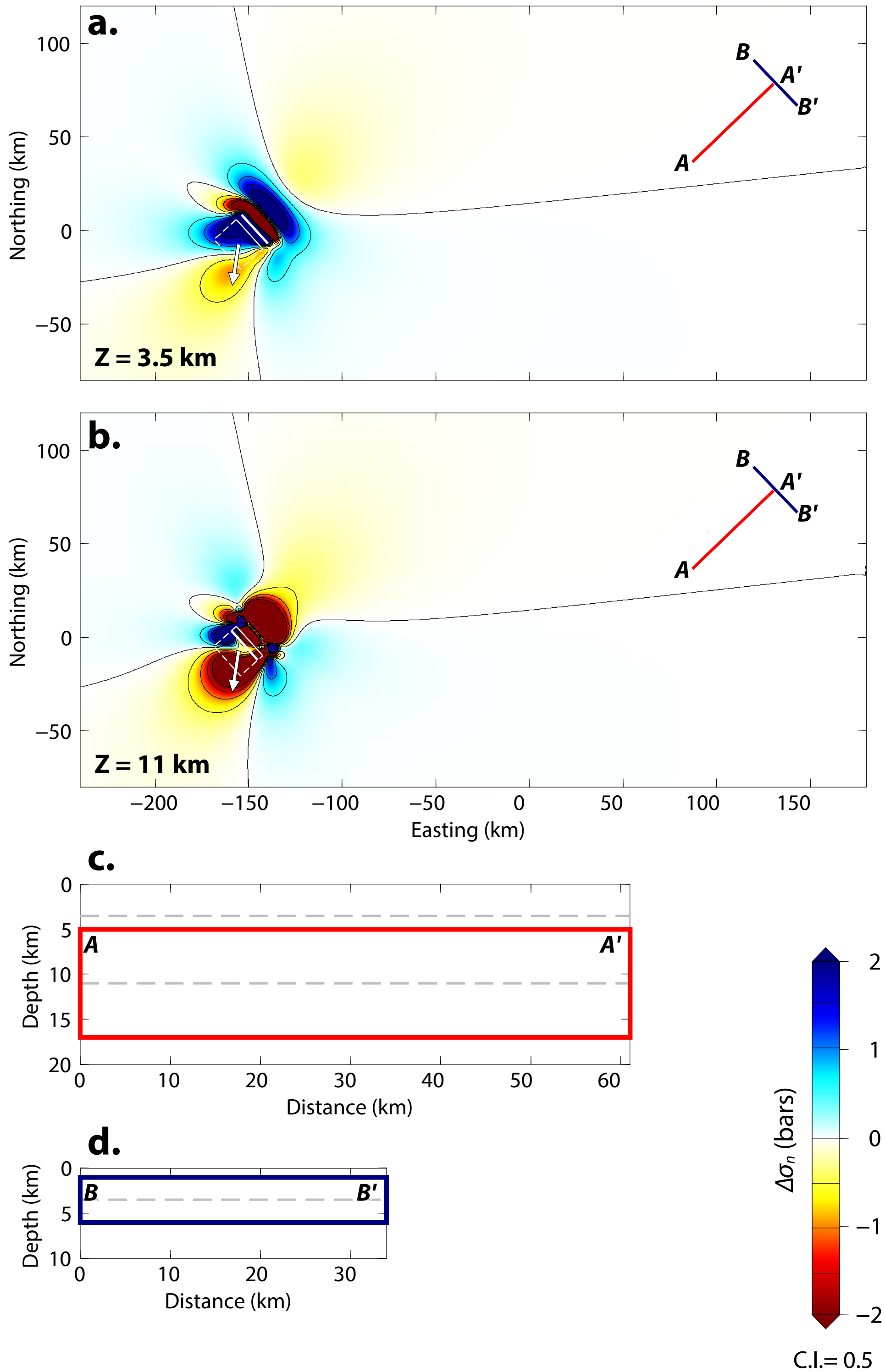

Figure 2.15. Normal stress changes due to the Borah Peak earthquake. See Figure 2.12 for explanation.

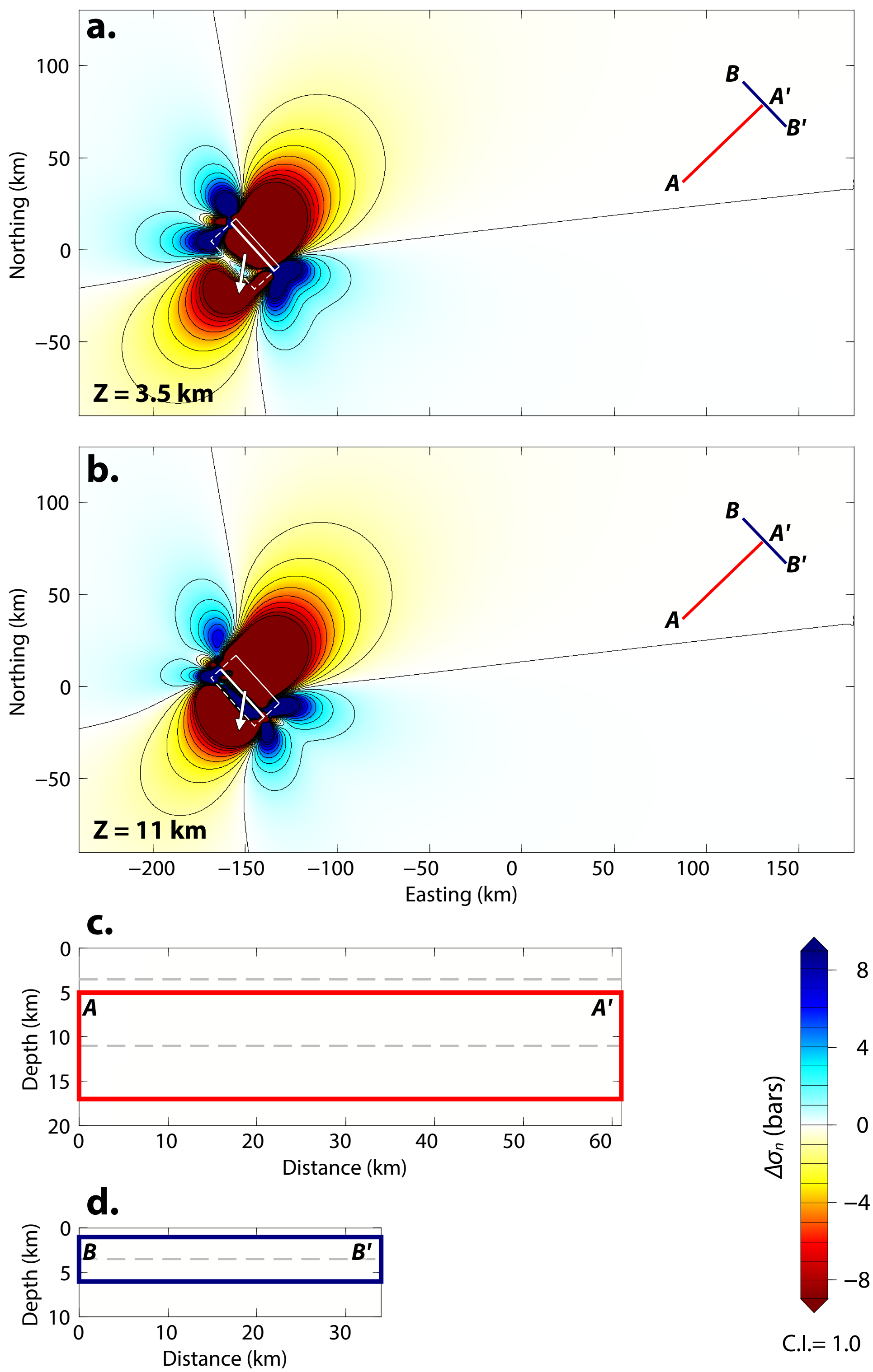

Figure 2.16. Normal stress changes due to Event 1 on the Lost River fault. See Figure 2.12 for explanation.

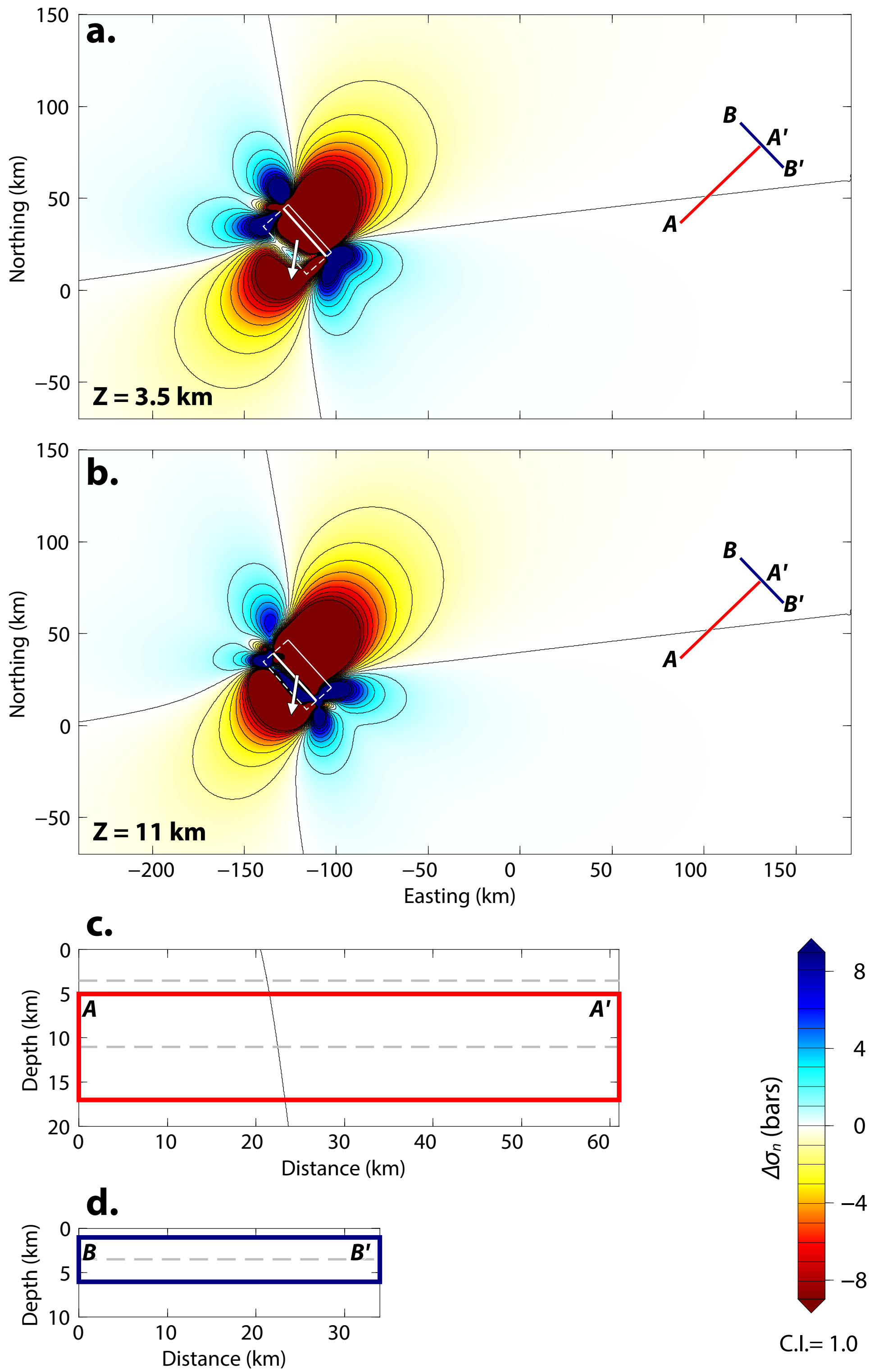

Figure 2.17. Normal stress changes due to Event 2 on the Lemhi fault. See Figure 2.12 for explanation.

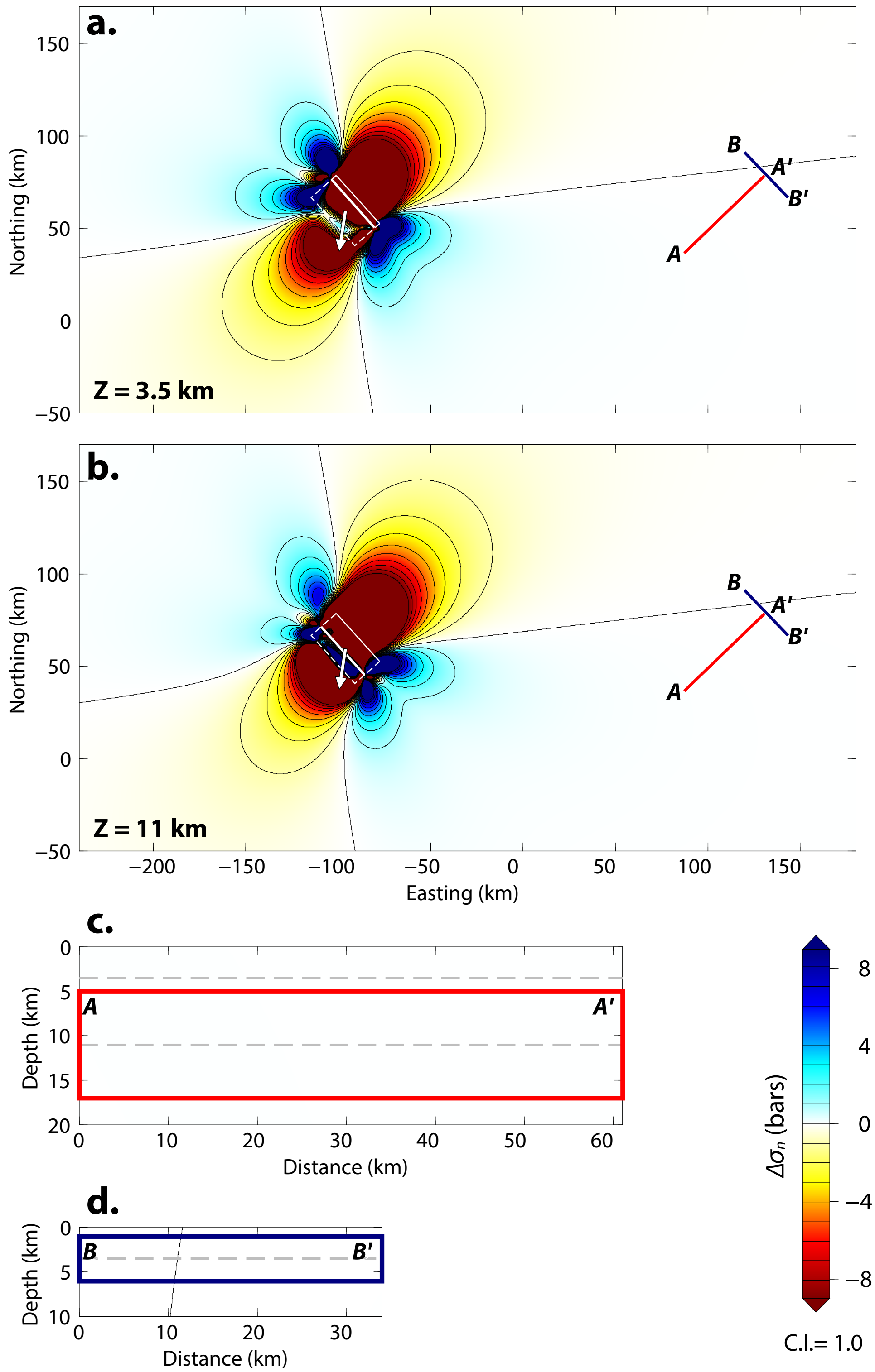

Figure 2.18. Normal stress changes due to Event 3 on the Beaverhead fault. See Figure 2.12 for explanation.

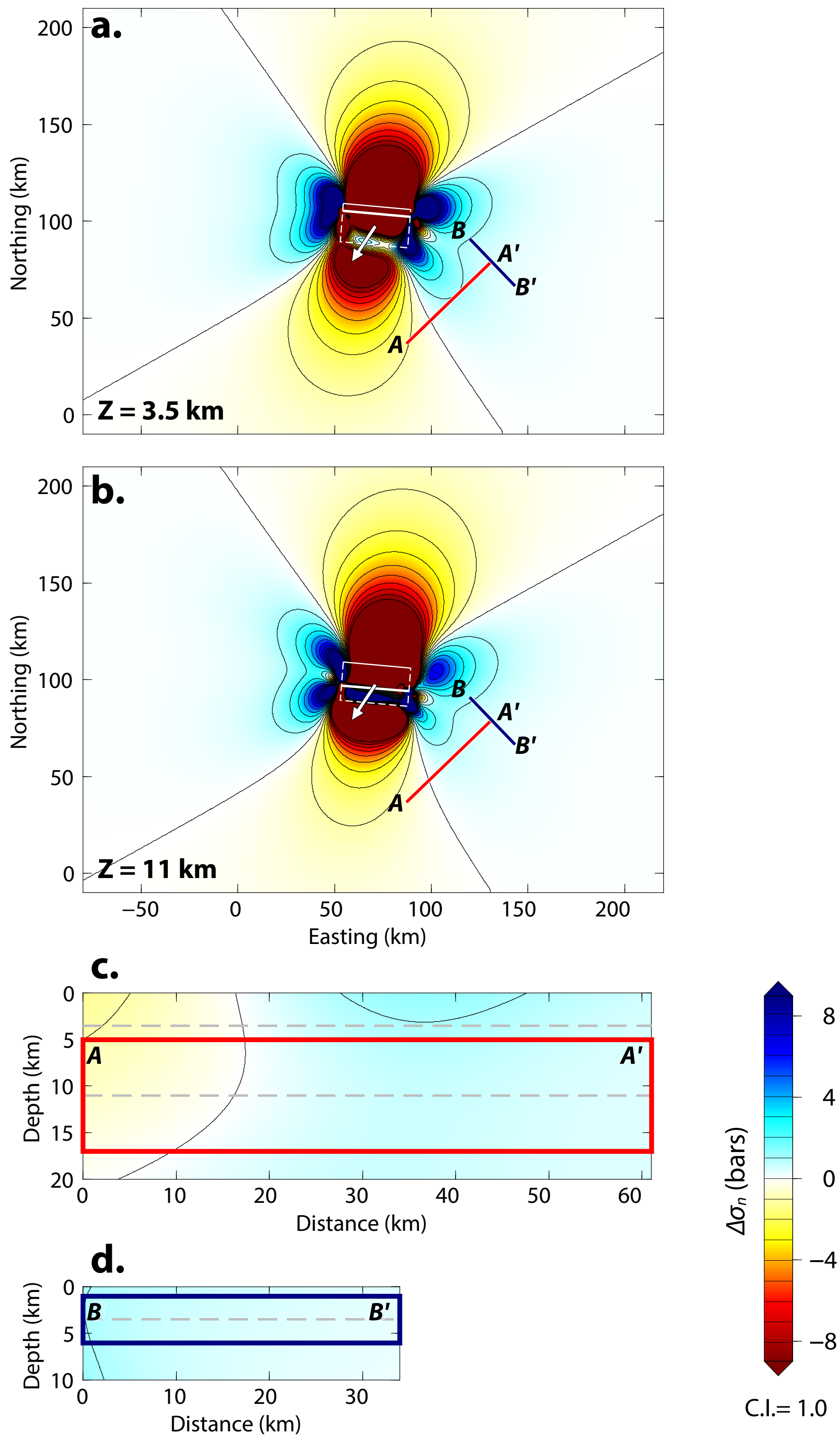

Figure 2.19. Normal stress changes due to Event 4, Hebgen Lake 1. See Figure 2.12 for explanation.

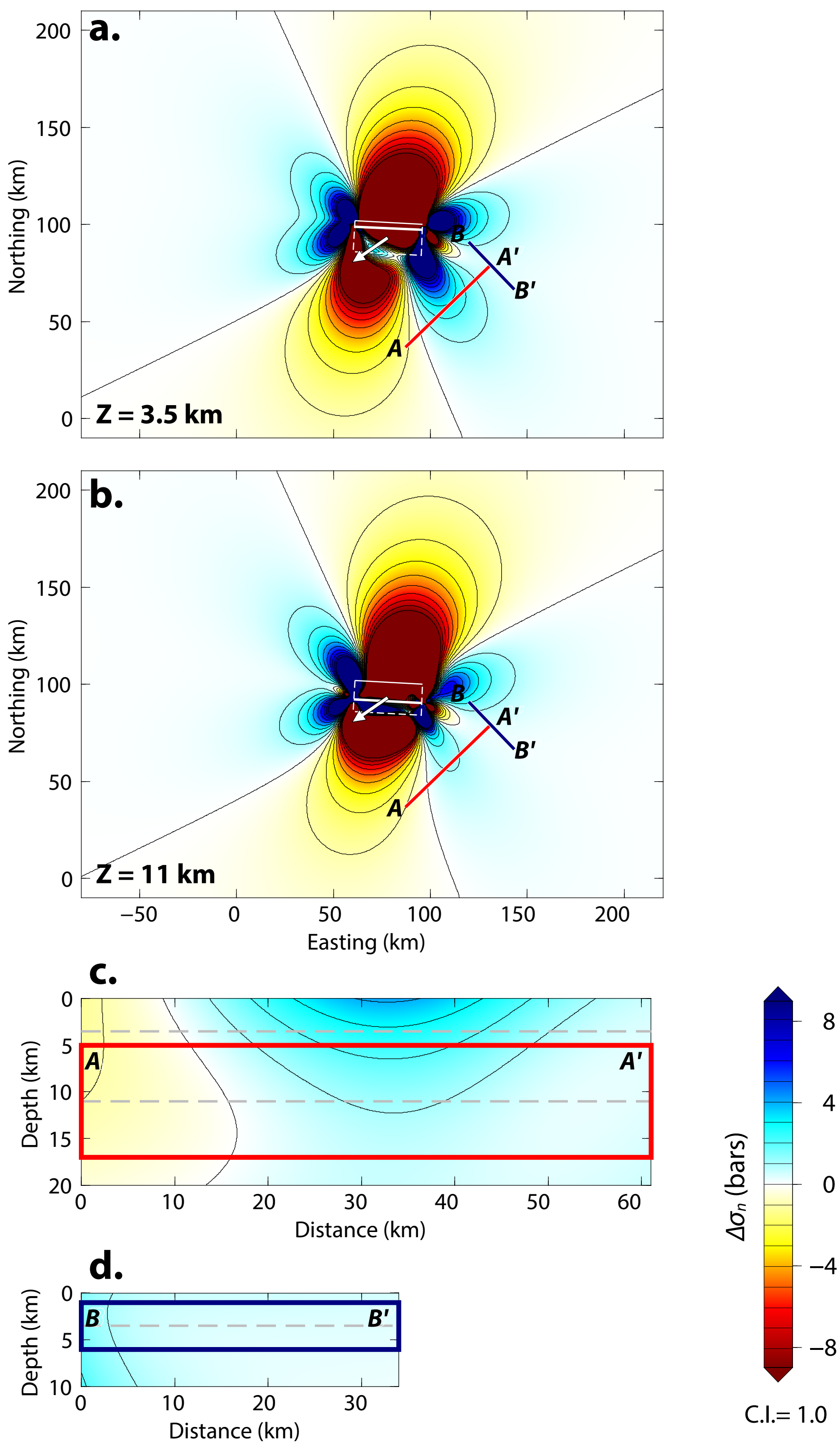

Figure 2.20. Normal stress changes due to Event 5, Hebgen Lake 2. See Figure 2.12 for explanation.

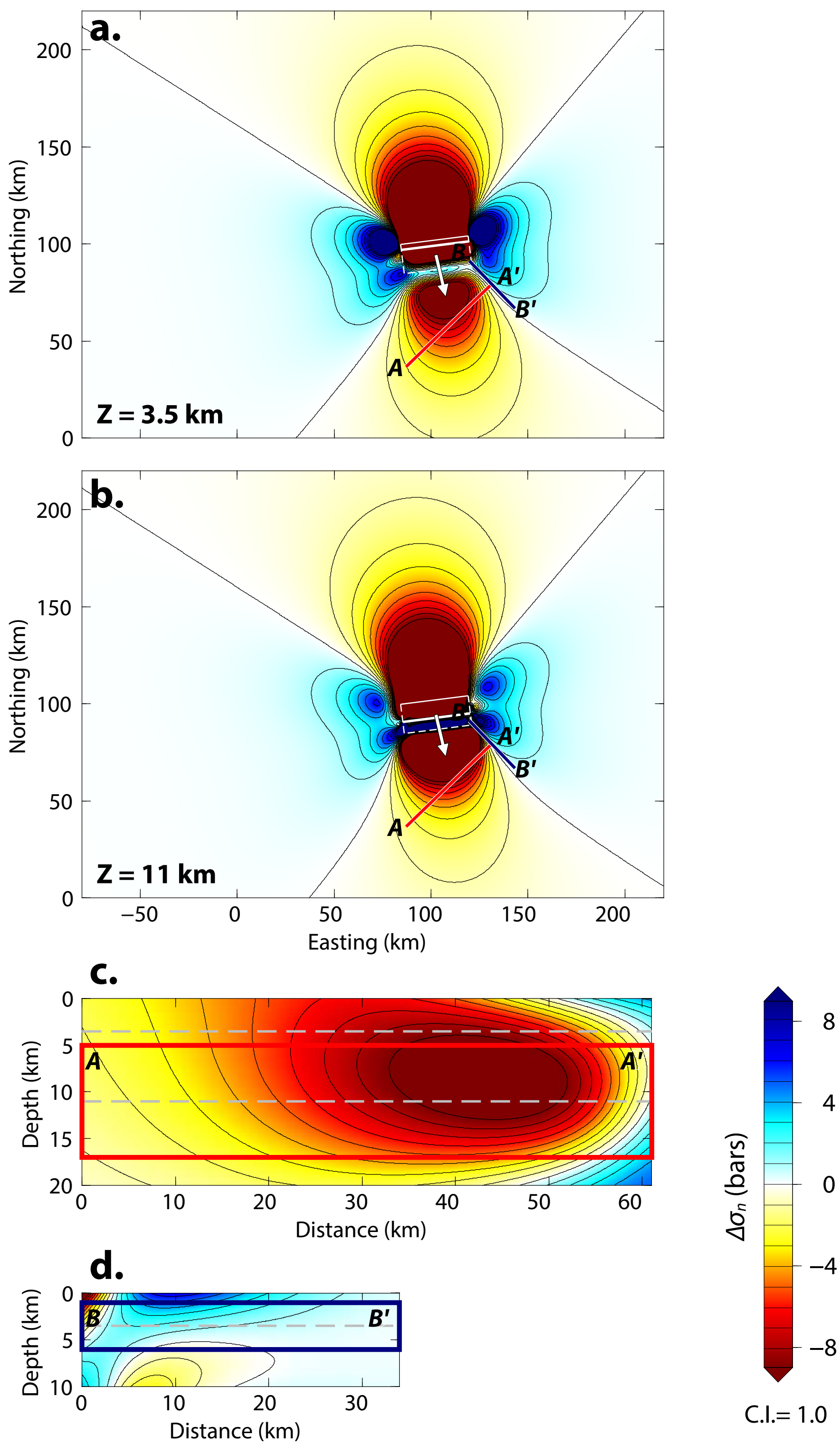

Figure 2.21. Normal stress changes due to Event 6, Hebgen Lake 3. See Figure 2.12 for explanation.

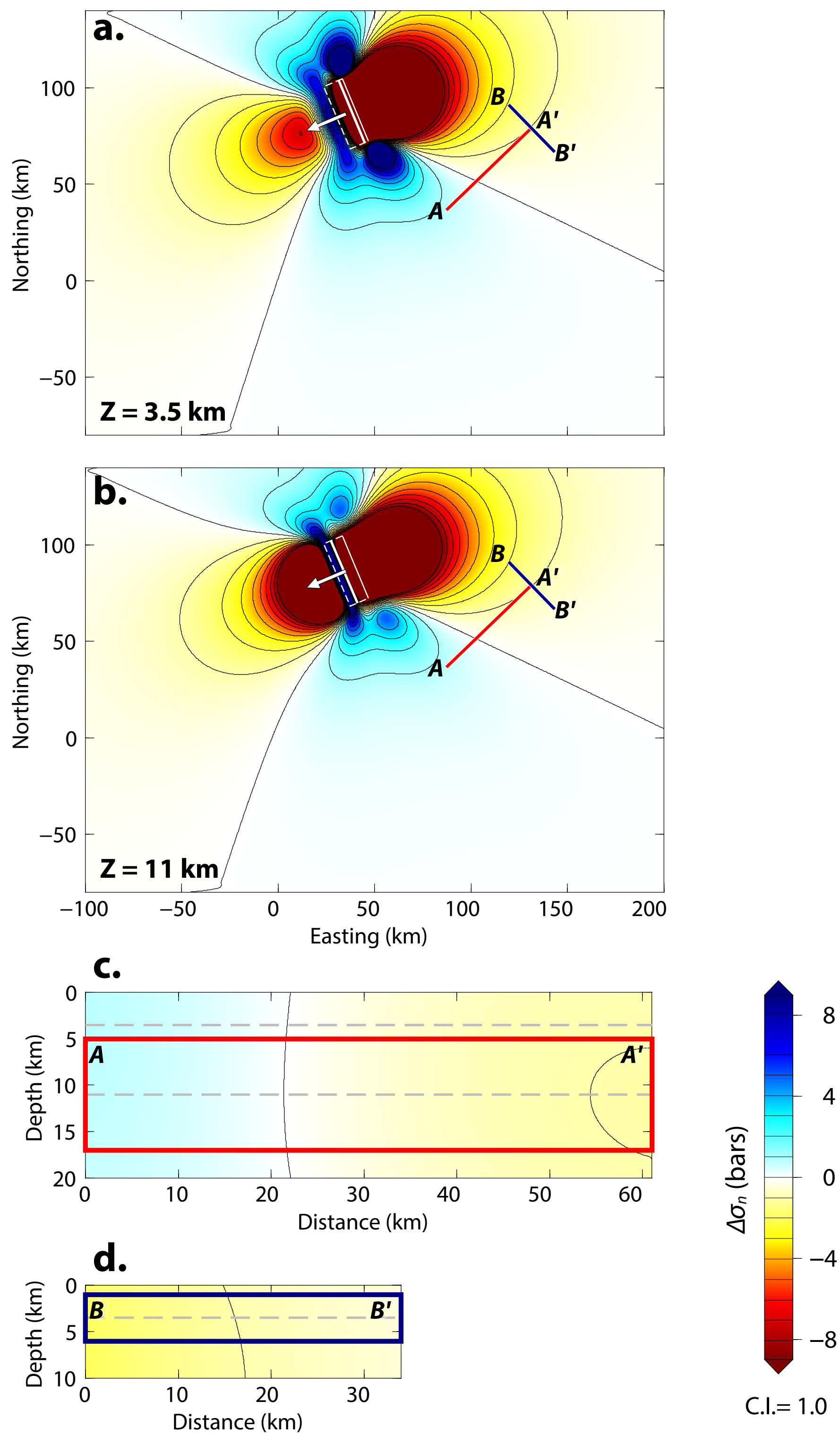

Figure 2.22. Normal stress changes due to Event 7 on the Madison fault. See Figure 2.12 for explanation.

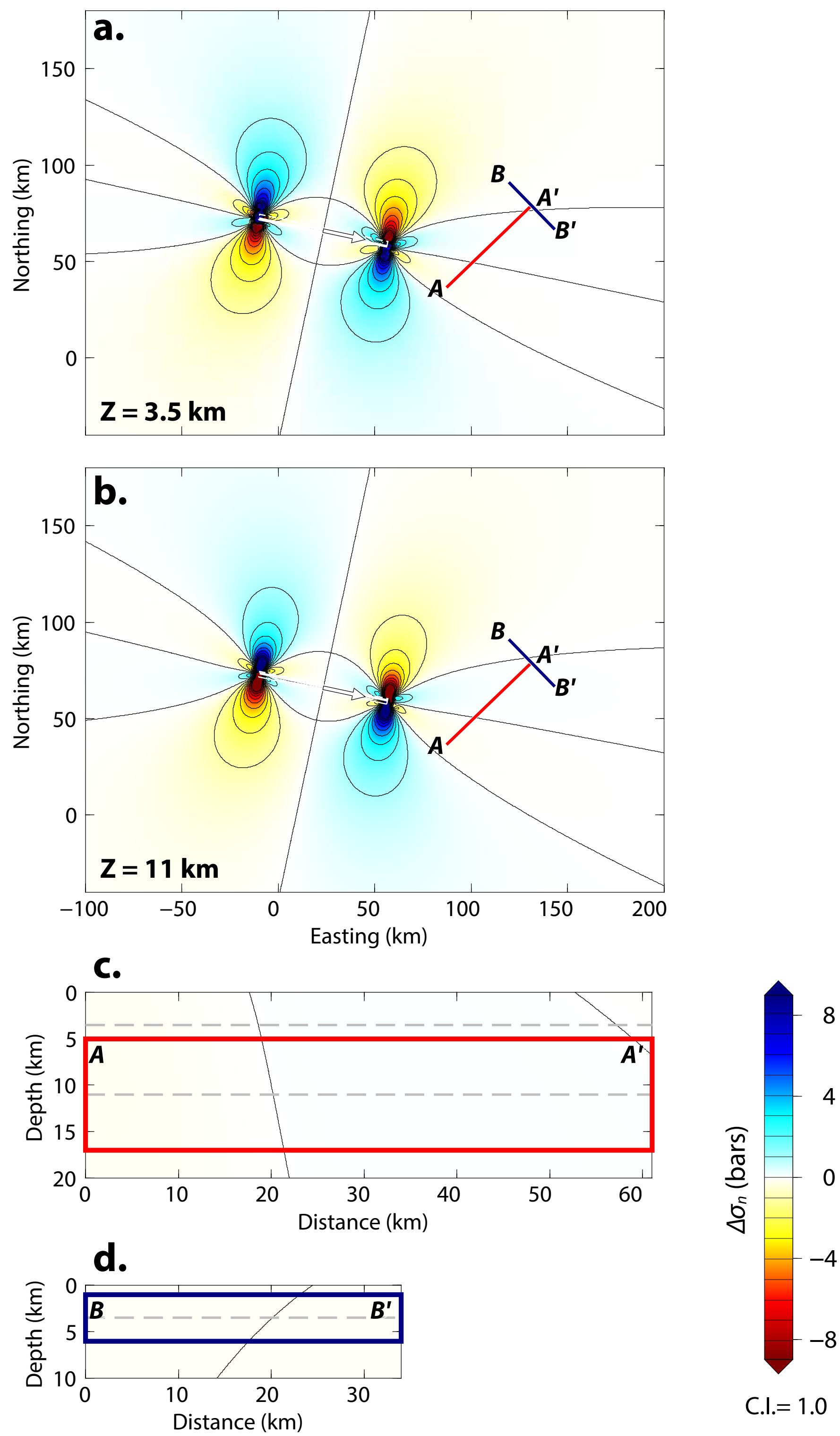

Figure 2.23. Normal stress changes due to Event 8 on the Centennial fault. See Figure 2.12 for explanation.

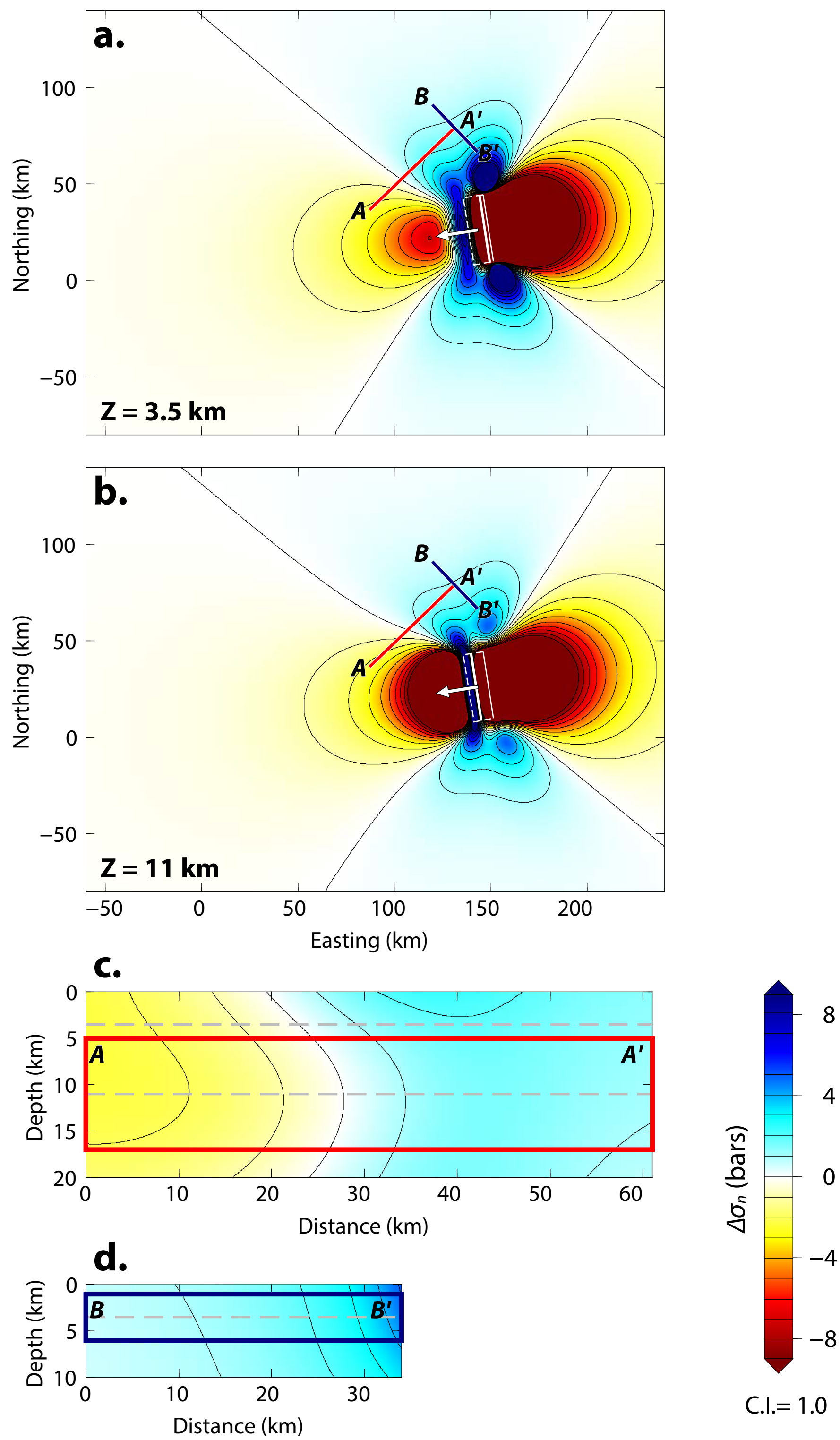

Figure 2.24. Normal stress changes due to Event 9 on the Upper Yellowstone Valley fault. See Figure 2.12 for explanation.

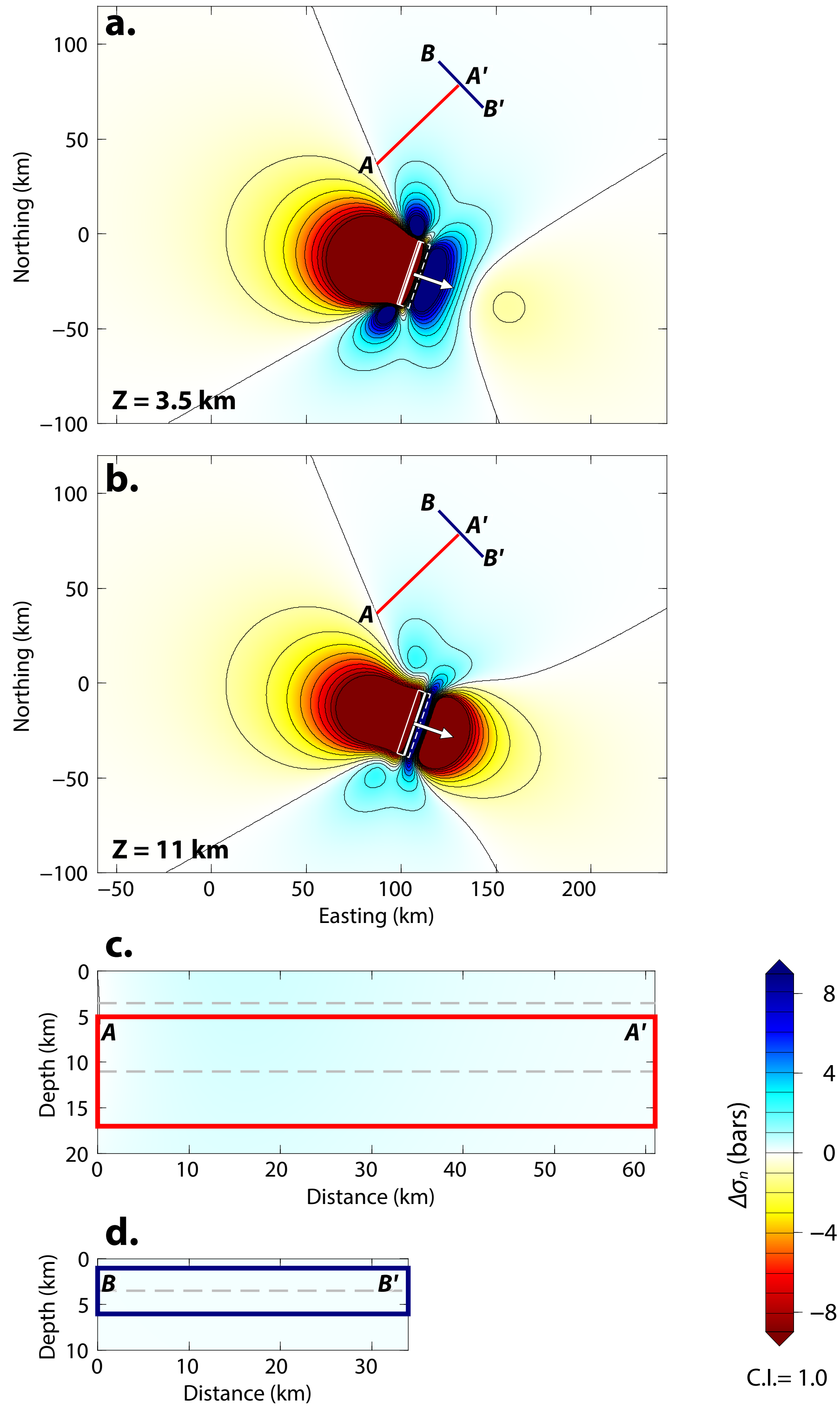

Figure 2.25. Normal stress changes due to Event 10, a normal faulting on the Teton fault. See Figure 2.12 for explanation.

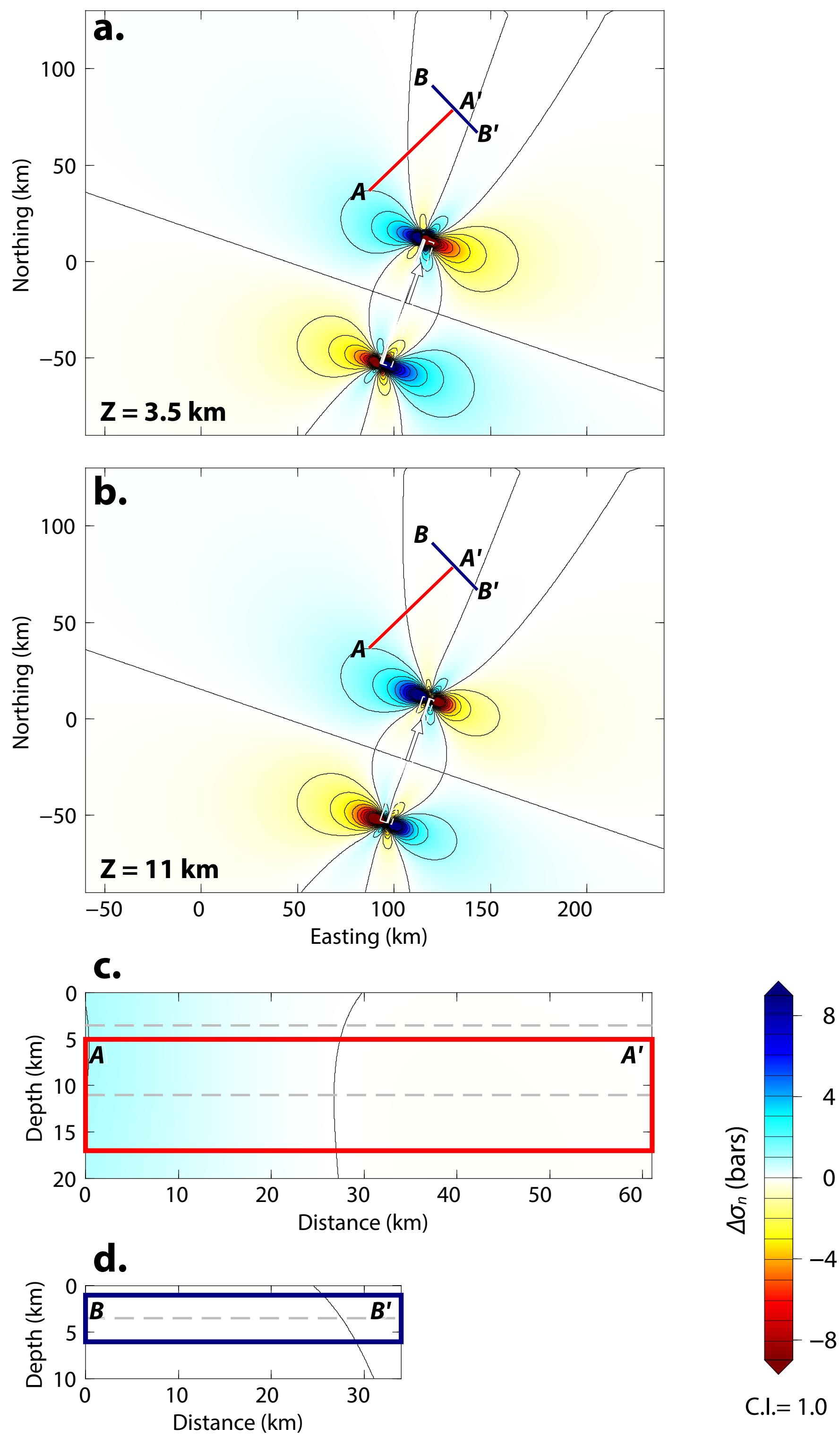

Figure 2.26. Normal stress changes due to Event 11, a strike-slip faulting on the Teton fault. See Figure 2.12 for explanation.

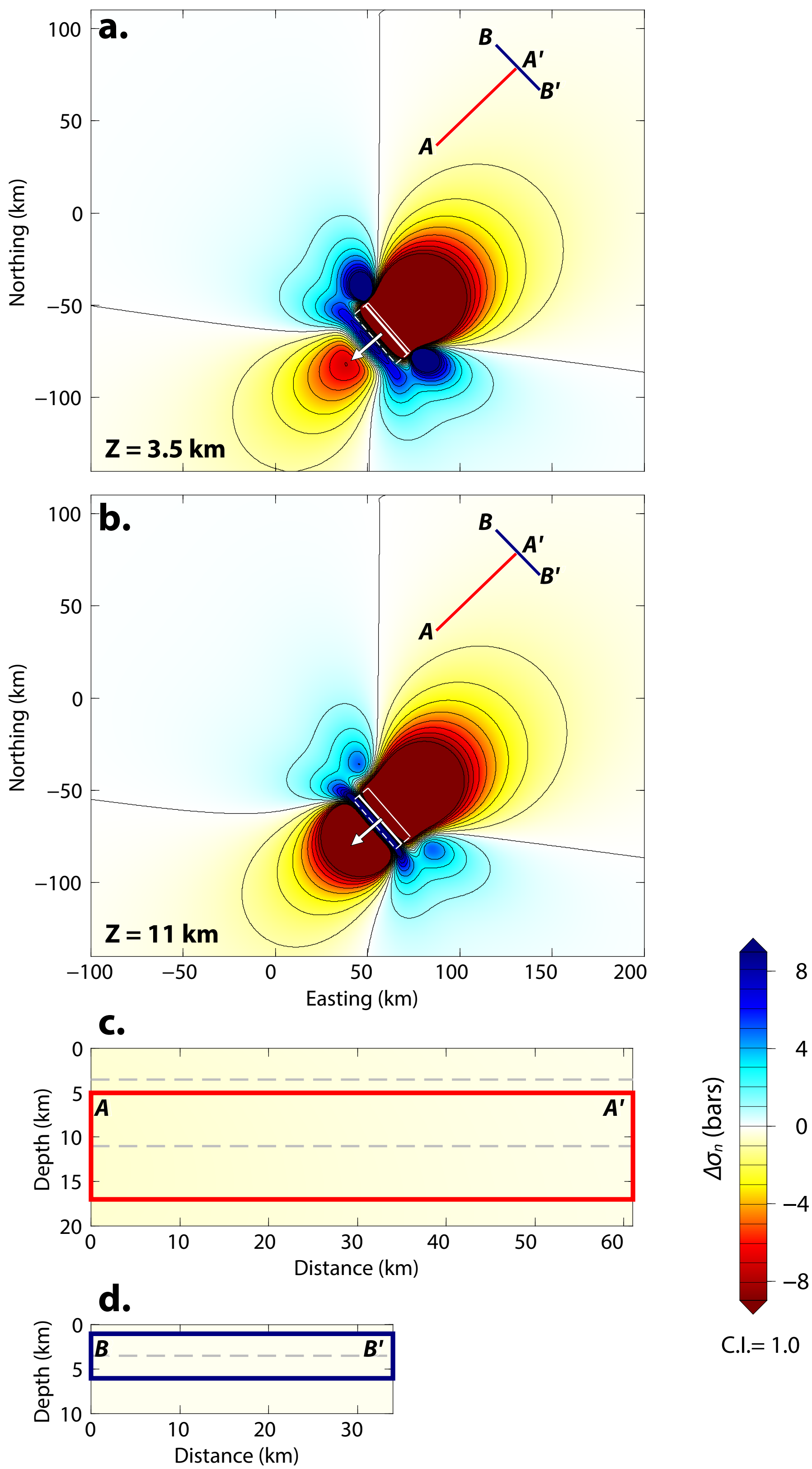

Figure 2.27. Normal stress changes due to Event 12 on the Grand Valley fault. See Figure 2.12 for explanation.

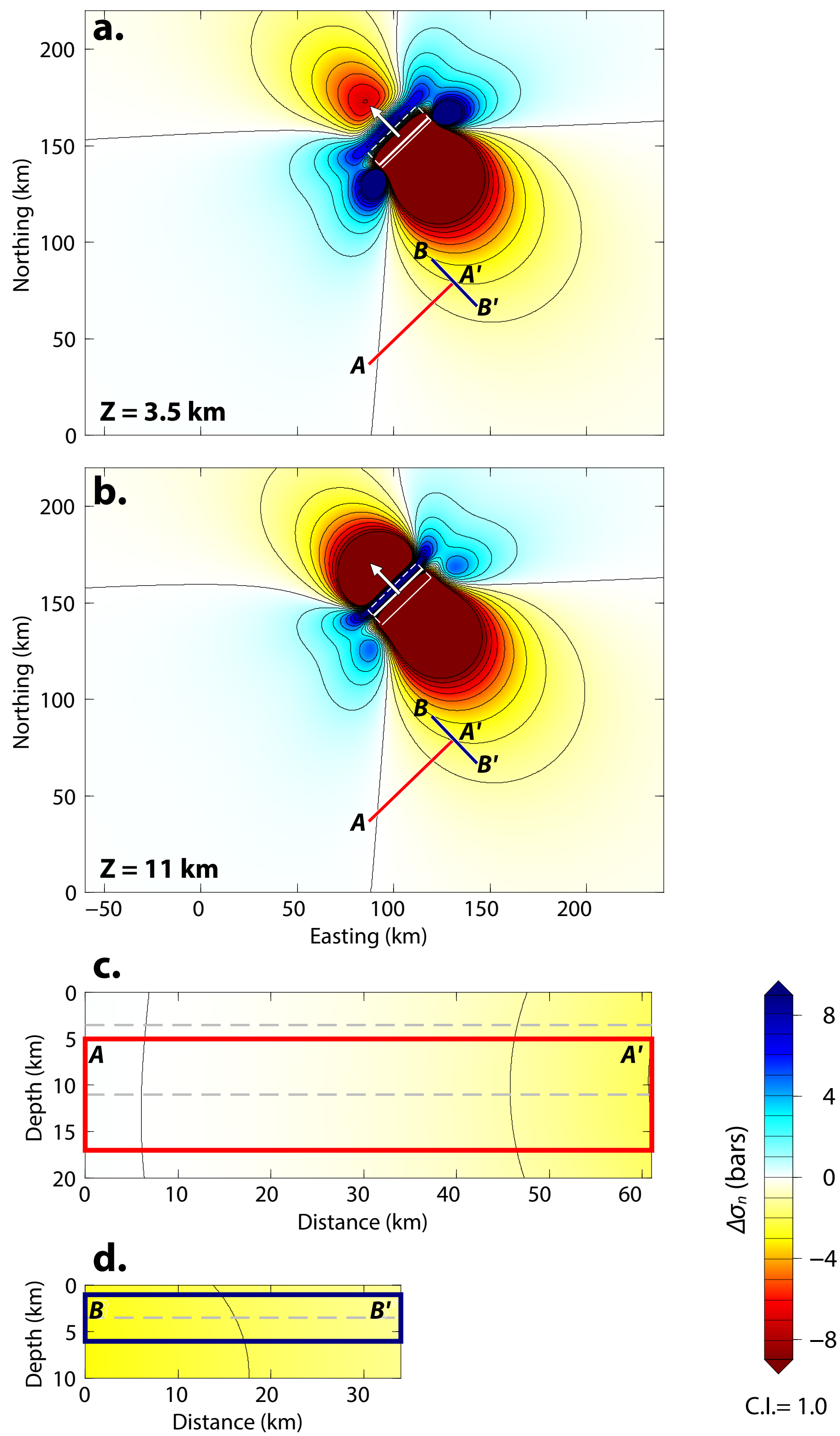

Figure 2.28. Normal stress changes due to Event 13 on the Emigrant fault. See Figure 2.12 for explanation.

CHAPTER 3: SEISMOTECTONIC INTERPRETATION OF THE 2015 SANDPOINT, IDAHO, EARTHQUAKE SEQUENCE

Kobayashi, D., K.F. Sprenke, M.C. Stickney, and W.M. Phillips (2016), Seismotectonic Interpretation of the 2015 Sandpoint, Idaho, Earthquake Sequence, *Idaho Geological Survey Staff Report S-16-1*

This chapter follows the style guidelines by the Idaho Geological Survey.

Abstract

A sequence of three earthquakes, M4.1, M4.2, and M3.5, occurred in the vicinity of Sandpoint, Idaho, on April 24th 2015. These events were followed by an elevated rate of seismicity. The mainshocks occurred southeast of the intersection between the southwest dipping Hope fault and east-southeast dipping Purcell Trench fault within the Lewis Clark Fault Zone (LCFZ), and weakly shook the area in eastern Washington, northern Idaho, and northwestern Montana. We present fault plane solutions of the three Sandpoint events from *P*-wave first motion data recorded at stations operated by the Montana Bureau of Mines and Geology, University of Washington, U.S. Geological Survey, Canadian Geological Survey, Idaho National Labs, University of Utah, and NIOSH Spokane Mining Research Division, and compare them with moment tensor solutions by the U.S. Geological Survey (USGS). All of our fault plane solutions show a reverse sense of oblique slip on a northeast striking southeast dipping nodal plane, which is inconsistent with focal mechanisms of the historical events in the central and eastern parts of the LCFZ, which indicates northeast-southwest extension. The reverse mechanisms are likely to represent a reactivation of the east-southeast dipping Purcell Trench fault. A recent GPS velocity field and strain analysis indicate possible contraction in the epicentral area. The Sandpoint earthquakes, along with

the adjacent reverse-faulting events, constrain the western extent of the northeast-southwest extension of the LCFZ.

Introduction

A sequence of three M3-4 earthquakes occurred around Lake Pend Oreille southeast of Sandpoint, Idaho, on April 24th 2015 (Figure 3.1). Because they were widely felt in much of northeastern Washington, northern Idaho, and northwestern Montana, a region of relatively low seismicity, these events were reported in the press across the region. These earthquakes occurred where the two major faults in the area, the Hope fault and Purcell Trench fault, meet (Figures 3.1 and 3.2). The southwest dipping Hope fault is in the western part of the Lewis Clark Fault Zone, a zone of complex series of steeply dipping faults that extends to western Montana (Foster and others, 2007, and references therein). The Hope fault is truncated against an east-southeast dipping segment of the Purcell Trench fault in the epicentral area (Figures 3.1 and 3.2). The Purcell Trench fault extends from the Lake Coeur d'Alene area to southeastern British Columbia (Clark, 1973), marking the eastern boundary of the Priest River metamorphic core complex (Figure 3.2) (e.g., Harms and Price, 1992; Doughty and Price, 1999, 2000). We found fault plane solutions of the three Sandpoint earthquakes inconsistent with a northeast-southwest extension indicated by historical seismicity in the Lewis Clark Fault Zone (Stickney and Bartholomew, 1987; Stickney, 2015). In this report, we present the fault plane solutions and a seismotectonic analysis to explain these unusual mechanisms.

Regional Tectonic Setting and Seismicity

The Sandpoint earthquake sequence occurred approximately 23 km (14 mi) southeast of Sandpoint, Idaho, near Lake Pend Oreille. The epicentral area is in the western part of the Lewis Clark Fault Zone, where major faults, the Hope, Purcell Trench, and Newport faults interact (Figures 3.1 and 3.2).

The epicenters of the Sandpoint earthquakes are in the western part of the Lewis Clark Fault Zone (LCFZ), a ~800 km (500 mi) long, 80-100 km (50-62 mi) wide, east-southeast trending structural discontinuity extending from central Washington to western Montana (Figure 3.1) (Harrison and others, 1974; Stickney and Bartholomew, 1987). The fault zone is characterized by a complex series of steeply dipping, northwest striking strike-slip, oblique-slip, and dip-slip faults due to multiple reactivation episodes (Harrison and others, 1974; Foster and others, 2007). The fault zone formed in early Mesoproterozoic (1.5 to 1.4 Ga) in association with rifting and the Belt basin formation (Smith, 1965; Harrison and others, 1974; Reynolds, l979; Winston, 1986; Wallace and others, 1990; Sears and Hendrix, 2004). During Cretaceous to Paleogene, the LCFZ accommodated sinistral transpression, crustal shortening in a left-lateral sense, as a result of thrusting and batholith intrusions (Hyndman and others, 1988; Sears and others, 2000; Sears and Hendrix, 2004). In response to crustal collapse of the Cretaceous-Paleocene orogenic wedge (Coney, 1987; Harry and others, 1993; Livaccari, 1991; Sonder and others, 1987; Wernicke and others, 1987), the Eocene extension took place, reactivating the LCFZ as a dextral shear zone to accommodate differential extension (Reynolds, 1979; Doughty and Sheriff, 1992; Foster and Fanning, 1997; Sears and Fritz, l998; Lewis and others, 2005).

Active seismicity has been observed within the LCFZ and the adjacent areas (Figure 3.1). The eastern LCFZ is associated with recurrent seismicity including multiple M~6 events resulted from normal slip near Helena, Montana (Freidline and others, 1976; Stickney, 1978; Stickney and Bartholomew, 1987). In the central and eastern LCFZ and the area south of the LCFZ, both major and small events indicate a northeast-southwest extension (Figure 3.1) (Stickney and Bartholomew, 1987; Stickney, 2015). To the north of the LCFZ, predominant directions of principal stress have been unclear (Sbar and others, 1972; Stevenson, 1976; Stickney, 1980; Qamar and others, 1982) until a recent seismotectonic analysis by Stickney (2015) suggested an east-west extension (Figure 3.1). In the western part of the LCFZ, diffuse seismicity, including events as large as M~5, has been recorded. M~5 events occurred in 1918 in Rathdrum, Idaho, and in 1942 in Sandpoint (Sprenke and Breckenridge, 1992). Figure 3.2 shows instrumentally recorded earthquakes since 2000 and focal mechanisms of the major events in eastern Washington, northern Idaho, and northwestern Montana. The August 1, 1988 tectonic earthquake (M4.1) northeast of Mullan resulted from dextral slip, possibly along the west-northwest striking Thompson Pass Fault (Sprenke and others, 1991). Another notable earthquake in the area is the 1994 M3.5 Hoyt Mountain event followed by a M2.9 aftershock. Both mainshock and aftershock indicate a reverse reactivation of a steeply dipping (~75°) northwest-southeast striking relict normal fault (Sprenke and others, 1994). The 2009 M3.1 Trout Creek and the 2014 M2.9 Moose Peak earthquakes were located near Trout Creek, Montana, about 90 km (56 mi) southeast of Sandpoint. Relatively concentrated seismicity in the Wallace area is mostly from mining-related rockbursts (Figure 3.1) (Stickney and Bartholomew, 1987; Sprenke and others, 1991). In the Spokane area, there is another concentrated seismicity, which represents a five-month long swarm of small earthquakes that occurred in 2001 (Wicks and others, 2013).

The main fault in the LCFZ is splayed in northwestern Montana toward the western end of the fault zone (Figure 3.1). The northernmost of these splay faults is the southwest dipping Hope fault, which terminates against the Purcell Trench fault in the epicentral area (Figure 3.2). The Hope fault formed in Proterozoic (Harrison and others, 1972) and reactivated as a dip-slip fault in early Eocene (Fillipone and Yin, 1994; Fillipone and others, 1995). A dextral normal sense of motion is indicated along the Hope fault (e.g., Harrison and Jobin, 1963), which is consistent with the fault plane solution of the events that occurred near the fault (i.e., the 2000 Trout Creek and 2014 Moose Peak events; Figure 3.2).

The Purcell Trench fault is an east-southeast dipping listric detachment fault that extends from Coeur d'Alene Lake to southeastern British Columbia (Figures 3.1 and 3.2) (Reynolds 1980; Rehrig and others, 1987; Doughty and Price, 1999, 2000). Along its trace, the Purcell Trench fault forms a half-graben, the Purcell trench, which is a 5-7 km (3-4.3 mi) wide topographic depression (Figure 3.2) locally filled with Tertiary sediments and covered by glacial deposits. The Hope fault terminates against the Purcell Trench fault to the immediate north of Sandpoint (Figure 3.2). The Purcell Trench fault formed to accommodate the Eocene extension and became a detachment fault verging to the east that unroofed the Priest River metamorphic core complex on its western side (Figure 3.2) (Rehrig and others, 1987; Harms and Price, 1992; Doughty and Price, 1999, 2000).

The presence and nature of the Purcell Trench fault and its relation to the Hope fault were unclear for decades mainly because: (1) the fault was mostly covered by glacial deposits in the Purcell trench; and (2) metamorphic core complexes (MCC), one of which forms the foot-wall block of the Purcell Trench fault, were not understood. Metamorphic core complexes are extensional structures that expose deep crust. As the understanding of MCC formation became clear in the 1980’s, the adjacent Priest River MCC was identified and more field studies were conducted in the area, which led to better understanding of the interaction between the Purcell trench and Hope faults. In the history of early geological study of the area, Daly (1906) first identified and named the narrow topographic low the Purcell trench. Calkins (1909) identified and named the Hope fault and reported evidence of faulting in the Purcell trench, which became a basis of a long-standing interpretation that the Hope fault cross-cuts the Purcell trench or Purcell trench fault after the fault was identified. Daly (1912) suggested the possibility that the Purcell trench represented a full graben. Kirkham and Ellis (1926) identified an east dipping fault along the Purcell trench to the north of the Lake Pend Oreille, which is a segment of what is now known as the Purcell Trench fault. Anderson (1930) extended the east dipping fault identified by Kirkham and Ellis (1926) to the south. In the geologic map by Anderson, the extended fault was cross-cut and offset by the Hope fault. Figure 3.3a shows an interpretation by Harrison and Schmidt (1971) and Harrison and others (1972), a full graben-style Purcell Trench faults cross-cut and offset in a dextral sense by the Hope fault and its splayed segments. Until the 1970’s, some researchers did not include any faults along the Purcell trench (e.g., Park and Cannon, 1943; Miller and Engels, 1975).

The current consensus about the relationship between the Hope and Purcell Trench faults is that: (1) the Purcell trench is a half-graben bounded on the west by the Purcell Trench fault; and (2) the Hope fault and its splayed segments are truncated against the east-southeast dipping Purcell Trench fault (Figure 3.2). These interpretations arose in the geologic map by Bayley and Muehlberger (1968). Clark (1973) showed the dextral Hope fault system truncated against the Purcell Trench fault (Figure 3.3b). This interpretation has been adopted and refined by researchers who carried out field studies in the area (e.g., Harms, 1982; Harms and Price, 1992; Doughty and Price, 1999, 2000), and now widely accepted (e.g., Lewis and others, 2006, 2008; Foster and others, 2007).

The Newport fault system located to the west of the Purcell Trench fault and to the north of Newport, Washington, has a U-shaped trace with its opening in the north (Figure 3.2). The two fault tips are located ~15 km (~9 mi) south of the US-Canada border. The fault is shallowly dipping in a normal sense toward the center of the fault system (Rehrig and others, 1987; Harms and Price, 1992; Doughty and Price, 1999, 2000). The Newport fault delineates a partially isolated hanging-wall block underlain by the metamorphosed basement as a result of the formation of the Priest River MCC in response to the Eocene extension (Figure 3.2) (Rehrig and others, 1987; Harms and Price, 1992; Doughty and Price, 1999, 2000).

The Packsaddle and Cascade faults run about 10-15 km (6-9 mi) southeast of the epicenters (Figure 3.2) (Lewis and others, 2008). They strike northeast-southwest and dip nearly vertically at the surface with the northwestern blocks down. Their dip directions at greater depths are poorly known. If they formed in response to an extension, they should be dipping to the northwest. The faults formed in Precambrian time and developed in Cretaceous as a result of block tilting associated with a granodiorite intrusion, forming half-grabens (Harrison and Jobin, 1963; King and others, 1970).

The Lake Pend Oreille area has exhibited relatively low seismicity since regional seismic monitoring began in 1982. Figure 3.4 shows temporal distribution of seismicity in the area from 1988 through 2015. Detection and location of earthquakes prior to 1996, when northwestern Montana stations began operating, is probably incomplete for M<2.5 events. Small earthquakes have occurred annually in this area since 1999 except for a five-year period from 2004 to 2009. The first instrumentally located earthquake occurred about 15 km (9 mi) east-southeast of Sandpoint on June 18, 1988 with a magnitude of 3.4. Nine more earthquakes occurred from mid-1999 through mid-2003. The largest of these was a M3.5 event centered about 25 km (15.5 mi) south-southeast of Sandpoint on January 1, 2000. Ten additional small earthquakes occurred between 2009 and 2015, the largest was a magnitude 2.2 on August 3, 2014. The detection threshold appears to be about M1.5 since seismograph stations began operating in northwestern Montana in the late 1990's. From this perspective, the 2015 seismicity exceeds any previous seismicity in the region since regional networks began operating (Figure 3.4b).

Figure 3.5 shows the spatial distribution of the instrumental earthquakes in the Lake Pend Oreille region since 1982. The largest earthquakes cluster within a three-kilometer diameter area at 48.10°N, 116.38°W, near the east shore of Lake Pend Oreille. Six events lie about 2.5 km (1.6 mi) northeast of the largest earthquakes and six small events (magnitudes 1.3 to 1.8) scatter up to 20 km (12 mi) northward. The north-south scatter of these epicenters very likely has more to do with poor seismograph station distribution around the events (i.e., no station control north or south of the epicenters) than any sort of north-south trending seismogenic structure. This poor station geometry probably also contributes to the scattered distribution of smaller, pre-2015 earthquakes across the northeastern part of Lake Pend Oreille. A regional seismic network in northern Idaho would contribute to a better understanding of both tectonic and mining-related earthquakes in northern Idaho.

The 24 April 2015 Sandpoint Earthquake Sequence

The three principal events of the Sandpoint sequence occurred immediately southeast of Lake Pend Oreille within a radius of 2 km (1.2 mi) (Figure 3.6) at 02:32, 05:43, and 08:28 on April 24th, 2015 (UTC) (Table 3.1). Estimates of both hypocenter and origin time show good agreement between this study and the USGS for the size of the events (M~4). The largest discrepancy in hypocenter is of the first event and is ~3.9 km (~2.4 mi) (Table 3.1; Figure 3.6). The USGS (U.S. Geological Survey, 2015a) reports the horizontal uncertainty of the epicenter of the first event to be ±5.0 km (3.1 mil), whereas our estimate is ±1.2 km (0.7 mi). Therefore, the location determined in this study is in the range of the uncertainty of the epicenter by the USGS. The second event has the largest magnitude (M4.2), and that of the first and third events are M4.1 and M3.5, respectively (Table 3.1). The earthquakes were felt in much of northeastern Washington and northern Idaho to northwestern Montana (U.S. Geological Survey, 2015abc). Seismograms of the second event recorded at selected sites are shown in Figure 3.7.

Table 3.1. Origin details of the Sandpoint earthquakes sequence on April 24th, 2015.

	Event	Origin time (UTC)	Longitude	Latitude	Horizontal uncertainty (km)	Depth (km)	Vertical uncertainty (km)
This study	1	02:32 20.21	-116.384	48.099	± 1.2	14.0	± 1.1
	2	05:43 36.33	-116.378	48.103	± 1.3	14.2	± 1.3
	3	08:28 28.79	-116.367	48.103	± 1.2	11.7	± 1.1
USGS[a]	1	02:32 20.370	-116.389	48.127	± 5.0	11.5	± 2.9
	2[b]	05:43 36.400	-116.367	48.118	± 4.9	15.0	± 5.5
	3[b]	08:28 28.800	-116.345	48.117	± 4.4	9.5	± 6.3

Table 3.1 (continued)

	Event	Minimum Distance[c] (km)	Travel time residual (sec)	Azimuthal Gap (°)	Magnitude
This study	1	58.0	0.35	120	Md[d] 4.1
	2	58.0	0.37	120	Md 4.2
	3	59.0	0.34	121	Md 3.5
USGS[a]	1	56.77	0.64	36	M_{wr} 3.7
	2[b]	58.33	1.28	118	M_{wr} 3.9
	3[b]	59.89	1.00	118	M_l 3.3

[a] From U.S. Geological Survey (2015ab)
[b] Location is determined by the Montana Bureau of Mines and Geology.
[c] Distance to the nearest station
[d] Coda duration magnitude (Eaton, 1992)

The USGS estimated peak acceleration, peak velocity, and instrumental intensity (Worden and others, 2012) of the first and second events (Figure 3.8) (U.S. Geological Survey, 2015ab). The first event made a record of peak acceleration at ~1.5%g at ~10 km (6 mi) away from the epicenter, and at 0.3%g at 30-40 km (19-25 mi) away from the epicenter (Figure 3.8a). The peak velocities are ~0.16 cm/s at 10 km (6 mi) away from the epicenter, and ~0.04 cm/s at ~ 30 km (19 mi) (Figure 3.8b). Weak shaking associated with intensity II-IV (Wood and Neumann, 1931; U.S. Geological Survey, 1989) was recorded in the radius of 50 km (31 mi) (Figure 3.8c). For the second event, at ~10 km (~6 mi) from the epicenter, the peak acceleration was 2.1%g, and at ~50 km (~31 mi) 0.3%g (Figure 3.8d). The peak velocity of ~0.18 cm/s and 0.03 cm/s were observed at ~10 km (~6 mi) and ~50 km (~31 mi), respectively, from the epicenter (Figure 3.8e). The second event caused weak shaking (intensity II-IV) in the radius of 60 km (37 mi) (Figure 3.8f). The second event was felt widely in northeastern Washington, northern Idaho, and northwestern Montana (U.S. Geological Survey, 2015b). For the Sandpoint area, the USGS (U.S. Geological Survey, 2014) estimates two- and ten-percent probabilities of exceeding 20%g and 7%g, respectively, in 50 years of peak ground acceleration. From the standpoint of the size of ground motion, the Sandpoint events were well predicted.

Small (M1-3) aftershocks have followed the Sandpoint earthquakes. They exhibit a typical temporal aftershock distribution for approximately two weeks following the mainshocks (Figure 3.4b). Six additional small earthquakes through the end of June, 2015 indicate a somewhat elevated rate of seismicity compared to 1999 to 2014 levels (Figure 3.4). Figure 3.5 shows the spatial distribution of the aftershocks (U.S. Geological Survey, 2015c). Most of the aftershocks are located south of the Hope fault and east of the Purcell Trench fault, and eight aftershocks are concentrated within a three-kilometer radius of the epicenters area of the main shocks (Figure 3.6).

Fault Plane Solutions

We determined fault plane solutions for the three largest earthquakes using *P*-wave first motions from seismograph stations in Montana, Idaho, eastern Washington, and southern Canada. We used *P*-wave arrival times recorded at stations within 450 km (280 mi) of the epicenter and the western Montana crustal velocity model (Zeiler and others, 2005) together with HYPO71PC (Lee and Valdes, 1985) to determine earthquake hypocenters. The Newport, Washington, seismograph station (NEW; Figure 3.7) is the closest station to the epicenters at a distance of approximately 60 km (37 mi). The computed hypocenter depths range from about 10 to 14 km (6 to 9 mi) but are poorly constrained due to the lack of nearby seismograph stations. The fault plane solutions are presented in Table 3.2 and Figure 3.9 in lower hemisphere, equal-area projection. Moment tensor solutions of the first and second events reported by the USGS are also presented in Figure 3.10 for comparison.

Table 3.2. Fault plane solution of the Sandpoint earthquakes.

Event	Strike	Dip	Rake	Uncertainties (90% confidence range)			Number of first motion observations
				Strike	Dip	Rake	
1	42	28	66	8	8	15	54
2	50	35	80	18	5	20	43
3	80	50	100	3	0	10	22

The focal mechanism of the first event (Figure 3.9a; Table 3.2) indicates an oblique reverse motion with northeast striking nodal planes. The mechanism has a well-constrained southeast dipping nodal plane with a strike of 42 ± 8° and dip of 28 ± 8°. The other nodal plane strikes at 249° and dips at 65° to the north-northwest although this plane is not as well constrained as the first one. The tension axis is at a trend of 182° and a plunge of 68°, and the compressional axis at a trend of 330° and a plunge of 19°. Assuming the northeast striking plane represents the fault plane, the rake is 66° indicating a sinistral component. This lateral component is well constrained by stations located to the west-southwest of the hypocenter (i.e., DAVN, EPH, OD2, and WOLL; Figure 3.9a).

The fault plane solution of the second event is consistent with that of the first event (Figure 3.9b; Table 3.2). The northeast striking nodal plane strikes at 50 ± 18° and dips at 35 ± 5°. The other plane strikes at 242° and dips at 56°. The tension axis trends at 177° and plunges at 78°, and the compressional axis is at a trend of 327° and plunge of 10°. The second event also has a small lateral component; the rake on the northeast striking plane is 80°. This oblique slip is constrained by the reading of a station, DAVN (Figure 3.9b).

The third event also has a slightly oblique reverse mechanism consistent with the first event (Figure 3.9c; Table 3.2). The strike, dip, and rake of the northeast striking plane are 80 ± 3°, 50 ± 0°, and 100°, respectively. The other plane strikes at 245° and dips at 42°.

The tension axis orients at a trend of 43° and a plunge of 81°, and the compressional axis orients at a trend of 163° and a plunge of 5°.

Figure 3.10 and Table 3.3 present moment tensor solutions of the first two events reported by the USGS. The first event has a large discrepancy between our fault plane solution and the moment tensor solution by the USGS (2015a) (Figures 3.9a and 3.10a). The USGS' solution shows an oblique normal sense of motion with a north striking plane and an east-southeast striking plane (Figure 3.10a) (U.S. Geological Survey, 2015a) while our fault plane solution indicates a reverse motion with a northeast striking plane and west-southwest striking plane (Figure 3.9a). The USGS' moment tensor solution of the first event is also discrepant with that of the second event (Figure 3.10b) (U.S. Geological Survey, 2015b) although our *P*-wave first motion readings for both first and second events are very similar (Figures 3.9ab). The comparisons make the moment tensor solution of the first event questionable. The large discrepancy may have resulted from the nature of the determination method of moment tensor solutions. Moment tensor solutions are obtained by analyzing low-frequency signals (i.e., period of tens to hundreds of seconds) of a waveform. If an earthquake is M~4 or smaller as in the case of the Sandpoint event, significant low frequency signals are not produced, which makes its moment tensor solution unreliable.

Table 3.3 Source parameters of the Sandpoint earthquakes determined by the U.S. Geological Survey (2015ab).

Event	Seismic moment ($\times 10^{14}$ Nm)	Magnitude	Depth (km)	Double Couple (%)	Strike	Dip	Rake
1	4.501	3.70	18.0	60	353	63	-45
2	7.597	3.85	20.0	37	251	84	113

Table 3.3 (continued)

Event	T axis			N axis			P axis		
	Value	Plunge	Azimuth	Value	Plunge	Azimuth	Value	Plunge	Azimuth
1	3.931	8	53	0.979	39	149	-4.910	50	314
2	5.868	46	184	2.714	23	68	-8.581	35	320

Tectonic Implications

From the hypocenter locations of the earthquake sequence, it is probable that the events occurred either on the Hope fault or on the Purcell Trench fault (Figure 3.11a). None of the nodal planes of the sequence that generally strike northeast-southwest agree with the attitude of the southeast striking Hope fault. The well-defined nodal planes of the first and second events that strike at 42° and 50°, respectively, are in agreement with the strike of the closest segments of the Purcell Trench fault (Figure 3.11a). The listric nature of the Purcell Trench fault (Reynolds, 1980; Rehrig and others, 1987; Doughty and Price, 1999, 2000) is also consistent with the shallow dip of the nodal planes at about 30°. Figure 3.11b shows a schematic cross section and the proposed mechanism of the first event, which is the best constrained, of the Sandpoint sequence with a rotated fault plane solution projected on the cross sectional plane. The cross section is perpendicular to the surface trace of the closest segment of the Purcell Trench fault. The reverse mechanism on the Purcell Trench fault may represent a reactivation of the normal fault as a result of compression. Although the closest segment of the western 'limb' of the Newport fault has a similar strike (10-30°) to the well-constrained nodal plane, its dipping to the west does not agree with the nodal plane (Figure 3.11). Similarly, it is unlikely for the Packsaddle and Cascade faults to have slipped to cause the Sandpoint earthquakes as they probably dip to the northwest even though they strike northeast-southwest (Figure 3.11).

It is tectonically reasonable to expect contractional deformation in the Sandpoint area. A recent GPS velocity field presented by McCaffrey and others (2013) in Figure 3.12 shows a large-scale clockwise crustal rotation in the northwestern United States relative to stable North America. The pole of rotation is in central Idaho. The trailing edge of the whole rotating region is located around Yellowstone and the Wasatch Front in Utah, and the leading edge is diffuse in southeastern Washington. Kinematic block modeling by McCaffrey and others (2013) suggests that most compression around the leading edge is accommodated in the Yakima fold-thrust belt (YFTB) ranging from southeastern Washington to northeastern Oregon (Figure 3.12) (Reidel and others, 2003). It is possible that the residual compression is accommodated in a broader region including the epicentral area to the northeast of the YFTB (Figure 3.12).

Past natural seismicity in the region indicates contractional deformation. The 1994 Hoyt Mountain earthquake, which occurred about 95 km (59 mi) south-southeast of the Sandpoint earthquakes, has a reverse mechanism on a northwest-southeast striking nodal plane (Figure 3.12) (Sprenke and others, 1994). The earthquake was followed by a M2.9 aftershock identical to the mainshock in location and focal mechanism (Sprenke and others, 1994). In 2001, a total of 105 shallow small magnitude earthquakes occurred in the Spokane area (Wicks and others, 2013). The station distribution of the nearby seismic network was not optimal to determine the location and mechanism of those small events. Wicks and others (2013) modeled a previously unknown blind fault and a collective slip direction indicated by the earthquake swarm, using InSAR data showing a pattern of surface deformation. The best fit model in the InSAR study suggests oblique thrusting on the fault that strikes northeast-southwest and dips at ~30° to the northwest (Wicks and others, 2013).

The modeled fault plane and slip direction is shown in Figure 3.12 as a focal mechanism plot. Figure 3.13 shows T-axes of the Sandpoint earthquakes and the adjacent events including the 2001 Spokane. The T-axis plot indicates that the adjacent dextral slip events, the 1988 NE Mullan and 2014 Moose Peak events, are not kinematically compatible with the three earthquake sequences that indicate contractional deformation, the 1994 Hoyt Mountain, the 2001 Spokane, and the Sandpoint earthquakes (Figure 3.13). Therefore, the Sandpoint earthquakes, along with the Hoyt Mountain events and the Spokane swarm, constrain the western extent of the northeast-southwest extension of the LCFZ to the Idaho-Montana border area (Figure 3.12).

It is also probable that the epicentral area is compressed by localized crustal deformation. Figure 3.14 shows a distribution of dilatational strain derived from the GPS horizontal velocities (McCaffrey and others, 2007, 2013). If the velocity field is controlled mainly by localized crustal deformation, the Sandpoint area is compressed as indicated by weak contraction (i.e., negative dilatation of ~5-10 nanostrain/year) although it is poorly constrained (i.e., there is only one GPS site in the northeast of the area; Figure 3.13). Assuming that the slip of the Sandpoint events is in the order of meters, and that shortening rate in the area is in the order of millimeters per year, the order of the recurrence interval of the same type of earthquake on the same fault segment is thousands of years. The same type of earthquake, possibly M~5, can occur on a different segment of the Purcell Trench fault at any point in future; note that the 1942 M~5 event occurred in the Sandpoint area (Sprenke and Breckenridge, 1992) although its exact location is unknown. Since the general strike of the Purcell Trench fault is north-south (Figure 3.2), it is vital to have seismic stations in the Idaho Panhandle to determine what segment of the fault future earthquakes occur on.

Conclusions

The largest first two events of the Sandpoint earthquake sequence on April 24th, 2015, have a focal mechanism indicative of an oblique reverse motion with a well-defined northeast striking nodal plane and a southwest striking nodal plane. The attitude of the well-constrained nodal plane well corresponds to the northeast striking, listric normal Purcell Trench fault. The events are likely to represent a reactivation of the Purcell Trench fault in a reverse sense as a result of regional compression. A regional velocity field and strain analysis suggest that the epicentral Sandpoint area is in a zone of weak contraction, which may be responsible for the reverse mechanism of the events. The earthquake sequences indicating reverse sense of motions in the region, the 1994 Hoyt Mountain, the 2001 Spokane, and the Sandpoint events, possibly mark the western extent of the northeast-southwest extension of the LCFZ. Seismic stations in northern Idaho would contribute to a better constraint on earthquake locations and enhance seismic predictions in the region.

Acknowledgements

We thank Russell Burmester and Reed Lewis for providing us with valuable comments on northern Idaho geology. Reed Lewis and Ed Ratchford reviewed the final manuscript. The use of seismic data recorded by the NIOSH Spokane Mining Research Division, the University of Washington, the University of Utah Seismograph Stations, the Idaho National Labs, the US Geological Survey, and the Canadian Geological Survey is gratefully acknowledged. The maps were produced using the Generic Mapping Tools (GMT) software, and the tension axes plot was produced using Stereonet 9.

References

Anderson, A.L., 1930, Geology and ore deposits of the Clark Fork district, Idaho: Idaho Bureau of Mines and Geology Bulletin 12, 152p.

Bayley, R.W., and W.R. Muehlberger, 1968, Basement rock map of the United States (exclusive of Alaska and Hawaii): U.S. Geological Survey Map, scale 1:2,500,000.

Calkins, F.C., 1909, A geological reconnaissance in northern Idaho and northwestern Montana, with notes on the economic geology: U.S. Geological Survey Bulletin 384, 112p.

Clark, S.H.B., 1973, Interpretation of a high-grade Precambrian terrane in northern Idaho: Geological Society of America Bulletin, v. 84, p. 1999-2004.

Coney, P.J., 1987, The regional tectonic setting and possible causes of Cenozoic extension in the North American Cordillera *in* M.P. Coward, J.F. Dewey, and P.L. Hancock, eds., Continental Extensional Tectonics: Geological Society Special Publication 28, p. 177-186.

Daly, R.A., 1906, The nomenclature of the North American Cordillera between the 47th and 53d parallels of latitude: The Geographical Journal, v. 27, p. 586-606.

Daly, R.A., 1912, Geology of the North American Cordillera at the forty-ninth parallel: Canada Geological Survey Memoir 38, 546p.

Doughty, P.T., 1995, Tectonic evolution of the Priest River complex and the age of basement gneisses: Constraints from geochronology and metamorphic thermobarometry: Queen's University Ph.D. dissertation, 408 p.

Doughty, P.T., and S.D. Sheriff, 1992, Paleomagnetic evidence for en echelon crustal extension and crustal rotations in western Montana and Idaho: Tectonics, v. 11, p. 663-671.

Doughty, P.T., and R.A. Price, 1999, Tectonic evolution of the Priest River complex, northern Idaho and Washington: A reappraisal of the Newport fault with new insights on metamorphic core complex formation: Tectonics, v. 18, p. 375-393.

Doughty, P.T., and R.A. Price, 2000, Geology of the Purcell Trench rift valley and Sandpoint Conglomerate: Eocene en echelon normal faulting and synrift sedimentation along the eastern flank of the Priest River metamorphic complex, northern Idaho: Geological Society of America Bulletin, v. 112, p. 1356-1374.

Eaton, J.P., 1992, Determination of amplitude and duration magnitudes and site residuals from short-period seismographs in northern California: Bulletin of the Seismological Society of America, v. 82, p. 533-579.

Foster, D.A., and C.M. Fanning, 1997, Geochronology of the northern Idaho batholith and the Bitterroot metamorphic core complex: Magmatism preceding and contemporaneous with extension: Geological Society of America Bulletin, v. 109, p. 379-394.

Fillipone, J.A., and A. Yin, 1994, Age and regional tectonic implications of Late Cretaceous thrusting and Eocene extension, Cabinet Mountains, northwest Montana and northern Idaho: Geological Society of America Bulletin, v. 106, p. 1017-1032.

Fillipone, J.A., A. Yin, T.M. Harrison, G. Gehrels, M. Smith, and J.C. Sample, 1995, Age and magnitude of dip-slip faulting deduced from differential cooling histories: An example from the Hope fault, northwest Montana: The Journal of Geology, v. 103, p. 199-211.

Foster, D.A., P.T. Doughty, T.J. Kalakay, C.M. Fanning, S. Coyner, W.C. Grice, and J. Vogl, 2007, Kinematics and timing of exhumation of metamorphic core complexes along the Lewis and Clark fault zone, northern Rocky Mountains, USA *in* S.M. Roeske, A.B. Till, D.A. Foster, and J.C. Sample, eds., Exhumation Associated with Continental Strike-Slip Fault Systems: Geological Society of America Special Paper 434, p. 207-232.

Freidline, R.A., R.B. Smith, and D.D. Blackwell, 1976, Seismicity and contemporary tectonics of the Helena, Montana area: Bulletin of Seismological Society of America, v. 66, p. 81-95.

Gesch, D.B., 2007, The National Elevation Dataset, *in* D. Maune, eds., Digital Elevation Model Technologies and Applications: The DEM Users Manual, 2nd Edition: Bethesda, Maryland, American Society for Photogrammetry and Remote Sensing, p. 99-118.

Gesch, D., M. Oimoen, S. Greenlee, C. Nelson, M. Steuck, and D. Tyler, 2002, The National Elevation Dataset: Photogrammetric Engineering and Remote Sensing, v. 68, p. 5-11.

Harms, T.A., 1982, The Newport fault. Low-angle normal faulting and Eocene extension, northeast Washington and northwest Idaho: Queen's University M.S. thesis, 157 pp.

Harms, T.A., and R.A. Price, 1992, The Newport fault: Eocene listric normal faulting, mylonitization, and crustal extension in northeast Washington and northwest Idaho: Geological Society of America Bulletin, v. 104, p. 745-761.

Harrison, J.E., and D.A. Jobin, 1963, Geology of the Clark Fork quadrangle Idaho-Montana: U.S. Geological Survey Bulletin 1141-K.

Harrison, J.E., and P.W. Schmidt, 1971, Geologic map of the Elmira quadrangle, Bonner County, Idaho: U.S. Geological Survey Geological Quadrangle Map GQ-953, scale 1:63,500.

Harrison, J.E., M.D. Kleinkopf, and J.D. Obradovich, 1972, Tectonic events at the intersection between the Hope fault and the Purcell Trench, northern Idaho: U.S. Geological Survey Professional Paper, v. 719, 24p.

Harrison, J.E., A.B. Griggs, and J.D. Wells, 1974, Tectonic features of the Precambrian Belt basin and their influence on post-Belt structures: U.S. Geological Survey Professional Paper, v. 866, 15p.

Harry, D.L., D.S. Sawyer, and W.P. Leeman, 1993, The mechanics of continental extension in western north America: Implications for the magmatic and structural evolution of the Great Basin: Earth and Planetary Science Letters, v. 117, p. 59-71.

Hyndman, D.W., D. Alt, and J.W. Sears, 1988, Post-Archean metamorphic and tectonic evolution of western Montana and northern Idaho *in* W.G. Ernst, eds., Metamorphism and Crustal Evolution of the Western United States, Rubey Volume VII, p. 332-361.

King, E.R., J.E. Harrison, and A.B. Griggs, 1970, Geologic implications of aeromagnetic data in the Pend Oreille area, Idaho and Montana: U.S. Geological Survey Professional Paper, v. 646-D, 17p.

Kirkham, V.R.D., and E.W. Ellis, 1926, Geology and ore deposits of Boundary County, Idaho: Idaho Bureau of Mines and Geology Bulletin 10, 78p.

Lee, W.H.K., and C.M. Valdes, 1985, HYPO71PC: A personal computer version of the HYPO71 earthquake location program: U.S. Geological Survey Open-file Report 85-749, 44 p.

Lewis, R.S., R.F. Burmester, M.D. McFadden, J.D. Kauffman, P.T. Doughty, W.L. Oakley, and T.P. Frost, 2005, Geologic map of the Headquarters 30 $\times$ 60 minute quadrangle, Idaho: Idaho Geological Survey Geologic Map, scale 1:100,000.

Lewis, R.S., R.F. Burmester, R.M. Breckenridge, S.E. Box, and M.D. McFaddan, 2006, Geologic map of the Sandpoint quadrangle, Bonner county, Idaho: Idaho Geological Survey Geologic Map, scale 1:24,000.

Lewis, R.S., R.F. Burmester, R.M. Breckenridge, M.D. McFaddan, and W.M. Phillips, 2008, Preliminary geologic map of the Sandpoint 30 x 60 minute quadrangle, Idaho and Montana, and the Idaho part of the Chewelah 30 x 60 minute quadrangle: Idaho Geological Survey Geologic Map, scale 1:100,000.

Livaccari, R.F., 1991, Role of crustal thickening and extensional collapse in the tectonic evolution of the Sevier-Laramide orogeny, western United States: Geology, v. 19, p. 1104-1107.

McCaffrey, R., A.I. Qamar, R.W. King, R. Wells, G. Khazaradze, C.A. Williams, C.W. Stevens, J.J. Vollick, and P.C. Zwick, 2007, Fault locking, block rotation and crustal deformation in the Pacific Northwest: Geophysical Journal International, v. 169, p. 1315–1340.

McCaffrey, R., R.W. King, S.J. Payne, and M. Lancaster, 2013, Active tectonics of northwestern U.S. inferred from GPS-derived surface velocities: Journal of Geophysical Research: Solid Earth, v. 118, p. 709-723.

Miller, F.K., and J.C. Engels, 1975, Distribution and trends of discordant ages of the plutonic rocks of northeastern Washington and northern Idaho: Geological Society of America Bulletin, v. 86, p. 517-528.

Northern California Earthquake Data Center, 2015, UC Berkeley Seismological Laboratory. Dataset. Available at: http://www.ncedc.org (accessed 1 August 2015).

Park, C.F., Jr., and R.S. Cannon Jr., 1943, Geology and ore deposits of the Metaline quadrangle, Washington: U.S. Geological Survey Professional Paper v. 202, 81 p.

Qamar, A.I., J. Kogan, and M.C. Stickney, 1982, Tectonics and recent seismicity near Flathead Lake, Montana: Bulletin of Seismological Society of America, v. 72, p. 1591-1599.

Rehrig, W.A., S.J. Reynolds, and R.L. Armstrong, 1987, A tectonic and geochronologic overview of the Priest River crystalline complex, northeastern Washington and northern Idaho in J.E. Schuster, eds., Selected Papers on the Geology of Washington: Washington Division of Geology and Earth Resources Bulletin 77, p. 1-14.

Reidel, S.P., B.S. Martin, H.L. Petcovic, 2003, The Columbia River flood basalts and the Yakima fold belt: Geological Society of America Field Guide 4, p. 87-105.

Reynolds, M.W., 1979, Character and extent of Basin-Range faulting, western Montana and east-central Idaho *in* G.W. Newman and H.D. Goode, eds., Basin and Range Symposium and Great Basin Field Conference: Denver, Colorado, Rocky Mountain Association of Geologists and Utah Geological Association, p. 185-193.

Reynolds, S.J., 1980, The Selkirk crystalline complex *in* P.J. Coney and S.J. Reynolds, eds., Cordilleran metamorphic core complexes and their uranium favorability: U.S. Department of Energy, p. 523-531.

Sbar, M.L., M. Barazangi, J. Dorman, C.H. Scholz, and R.B. Smith, 1972, Tectonics of the Intermountain Seismic Belt, western United States: Microearthquake seismicity and composite fault plane solutions: Geological Society of America Bulletin, v. 83, p. 13-28.

Sears, J.W., and W.J. Fritz, 1998, Cenozoic tilt domains in southwestern Montana: Interference among three generations of extensional fault systems *in* J.E. Faulds and J.H. Stewart, eds., Accommodation Zones and Transfer Zones: The Regional Segmentation of the Basin and Range Province: Geological Society of America Special Paper 323, p. 214-247.

Sears, J.W., M. Hendrix, A. Waddell, B. Webb, B. Nixon, T. King, E. Roberts, and R. Lerman, 2000, Structural and stratigraphic evolution of the Rocky Mountain foreland basin in central-western Montana *in* S. Roberts and D. Winston, eds., Geologic Field Trips, Western Montana and adjacent Areas: Rocky Mountain Section of the Geological Society of America, p. 131-155.

Sears, J.W., and M.S. Hendrix, 2004, Lewis and Clark line and the rotational origin of the Alberta and Helena salients, North American Cordillera *in* A.J. Sussman and A.B. Weil, eds., Orogenic Curvature: Integrating Paleomagnetic and Structural Analysis: Geological Society of America Special Paper 383, p. 173-186.

Smith, J.G., 1965, Fundamental transcurrent faulting in Northern Rocky Mountains: Bulletin of the American Association of Petroleum Geologists: v. 49, p. 1398-1409.

Sonder, L.J., P.C. England, B. Wernicke, and R.L. Christiansen, 1987, A physical model for Cenozoic extension of western North America *in* M.P. Coward, J.F. Dewey, and P.L. Hancock, eds., Continental Extensional Tectonics: Geological Society Special Publication 28, p. 187-201.

Sprenke, K.F., and R.M. Breckenridge, 1992, Seismic intensities in Idaho: Idaho Geological Survey Information Circular 50, 36p.

Sprenke, K.F., M.C. Stickney, D.A. Dodge, and W.R. Hammond, 1991, Seismicity and tectonic stress in the Coeur d'Alene mining district: Bulletin of the Seismological Society of America, v. 81, p. 1145-1156.

Sprenke, K.F., Stickney, M.C. and Breckenridge, R.M., 1994, The Hoyt Mountain earthquakes Shoshone County, Idaho March 7 and June 3, 1994: Idaho Geological Survey Staff Report 94-4, 20 p.

Stevenson, P.R., 1976, Microearthquakes at Flathead Lake, Montana: A study using automatic earthquake processing: Bulletin of Seismological Society of America, v. 66, p. 61-80.

Stickney, M.C., 1978, Seismicity and faulting of central western Montana: Northwest Geology, v. 7, 1-9.

Stickney, M.C., 1980, Seismicity and gravity studies of faulting in the Kalispell valley, northwestern Montana: University of Montana M.S. thesis, 82p.

Stickney, M.C., 2015, Seismicity within and adjacent to the eastern Lewis and Clark Line, west-central Montana: Northwest Geology, v. 44, p. 19-36.

Stickney, M.C., and M.J. Bartholomew, 1987, Seismicity and late Quaternary faulting of the northern Basin and Range Province, Montana and Idaho: Bulletin of the Seismological Society of America, v. 77, p. 1602-1625.

U.S. Geological Survey, 1989, The Severity of an Earthquake. U. S. Geological Survey General Interest Publication. U.S. GOVERNMENT PRINTING OFFICE: 1989-288-913.

U.S. Geological Survey, 2014, Seismic Hazard Lower 48 Maps and Data. Available at: http://earthquake.usgs.gov/hazards/products/conterminous (accessed 20 July 2015).

U.S. Geological Survey, 2015a, M3.7 – 20 km SW of Sandpoint, Idaho. Available at: http://earthquake.usgs.gov/earthquakes/eventpage/us200028q3#general_summary (accessed 1 June 2015).

U.S. Geological Survey, 2015b, M3.9 – 12 km ESE of Sandpoint, Idaho. Available at: http://earthquake.usgs.gov/earthquakes/eventpage/us200028ri#general_summary (accessed 1 June 2015).

U.S. Geological Survey, 2015c, M3.3 – 15 km ESE of Sandpoint, Idaho. Available at: http://earthquake.usgs.gov/earthquakes/eventpage/us200028sf#general_summary (accessed 1 June 2015).

U.S. Geological Survey, 2015d, Search Earthquake Archives. Available at: http://earthquake.usgs.gov/earthquakes/search (accessed 1 August 2015).

Wallace, C.A., D.J. Lidke, and R.G. Schmidt, 1990, Faults of the central part of the Lewis and Clark line and fragmentation of the Late Cretaceous foreland basin in west-central Montana: Geological Society of America Bulletin, v. 102, p. 1021-1037.

Wernicke, B., R.L. Christiansen, P.C. England, and L.J. Sonder, 1987, Tectonomagmatic evolution of Cenozoic extension in the North American Cordillera, *in* M.P. Coward, J.F. Dewey, and P.L. Hancock, eds., Continental Extensional Tectonics: Geological Society Special Publication 28, p. 203-221.

Wicks, C., C. Weaver, P. Bodin, and B. Sherrod, 2013, InSAR evidence for an active shallow thrust fault beneath the city of Spokane Washington, USA: Journal of Geophysical Research: Solid Earth, v. 118, p. 1268-1276.

Winston, D., 1986, Middle Proterozoic tectonics of the Belt Basin, western Montana and northern Idaho *in* S.M. Roberts, eds., Belt Supergroup: A Guide to Proterozoic Rocks of Western Montana and Adjacent Areas: Montana Bureau of Mines and Geology Special Publication 94, p. 245-257.

Wood, H.O. and F. Neumann, 1931, Modified Mercalli intensity scale of 1931: Bulletin of the Seismological Society of America, v. 21, p. 277-283.

Worden, C.B., M.C. Gerstenberger, D.A. Rhoades, and D.J. Wald, 2012, Probabilistic relationships between ground-motion parameters and modified Mercalli intensity in California: Bulletin of the Seismological Society of America, v.102, p. 204-221.

Zeiler, C.P., M.C. Stickney, and M.A. Speece, 2005, Revised Velocity Structure of Western Montana: Bulletin of the Seismological Society of America, v. 95, p. 759-762.

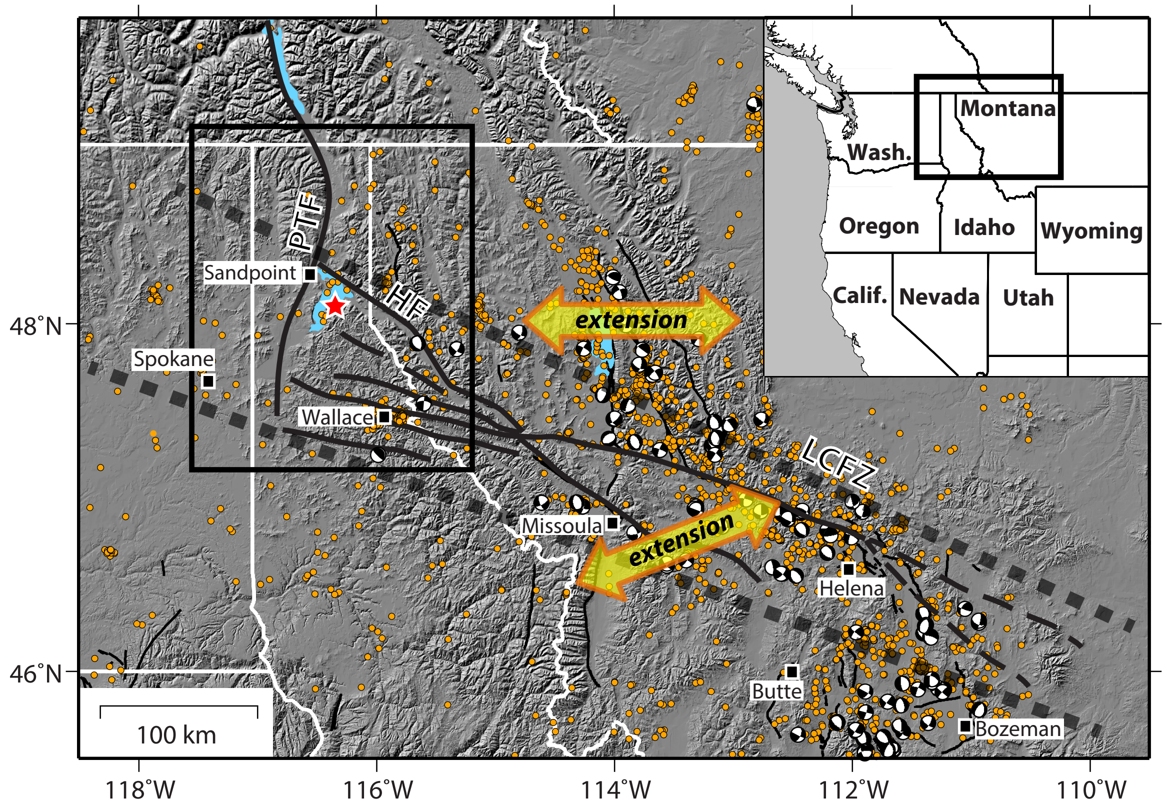

Figure 3.1. Regional tectonic setting and seismicity. Red star indicates the epicentral area of the 24 April 2015 Sandpoint sequence. Thick dark gray dotted lines bracket the Lewis Clark Fault Zone (LCFZ). Thick black lines represent the Purcell Trench fault (PFT) and the major faults in the LCFZ including the Hope fault (HF) (modified from Foster and others, 2007). Thin black lines represent Quaternary faults. Orange dots represent earthquake epicenters (M>1.5; 2000-2013), and focal mechanisms are for M>2.5 events (1982-2014) (M.C. Stickney, personal communication, 2013). Seismicity indicates east-west extension to the north of the LCFZ and northeast-southwest extension within and south of the central and eastern LCFZ (yellow arrows; Stickney, 2015). Box in main map outlines area of Figure 3.2. White lines indicate national and state boundaries. Elevation data from Gesch (2007) and Gesch and others (2002). Inset shows location of the map area.

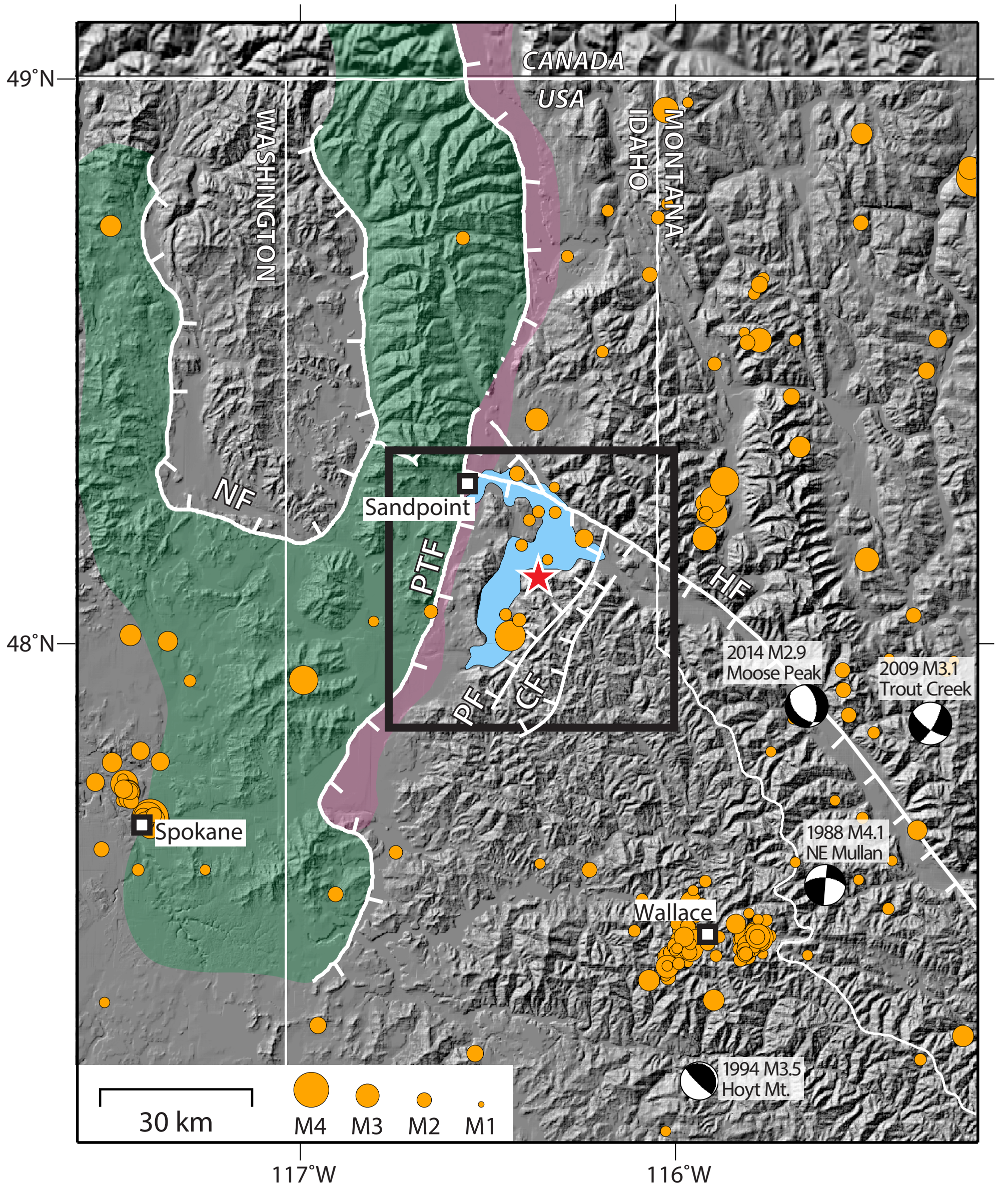

Figure 3.2. Tectonic map of eastern Washington, northern Idaho, and northwestern Montana showing major faults (modified from Doughty and Price 1999, 2000; Foster and others, 2007). See Figure 3.1 for location of the map area. Hachures on a fault trace indicate the down-thrown side of a normal fault. NF, Newport fault; PTF, Purcell Trench fault; HF, Hope fault; PF, Packsaddle fault; CF, Cascade fault. Dotted line represents an unfaulted segment of the Purcell Trench Fault (Doughty and Price, 1999, 2000). Red star indicates the epicentral area. Orange dots represent earthquake epicenters (M>1.5; 2000-2013; scaled by magnitude), and focal mechanisms are for major earthquakes around the epicenters (Sprenke et al., 1991, 1994; M.C. Stickney, personal communication, 2013). Green shaded area represents the Priest River metamorphic core complex, and pink shaded area represents the Purcell trench. Light blue area represents Lake Pend Oreille. Box outlines area for earthquake timelines in Figure 3.4.

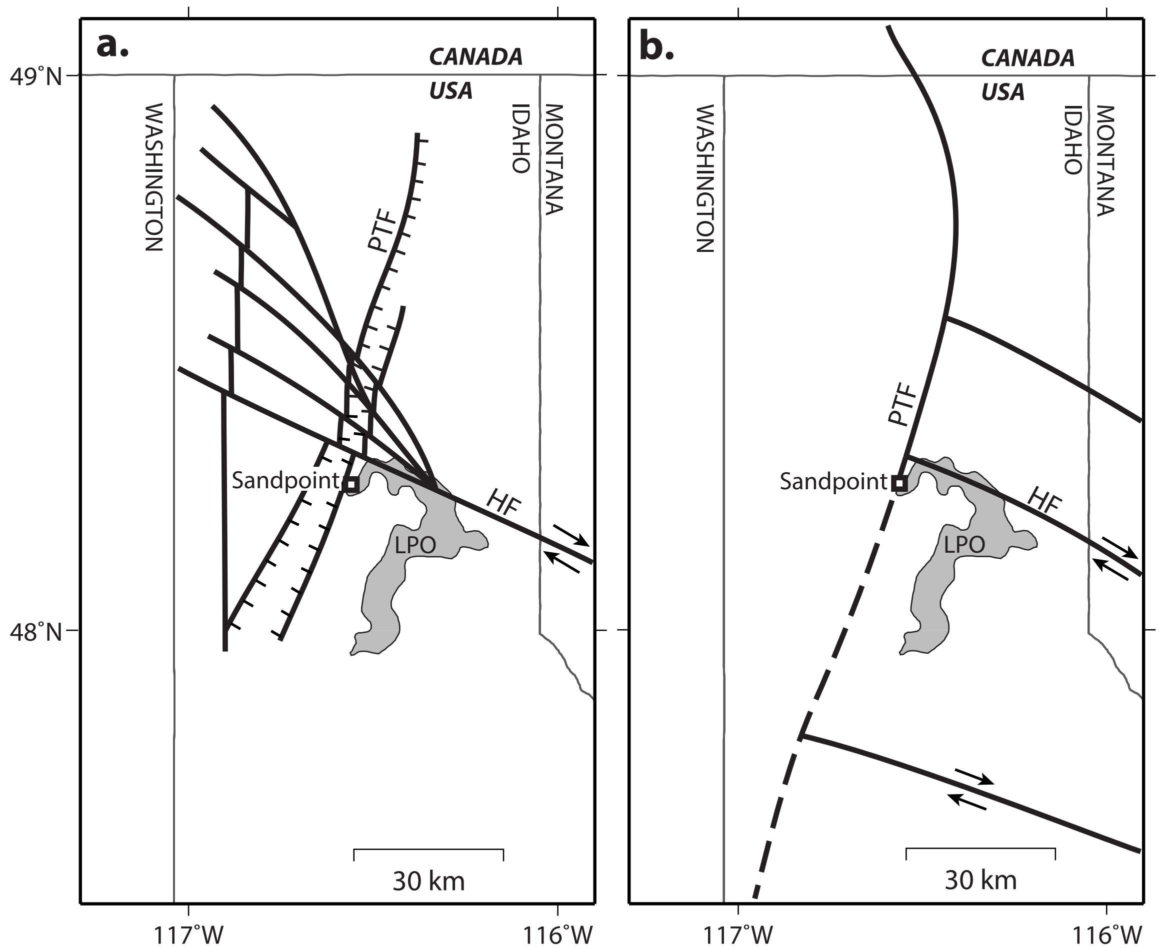

Figure 3.3. Simplified early interpretations of the relation between the Hope and Purcell Trench faults by (a) Harrison and others (1972) and (b) Clark (1973). PTF, Purcell Trench fault; HF, Hope fault; LPO, Lake Pend Oreille. Harrison and others (1972) show a full graben-style Purcell Trench faults that are cross-cut and offset by the Hope fault and its splayed segments. Clark (1973) shows the Hope fault system truncated against the Purcell Trench fault.

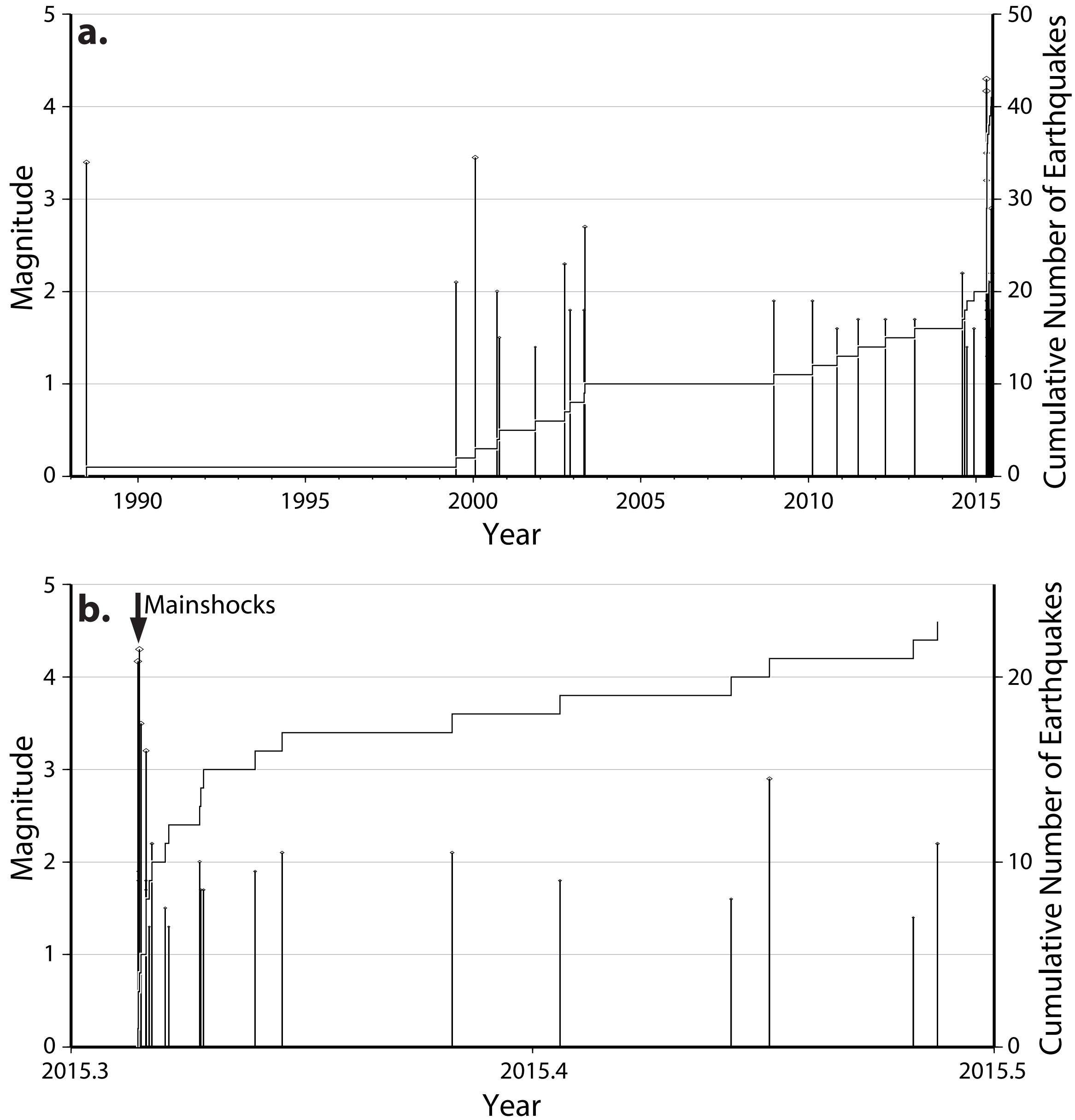

Figure 3.4. Timelines of instrumentally determined earthquakes in the Lake Pend Oreille area (lat 47.85° to 48.35°N. and long 116.00° to 116.75°W.; see Figure 3.2 for the area) (a) from 1988 through 2015, and (b) in 2015. Vertical bars topped by small diamonds (scaled to magnitude) indicate the date and magnitude of earthquakes (left scale). Stair-step curve indicates the cumulative number of earthquakes (right scale). Detection and location of earthquakes prior to 1996, when northwestern Montana stations began operating, is probably incomplete for M<2.5 events.

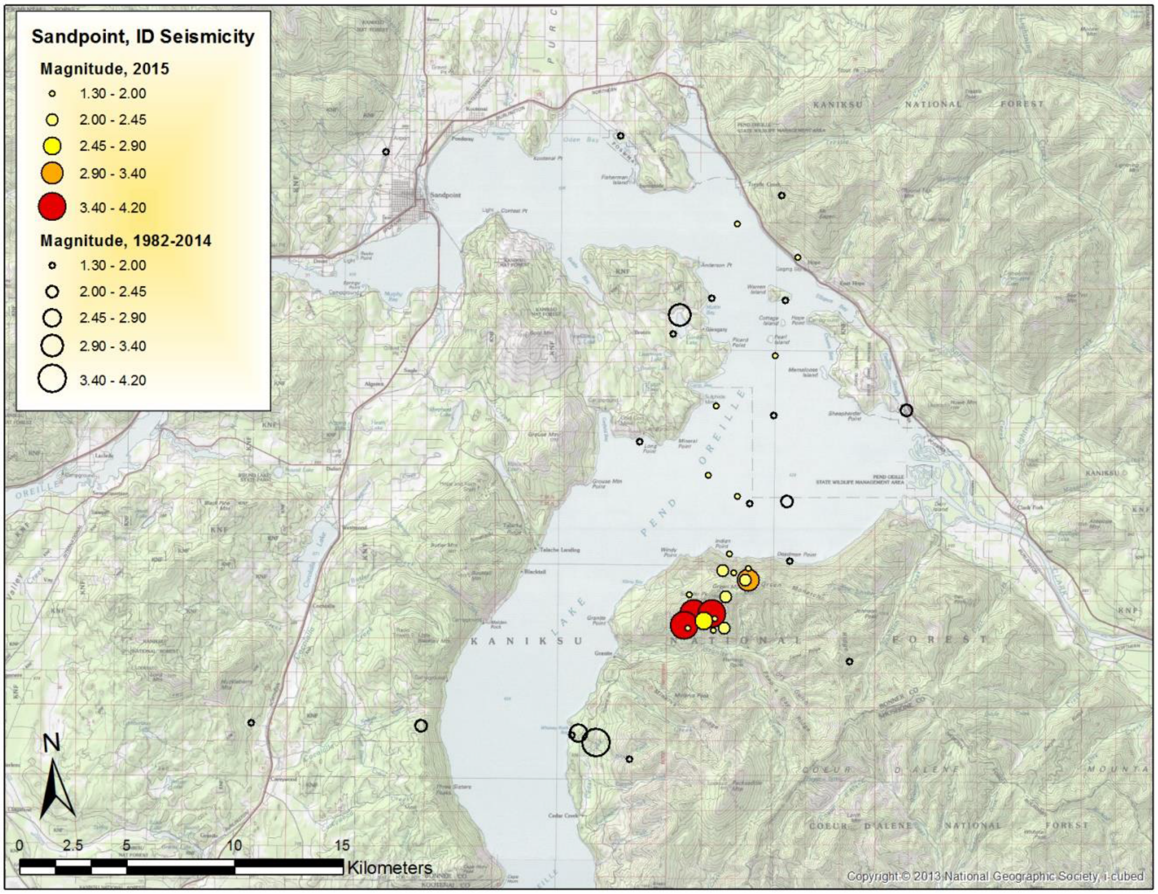

Figure 3.5. Spatial distribution of epicenters of events from 1982 through 2014 (open circles scaled by magnitude) and in 2015 (colored circles scaled by magnitude).

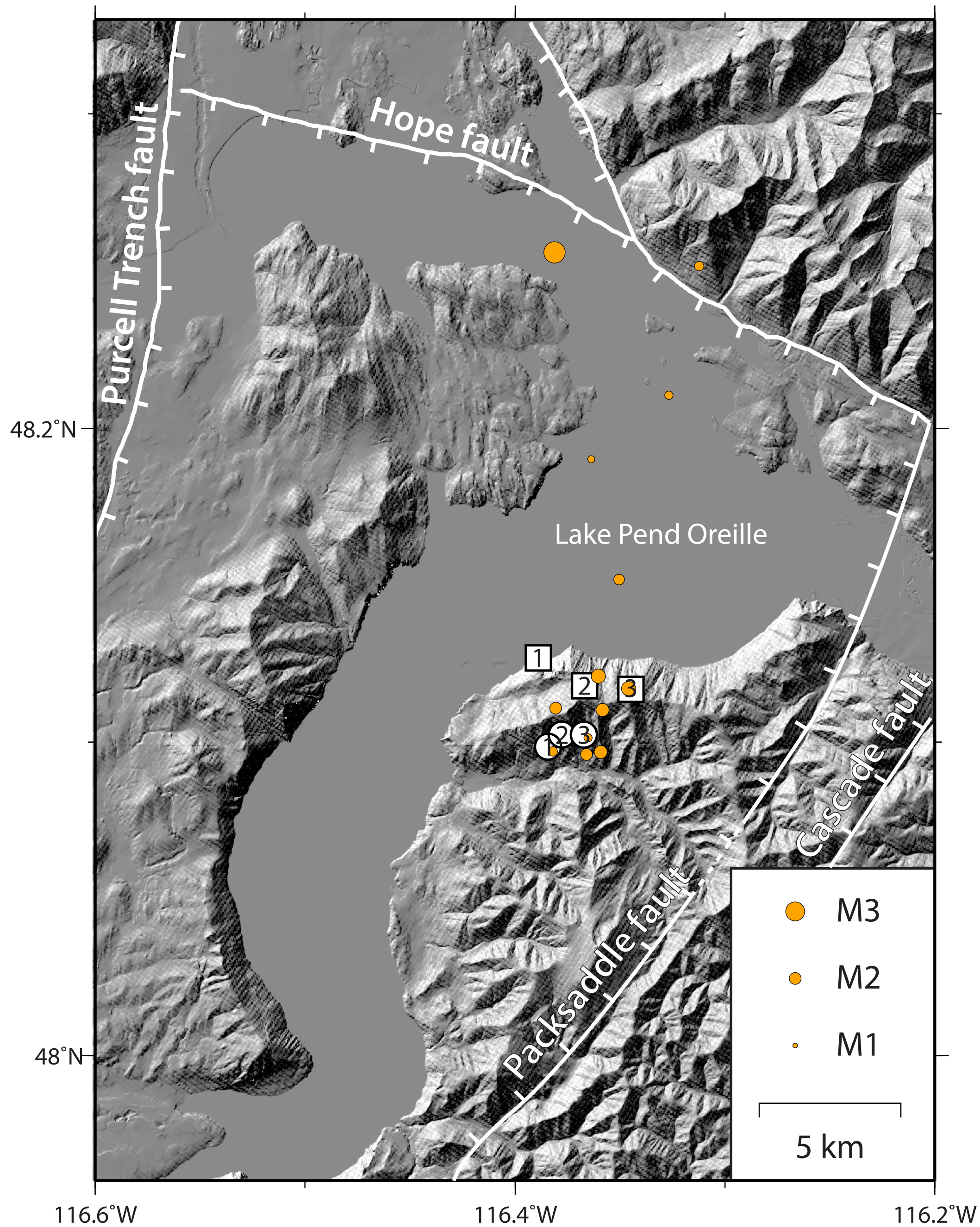

Figure 3.6. Epicenters of the Sandpoint earthquakes by this study (white circles) and the USGS (U.S. Geological Survey, 2015ab; white squares), and aftershocks during the first three months after the Sandpoint events (orange dots). Number in symbol represents the order of an event in the Sandpoint sequence.

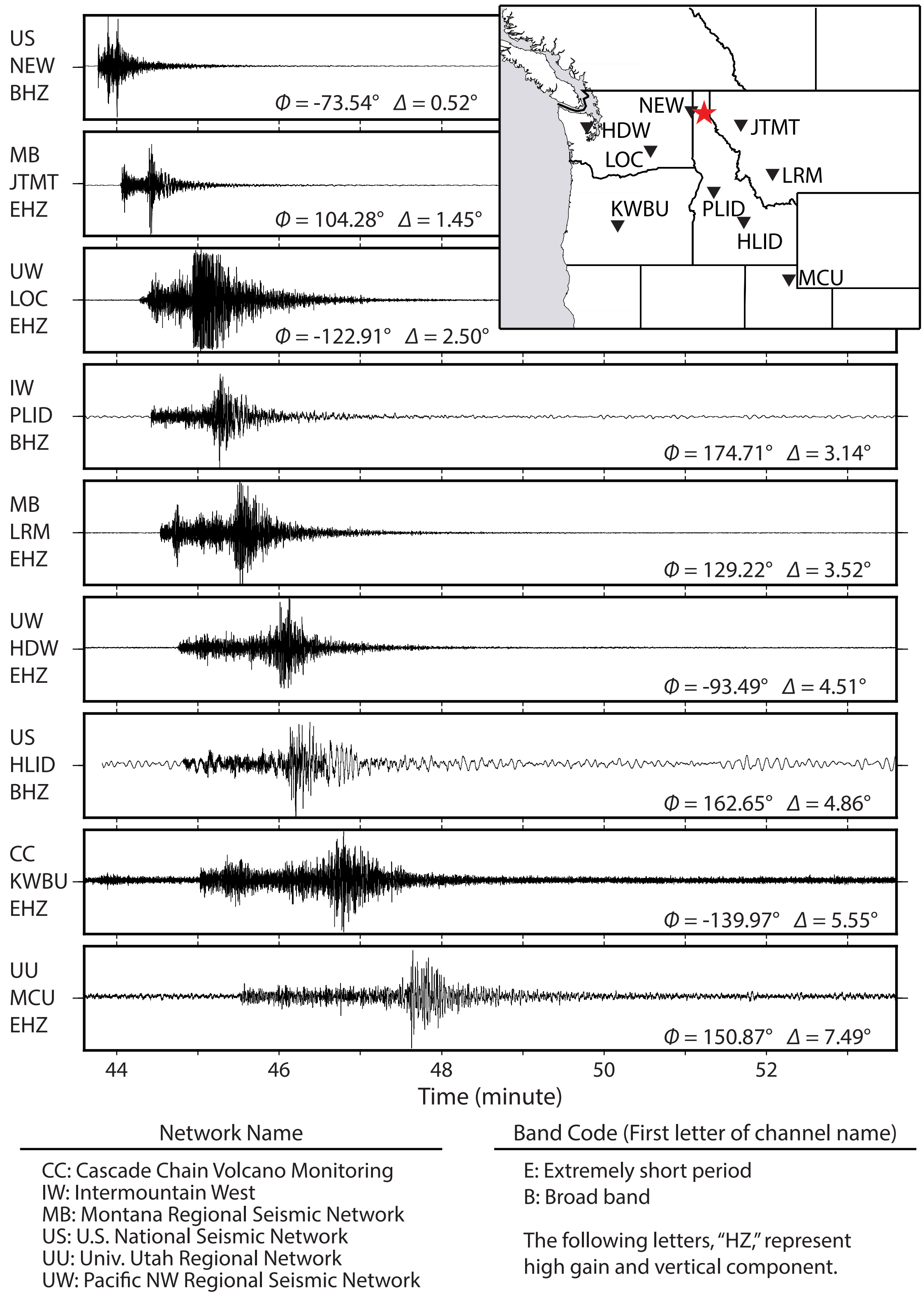
US
NEW
BHZ
Φ = -73.54° Δ = 0.52°
MB
JTMT
EHZ
Φ = 104.28° Δ = 1.45°
UW
LOC
EHZ
Φ = -122.91° Δ = 2.50°
IW
PLID
BHZ
Φ = 174.71° Δ = 3.14°
MB
LRM
EHZ
Φ = 129.22° Δ = 3.52°
UW
HDW
EHZ
Φ = -93.49° Δ = 4.51°
US
HLID
BHZ
Φ = 162.65° Δ = 4.86°
CC
KWBU
EHZ
Φ = -139.97° Δ = 5.55°
UU
MCU
EHZ
Φ = 150.87° Δ = 7.49°
NEW
HDW
LOC
JTMT
LRM
KWBU
PLID
HLID
MCU
44
46
48
50
52
Time (minute)
Network Name
CC: Cascade Chain Volcano Monitoring
IW: Intermountain West
MB: Montana Regional Seismic Network
US: U.S. National Seismic Network
UU: Univ. Utah Regional Network
UW: Pacific NW Regional Seismic Network
Band Code (First letter of channel name)
E: Extremely short period
B: Broad band
The following letters, "HZ," represent high gain and vertical component.

Figure 3.7

Figure 3.7. Seismograms of the second event of the Sandpoint sequence recorded at selected stations. All the seismograms are normalized vertical components. The origin of the time axis is the origin time of the second event at 05:43:36 (UTC). Network, station, and channel names are listed by the individual seismograms. Φ and Δ represent azimuth and distance, respectively. Inset shows the epicentral area (red star) and station locations (inverted triangles).

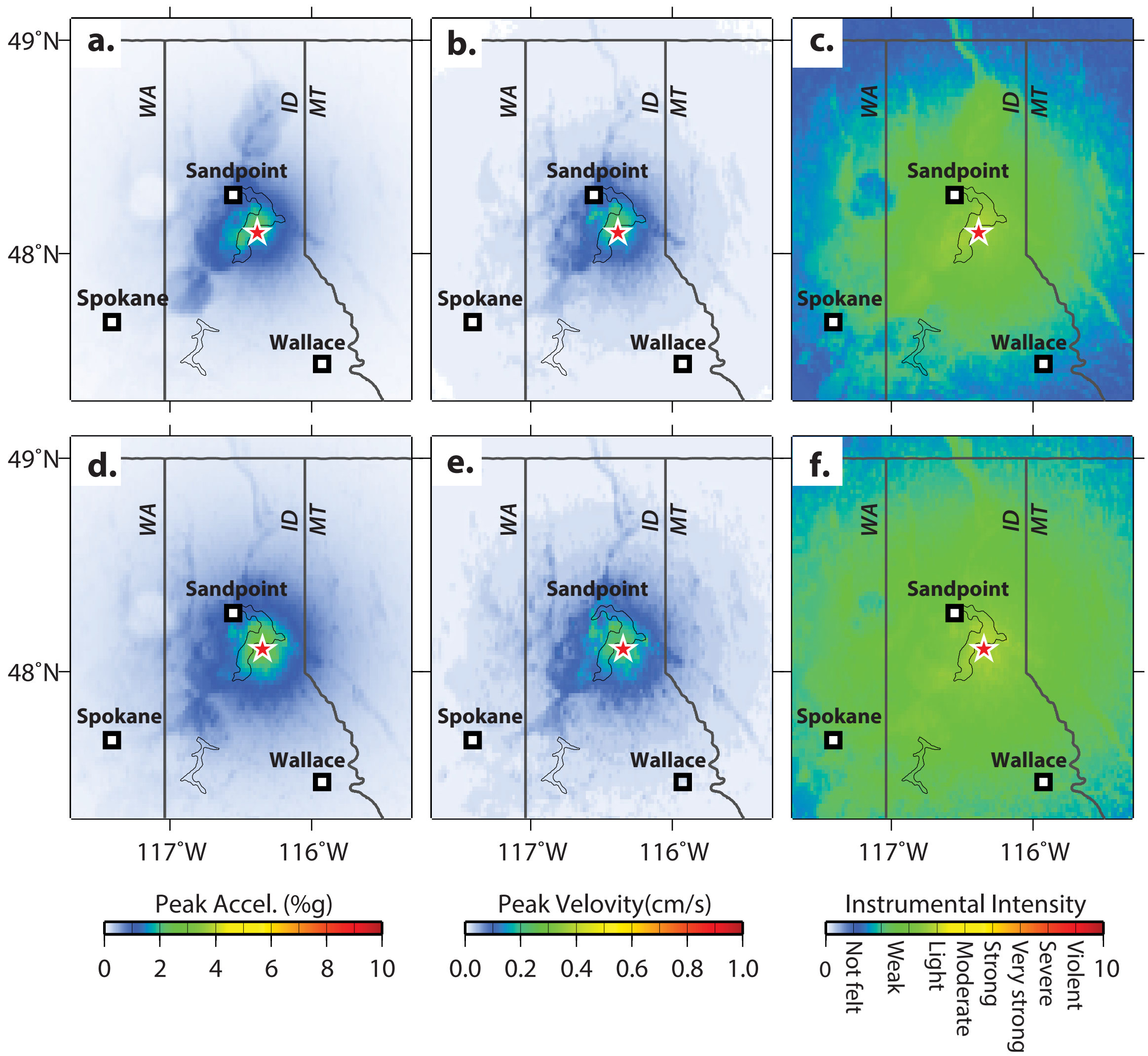

Figure 3.8. Recorded (a) peak acceleration, (b) peak velocity, and (c) instrumental intensity of the first event of the Sandpoint sequence, and (d-f) those of the second event. Data from the U.S. Geological Survey (2015a).

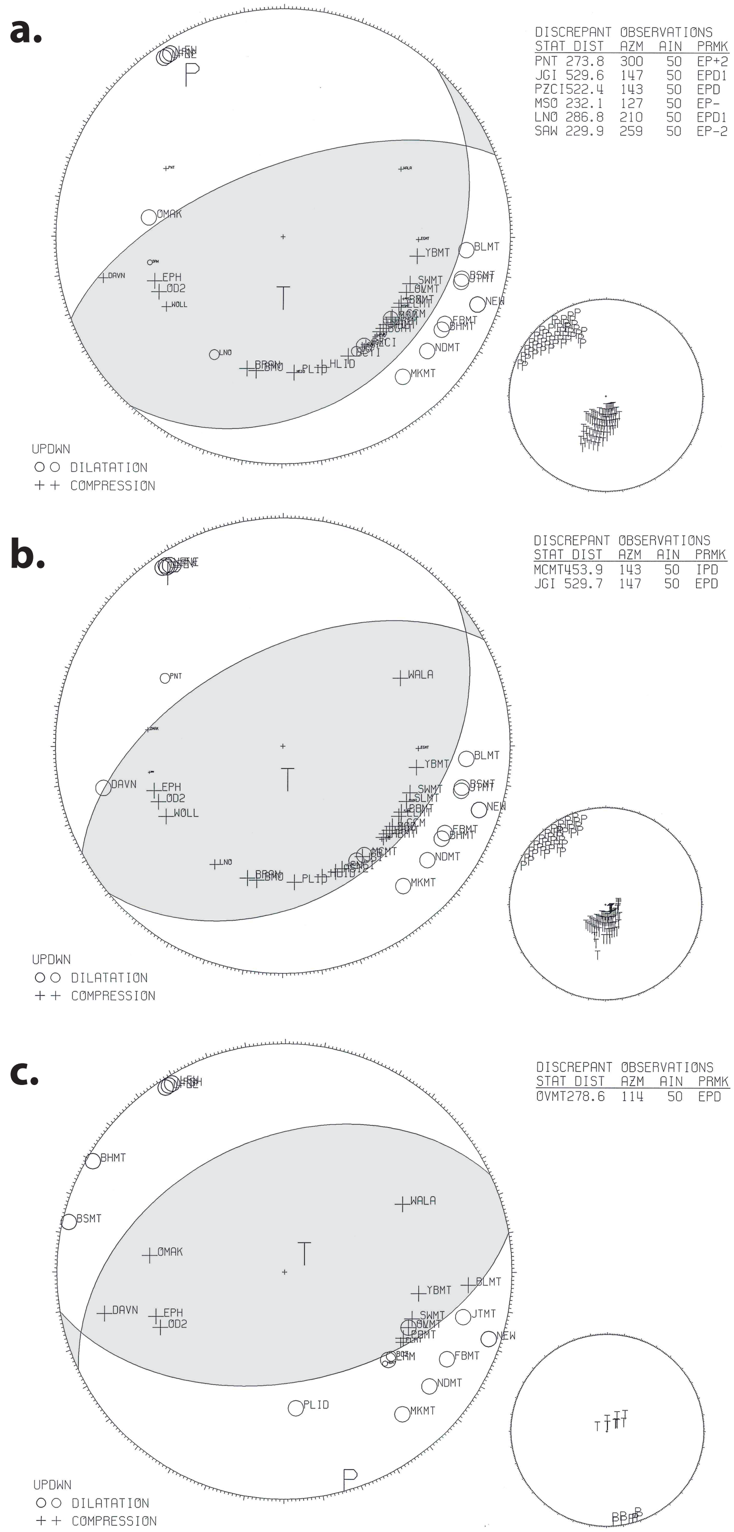

Figure 3.9. Fault plane solutions for the (a) first, (b) second, and (c) third events of the Sandpoint earthquakes. Symbols P and T mark the orientation of possible directions of the P and T axes, respectively, on an equal-area stereonet with lower hemisphere projection.

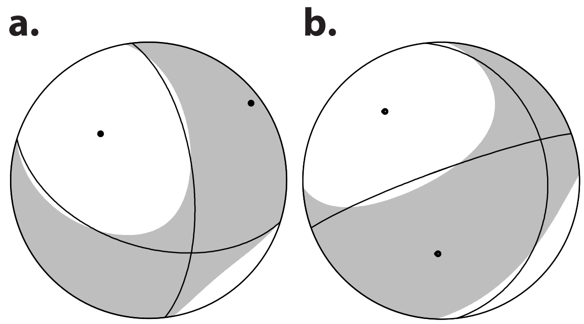

Figure 3.10. Moment tensor solutions for the (a) first and (b) second events of the Sandpoint earthquakes by the USGS (U.S. Geological Survey, 2015ab). Dots mark the orientation of possible directions of the P and T axes. The moment tensor solution of the first event has a large discrepancy with the fault plane solution (Figure 3.7a).

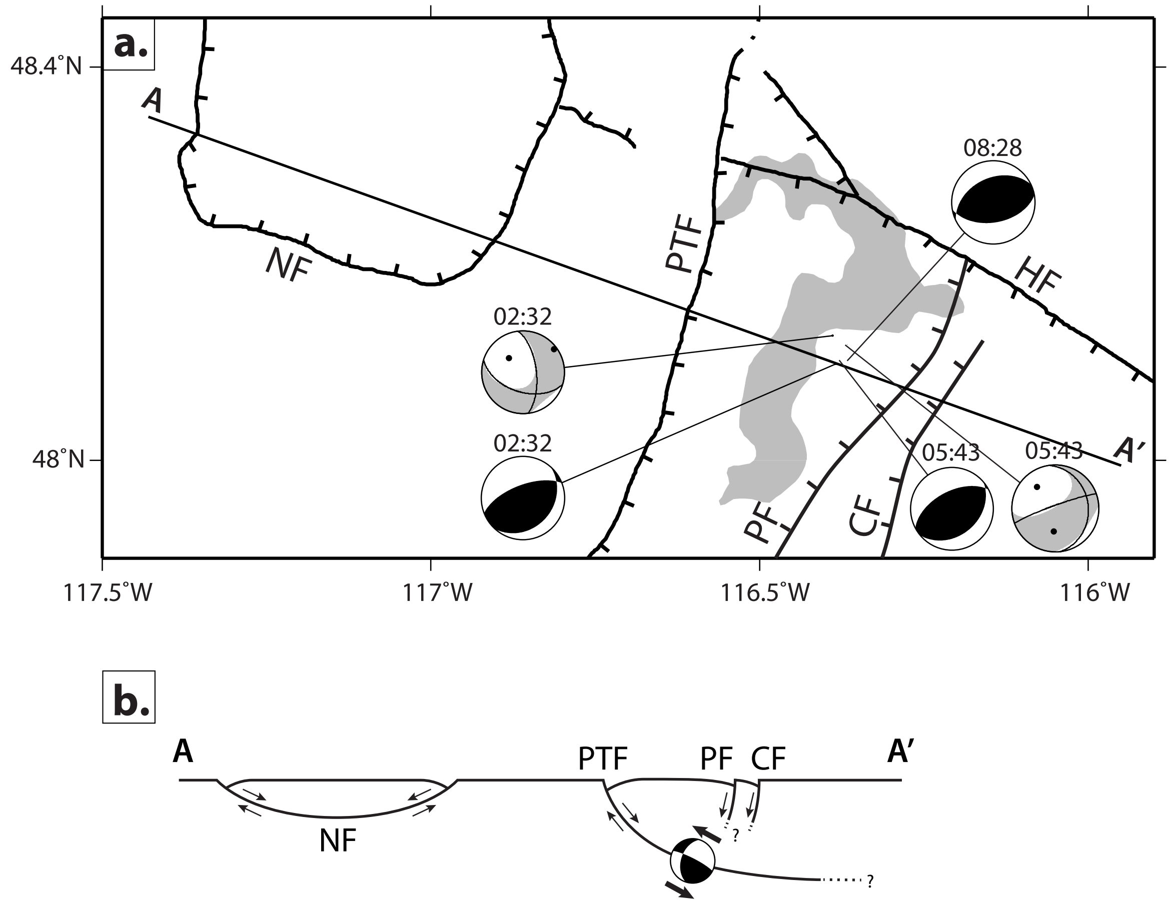

Figure 3.11. (a) Epicenters and focal mechanism solutions of the Sandpoint sequence by this study (black compressive quadrants) and the U.S. Geological Survey (2015ab; gray compressive quadrants), and fault distribution in the epicentral area. Origin time is shown on each focal mechanism. NF, Newport fault; PTF, Purcell Trench fault; HF, Hope fault; PF, Packsaddle fault; CF, Cascade fault. Line A-A′ indicates location of schematic cross section shown in Figure 9b. (b) Schematic cross section through the Newport and Purcell Trench Faults. The cross section is perpendicular to the surface trace of the Purcell Trench fault. Focal mechanism is for the fault plane solution of the first event of the Sandpoint sequence projected on the cross-sectional plane. The reverse mechanism (thick arrows) may represent a reactivation of the Purcell Trench fault.

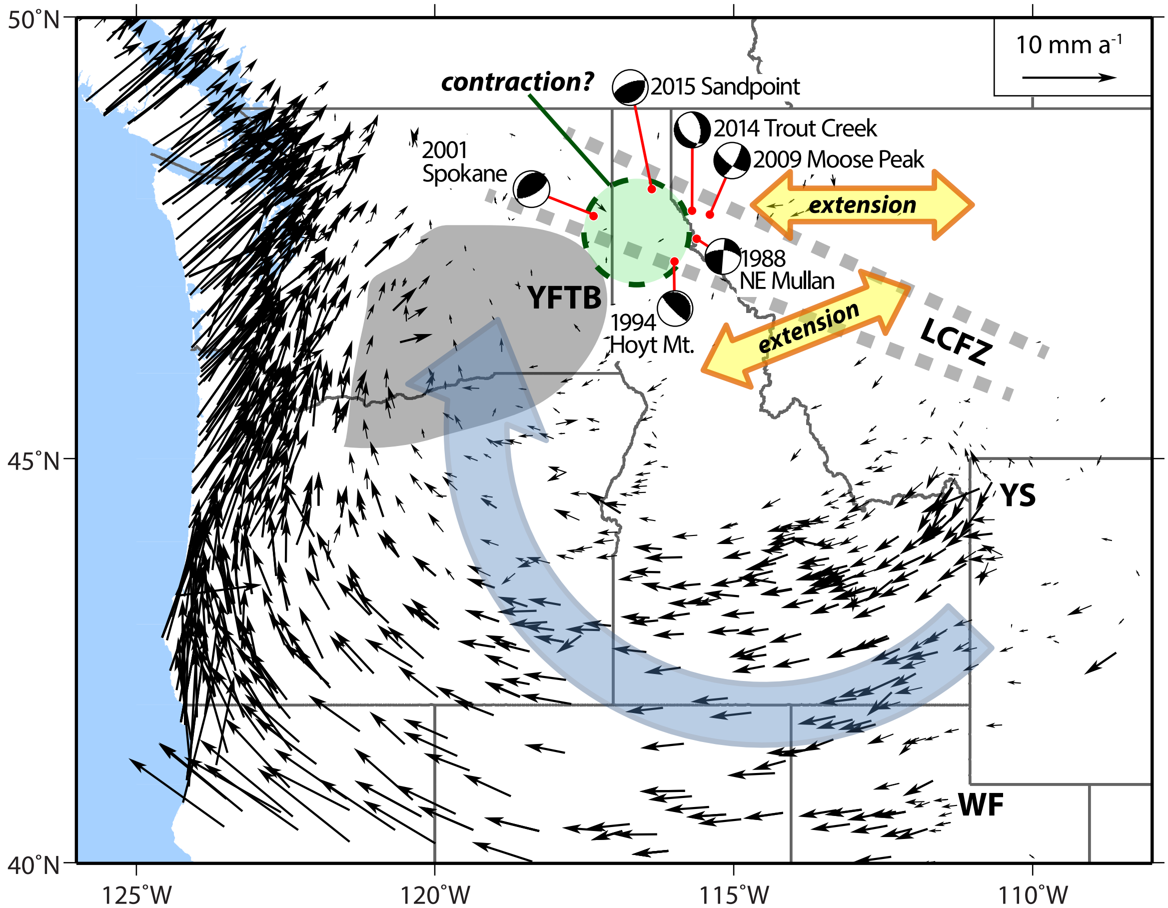

Figure 3.12. GPS velocity field of the northwestern U.S. (McCaffrey and others, 2007, 2013) showing a clockwise crustal rotation (blue arrow) relative to the North America. The leading edge of the rotating region is in the Yakima fold-thrust belt (YFTB; shaded area; Reidel and others, 2003), and the trailing edge is around Yellowstone (YS) and the Wasatch Front (WF). Extension directions indicated by seismicity (yellow arrows; Stickney, 2015). Dashed green circle indicates the area of possible contraction.

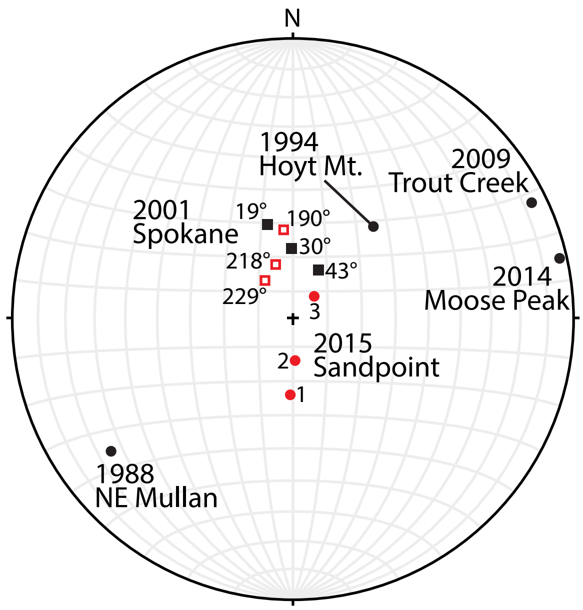

Figure 3.13. T-axes from fault plane solutions of the Sandpoint earthquakes (red dots) and the adjacent events (black dots; see Figure 12 for earthquake location), and from the best-fit (solid square) and alternate allowable (open square) models of the 2001 Spokane sequence (Wicks and others, 2013). Numbers by solid squares indicate a dip variation (minimum, best-fit, and maximum). Numbers by open squares indicate a strike variation (minimum, best-fit, and maximum) of the alternate allowable model. The dextral slip earthquakes, the 1988 NE Mullan and 2014 Moose Peak, and the normal-faulting 2009 Trout Creek event are not kinematically compatible with the three earthquake sequences that indicate contractional deformation.

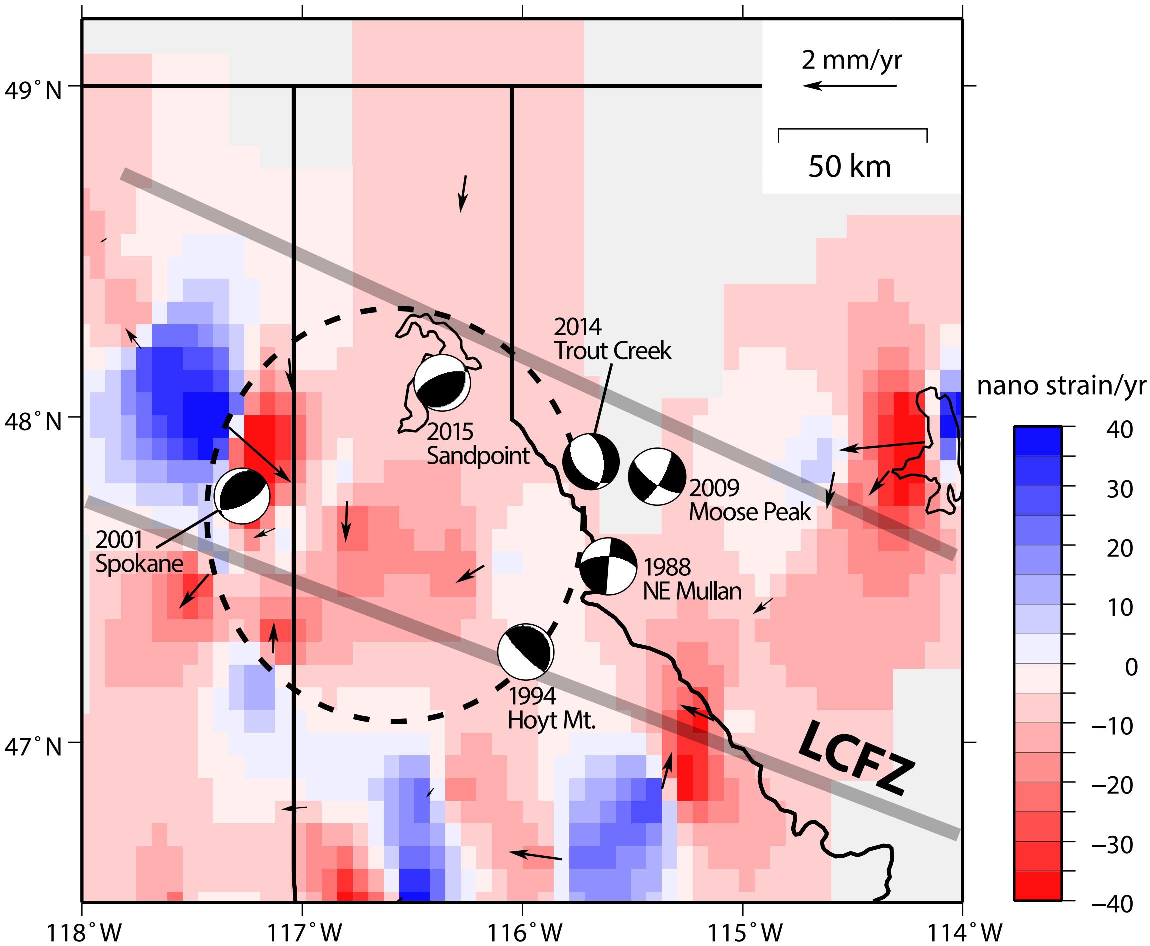

Figure 3.14. Dilatational strain rate (dilatation positive) calculated from GPS horizontal velocities. Thick gray lines bracket the LCFZ. Contractional strain (negative dilatation) is dominant in the proposed area of contraction (dashed circle) indicated by seismicity.

CHAPTER 4: ESTIMATE OF THE EFFECTIVE ELASTIC THICKNESS IN THE NORTHERN ROCKIES FROM FREE-AIR GRAVITY ADMITTANCE

> Mountains, mountain ranges, and valleys of magnitude equivalent to mountains exist generally in view of the rigidity of the Earth's crust; continents, continental plateaus, and oceanic basins exist in virtue of isostatic equilibrium in a crust heterogeneous as to density.
>
> –G. K. Gilbert, 1890, p. 25

Abstract

Estimates of effective elastic thickness (T_e) of the Northern Rockies are presented. This study is the first to estimate T_e in the area using the free-air admittance method. Through the T_e modeling, we investigate the effects from the upper mantle density anomalies on gravity and elevation measurements used in the T_e estimation. The best fit model is obtained by iterations varying T_e, as well as the fractions of loads at the surface and the Moho. The resultant estimate is compared with the distribution of the seismicity, the regional pattern of crustal deformation, and previous T_e estimates from the Bouguer coherence method.

The result predicts a general trend that the transition zone from small to large (>10 km) T_e coincides with the Intermountain Seismic Belt. The resultant T_e variation shows a moderately positive correlation with the area of positive gravity effect from the upper mantle, which may result from a crust strengthened by low temperature mantle and/or an overestimate of T_e due to the gravity effect. The spatial variation in T_e estimate largely agrees with the T_e map from the Bouguer coherence method. One discrepancy is that T_e from

the Bouguer coherence method is ~20-35 km in central Montana, while the free-air admittance method finds T_e in the area to be ~10-20 km. This discrepancy may be explained as a result from a T_e overestimation of the Bouguer coherence method that assumes that all loads are expressed on the surface. Our result indicates relatively large internal loads in the area, which may be due to large ultramafic to mafic intrusive bodies. Our T_e map shows a large T_e (~15-80 km) zone extending from south central Montana to northwestern Colorado, which correlates with the location of the thick and strong Wyoming craton. The T_e estimate is small (~3 km) in the area to the immediate west of the Western Idaho Suture Zone, which may suggest inherent crustal weakness due to the amalgamation of multiple terranes.

4.1 Introduction

Locality of crustal deformation and intraplate seismicity is likely to be controlled by the horizontal variation in lithospheric strength. Lithospheric strength is measured by the flexural rigidity, which is commonly represented by the effective elastic thickness (T_e). In the western U.S., significant extension is limited to areas of low T_e [*Lowry and Smith*, 1995]. In the Himalayas, shortening deformation fronts occur along the transitional zones of T_e on the higher strength side [*Lyon-Caen and Molnar*, 1983]. *Maggi et al.* [2000] suggested that thickness of a seismogenic layer is proportional to the T_e. The amount of shortening in orogenic belts appears to correlate with the age of the foreland lithosphere that is indicated by a T_e model [*Mouthereau et al.*, 2013].

In this study, we estimate continental T_e in and around the Northern Rockies (i.e., Idaho, western Montana, western Wyoming, northern Nevada, and northern Utah), using admittance between topography and free-air gravity anomaly. We also test gravity effects from the upper mantle heterogeneity on T_e estimates. The result is compared with the spatial distribution of the seismicity and the regional pattern of crustal deformation, as well as previous T_e estimates from the Bouguer coherence method.

4.1.1 Background

The concept of elastic thickness stems from studies on isostasy and flexure of lithosphere due to topographic loads. Seminal models of lithospheric isostasy were proposed in the middle 19th century by *Airy* [1855] and *Pratt* [1855]. In Airy's model, compensation is achieved by thickening a uniform density crust (Figure 4.1a) while Pratt's model assumes a constant compensation depth achieved by lateral changes in crustal density (Figure 4.1b). In both models, topographic loads, however small, are compensated without bending the surrounding crust, which is referred to as *local compensation*. In other words, these models disregard lithospheric strength that can prevent topographic features from being completely compensated by the Airy or Pratt models.

The local compensation models by Airy and Pratt (Figure 4.1ab) were favorably accepted by geodesists, including those at the U.S. Coast and Geodetic Survey (USCGS), at the turn of the 20th century because those models agreed with their geodetic observation [*Watts*, 2001]. As a result, it took decades and much research for *regional compensation* models, which involved the flexure caused by lithospheric strength (Figure 4.1c), to be established and widely accepted.

An American Geologist G. K. Gilbert argued that local topographic features needed to be considered in the light of crustal rigidity rather than isostasy based on his study on isostatic rebound in the vicinity of Lake Bonneville [*Gilbert*, 1889; 1890]. An Associate

Professor at Yale University J. Barrel extended Gilbert's study by reviewing evidence from various geologic features, such as mountain ranges, volcanic cones, erosion cycles, and river deltas. As a result of his studies, Barrel was convinced that Earth's crust was sufficiently strong to support some geologic loads [*Barrell*, 1914]. Unlike his colleagues at USCGS, a Geodesist G. R. Putnam advocated regional compensation. After analyzing the first extensive gravity measurements in the western U.S., Putnam concluded that the extent of a regional compensation corresponded to the crustal strength [*Putnam*, 1930]. The concepts of the regional compensation and crustal strength are well explained by the elastic plate models proposed by two coeval researchers, *H. Jeffreys* [1926] and *F. A. Vening Meinesz* [1931]. In the elastic plate models, a load bends the plate, causing a broader low-density root. The load is supported by both local isostasy and lithospheric strength. An American Physicist R. Gunn questioned the local compensation model from the aspect of vertical shear stress. In his view, a loaded column of crust drags down its adjacent columns through vertical shear stress because the columns are mechanically attached to each other (Figure 4.1c). Knowing that the regional compensation model was more realistic than the local models, Gunn examined the extent of regional compensation at various geological features, such as mountain ranges [*Gunn*, 1937], volcanic islands [*Gunn*, 1943a], and island arcs [*Gunn*, 1943b]. After the introduction of plate tectonics, R. I. Walcott considered the elastic plate model in light of the groundbreaking theory. *Walcott* [1970] showed vertical extent of mechanical strength, referred to as elastic thickness, of the lithosphere in the plate interiors.

Researchers have attempted various methods to estimate T_e of both oceanic and continental lithospheres since detailed gravity data became available. For oceanic lithosphere, T_e generally increases with the thermal age of the plate [*Watts*, 2001]. On the other hand, few systematic relationships between T_e and the lithosphere's thermal property have been suggested for continental lithosphere. As an alternative means, frequency spectral analyses of gravity and topography data have been attempted to estimate T_e. Two typical approaches are the admittance and coherence methods. The admittance is the amplitude ratio between an input function and its linear output function, in cases of estimating T_e, topography and gravity [e.g., *McKenzie and Bowin*, 1976]. It is a measure of how much gravity anomaly is caused by the surface topography (see section 4.2.1 for details). When the relationship between the input and output functions is non-linear, the coherent parts of the functions are compared. The ratio between the coherent parts is termed the coherence.

Spectral approaches to estimate continental T_e have undergone protracted debates and refinement since the 1970s (Table 4.1). *Lewis and Dorman* [1970; see also *Dorman and Lewis*, 1970] proposed a spectral analysis of Bouguer gravity anomaly and topography to explain isostatic responses to surface loads. They adopted the classic local compensation models of *Airy* [1855] and *Pratt* [1855] that assume no mechanical strength in the crust for vertical loads (Figure 4.1ab). In those models, any surface load, however small, produces local vertical movements in the crust to achieve isostasy. In order to address this unreality, subsequent studies [*McKenzie and Bowin*, 1976; *Banks et al.*, 1977; *McNutt and Parker*, 1978; *Cochran*, 1980] adopted the regional compensation model [*Barrel*, 1914; *Gunn*, 1943a], in which surface loads are partially supported by elastic stresses within the lithosphere (Figure 4.1c). To estimate T_e, those early studies used admittance between topography and Bouguer anomalies, assuming that the lithosphere is laterally homogeneous in density [*McKenzie and Bowin*, 1976; *Banks et al.*, 1977; *McNutt and Parker*, 1978; *Cochran*, 1980]. Those Bouguer admittance methods were used mainly for the estimation of oceanic T_e because the assumption of homogeneous lithosphere was acceptable for oceanic settings. For continental settings, the methods found relatively small values of T_e (10–20 km) even for cratons and shields [*Forsyth*, 1985] because the assumption disregarded internal loads, such as plutonic and metamorphic bodies. To overcome this issue, *Forsyth* [1985] proposed a method using coherence between Bouguer gravity and topography, taking the presence of internal loads into account. This method gave values of T_e as large as 130 km for cratons [e.g., *Zuber et al.*, 1989].

Table 4.1. List of spectral methods for isostatic analyses.

Method	Compensation Model	Reference
Bouguer admittance	Local	*Lewis and Dorman*, 1970
Bouguer admittance	Regional	*McKenzie and Bowin*, 1976
Bouguer coherence	Regional	*Forsyth*, 1985
Free-air admittance	Regional	*McKenzie and Fairhead*, 1997

Forsyth's method has been accepted and used by some researchers [e.g., *Zuber et al.*, 1989; *Ebinger et al.*, 1989]. *Lowry et al.* [2000] adopted the Bouguer coherence method to estimate T_e in the western U.S. In their estimate shown in Figure 4.2, a zone of high seismicity (i.e., the Intermountain Seismic Belt (ISB), for details see section 4.3.1) coincides with an area of high gradient in T_e from northwestern Montana to southwestern Utah. T_e is relatively thin (3-10 km thick) to the west of the ISB in Idaho, southeastern Oregon, Nevada, and eastern Utah (Figure 4.2). To the east of the ISB, T_e is thicker ranging from 20 to 80 km (Figure 4.2).

McKenzie and Fairhead [1997] pointed out a potential shortcoming of the Bouguer coherence method proposed by *Forsyth* [1985]. Forsyth's method assumed that all loads deflect the plate and produce a direct topographic signature. In response to this assumption, *McKenzie and Fairhead* [1997] argued that effects of erosion and sedimentation can form a flat and horizontal surface after deflection [see also *McKenzie*, 2003]. McKenzie and Fairhead also pointed out that very large T_e values given by Forsyth's method were unreasonable from the standpoint of geotherm and rheology. *Zuber et al.* [1989] estimated T_e for Archaean and Proterozoic shields to be as large as 130 km using the Bouguer coherence method. At the depth of 130 km, the temperature beneath shields is ~1000°C, a temperature too high to support loads elastically in a geologic time scale [*McKenzie and Fairhead*, 1997].

In order to estimate T_e, *McKenzie and Fairhead* [1997] proposed a method that used admittance between free-air gravity anomaly and topography. This method takes into account internal loads that are not indicated by surface topography, and simultaneously solves for T_e and the ratio of such loads to the total loads. The free-air admittance method caused controversy [e.g., *Swain and Kirby*, 2003; *Simons et al.*, 2000; *Banks et al.*, 2001; *Armstrong and Watts*, 2001; *McKenzie*, 2003]. However, the method has been used to estimate T_e of Earth's and other terrestrial celestial bodies' lithospheres (e.g., Mars [*Hoogenboom and Smrekar*, 2006; *Mancinelli et al.*, 2015], Venus [*Barnett et al.*, 2002; *Hoogenboom et al.*, 2004], and the Moon [*Crosby and McKenzie*, 2005]).

The debate on the methods for T_e estimation is ongoing. Recent studies suggest that effects of erosion on T_e estimation are not as simple as *Forsyth* [1985] or *McKenzie and Fairhead* [1997] modeled [*Simons et al.*, 2000; *Armstrong and Watts*, 2001; *Watts and

Burov, 2003; *Pérez-Gussinyé et al.*, 2004]. From synthetic modeling, *Crosby* [2007] estimated the largest T_e bias to be only 10 km, which is not large enough to solve discrepancy in the average T_e range between Forsyth's and McKenzie and Fairhead's methods. *Pérez-Gussinyé et al.* [2004], *Pérez-Gussinyé and Watts* [2005], and *Kirby and Swain* [2009] tested both methods to compare the results and found T_e values of over 100 km in some locations. In response, *McKenzie* [2010] suggested the possibility that the large T_e values found by *Kirby and Swain* [2009] for the Canadian shield is an artifact due to effects of mantle convection and glacial isostatic adjustment. After investigating such effects, *Kirby and Swain* [2013; 2014] computed T_e of at least 80 km in the Canadian shield. Technicalities of various T_e estimation operations including Forsyth's as well as McKenzie and Fairhead's are reviewed in detail by *Kirby* [2014].

4.1.2 Objectives

In this study, we estimate T_e in and around the Northern Rockies, using the free-air admittance method [*McKenzie and Fairhead*, 1997; *McKenzie*, 2003]. In order to find a variation in T_e in a good resolution, we set up submaps and find T_e of each submap. Recent seismic tomographic models revealed strong velocity anomalies in the upper mantle beneath the study area [e.g., *James et al.*, 2011; *Porritt et al.*, 2014]. We test the effects from the upper mantle heterogeneity on T_e estimates by developing other T_e maps, taking into account the gravity effects from the upper mantle. The resultant T_e variation is compared with the spatial (both horizontal and depth) distribution of the seismicity. The result is also compared with the T_e map from the Bouguer coherence method presented by *Lowry et al.* [2000]. We also consider the implication of the T_e pattern in the light of the regional tectonics and cratonic configuration.

4.2 Tectonic Setting

It is of interest to investigate potential relationships between T_e variation and the regional seismicity, tectonics, and cratonic configuration in the Northern Rockies. The most prominent seismic zone in the study area is the Intermountain Seismic Belt (ISB), which extends from northwestern Montana to northwestern Arizona (Figure 4.3). One of the largest intra-continental hotspot, Yellowstone is located in the ISB. The ISB marks the boundary between a broad area of extension tectonism to its west and the stable North American craton. The study area is located in the transition zone from Precambrian cratons to the Phanerozoic accreted terranes, which adds complexity to the area's tectonism.

4.2.1 Tectonics and Seismicity along the ISB

In the western U.S., the boundary between active and stable tectonism is marked by the ISB, an arcuate zone of elevated intraplate seismicity [*Smith and Sbar*, 1974]. The ISB is ~75-300 km wide and 1300 km long, extending from northwestern Montana and then southeastward to the seismically and volcanically active Yellowstone region, along the Idaho-Wyoming border as well as through central Utah to northwestern Arizona [*Smith and Arabasz*, 1991] (Figure 4.3). The dominant deformation style in the ISB is tectonic extension characterized by late-Quaternary normal faulting, diffuse shallow, up to ~20 km deep seismicity, and episodic scarp-forming earthquakes (M6-7.5) [*Smith and Sbar*, 1974; *Smith and Arabasz*, 1991]. To the west of the ISB, late-Cenozoic active extensional deformation is exhibited, while stable cratons of the North American Plate lie to the east with a lower level of seismicity.

In northwestern Montana, the ISB is trending southeast with the width as large as 300 km (Figure 4.3). Its margins are not sharply defined as the seismicity is diffuse with a few concentrations of relatively small (M<4) events [*Stickney and Bartholomew*, 1987]. Not only the density of seismicity but also the total number of events in northwestern Montana is lower than the other parts of the ISB [*Stickney and Bartholomew*, 1987]. In this segment, seismicity is more concentrated on the western side of the seismic belt (i.e., west of the stable craton). Notable earthquake swarms on the side are the 1969 and 1971 West of Flathead Lake [*Stevenson*, 1976], and the 1975 North of Flathead Lake [*Stickney*, 1980]. In the area, abundant late-Quaternary scarp-forming normal faulting is observed [*Stickney and Bartholomew*, 1987].

Around Helena, Montana, the ISB changes its trend to south-southwest (Figure 4.3). At the sharp right-angle bend, the Lewis Clark Fault Zone (LCFZ) merges into the ISB, marking the southern margin of the diffuse seismicity in northwestern Montana. The LCFZ is a ~800 km long, east-southeast trending, seismically active structural discontinuity extending from central Washington to western Montana (see Chapter 3 for the details) [*Smith*, 1965; *Weidman*, 1965; *Harrison et al.*, 1974; *Stickney and Bartholomew*, 1987]. The LCFZ is a result of multiple tectonic episodes dating from the Proterozoic [*Smith*, 1965; *Harrison et al.*, 1974]. In the present day, diffuse seismicity, including events as large as M~5, has been recorded in the western part of the fault zone. M~5 events occurred in 1918 in Rathdrum, Idaho, and in 1942 in Sandpoint [*Sprenke and Breckenridge*, 1992]. Three M~4 events occurred in Sandpoint, Idaho, in April 2015, indicating a reactivation of a major normal fault in the area (see Chapter 3). In the Helena area, where the LCFZ and ISB merge, the largest historical events in the fault zone, the 1935 Helena Valley earthquakes (M6.3 and M6.0) occurred [*Stickney*, 1978].

The ISB has sharp margins marked by M<5 events along the segment from the Helena area to Yellowstone [*Stickney and Bartholomew*, 1987] (Figure 4.3). Persistent seismicity has been observed in the Clarkston Valley area, ~70 km southeast of Helena, where the 1925 M6.8 Montana earthquake occurred [*Pardee*, 1926]. Published studies on the 1925 event suggest east-west trending T-axes [*Qamar and Hawley*, 1979] and an anomalous south-southeast trending T-axis with a strike-slip faulting mechanism [*Dewey et al.*, 1973]. Another significant historical event in the area is the 1947 M_L6.3 Virginia City [*Doser*, 1985; 1989].

Where the ISB meets the Idaho-Montana border in the southwestern corner of Montana, the Centennial Tectonic Belt (CTB; also called Central Idaho Seismic Zone) transects the ISB (Figure 4.3) [*Stickney and Bartholomew*, 1987]. The CTB is an approximately 350 km long and 80-100 km wide zone, flanking the northern margin of the central and eastern Snake River Plain (SRP) from east central Idaho to Yellowstone [*Anders et al.*, 1989]. The ISB includes the eastern half of the CTB. The zone is most tectonically and seismically active in the area north of the SRP, characterized by Quaternary active normal faults that form the basin-range topography [*Stickney and Bartholomew*, 1987]. The well-developed Lost River, Lemhi, and Beaverhead faults are in the western part of the CTB. The Lost River fault was ruptured by the 1983 M6.8 Borah Peak earthquake [e.g., *Doser and Smith*, 1985; *Smith et al.*, 1985; *Zollweg and Richins*, 1985; *Richins et al.*, 1987; *Barrientos et al.*, 1987]. In 2014, an earthquake swarm consisting of over 100 m_b1.5-4.7

events occurred near Challis, Idaho, about 20-30 km northwest of the focus of the 1983 event [*Pankow et al.*, 2014]. In the eastern CTB, where it overlaps the ISB, the 1959 M7.3 Hebgen Lake earthquake, which is the largest historic event within both the ISB and CTB, ruptured the ground surface immediately west of Yellowstone National Park [e.g., *Witkind et al.*, 1962; *Ryall*, 1962; *Tocher*, 1962; *Doser*, 1985].

The Yellowstone volcanic province is included in the ISB because the area is characterized by elevated seismicity (Figure 4.3). Since 1972, over 45,000 M<6.1 earthquakes have been recorded by the local seismic network [*Farrell et al.*, 2014]. The frequent seismicity occurs because the area is under the influence of not only tectonism but also magmatism and hydrothermal activities. Yellowstone is one of the world's largest continental hotspots, whose progressive track formed the central and eastern SRP. Tomographic studies image Yellowstone's mantle plume extending from the mid-mantle to ~50 km depths [e.g., *Porritt et al.*, 2014; *Schmandt and Humphreys*, 2010; *Smith et al.*, 2009] (Figure 4.4), which feeds two magma reservoirs: a shallow (~5-17 km depths) rhyolitic one and a deep (~25-50 km depths) basaltic one [*Farrell et al., 2014*; *Huang et al.*, 2015] (see Chapter 2). The three most recent major caldera-forming eruptions of Yellowstone took place around the current location of the hotspot at 2.1, 1.3, and 0.64 Ma, producing approximately 2450, 280, and 1000 km^3 of volcanic material, respectively [*Christiansen*, 2001]. Following these, more volcanic loads have been added by ~60 smaller eruptions with the most recent at ~70 Ka [*Christiansen*, *2001*].

The ISB trends southwest from Yellowstone to north central Utah [*Doser and Smith*, 1983] (Figure 4.3). To the immediate south of Yellowstone is the Yellowstone-Teton region known for a high level of seismicity. A notable fault in the area is the seismically active

Teton fault marked by a 3-52 m high, 55 km long fault scarp [*Byrd et al.*, 1994]. Even though the Teton fault appears to be seismically quiescent for M>3 events [*Smith et al.*, 1990, 1993; *Smith and Arabasz*, 1991], geological evidence indicates a potential to produce an earthquake as large as M7.5, and recurrence intervals of 1600-6000 years for scarp-forming events [*Smith et al.*, 1993]. The seismic hazard in the area is the highest in the Intermountain West because the area is influenced by both extension tectonism and stress perturbation from the Yellowstone magmatism [*Petersen et al.*, 2008].

In Utah, the ISB runs roughly north-south along the Wasatch fault zone, which exhibits prominent fault scarps [*Machette et al.*, 1991] (Figure 4.3). The fault zone extends ~380 km from southern Idaho to central Utah, marking the eastern boundary of the basin-range extension tectonism. Small to moderate earthquakes dominate the historical earthquake record [*Arabasz et al.*, 1992]. Although no historical large earthquake on the Wasatch fault has been recorded, paleoseismic studies present lines of evidence for repeated Holocene M>6 earthquakes including 16 M>7 earthquakes in the past 5600 years [*Swan et al.*, 1980; *McCalpin and Nishenko*, 1996].

4.2.2 Variation in the extension tectonics in the western U.S.

In the western U.S., the ISB marks the eastern margin of a broad region undergoing east-west extensional tectonics (Figure 4.3), which began after the cessation of the Sevier and Laramide orogeny ~35-55 Ma and escalated around 17 Ma [e.g., *Gilbert*, 1874; 1875; *King*, 1878; *Dutton*, 1880; *Stewart*, 1978]. The extension creates an area of distinct topography, which is referred to as the Basin and Range province, characterized by multiple series of fault block mountains that resulted from high-angle normal faulting within the ISB and to its west [*Fenneman*, 1931]. The extension is most active in the Great Basin section [*Eaton*, 1979a], which contains most of Nevada and extends into southeastern Idaho, western Utah, southeastern Oregon, and southeastern California (Figure 4.3). The Northern Rockies exhibits a slightly different style of extension tectonics.

Because of a variation in the style of extension and the lack of sharp boundary, the northern boundary of the Basin and Range province has been drawn at different places. When defining the physiographic regions of the United States, *Fenneman* [1928; 1931] marked the northern boundary at the southern edge of the SRP (Figure 4.3). His division is solely based on physiography. Later, by considering the distribution of the similar high-angle normal faulting to the north, *Pardee* [1950] and *Lawrence* [1976] argued that the extension tectonics continued to the Northern Rockies and terminated at the LCFZ (Figure 4.3). Based on the similar style of crustal extension between the Northern Rockies and the Great Basin section, *Reynolds* [1979] proposed the northern boundary at the LCFZ. *Eaton* [1979a; 1982] argued that the Northern Rockies was a broad transition zone which had common geologic features and a different post-Laramide tectonic history from the Great Basin section. This difference is reflected in the age of basin fill. In the Great Basin section, the grabens are filled with Pliocene and Quaternary sediments whereas the basin fill is predominantly Miocene in age in the Northern Rockies [*Eaton*, 1979a].

Another difference between the Great Basin section and the Northern Rockies is reflected in the extension directions. In the Great Basin section, the extension directions are west to northwest (Figure 4.3), which agrees with the direction of the minimum principal stress [*Eaton*, 1979b; 1980; *Zoback and Zoback*, 1980]. From east to west in the section, the extension direction gradually changes from west to northwest [*Eaton*, 1979b; 1980]. In the

Northern Rockies, the observed seismicity indicates the extension direction ranging from west to southwest (Figure 4.3). To the north of the LCFZ, a recent seismotectonic analysis suggests an east-west extension [*Stickney*, 2015] (Figure 4.3). From the central and eastern LCFZ to the northern edge of the SRP, both large and small earthquakes indicate a northeast-southwest extension [*Stickney and Bartholomew*, 1987; *Stickney*, 2015] (Figure 4.3).

There are some researchers who include the Northern Rockies in the Basin and Range province. For example, *McCaffrey et al.* [2007] and *Payne et al.* [2012] refer to the Northern Rockies as the northern Basin and Range. However, most researchers distinguish between the Great Basin section and the Northern Rockies separated by the SRP (Figure 4.3) because of the tectonic differences between the two regions. The term, the northern Basin and Range, has more commonly referred to the area to the immediate south of the SRP [e.g., *Furlong*, 1979; *Klemperer et al.*, 1986; *Liu and Shen*, 1998; *Hampel et al.*, 2007; *Eagar et al.*, 2010]. *Stickney and Bartholomew* [1987] defined the Northern Rockies as a section of the Basin and Range province, and named it the Montana-Idaho basin and range.

4.2.3 Major Cratonic Province Configuration

Our study area shows a part of the transition zone from the Precambrian cratons to the Phanerozoic accreted terranes in western north America. In the east of the study area is the Archaean Wyoming craton (also known as the Wyoming Province), an initial core of the North American craton (Figure 4.3). The northwestern corner of the Wyoming Province is bounded by the Proterozoic mega-shear zone, the Great Falls tectonic zone. In the west, the Western Idaho Suture Zone marks the boundary between the Archaean-Proterozoic provinces in Idaho (i.e., the Priest River complex, Selway terrane, and Grouse Creek block) and the Phanerozoic accreted terranes (Figure 4.3).

The Wyoming craton extends from Wyoming to southeastern Montana, eastern Idaho, northeastern Utah, and western South Dakota. The Wyoming craton consists of late Archaean basement units [*Wooden and Mueller*, 1988; *Wooden et al.*, 1988; *Mogk et al.*, 1992; *Frost et al.*, 1998; *Henstock et al.*, 1998; *Chamberlain et al.*, 2003]. Seismic surveys revealed that the Wyoming craton is anomalously thick and dense compared to the surrounding provinces [*Thomas et al.*, 1987; *Henstock et al.*, 1998; *Dueker et al*., 2001]. Recent seismic tomography models image the Wyoming craton lithosphere as a thick (~250 km) high-velocity body [e.g., *Dueker et al.*, 2001; *James et al.*, 2011; *Porritt et al.*, 2014] (Figure 4.4). The lithosphere is also shown as a thick (~280km), highly resistive body in a magnetotelluric study using the EarthScope Transportable Array data [*Meqbel et al.*, 2014].

The Great Falls tectonic zone (GFTZ) is an Archaean basement reactivated in the Proterozoic, which runs from southwestern to northwestern Montana (Figure 4.3). It consists of high-angle faults that have been repeatedly reactivated throughout the Phanerozoic, and possibly as late as the Holocene [*Hayden and Wehernberg*, 1959; *Boerner et al.*, 1998; *Foster et al.*, 2006; *Gifford et al.*, 2014]. The deformation pattern within the GFTZ basement affects the geometry and orientation of the younger superposing structures [*Gifford et al.*, 2014]. The inception of the tectonic zone remains open to debate. Geochronologic and geochemical data suggest that the tectonic zone resulted from a collision and suturing on the basis of a subduction-generated igneous arc signature [*Mueller et al.*, 2002]. On the other hand, geophysical studies imply a continuity of the lithosphere across the GFTZ, supporting the alternative shear-origin hypothesis [*Gorman et al.*, 2002; *Ross*, 2002].

Along the Western Idaho Suture Zone (WISZ; Figure 4.3), multiple crustal fragments have accreted to the western margin of the paleo-North American continent throughout the Phanerozoic [e.g., *Fleck and Criss*, 2004]. There are four major accreted terranes Paleozoic-Mesozoic in age [e.g., *Vallier*, 1977; 1995]. The suture zone is characterized by a belt of deformation that includes thrust sheets [*Hamilton*, 1963; *Selverstone et al.*, 1992; *Manduca et al.*, 1993] and flower structures [*Lund and Snee*, 1988]. The structures along the WISZ indicate at least two stages of deformation history: thrusting associated with the accretion episodes and post-accretion shear deformation by transpression [*McClelland et al.*, 2000].

4.3 Theories

Effective elastic thickness is a measure to describe the flexural rigidity of the lithosphere. It is the conceptual thickness of the purely elastic layer within lithosphere, indicating the resistance to bending under the applied vertical loads. Thus, T_e does not necessarily represent a depth of any physical boundary or discontinuity [e.g., *Burov and Diament*, 1995; *Watts and Burov*, 2003]. Even though various rheological behaviors (e.g., elastic, plastic, viscous, and viscoelastic) are observed in the actual lithosphere, T_e can represent a mechanical property because the lithosphere behaves as an elastic plate in timescales of tens of millions of years [e.g., *Watts*, 2001; *Watts and Burov*, 2003].

Since detailed gravity data became available, spectral relationship of gravity and topography data have been used to estimate continental T_e. All spectral methods are based on the following fundamental assumptions: (1) topography of longer wavelength is supported largely by isostasy (i.e., *local isostatic support*), whereas shorter-wavelength topography is supported by mechanical strength of the lithosphere (i.e., *elastic support*) and therefore causes gravity anomalies over a broad range of wavelengths, and (2) the transitional wavelengths from isostatic to elastic support indicate T_e. The degree of elastic support decreases from 100% at the shortest wavelengths to zero at the longest wavelengths, affecting gravity spectra in a predictable manner. Below are model assumptions for the spectral methods: (1) the lithosphere is laterally isotropic, and (2) loads that require isostatic support are fully compensated. It is evident that both are not always true when a load is geologically young (e.g., Yellowstone). Such loads cause an apparent T_e larger than the value translated from the actual rigidity.

To estimate T_e, we adopt a spectral method that uses admittance between topography and free-air gravity anomaly as proposed by *McKenzie and Fairhead* [1997]. The result is compared with the T_e map from the Bouguer coherence method [*Lowry et al.*, 2000].

4.3.1 Free-Air Gravity Admittance

This study uses free-air admittance to estimate T_e. Free-air gravity anomaly indicates a degree of isostatic compensation, and therefore it partially correlates with topography. If topography is fully compensated locally as in the Airy or Pratt compensation models, the free-air anomaly is theoretically zero, disregarding other factors. If topographic loads are partially compensated by the flexure of the crust, the free-air anomaly mimics topography. This partial correlation is used to find T_e through admittance between free-air anomaly and topography data.

The admittance in solid earth geophysics is an amplitude ratio between topography and the gravity anomaly [e.g., *Lewis and Dorman*, 1970; *Dorman and Lewis*, 1970]. It is a measure of how much gravity anomaly is caused by the surface topography. Therefore, the admittance method is an example of a transfer function, which is a mathematical representation to describe inputs and outputs of a system (i.e., topography and gravity anomaly, respectively, in T_e estimation). The conceptual relationship between the input, output, and the observed admittance $Z(k)$ is given in the spatial frequency domain by

$$\Delta g(k) = Z(k)H(k) \tag{4.1}$$

where the gravity anomaly is $\Delta g(k)$, and the surface topography (i.e., elevation) is $H(k)$ (see section 4.2.2 for details). The admittance Z is a function of wavenumber k as $g(k)$ and $H(k)$ are the Fourier transforms of gravity and elevation, respectively. In the wave analysis, the wavenumber is the spatial frequency of a wave, which can be viewed as the number of waves per unit length. The topography-gravity admittance is usually in a unit of mGal/km.

Theoretical admittance and T_e are related in the flexure model of isostasy. In this model, an elastic plate of a thickness T_e deflects when supporting a surface load (Figure 4.1c). This causes the compensation to be distributed over a broad region. Figure 4.5 demonstrates the relationship between surface and Moho topographies and free-air anomaly with simplified theoretical examples. A theoretical lithosphere with no mechanical strength (T_e = 0; Figure 4.5a) is equivalent to the local compensation model in which the surface topography is completely compensated no matter how small a load is. In this case, the Moho topography is the perfect inversion of the surface topography, and the free-air anomaly has no signal. If $T_e = \infty$, (Figure 4.5b), topography is fully supported by elastic stress within the lithosphere, and therefore no local isostatic compensation occurs. As a result, the free-air anomaly mimics the surface topography.

In the flexure model (i.e., nonzero T_e), long-wavelength (i.e., low-wavenumber) component of the topography is supported by local isostasy, and therefore is not indicated by the signal of free-air anomaly. On the other hand, topography of short wavelength (i.e., localized, small-scale topography) is supported by elastic stress within the lithosphere, causing signals in free-air anomaly. When T_e is small, only the topography of short wavelength is on the elastic support, which is indicated in the free-air anomaly signal (Figure 4.5c). When T_e is large, only the long-wavelength component of the topography is supported by isostasy (Figure 4.5d). Figure 4.6 shows example admittance curves in the frequency domain. At low k values, admittance is also low because most long-wavelength (i.e., low-k) topography components are locally supported, causing little free-air gravity signal. As k increases to approach the critical value k_c, the ratio of elastic support increases, causing larger free-air signals and therefore larger admittance values. Topographic loads of the critical wavelength (at k_c) or smaller are fully supported regionally. Therefore, the admittance curve hits the plateau at k_c.

The admittance curve at the transitional wavenumbers ($0 < k < k_c$), which corresponds to the transition from local isostatic support to regional elastic support, is a function of T_e. Figure 4.6 also shows a change in admittance curve due to a difference in T_e. When a T_e value is small (solid curve in the figure), high admittance is attained at a high wavenumber because only short-wavelength (i.e., high-wavenumber) components are supported elastically. When T_e is larger, the admittance curve hits the plateau at a lower k_c because loads of the broader spectrum are supported elastically. This change in admittance curve allows for T_e estimation.

Flexural rigidity relates T_e to admittance. A flexural rigidity D is calculated from [*Love*, 1906, p. 443]

$$D = \frac{ET_e^3}{12(1-\sigma^2)} \tag{4.2}$$

where E is Young's modulus, and σ is Poisson's ratio [e.g., *Gunn*, 1943a]. As shown in the equation, flexural rigidity is proportional to T_e^3. Admittance is related to the amount of deflection when a load is added to the surface, and the amount of deflection is controlled by flexural rigidity. If a layer of thickness s is added to the surface as a load on two-layered crust (Figure 4.7), the deflection of the elastic plate w is given by

$$[(Dk^4/g) + \rho_m - \rho_w]\bar{w} = -(\rho_u - \rho_w)\bar{s} \tag{4.3}$$

where g is the gravitational acceleration, and ρ_m, ρ_w, and ρ_u are the densities of mantle, the fluid overlying the crust (air or water), and the upper crust, respectively. The overbars denote Fourier-transformed variables. The equation above indicates that deflection is inversely proportional to the flexural rigidity. The thickness of the added load and the amount of deflection together determine the elevation e (Figure 4.7), given by

$$e = s + w \tag{4.4}$$

Free-air gravity anomaly Δg due to the elevated topography is

$$\Delta\bar{g} = Z\bar{e} = 2\pi G(\rho_u - \rho_w)(1 + Z')\bar{e} \tag{4.5}$$

where G is the gravitational constant. Z' is

$$Z' = -\frac{[(\rho_l - \rho_u)\exp(-kt_u) + (\rho_m - \rho_l)\exp(-kt_c)]}{\left[\left(\frac{Dk^4}{g}\right) + \rho_m - \rho_l\right]} \tag{4.6}$$

where ρ_l is the density of the lower crust, t_u is the thickness of the upper crust, and t_c is the total thickness of the upper and lower crust (Figure 4.7). The equation 4.5 allows for the admittance. See Appendix A in *McKenzie* [2003] for more detailed operations.

4.3.2 The Free-Air Admittance Method by McKenzie and Fairhead

The spectral method introduced by *McKenzie and Fairhead* [1997] has two major differences from earlier methods. Their method uses free-air admittance and takes account of effects of subsurface loads.

Early works use admittance between the Bouguer gravity anomaly and topography [*McKenzie and Bowin*, 1976; *Banks et al.*, 1977; *McNutt and Parker*, 1978; *Cochran*, 1980]. A method proposed by *Forsyth* [1985] uses Bouguer coherence. These methods using the Bouguer anomaly are based on an assumption that all long-wavelength loads deflect the plate, producing a topographic signature. However, erosion and sedimentation can form a flat plain which can never correlate with the subsurface loads. *McKenzie* [2003] presents such a case where a Precambrian mid-continental rift filled with dense volcanics is covered by Phanerozoic sediments in central North America [*Hinze et al.*, 1992]. McKenzie and Fairhead's method uses free-air anomaly to clear the problem associated with using Bouguer anomaly. A part of free-air anomaly is always correlated with the surface topography regardless of the presence of subsurface loads.

Gravity anomalies caused by subsurface loads with no topographic expression (i.e., uncompensated loads whose topographic expressions have been eroded or covered by sediments, or simply "unexpressed loads" as coined by *Kirby* [2014]) work as model noise in the spectral methods in the signal processing sense [*McKenzie and Fairhead*, 1997; *McKenzie*, 2003; *Kirby*, 2014]. When unexpressed loads are present, Forsyth's coherence method assumes that the loads are supported solely by elastic stress in the plate despite the possibility of partial local isostatic support. This assumption often results in an unreasonably high T_e (~130 km) [*Forsyth*, 1985; *McKenzie and Fairhead*, 1997; *McKenzie*, 2003]. McKenzie and Fairhead's admittance method simultaneously solves for T_e and effects of subsurface loads. In this way, incoherence between subsurface loads and topography only affects the goodness of fit and increases the uncertainty, but does not affect the estimate of T_e. Below is the summary of *McKenzie and Fairhead*'s [1997; see also *McKenzie*, 2003] methods to find a theoretical admittance when internal loads are considered.

Gravity anomalies are caused by surface loads as well as internal loads. In order to model internal loads, the example by *McKenzie and Fairhead* [1997] assumes a two-layer crust model shown in Figure 4.7. The crust model of thickness t_c consists of a lower-density (ρ_u) upper layer of thickness t_u and a higher-density (ρ_l) lower layer. Surface loads are included by adding a layer of density ρ_u on the surface. Loads acting the interface between the upper and lower curst are imposed by adjusting the thicknesses of the layers, keeping the total thickness constant. Loads at the Moho are imposed by adding a layer of mantle density (ρ_m). Gravity anomaly by surface loads is obtained using equations (4.5) and (4.6). By applying those equations for surface loads, gravity anomaly by loads on the mid-interface Δg_2 is given by

$$\Delta\overline{g_2} = Z_2\overline{e_2} = 2\pi G(\rho_u - \rho_w)(1 + Z_2{}')\overline{e_2} \tag{4.7}$$

where $Z_2{}'$ is

$$Z_2{}' = -\left[\frac{\left(\frac{Dk^4}{g}\right) + \rho_m - \rho_w - \rho_l + \rho_u}{\rho_u - \rho_w}\right]\exp(-kt_u) + \left(\frac{\rho_m - \rho_l}{\rho_u - \rho_w}\right)\exp(-kt_c) \tag{4.8}$$

Similarly, gravity anomaly by loads on the Moho Δg_3 is given by

$$\Delta\overline{g_3} = Z_3\overline{e_3} = 2\pi G(\rho_u - \rho_w)(1 + Z_3')\overline{e_3} \tag{4.9}$$

where $Z_3{}'$ is

$$Z_3{}' = -\left[\frac{\left(\frac{Dk^4}{g}\right) + \rho_l - \rho_w}{\rho_u - \rho_w}\right]\exp(-kt_c) + \left(\frac{\rho_l - \rho_u}{\rho_u - \rho_w}\right)\exp(-kt_u) \tag{4.10}$$

Fractions of loads at the surface, mid-interface, and Moho are denoted by F_1, F_2, and F_3, respectively, assuming no other loads, where

$$\sum_i F_i = 1 \tag{4.11}$$

When all the loads are considered, the resultant admittance is described by

$$Z = \frac{\sum_i F_i^2 Y_i^2 Z_i}{\sum_i F_i^2 Y_i^2} \tag{4.12}$$

where Y_1, Y_2, and Y_3 are given by

$$Y_1 = \left(\frac{1}{\rho_u - \rho_w}\right)\frac{\left(\frac{Dk^4}{g}\right) + \rho_m - \rho_u}{\left(\frac{Dk^4}{g}\right) + \rho_m - \rho_w} \tag{4.13}$$

and

$$Y_2 = Y_3 = -\frac{1}{\left[\left(\frac{Dk^4}{g}\right) + \rho_m - \rho_w\right]} \tag{4.14}$$

The calculated admittance Z is a function of T_e and F_2 when F_3 is set to be zero, and the other parameters are fixed. Similarly, it is a function of T_e and F_3 when F_2 is set to be zero.

The best fit model is found by iterations varying T_e and F_n to minimize misfit H given by

$$H = \left[\frac{1}{N}\sum_{n=1}^{N}\left(\frac{Z_o^f - Z_c^f}{\Delta Z_o^f}\right)^2\right]^{1/2} \tag{4.15}$$

where Z_o^f is the observed admittance with standard deviation ΔZ_o^f, and Z_c^f the admittance calculated using equation (4.13).

4.3.3 The Bouguer Coherence Method by Forsyth

Lowry et. al. [2000] applied the Bouguer coherence method by *Forsyth* [1985] to estimate T_e in the western U.S. (Figure 4.2). By using the Bouguer gravity anomaly, which indicates subsurface density variation, this spectral method incorporates internal loads. Coherence is a measure of correlation between two signals in signal processing. Mathematically, the coherence here is the square of the Pearson product-moment correlation coefficient in the wavenumber domain. When two signals of the same frequency bear a constant relationship in amplitude and phase, the two signals are coherent. Values of coherence vary in the interval between 1 (perfect correlation) and 0 (no correlation). In a gravity-topography analysis, if a topographic load is locally supported, causing a deflection of the plate and a deep root, the elevation and Moho topography indicated by the Bouguer anomaly are coherent (opposite in phase). A load supported regionally does not cause a deflection, and therefore the elevation and Moho topography signals are incoherent. At long wavelengths, which corresponds to large, regional loads, coherence values are around 1. At short wavelengths (small, local loads), coherence values are near zero.

In the Bouguer coherence method by *Forsyth* [1985], the coherence γ^2 is given by

$$\gamma^2 = \frac{C^2}{E_0 E_1} \tag{4.16}$$

where C is the power of the cross spectrum of Moho topography and surface topography, and E is a power of the topographies. C is given by

$$C = \langle W \cdot H^* \rangle \, 2\pi\Delta\rho G \exp(-kz_m) \tag{4.17}$$

where W is the Moho topography, $\Delta\rho$ is the density contrast at Moho, and z_m is the Moho depth. The brackets indicate averaging over discrete wave number band, and the asterisk indicates the complex conjugate. E_0 and E_1 are given by

$$E_0 = \langle H \cdot H^* \rangle \tag{4.18}$$

and

$$E_1 = \langle W \cdot W^* \rangle \, (2\pi\Delta\rho G)^2 \exp(-2kz_m) \tag{4.19}$$

The Moho topography *W* is described by the Bouguer anomaly *B* as follows:

$$W(k) = \frac{B(k)\exp(kz_m)}{2\pi\Delta\rho G} \tag{4.20}$$

The operations are detailed in *Forsyth* [1985].

4.4 Methods

In order to estimate T_e, we find admittance spectra of free-air gravity and topography data from the Northern Rockies. Then, the best fit theoretical admittance curve is found by varying T_e and a fraction of loads placed on Moho (i.e., F_3). We adopt and extend *McKenzie and Fairhead*'s [1997] two-layer crust model (Figure 4.7) and admittance method. In order to find horizontal variations in T_e, we calculate a localized admittance spectrum for a submap of 250 km radius centered at each grid point (Figure 4.8). We also find the gravity effect from the upper mantle to see its effects on the T_e estimate.

4.4.1 Observed Admittance

An observed admittance is an amplitude ratio between gravity anomaly and topography (Equation 4.1). We compute an admittance spectrum for each 250 km radius submap centered at a 20 km spacing grid point (Figure 4.8). Preprocessed gravity anomaly and elevation data sets are Fourier-transformed to find ratios in the frequency domain.

We use free-air anomaly (Figure 4.9) and topography (Figure 4.10) data compiled by *Pan American Center for Earth & Environmental Studies* (PACES) at University of Texas at El Paso [2015]. The plotted free-air anomaly data well mimic the basin-range topography in Nevada, western Utah, and central Idaho (Figure 4.9). We interpolate the gravity and topography data onto a 5 km grid using the natural neighbor interpolation algorithm [*Sibson*, 1981] on the Albers projection, which minimizes distortion in the middle-latitude areas.

In order to find variation in T_e in the study area, we set up a 20 km grid and perform a 2-D Fourier transform for a 250 km radius circular submap centered at each grid point and zero values elsewhere (Figure 4.8; Appendix 4.A). The 500 km diameter allows for a spectrum analysis of a wavenumber domain of $k > 0.002$ km^{-1}, which sufficiently includes a typical domain correspondent to the transitional wavelengths from isostatic to elastic support. The relationship between wavenumber k and wavelength λ is described by the equation

$$k = 2\pi/\lambda \tag{4.21}$$

Before operating the Fourier transform, both gravity and topography data sets are preprocessed as shown in Figure 4.11. First, the linear regression plane is subtracted from the data values in a submap to remove the DC component and signals whose wavelengths are larger than 500 km (Figure 4.11ab). Next, we apply the Hann window function [*Blackman and Tukey*, 1958; *Harris*, 1978] (Figure 4.11cd) in order to avoid edge effects [cf. *Ojeda and Whitman*, 2002] when performing the Fourier transform. The window function is given by

$$w(n) = 0.5\left(1 - \cos\left(\frac{2\pi n}{N-1}\right)\right), \text{if } 0 \le n \le 1 \tag{4.22}$$

Then, a 2-D Fourier transform is performed for both preprocessed gravity and topography data. Observed admittance Z is given by

$$Z(k) = \frac{\langle \bar{g}\bar{e}^{*} \rangle}{\langle \bar{e}\bar{e}^{*} \rangle} \tag{4.23}$$

where asterisks denote the complex conjugates and the angle brackets denote the average value over a wavenumber band centered on k.

4.4.2 Calculated Admittance

A calculated admittance in McKenzie and Fairhead's method is a function of T_e, fractions of loads, and the thicknesses and densities of the modeled crustal layers. We adopt their crustal structure model, which consists of two layers of different densities overlying a higher density mantle (Figure 4.7). For each circular submap centered at a grid point, we find the best fit admittance curve in the frequency domain by varying T_e and a fraction of internal load.

To define the thickness and density of the modeled crustal layers, we use the *P*-wave 1-D velocity model for southwestern Montana by *Stickney* [1984] (Table 4.2). We assume and fix the upper crust thickness t_u to be 6.5 km, which is the bottom of the second layer in the velocity model. The total crustal thickness t_c is calculated using crustal thickness estimates from the receiver function analysis, the EarthScope Automated Receiver Survey (EARS), provided by the Incorporated Research Institutions for Seismology (IRIS) [*IRIS DMC*, 2010; *Crotwell and Owens*, 2005] (Figure 4.12). We assume the median of the t_c values in a submap to be the t_c at the center of the submap.

Table 4.2. *P*-wave velocity model for southwestern Montana from *Stickney* [1984].

P-wave velocity (km/s)	Depth to layer top (km)
4.8	0.0
5.6	1.1
6.15	6.5
6.8	18.0
8.0	40.0

The crustal density structure is estimated by relating crustal refraction seismic velocities to density [*Jones et al.*, 1992]. We convert values from the *P*-wave velocity model of the area [*Stickney*, 1984] into density structures using the non-linear continental velocity-density relationship parameters from *Christensen and Mooney* [1995]. The authors provide the coefficients for the velocity-density regression lines for continental crust, $\rho = a + b/V_p$ (Table 4.3), which is based on seismic refraction data. From the *P*-wave velocity model and the velocity-density parameters, the 1-D density structure for the study area is obtained (Table 4.4). The density structure allows for a bulk density of the upper crust, 2488 kg m^{-3}, and that of the lower crust, which depends on t_c.

Table 4.3. Parameters for nonlinear velocity-density regression line, $\rho = a + b/V_p$, from *Christensen and Mooney* [1995].

Depth (km)	a (kg m^{-3})	b (kg m^{-3} / km s^{-1})
10	4929	-13294
20	5055	-14094
30	5141	-14539
40	5212	-14863
50	5281	-15174

Table 4.4. Density structure for bulk density calculation.

Depth to layer top (km)	Density (kg m^{-3})
0.0	2159
1.1	2555
6.5	2767
10	2763
18	2982
20	3003
30	3026
40	3384

In addition to the crustal thicknesses and densities, elastic moduli are also parameters necessary for the admittance calculation. We adopt Young's modulus of 10^{11} Pa and Poisson's ratio of 0.25 from previous studies, *McKenzie and Fairhead* [1997] and *Lowry et al.* [1994], respectively. Assumed values and physical constants used in this study are listed in Table 4.5.

Table 4.5. Assumed values and physical constants in this study.

Upper crust thickness, t_u	6500 m
Upper crust density, ρ_u	2488 kg m^{-3}
Mantle density, ρ_m	3330 kg m^{-3}
Young's modulus, E	10^{11} Pa
Poisson's ratio, σ	0.25
Gravity constant, G	6.674×10^{-11} m^3 kg^{-1} s^{-2}
Gravity acceleration, g	9.807 m s^{-2}

The numerical operations are performed following the methods detailed in section 4.2.2. In this study, we set $F_2 = 0$ and vary T_e and F_3 to attain the best fit model because *McKenzie and Fairhead* [1997] found small F_2 values when observing the behavior of admittance curves for the most major continents.

4.4.3 Inversion

The inversion finds the best fit model with a set of parameters, T_e and F_3, that minimize the summation of misfit between the observed and calculated admittances given by Equation 4.15. It is known that the misfit has a global minimum and no local minimum in the T_e-F_n model space when a tested T_e is in a realistic range, and that the misfit plot often shows a “flat-bottomed valley” around the global minimum [cf. *McKenzie*, 2003] (Figure 4.13). For those characteristics, the misfit minimization is performed by the simple hill-climbing algorithm with decreasing step size.

4.4.4 Upper Mantle Gravity Effect

The resultant T_e map is statistically compared with a gravity contribution from the upper mantle to see if its density variation affects the T_e estimate. The mantle gravity effect is of interest because the underlying mantle in the study area has zones of significant velocity anomalies. For instance, a strong low-velocity zone is revealed beneath the central and eastern Snake River Plain at ~50-200 km depths by seismic tomographic models using data from USArray [e.g., *Schmandt and Humphreys*, 2010; *Obrebski et al.*, 2011; *James et al.*, 2011; *Porritt et al.*, 2011; *Porritt et al.*, 2014] (Figure 4.4).

We find the mantle gravity effect using velocity perturbation data from one of the latest tomographic models, DNA13 [*Porritt et al.*, 2014] (Figure 4.4). For this study, the *P*-wave tomographic model is used as the effects of melt in mantle is limited compared to *S*-wave models. First, we obtain the 3-D mantle velocity structure from the *P*-wave velocity perturbation data and a 1-D earth model, the Preliminary Reference Earth Model (PREM) by *Dziewonski and Anderson* [1981] (Table 4.6). Then, the 3-D velocity model is converted into a density model using the mantle density-velocity relationship by *Birch* [1964],

$$\rho = 0.768 + 0.328V_P \tag{4.24}$$

Next, the density variation is converted into a gravity effect at the surface. For the conversion, we assume flat horizontal layers which have a density variation only in the horizontal direction (i.e., a function of x and y). The gravity effect from one layer in a depth range is given by

$$\mathcal{F}[g_z] = \mathcal{F}[\rho]\left\{\frac{2\pi G}{|k|}e^{|k|z_0}\left(e^{-|k|z_1} - e^{-|k|z_2}\right)\right\}, \quad z_0 < z_1, \; z_1 < z_2 \tag{4.25}$$

where g_z is the gravity effect, which is a function of x and y, z_0 is the depth of measurement, and z_1 and z_2 are the depths to the top and bottom of the layer, respectively. Since the gravity effect at the surface is of interest, z_0 is 0 km in this particular case. The layer thickness, $z_2 - z_1$, is set to be 10 km because the DNA13 tomography model provides the perturbation data with a 10 km depth increment. Finally, gravity effects of the layers from 50 km to 600 km depths are integrated in the z-direction (Figure 4.14). An effect of the mantle at >600 km depths is negligibly small.

Table 4.6. *P*-wave velocities from PREM [*Dziewonski and Anderson*, 1981].

Radius	V_p (km/s)	Radius	V_p	Radius	V_p	Radius	V_p
6371	5.8000	6151	7.9897	5701	10.7513	4500	12.6655
6368	5.8000	6151	8.559	5650	10.9101	4400	12.7839
6368	5.8000	6106	8.6455	5600	11.0656	4300	12.9004
6356	5.8000	6061	8.7321	5600	11.0656	4200	13.0158
6356	6.8000	6016	8.8187	5500	11.2449	4100	13.1305
6346.6	6.8000	5971	8.9052	5400	11.4156	4000	13.2453
6346.6	8.1106	5971	9.134	5300	11.5783	3900	13.3607
6331	8.1012	5921	9.3899	5200	11.7336	3800	13.4774
6311	8.0891	5871	9.6459	5100	11.8821	3700	13.596
6291	8.0769	5821	9.9018	5000	12.0245	3630	13.6804
6291	8.0769	5771	10.1578	4900	12.1613	3630	13.6804
6256	8.0554	5771	10.1578	4800	12.2932	3600	13.6875
6221	8.0337	5736	10.212	4700	12.4208	3500	13.7117
6186	8.0118	5701	10.2662	4600	12.5447	3480	13.7166

The effect of the mantle gravity effect is estimated by computing the 2-D correlation coefficient ρ between the maps of the resultant T_e and mantle gravity effect. When two images *A* and *B* of a size *m* by *n* are compared, ρ is given by

$$\rho = \frac{\sum_m \sum_n (A_{mn} - \bar{A})(B_{mn} - \bar{B})}{\sqrt{\left(\sum_m \sum_n (A_{mn} - \bar{A})^2\right)\left(\sum_m \sum_n (B_{mn} - \bar{B})^2\right)}} \tag{4.26}$$

where $\bar{A}$ and $\bar{B}$ are the means of respective matrices. We also find another T_e map, taking into account the gravity contribution from the upper mantle. The correction is applied to the free-air anomaly data by subtracting a gravity effect from the upper mantle.

4.4.5 Thermal Elevation Correction

In addition to the basic model using the raw elevation (Figure 4.10) for the observed admittance calculation, we also test a model using corrected elevation data based on mantle mass anomalies. The mantle mass anomalies affect the amount of elevation adjustment, called thermal elevation [e.g., *Han and Chapman*, 1995; *Nagihara et al.*, 1996; *Hasterok and Chapman*, 2007]. Subtracting the thermal elevation from the raw elevation yields the corrected elevation, which may better represent the surface loads [cf. *Prezzi et al.*, 2014].

Lowry et al. [2000] present the thermal elevation of the western U.S. (Figure 4.15) from surface heat flow measurements. Continental geotherms expressed in the surface heat flow are converted to a mass anomaly associated with thickness variation of the thermal boundary layer [*Chapman and Pollack*, 1977; *Turcotte and Schubert*, 2002; *Hasterok and Chapman*, 2007]. The thickness of the boundary layer is then converted to the thermal elevation [*Lowry et al.*, 2000]. Using the thermal elevation presented by *Lowry et al.* [2000], we apply the elevation correction to assess the effect of the mantle mass anomalies on the T_e estimate.

4.5 Results

The spatial variation of the T_e estimate was obtained using the free-air admittance method. The best fit model for each grid point was found by iterations varying T_e and F_3. We tested both models using the raw elevation (Figure 4.10) and corrected elevation based on mantle mass anomalies (Figure 4.15). Both models consistently predict a general trend that the transition zone from small to large (>10 km) T_e coincides with the ISB.

A pair of T_e and F_3 that minimizes the misfit H was found through iterations. Figure 4.16 shows plots of observed and calculated admittance as a function of k as well as contoured misfit plots for three selected grid points that have small, middle, and large T_e values. For all three admittance plots, the observed admittances show an increasing trend at low wavenumbers. A small T_e value (1.7 km) is predicted by a steady increase in admittance in the modeled wavenumber domain (Figure 4.16a). This indicates that the full elastic support is not easily attained when a T_e value is low. In the second and third plots (T_e of 10 km and 18 km; Figure 4.16bc), the admittances increase to constant values, showing the wavenumber domains where the elastic support is dominant. The contour plots of the misfit H in the T_e-F_3 model plane show that there is a single minimum, which lies within a "small valley" when the best fit T_e is small (Figure 4.16a), or within a "flat-bottomed basin" when the T_e is larger (Figure 4.16bc). The misfit plots indicate that the range of uncertainty of T_e increases as the best fit T_e value becomes larger. The uncertainty is approximately ±30% of each T_e estimate (Figure 4.16). The global minima generally occur when F_3 is small (<0.3). As a common trend, H increases rapidly as F_3 increases above 0.3. This trend results because the calculated admittance curve dips into the negative range as F_2 or F_3 increases [*McKenzie*, 2003].

For grid points in central Wyoming and northwestern Colorado, the T_e-F_3 misfit plot tends to have a large basin whose bottom is very slightly inclined toward the positive T_e direction. To such points, the minimum T_e value at $F_3 = 0$ in the basin is given to indicate a minimum possible T_e value with a large uncertainty.

The resulting T_e map is shown in Figure 4.17. As a general trend, T_e estimates are larger than 13 km to the east of the ISB and smaller to the west. The area of the largest T_e (~15-75 km) appears in central to western Wyoming. T_e is relatively smaller (~13-15 km) in western Montana. To the west of the ISB, there are several patches of very small T_e (~1-3 km). One is in the central to western SRP, which extends to southwestern Montana with an increasing trend. To the west, it connects to another low-T_e area in southeastern Oregon. A relatively low T_e area appears around the middle of the Nevada-Utah border. There is a large low T_e area along the Canada-U.S. border (i.e., northern end of the map), extending from the northeastern corner of Washington to the northwestern corner of Montana. This may result from an edge effect because the gravity and topography data sets used for this T_e analysis do not have any data points in Canada (Figures 4.9 and 4.10). For the other map limits, sufficient data points outside of the map area were included for the analysis to avoid edge effects. The estimated T_e values, F_3, and misfit H for each grid point are given in Appendices 4.A and 4.B.

The spatial variation of F_3, the fraction of the load at the Moho, is shown in Figure 4.18. F_3 is low (< 0.18) throughout the map area except for western Montana and central Wyoming.

4.6 Discussions

Through the resultant T_e estimate from the free-air admittance method, we aim to investigate the effect of the velocity and density anomalies in the upper mantle. Our results indicate that the effects of the upper mantle heterogeneity on estimating T_e is very limited. The result is also compared with *Lowry et al.*'s [2000] T_e model from the Bouguer coherence method. The results from the free-air admittance and Bouguer coherence methods largely agree with each other, except for the range of T_e values in central Montana, the eastern SRP, and Yellowstone. We explore spatial correlations between our T_e map and the seismicity, tectonics, and cratonic provinces in the study area, and discuss the tectonic and geologic implications. The spatial variation in T_e estimate demonstrates a notable correlation between the ISB and areas of high-T_e gradient.

4.6.1 Correlation with Mantle Gravity Effect

In order to find the gravity effect from the upper mantle on the T_e estimate, a 2-D correlation analysis is performed. We find the correlation coefficient between the resultant T_e from the raw gravity data (Figure 4.17) and the mantle gravity effect from the upper mantle density heterogeneity (Figure 4.14). The result is $\rho = 0.56$, a positive moderate correlation. Because of a possibility that the moderate ρ value results from averaging zones of strong and weak correlations, we compute a spatial variation in ρ using a 500 km square submap centered at each 5 km spacing grid point. Figure 4.19 shows the resultant ρ variation. As a rough trend, the correlation is strong (>0.6) in the area of large T_e values (i.e., the eastern side of the map area in central Montana, western Wyoming, and northern Utah). Comparing with the map of the mantle gravity effect (Figure 4.14), T_e values are large where the magnitude of positive gravity effect is strong. One scenario that explains the correlation is that the stronger gravity effect from the denser high-V_p bodies causes an overestimate of T_e. The increased free-air gravity could indicate a larger uncompensated load, which translates into a larger apparent T_e estimate. The other potential causation is that the lower mantle temperature indicated by the high-V_p anomaly contributes to a thicker and stronger crust, resulting in a larger T_e. The combination of the two mechanisms is also possible. Figure 4.20 shows a T_e map from the corrected free-air anomaly data, which is given by subtracting the mantle gravity contribution from the raw gravity data. The map is nearly identical to the T_e map of the basic model using the raw gravity data. This sameness indicates that the mantle gravity effect on the T_e estimate is highly limited despite a certain level of correlation. Therefore, the rheological connection is a more probable explanation for the correlation than the potential T_e overestimation.

4.6.2 Effect of Thermal Elevation Correction

The effect of mantle mass anomaly is considered using the corrected elevation data obtained by subtracting the thermal elevation (Figure 4.15). Figure 4.21 shows the resultant T_e estimate of the model that uses the corrected elevation. Overall, the T_e variation is very similar to that of the basic model (Figure 4.17), which suggests that the effect of the thermal elevation correction is limited. One notable difference is that the low-T_e zone (~1-2 km) along the northwestern map limit in the basic model does not appear in the corrected elevation model (Figures 4.17 and 4.21). Where the anomalous zone lies, trends of T_e (~3-10 km) are smoothly continued from the surrounding area in the corrected elevation model. The difference in T_e value in the anomalous zone is limited (~1-2 km) between the two models. (Note that the color bar is in a logarithmic scale.) Still, this difference is notable because the results of the two models are virtually identical to each other in the rest of the map area. The values of thermal elevation in the low-T_e zone are not necessarily anomalous, and the relief is moderate (Figure 4.15). The zone is not spatially correlative with any known shallow geological features.

It is difficult to suggest causes for the difference unless it is determined whether the low-T_e zone reflects an edge effect or the actual variation in crustal strength. If this is an artifact, then these results indicate that applying the thermal elevation correction could improve the model by avoiding an edge effect. It is also possible that the removal of the potential artifact occurred merely by chance. If the low-T_e zone represents the actual variation in T_e, it implies that the thermal elevation correction may be improper for free-air admittance analyses as it masks the T_e variation in some areas. Including gravity and topography data from Canada in the spectral analysis will shed light on this issue.

4.6.3 Comparison with Lowry et al.'s T_e Estimate

One of the main purposes of this study is to compare the T_e estimates in the Northern Rockies from the free-air admittance method [*McKenzie and Fairhead*, 1997; *McKenzie*, 2003] and the Bouguer coherence method [*Forsyth*, 1985]. We find T_e using the former whereas *Lowry et al.* [1995; 2000] present the result from the latter.

The results from those two methods largely agree with each other (Figures 4.17 and 4.2). For both estimates, T_e is relatively larger to the east of the ISB and smaller to the west. The ISB coincides with the transition zone from the larger to smaller T_e. In both maps, T_e is slightly smaller in central Idaho than the surrounding areas. Major discrepancies are: (1) that in *Lowry et al.*'s [2000] result (hereafter, Lowry's), T_e in central Montana is larger than our result by ~10-15 km, and (2) that the SRP is delineated by the T_e variation in Lowry's map, although it is not in our result.

In Lowry's result from the Bouguer coherence method, T_e is ~20-35 km in central Montana (Figure 4.2), while the free-air admittance method found T_e in the area to be ~10-20 km. It is possible that the Bouguer coherence method overestimated the T_e. It occurs when internal loads with no topographic expression are significant, as the Bouguer coherence methods assume that all loads are expressed on the surface [*McKenzie*, 2003]. Figure 4.18 shows the variation in F_3, fractions of loads at Moho, calculated in our T_e estimation. It shows relatively higher F_3 in central Montana than the surrounding areas. If the internal loads indicated by the F_3 are unexpressed, the large T_e from the Bouguer coherence should be a result of overestimation.

A part of the relatively high F_3 in southwestern Montana may be caused by large ultramafic to mafic intrusive bodies. The Stillwater igneous complex and the Big Timber stock are the known exposures of such intrusive features in south-central Montana (Figure 4.18). The Stillwater complex is an exposure of a large layered mafic to ultramafic intrusion [e.g., *Hess*, 1960; *Jackson*, 1961; *Page*, 1979; *Raedeke and McCallum*, 1984]. Studies in mineralogy and petrology suggest that the Stillwater complex was a sizable subvolcanic magma reservoir [*Lipin*, 1993; *Helz*, 1995]. The Stillwater complex has undergone multiple episodes of deformation since its emplacement in the Archaean [*Jones et al.*, 1960; *Czamanske and Bohlen*, 1990]. The roof and top of the intrusive bodies were eroded in the early Cambrian and overlain by Phanerozoic sedimentary formations [*Jones et al.*, 1960, and references therein]. Later, the igneous complex was thrusted and uplifted in the Laramide time, and more recently, deeply incised by the formation of the Stillwater and Boulder rivers [*Jones et al.*, 1960, and references therein]. Because of the deformation history, it is likely that the coherence between the internal load and the topography is low, causing overestimated T_e in the coherence method. The Big Timber stock is another extensive intrusive body of Eocene age in south central Montana [e.g., *du Bray and Harlan*, 1996; *du Bray et al.*, 2006]. If other unexposed intrusive bodies, maybe coeval with the Stillwater complex, are also present in the larger surrounding areas, which is possible considering the stratigraphic position of the Stillwater complex and the limited exposure of the basement rock in the area [e.g., *Jones et al.*, 1960; *Foster et al.*, 2006], it would explain the F_3 distribution in our result and the large T_e in Lowry's estimate in central Montana.

In Lowry's map, T_e values are small (3-7 km) throughout the SRP compared to the surrounding areas (Figure 4.2). The weak crust can be explained by the strong low-velocity mantle anomaly below the SRP indicated by tomographic models [e.g., *Schmandt and Humphreys*, 2010; *Obrebski et al.*, 2011; *James et al.*, 2011; *Porritt et al.*, 2011; *Porritt et al.*, 2014] (Figure 4.4). In our result, the distribution of small T_e does not match the SRP; T_e increases from the western to eastern SRP (Figure 4.17). This discrepancy may be from the *P*-wave models used in T_e estimation. The *P*-wave velocity model that Lowry et al. used had spatial variation, whereas we applied a 1-D model to the whole study area.

Lowry et al. [2000] used a horizontally variable *P*-wave velocity model given from seismic refraction profiles, two of which crisscross the eastern SRP, in order to find crustal elevation (Figure 4.22). Here the crustal elevation represents elevation contribution from the isostatic response to crustal mass variations. *Lowry et al.* [2000] applied a correction by subtracting crustal elevation from the raw elevation. The crustal elevation is a function of the thickness and average density of the crust [*Lowry et al.*, 2000]. The density variation is given by converting the crustal refraction *P*-wave velocities using the continental velocity-density regression parameters by *Christensen and Mooney* [1995]. Their crustal elevation model clearly shows a downwarp at the SRP due to dense mafic intrusions along the hotspot track [*Mabey*, 1982; *McQuarrie and Rogers*, 1998]. This crustal elevation correction may have resulted in the T_e variation that suggests the weak eastern-SRP crust.

In order to calculate theoretical T_e values, we found the lower crust densities using a 1-D *P*-wave velocity model for western Montana [*Stickney*, 1984] and crustal thickness data given from the receiver function analysis [*IRIS DMC*, 2010; *Crotwell and Owens*, 2005]. The 1-D velocity model was applied to the whole study area, causing no horizontal variation. On the other hand, the crustal thickness data had horizontal variation (Figure 4.12). However, the density of the data points is insufficient to differentiate the SRP from the surrounding areas. This may be a result for the discrepancy in T_e variation in the eastern SRP.

Our result shows larger T_e (~8 km) in the eastern SRP than the central and western parts (Figure 4.17) even though the low-velocity mantle zone underlies the eastern SRP and Yellowstone (Figure 4.4), supposedly reducing brittle, seismogenic thickness. In fact, no apparent effect of the Yellowstone hotspot is shown in the pattern of T_e variation in both models of Lowry's and ours (Figures 4.2 and 4.17). This may suggest a balance between weakening due to the low-velocity zone and T_e overestimation due to uncompensated loads.

The underlying high-temperature mantle decreases T_e around Yellowstone [e.g., *Hyndman et al.*, 2009] while uncompensated young loads from Yellowstone volcanism cause the overestimation of T_e. Yellowstone, as a hotspot, is characterized by prominent positive free-air and geoid-height anomalies [*Tapley et al.*, 2005; *Roman et al.*, 2004]. The long-wavelength (~800 km) components of the positive anomalies result from the low-density plume and the topographic swell caused by the plume [*Crough*, 1978, 1983; *Richards et al.*, 1988; *Waschbusch and McNutt*, 1994; *Burov et al.*, 2007]. Those long-wavelength components have no effects on our spectral method because the diameter of each submap is 500 km (Figure 4.8). Instead, loads of relatively short wavelengths, which affect T_e estimation, probably represent uncompensated volcanic or plutonic loads [*Smith et al.*, 2009] because of their age range (1.3-0.07 Ma) [e.g., *Christiansen*, 2001]. Since the spectral methods for T_e estimation assume the long-term (>1 Ma) lithospheric elastic properties [e.g., *Cochran*, 1980], those uncompensated loads do cause the overestimation of

T_e. The weakening caused by the high-temperature mantle zone and the T_e overestimation due to the short-wavelength uncompensated loads may cancel each other to show no T_e signature in the Yellowstone area.

4.6.4 Correlation with the ISB

The spatial variation in T_e exhibits a correlation with the ISB. Most of the ISB seismicity occur in a zone of transition from low (<5 km) to high (>15 km) T_e (Figures 4.17 and 4.23). In the northern segment of the ISB, the wide (~120 km) transition zone corresponds to the spatially diffuse seismicity, whereas the narrow (~70 km) transition zone in the southern segment correlates with the concentrated seismicity (Figures 4.17 and 4.23ab). The variation in width of the transition zone and seismicity is consistent with the pattern of the differences in deformation style between the Great Basin section of the Basin and Range province and the Northern Rockies. Note that the T_e map from *Lowry et al.* [2000] (Figure 4.2) shows a narrow earthquake distribution along the northern ISB. Although they specify neither the time span nor the magnitude range for the plotted seismicity, it is evident that one or both of the parameters are small compared to the seismicity shown in our map of tectonic setting (Figure 4.3).

The relationship between T_e and seismogenic thickness T_s in the ISB is consistent with the analyses on other continental lithospheres. *Maggi et al.* [2000] demonstrate that T_s values of continental crusts are similar to or slightly smaller than the T_e in most continents. Through the result, they propose the “crème brûlée” model, in which the strength of a continental lithosphere resides in the top seismogenic layer, as opposed to the conventional view of the “jelly sandwich” model, which has strong lithospheric mantle [e.g., *Burov and*

Watts, 2006; *Kirby*, 2014]. *Maggi et al.* [2000] attribute the relatively weak mantle to water content. Our T_e estimate and the focal depth distribution agree with the prediction by Maggi et al. In the southern segment of the ISB, the values and changes in T_e and T_s are strikingly similar to each other (Figure 4.23b). For the northern segment, T_s is larger than T_e by ~10-15 km while T_e and T_s show the same along-profile increasing trend from west to east (Figure 4.23a). This relationship between T_e and T_s also signifies the difference between extensional areas north and south of the SRP. Figure 4.24 shows the depth difference between the focal depth of each earthquake and the T_e at each epicenter. In the area north of the SRP, the majority of the events occurred at greater depths than T_e while the most events along the ISB south of Yellowstone occurred within the range of T_e.

It is notable that the ISB seismicity correlates with the transition zone from low to high T_e rather than zones of low T_e (Figure 4.17). This implies a limited control on the location of the ISB from plate interactions. If plate interactions are responsible for the regional stress [cf. *Wernicke et al*., 1987; *Severinghaus and Atwater*, 1990; *Axen et al.*, 1993], the resultant strain would be accommodated in the weakest portions of the lithosphere [e.g., *Chen and Molnar*, 1983], which is indicated by zones of the lowest T_e. This is especially true for regions of extensional deformation because extensional strength of the lithosphere is linked to T_e by the common parameters [e.g., *Kusznir and Park*, 1987]. Nevertheless, this is not the case in the study area in both our result and *Lowry et al*.'s [2000]; the extension is accommodated in the zone of high T_e gradient rather than zones of the lowest T_e (Figure 4.17). Therefore, a local deformation mechanism is required to explain the ISB seismicity.

One possible mechanism is a lateral buoyancy variation, which has been proposed as a cause of intraplate extensional stresses [*Artyushkov*, 1973; *Zoback*, 1992]. In fact, the ISB spatially correlates with a major discontinuity in lithospheric buoyancy [*Smith and Arabasz*, 1991; *Lowry and Smith*, 1995]. *Lowry and Smith* [1995] suggest that the ISB seismicity is associated with the flux of low-viscosity crustal material caused by extensional stresses due to buoyancy gradients [*Bird*, 1991]. Another possible mechanism is the effect of upper mantle flow. Using mantle flow models, *Becker et al.* [2015] demonstrate the association between the ISB seismicity and the vertical normal stress change due to the underlying mantle flow.

4.6.5 Correlation with the Cratonic Provinces

There are several cratonic provinces in our study area as it is in a transition zone from the Precambrian cratons to Phanerozoic terranes. The spatial variation of our T_e estimate signifies differences in crustal strength between the Precambrian cratonic provinces, the Wyoming Craton and Great Falls tectonic zone. Our result also shows the contrast between the margin of the Phanerozoic accreted terranes and the surrounding areas.

Our T_e variation shows a zone of large T_e (~15-80 km), which extends from south central Montana to northwestern Colorado (Figure 4.17). This zone of large T_e coincides with the Wyoming craton (Figure 4.17). The large T_e values are consistent with the strong nature of the craton suggested by other studies. *Henstock et al.* [1998] reported on a long-range active seismic refraction survey conducted in 1995. The complete profile of the survey extended from the Colorado Plateau to southwestern Canada, longitudinally transecting the Wyoming craton. For the terrane, *Henstock et al.* [1998] found an anomalously large P_n

crossover distance (~260 km), which indicates a crust much thicker than the average. They also found high velocities (8.1-8.4 km/s) of P_n phases, which represent higher densities of the craton. Note that the average P_n crossover of continental crust is at ~150 km, and that the continental average of P_n velocity is ~8.1 km/s [e.g., *Mooney et al.*, 1998; *Christensen and Mooney*, 1995; *Tittgemeyer et al.*, 2000].

Compared to the high T_e in the Wyoming craton, the T_e range is small (~8-20 km) in the adjacent Great Falls tectonic zone (GFTZ; Figure 4.17) even though the tectonic zone formed in the Precambrian in common with the Wyoming craton [*O'Neill and Lopez*, 1985]. The smaller T_e values may hint that the GFTZ crust is weaker than that of Wyoming craton. The GFTZ has undergone deformation throughout the Phanerozoic [e.g., *O'neill and Lopez*, 1985; *Boerner et al.*, 1998; *Burberry and Palu*, 2016]. The fractures that formed in the development of the tectonic zone have been reactivated throughout the Phanerozoic, which has influenced the structural development of the younger superposing formations. Geologic and geophysical observations have found that the faults in the GFTZ: (1) have been recurrently reactivated to date, (2) influenced on the geometry and orientation of Late Cretaceous to early Tertiary igneous intrusions, and (3) controlled the uplift and orientation of an overlying thrust system even across the detachment [*O'neill and Lopez*, 1985; *Boerner et al.*, 1998; *Burberry and Palu*, 2016]. These deep-seated long-standing structural discontinuities developed and maintained by the histories of deformation could contribute to the small T_e values (Figure 4.17). However, the forecited tomographic models [*Dueker et al.*, 2001; *James et al.*, 2011; *Porritt et al.*, 2014] do not show a contrast in seismic velocity perturbation between the Wyoming craton and the GFTZ.

In the area to the immediate west of the WISZ, T_e is small (~3 km) compared to the surrounding areas (Figure 4.17). This zone of small T_e may suggest inherent crustal weakness due to the amalgamation of multiple terranes. In the relatively small area, at least three major Paleozoic-Mesozoic oceanic terranes are accreted against the Precambrian continental crust along the WISZ, causing faults and inhomogeneity [e.g., *Lund and Snee*, 1988; *Strayer et al.*, 1989; *Fleck and Criss*, 2004; *Dorsey and LaMaskin*, 2008]. Upon the accretions, at least two shear zones interacted in the area [*McClelland and Oldow*, 2007; *Giorgis et al.*, 2008]. The lithology associated with the accretion may also contribute to the lack of cohesion. Along the WISZ is the western Idaho ultramafic belt, which contains serpentinite and foliated chlorite-rich greenschist [e.g., *Hamilton*, 1963; *Vallier*, 1977; *Bonnichsen and Godchaux*, 1994]. Most of those "lubricating" ultramafic bodies are emplaced along the faults [*Bonnichsen and Godchaux*, 1994]. Although not dense, some seismicity occurs in the area (Figure 4.3), which indicates crustal strain being accommodated in the weak zone.

Conclusions

This study is the first to estimate T_e in the Northern Rockies using the free-air admittance method. The resultant estimate is compared with the distribution of the seismicity, upper mantle heterogeneity, and previous T_e estimates from the Bouguer coherence method. The following is a summary of the major results and their implications.

1. As a general trend, T_e estimates are larger than 13 km to the east of the ISB and smaller to the west. The area of the largest T_e (~15-75 km) appears in central to western Wyoming. T_e is relatively smaller (~13-15 km) in western Montana. Most of

the ISB seismicity occur in a zone of transition from low (<5 km) to high (>15 km) T_e.

2. The result after applying the thermal elevation correction is very similar to the basic model, which used the raw elevation data, indicating the limited effect from the correction.
3. The 2-D correlation between the T_e variation and mantle gravity effect is strong (>0.6) in the area of large T_e values (i.e., the eastern side of the map area in central Montana, western Wyoming, and northern Utah). T_e values are large where the magnitude of positive gravity effect is strong. This trend indicates an overestimate of T_e caused by the high-density mantle, and/or a strengthened lithosphere due to the underplating lower temperature mantle.
4. The resultant T_e variation largely agrees with the estimate from the Bouguer coherence method. A notable discrepancy is the ~10-15 km larger T_e estimates in south central Montana from the Bouguer coherence method. These larger values may result from an overestimate from the Bouguer coherence method that assumes that all loads are expressed on the surface. Our result indicates relatively large internal loads in the area, which may be due to large ultramafic to mafic intrusive bodies.
5. In the southern segment of the ISB, the values and changes in T_e and T_s are similar to each other as predicted. For the northern segment, T_s is larger than T_e by ~10-15 km while T_e and T_s show the same along-profile trend. This relationship between T_e and T_s may signify the difference between extensional areas north and south of the SRP.
6. The spatial variation in our T_e estimate correlates with some Cratonic provinces. The zone of large T_e (~15-80 km), which extends from south central Montana to

northwestern Colorado, correlates with the Wyoming craton, which has a thick dense crust. The relatively small T_e range (~8-20 km) in the Great Falls tectonic zone may suggest a weaker crust resulted from repeated deformations throughout the Phanerozoic. In the area to the immediate west of the WISZ, T_e is small (~3 km) compared to the surrounding areas, which may suggest inherent crustal weakness due to the amalgamation of multiple terranes.

References

Airy, G. B. (1855), On the computation of the effect of the attraction of mountain-masses, as disturbing the apparent astronomical latitude of stations of geodetic surveys, *Phil. Trans. R. Soc.*, *145*, 101–104.

Anders, M. H., J. W. Geissman, L. A. Piety, and J. T. Sullivan (1989), Parabolic distribution of circumeastern Snake River Plain seismicity and latest Quaternary faulting: Migratory pattern and association with the Yellowstone hotspot, *J. Geophys. Res.*, *94*(B2), 1589–1621, doi:10.1029/JB094iB02p01589.

Arabasz, W. J., J. C. Pechmann, and E. D. Brown (1992), Observational seismology and the evaluation of earthquake hazards and risk in the Wasatch front area, *U.S. Geol. Surv. Prof. Pap.*, *1500*-D.

Armstrong, G. D., and A. B. Watts (2001), Spatial variations in T_e in the southern Appalachians, eastern United States, *J. Geophys. Res.*, *106*(B10), 22009–22026, doi:10.1029/2001JB000284.

Banks, R. J., R. L. Parker, and S. P. Huestis (1977), Isostatic compensation on a continental scale: Local versus regional mechanisms, *Geophys. J. R. Astr. Soc.*, *51*(2), 431–452, doi:10.1111/j.1365-246X.1977.tb06927.x.

Banks, R. J., S. C. Francis, and R. G. Hipkin (2001), Effects of loads in the upper crust on estimates of the elastic thickness of the lithosphere, *Geophys. J. Int.*, *145*(1), 291–299, doi:10.1046/j.0956-540x.2001.01380.x.

Barnett, D. N., F. Nimmo, and D. McKenzie (2002), Flexure of Venusian lithosphere measured from residual topography and gravity, *J. Geophys. Res.*, *107*(E2), doi:10.1029/2000JE001398.

Barrel, J. (1914), The strength of the Earth's crust. I. Geologic tests of the limits of strength, *J. Geol.*, *22*, 22–48.

Barrientos, S. E., R. S. Stein, and S. N. Ward (1987), Comparison of the 1959 Hebgen Lake, Montana and the 1983 Borah Peak, Idaho, earthquakes from geodetic observations, *Bull. Seism. Soc. Am.*, *77*(3), 784–808.

Birch, F. (1964), Density and composition of mantle and core, *J. Geophys. Res.*, *69*(20), 4377–4388, doi:10.1029/JZ069i020p04377.

Blackman, R. B., and J. W. Tukey (1958), The Measurement of Power Spectra from the Point of View of Communications Engineering - Part I,. *Bell Syst. Tech. J.*, *37*(1), 185–282. doi:10.1002/j.1538-7305.1958.tb03874.x.

Bowie, W (1927), Isostasy – The Science of the Equilibrium of the Earth's Crust, New York, E. P. Dutton, 275 p.

Burov, E. B., and M. Diament (1995), The effective elastic thickness (T_e) of continental lithosphere: What does it really mean?, *J. Geophys. Res.*, *100*(B3), 3905–3927, doi:10.1029/94JB02770.

Burov, E. B., and A. B. Watts (2006), The long-term strength of continental lithosphere: "jelly sandwich" or "crème brûlée"?, *GSA Today*, *16*, 4–11.

Byrd, J. O. D., R. B. Smith, and J. W. Geissman (1994), The Teton fault, Wyoming: Topographic signature, neotectonics, and mechanisms of deformation, *J. Geophys. Res.*, *99*(B10), 20095–20122, doi:10.1029/94JB00281.

Cochran, J. R. (1980), Some remarks on isostasy and long-term behavior of the continental lithosphere, *Earth Planet. Sci. Lett.*, *46*(2), 266–274, doi:10.1016/0012-821X(80)90012-6.

Chapman, D., and H. Pollack (1977), Regional geotherms and lithospheric thickness, *Geology*, *5*(5), 265–268, doi:10.1130/0091-7613(1977)5<265:RGALT>2.0.CO;2.

Chen, W.-P., and P. Molnar (1983), Focal depths of intracontinental and intraplate earthquakes and their implications for the thermal and mechanical properties of the lithosphere, *J. Geophys. Res.*, *88*(B5), 4183–4214, doi:10.1029/JB088iB05p04183.

Christensen, N. I., and W. D. Mooney (1995), Seismic velocity structure and composition of the continental crust: A global view, *J. Geophys. Res.*, *100*(B6), 9761–9788, doi:10.1029/95JB00259.

Christiansen, R. L. (2001), The Quaternary and Pliocene Yellowstone plateau volcanic field of Wyoming, Idaho, and Montana, *U.S. Geol. Surv. Prof. Pap.*, *729-G*, 145.

Crosby, A. G. (2007), An assessment of the accuracy of admittance and coherence estimates using synthetic data, *Geophys. J. Int.*, *171*, 25–54, doi:10.1111/j.1365-246X.2007.03520.x.

Crosby, A., and D. McKenzie (2005), Measurements of the elastic thickness under ancient lunar terrain, *Icarus*, *173*(1), 100–107, doi:10.1016/j.icarus.2004.07.017.

Crotwell, H. P., and T. J. Owens (2005), Automated receiver function processing, *Seism. Res. Lett.*, *76*(6), 702–708, doi:10.1785/gssrl.76.6.702.

Dewey, J. W., W. H. Dillinger, J. Taggart, and S. T. Algermissen (1973), A technique for seismic zoning: analysis of earthquake locations as mechanisms in northern Utah, Wyoming, Idaho and Montana, *National Oceanic and Atmospheric Administration Technical Report ERL267-ESL30*, 28–48.

Dorman, L. M., and B. T. R. Lewis (1970), Experimental isostasy: 1. Theory of the determination of the Earth's isostatic response to a concentrated load, *J. Geophys. Res.*, *75*(17), 3357–3365, doi:10.1029/JB075i017p03357.

Doser, D. I. (1985), Source parameters and faulting processes of the 1959 Hebgen Lake, Montana, earthquake sequence, *J. Geophys. Res.*, *90*(B6), 4537–4555, doi:10.1029/JB090iB06p04537.

Doser, D. I. (1989), Source parameters of Montana earthquakes (1925-1964) and tectonic deformation in the northern Intermountain Seismic Belt, *Bull. Seism. Soc. Am.*, *79*(1), 31–51.

Doser, D. I., and R. B. Smith (1983), Seismicity of the Teton–southern Yellowstone region Wyoming, *Bull. Seism. Soc. Am.*, *73*(5), 1369–1494.

Doser, D. I., and R. B. Smith (1985), Source parameters of the 28 October 1983 Borah Peak, Idaho, Earthquake from body wave analysis, *Bull. Seism. Soc. Am.*, *75*(4), 1041–1051.

Dutton, C. E. (1880), Geology of the High Plateaus of Utah, *U.S. Geol. Surv. Rocky Mtn. Region.* 307 pp.

Dziewonski, A. M. and D. L. Anderson (1981) Preliminary reference Earth model, *Phys. Earth Planet. Inter.*, *25*, 297–356, doi:10.1016/0031-9201(81)90046-7.

Eaton, G. P. (1979a), A plate-tectonic model for late Cenozoic crustal spreading in the western United States. in *Rio Grande Rift: Tectonics and Magmatism*, ed. R. E. Riecker, pp. 7–32. Washington DC: Am. Geophys. Union.

Eaton, G. P. (1979b), Regional geophysics, Cenozoic tectonics, and geologic resources of the Basin and Range Province and adjoining regions, in *1979 Basin and Range Symposium*, eds. G. W. Newman, and H. D. Goode, pp. 11–39. Denver, Colo: Rocky Mtn. Assoc. Geol. and Utah Geol. Assoc.

Ebinger, C. J., T. D. Bechtel, D. W. Forsyth, and C. O. Bowin (1989), Effective elastic plate thickness beneath the East African and Afar plateaus and dynamic compensation of the uplifts, *J. Geophys. Res.*, *94*(B3), 2883–2901, doi:10.1029/JB094iB03p02883.

Farrell, J., R. B. Smith, S. Husen, and T. Diehl (2014), Tomography from 26 years of seismicity revealing that the spatial extent of the Yellowstone crustal magma reservoir extends well beyond the Yellowstone caldera, *Geophys. Res. Lett.*, *41*, 3068–3073, doi:10.1002/2014GL059588.

Fenneman, N. M. (1928) Physiographic divisions of the United States, *Ann. Assoc. Am. Geog. 3rd ed.*, 261-353.

Fenneman, N. M. (1931) *Physiography of Western United States*, McGraw-HilI, New York.

Fenneman, N. M. (1946), Physical divisions of the United States, map, 1:7,000,000 scale, *U.S. Geol. Surv.*, Reston, VA.,

Forsyth, D. W. (1985), Subsurface loading and estimates of the flexural rigidity of continental lithosphere, *J. Geophys. Res.*, *90*(B14), 12623–12632, doi:10.1029/JB090iB14p12623.

Foster, D. A., P. A. Mueller, D. W. Mogk, J. L. Wooden, and J. L. Vogl (2006), Proterozoic evolution of the western margin of the Wyoming craton: Implications for the tectonic and magmatic evolution of the northern Rocky Mountains, *Can. J. Earth Sci.*, *43*(10), 1601–1619, http://dx.doi.org/10.1139/E06-052.

Gilbert, G. K. (1874), Preliminary geologic report, expedition of 1872, *U.S. Geog. And Geol. Surv, Progress Rept.*

Gilbert, G. K. (1875), Report on the geology of portions of Nevada, Utah, Galifornia, and Arizona, examined in the years 1871 and 1872, *U.S. Geog. And Geol. Surv, Rept.*, *3*.

Gilbert, G. K. (1890), The strength of the Earth's crust, *Geol. Soc. Am. Bull.*, *1*, 23–27.

Gilbert, G. K. (1890), Lake Bonneville, *U.S. Geol. Surv. Mem.*, *1*, Washington DC, Government Printing Office, 438 pp.

Godson, R., and D. Plouff (1988), BOUGUER version 1.0—A microcomputer gravity-terrain-correction program, U.S. Geol. Surv. Open File Rep., 88-644-A-C.

Gunn, R. (1937), A quantitative study of mountain building on an unsymmetrical Earth, *J. Franklin Inst.*, *224*, 19–53.

Gunn, R. (1943a), A quantitative evaluation of the influence of the lithosphere on the anomalies of gravity, *J. Franklin Inst.*, *236*, 47–65.

Gunn, R. (1943b), A quantitative study of isobaric equilibrium and gravity anomalies in the Hawaiian Islands, *J. Franklin Inst.*, *236*, 373–390.

Han, U., and D. Chapman (1995), Thermal isostasy: Elevation changes of geologic provinces, *J. Geol. Soc. Korea*, *31*, 106–115.

Harris, F. J. (1978), On the use of windows for harmonic analysis with the discrete Fourier transform, *Proc. IEEE.*, *66*(1), 51–83, doi:10.1109/PROC.1978.10837.

Harrison, J. E., A. B. Griggs, and J. D. Wells (1974), Tectonic features of the Precambrian Belt basin and their influence on post-Belt structures, *U.S. Geol. Surv. Prof. Pap.*, *866*.

Hasterok, D., and D. S. Chapman (2007), Continental thermal isostasy: 1. Methods and sensitivity, *J. Geophys. Res.*, *112*, B06414, doi:10.1029/2006JB004663.

Hinze, W. J., D. J. Allen, A. J. Fox, D. Sunwood, T. Woelk, and A. G. Green (1992), Geophysical investigations and crustal structure of the North American Midcontinent Rift system, *Tectonophysics*, *213*(1-2), 17–31, doi:10.1016/0040-1951(92)90248-5.

Hoogenboom, T., and S. E. Smrekar (2006), Elastic thickness estimates for the northern lowlands of Mars, *Earth Planet*. *Sci*. *Lett*., *248*(3–4), 830–839, doi:10.1016/j.epsl.2006.06.035.

Hoogenboom, T., S. E. Smrekar, F. S. Anderson, and G. Houseman (2004), Admittance survey of type 1 coronae on Venus, *J. Geophys. Res.*, *109*, E03002, doi:10.1029/2003JE002171.

Huang, H.-H., F.-C. Lin, B. Schmandt, J. Farrell, R. B. Smith, and V. C. Tsai (2015), The Yellowstone magmatic system from the mantle plume to the upper crust, *Science*, *348*(6236), doi:10.1126/science.aaa5648.

IRIS DMC (2010), Data Services Products: EARS EarthScope Automated Receiver Survey, doi:10.17611/DP/EARS.1.

James, D. E., M. J. Fouch, R. W. Carlson, and J. B. Roth (2011), Slab fragmentation, edge flow and the origin of the Yellowstone hotspot track, *Earth Planet. Sci. Lett.*, *311*(1–2), 124–135, doi:10.1016/j.epsl.2011.09.007.

Jones, C. H., B. P. Wernicke, G. L. Farmer, J. D. Walker, D. S. Coleman, L. W. McKenna, and F. V. Perry (1992), Variations across and along a major continental rift: an interdisciplinary study of the Basin and Range Province, western USA. *Tectonophysics*, *213*(1-2), 57–96, doi:10.1016/0040-1951(92)90252-2.

Jeffreys, H. (1926), On the nature of isostasy: *Beitrage zur Geophysik*, *XV*(2), 153–174.

King, C. (1878), U.S. Geol. Expl. 40th Par. Rep., *1*. 803 pp.

Kirby, J. F. (2014), Estimation of the effective elastic thickness of the lithosphere using inverse spectral methods: The state of the art, *Toctonophysics*, *631*, 87–116, doi:10.1016/j.tecto.2014.04.021.

Kirby, J. F., and C. J. Swain (2009), A reassessment of spectral T_e estimation in continental interiors: The case of North America, *J. Geophys. Res.*, *114*, B08401, doi:10.1029/2009JB006356.

Kirby, J. F., and C. J. Swain (2013), Power spectral estimates using two-dimensional Morlet-fan wavelets with emphasis on the long wavelengths: jackknife errors, bandwidth resolution and orthogonality properties, *Geophys. J. Int.*, *194*(1), 78–99, doi:10.1093/gji/ggt103.

Kirby, J. F., and C. J. Swain (2014), The long-wavelength admittance and effective elastic thickness of the Canadian Shield, *J. Geophys. Res. Solid Earth*, *119*, 5187–5214, doi:10.1002/2013JB010578.

Lewis, B. T. R., and L. M. Dorman (1970), Experimental isostasy: 2. An isostatic model for the U.S.A. derived from gravity and topographic data, *J. Geophys. Res.*, *75*(17), 3367–3386, doi:10.1029/JB075i017p03367.

Love, A. E. H. (1906), *A Treatise on the Mathematical Theory of Elasticity*, Cambridge University Press, London.

Lowry, A. R., and R. B. Smith (1994), Flexural rigidity of the Basin and Range-Colorado Plateau-Rocky Mountain transition from coherence analysis of gravity and topography, *J. Geophys. Res.*, *99*(B10), 20123–20140, doi:10.1029/94JB00960.

Lowry, A. R., and R. B. Smith (1995), Strength and rheology of the western U.S. Cordillera, *J. Geophys. Res.*, *100*(B9), 17947–17963, doi:10.1029/95JB00747.

Lowry, A. R., N. M. Ribe, and R. B. Smith (2000), Dynamic elevation of the Cordillera, western United States, *J. Geophys. Res.*, *105*(B10), 23371–23390, doi:10.1029/2000JB900182.

Lyon-Caen, H., and P. Molnar (1983), Constraints on the structure of the Himalaya from an analysis of gravity anomalies and a flexural model of the lithosphere, *J. Geophys. Res.*, *88*(B10), 8171–8191, doi:10.1029/JB088iB10p08171.

Mabey, D. R. (1982), Geophysics and tectonics of the Snake River Plain, Idaho, in Cenozoic Geology of Idaho, edited by B. Bonnichsen and R.M. Breckenridge, *Bull. Idaho Bur. Mines Geol.*, *26*, 139–153.

Machette, M. N., S. F. Personius, A. R. Nelson, D. P. Schwartz, and W. R. Lund (1991), The Wasatch fault zone Utah: segmentation and history of Holocene earthquakes, *J. Struct. Geol.*, *13*(2), 137–149, doi:10.1016/0191-8141(91)90062-N.

Maggi, A., J. A. Jackson, D. McKenzie, and K. Priestley (2000), Earthquake focal depths, effective elastic thickness, and the strength of the continental lithosphere, *Geology*, *28*(6), 495–498, doi:10.1130/0091-7613(2000)28<495:EFDEET>2.0.CO;2.

Mancinelli, P., A. C. Mondini, C. Pauselli, and C. Federico (2015), Impact and admittance modeling of the Isidis Planitia, Mars, *Planet. Space Sci.*, *117*, 73–81, doi:10.1016/j.pss.2015.04.019.

McCalpin, J. P., and S. P. Nishenko (1996), Holocene paleoseismicity, temporal clustering, and probabilities of future large (M > 7) earthquakes on the Wasatch fault zone, Utah, *J. Geophys. Res.*, *101*(B3), 6233–6253, doi:10.1029/95JB02851.

McKenzie, D. (2003), Estimating T_e in the presence of internal loads, *J. Geophys. Res.*, *108*(B9), 24–38, doi:10.1029/2002JB001766.

McKenzie, D. (2010), The influence of dynamically supported topography on estimates of T_e, *Earth Planet. Sci. Lett.*, *295*(1–2), 127–138, doi:10.1016/j.epsl.2010.03.033.

McKenzie, D., and C. Bowin (1976), The relationship between bathymetry and gravity in the Atlantic Ocean, *J. Geophys. Res.*, *81*(11), 1903–1915, doi:10.1029/JB081i011p01903.

McKenzie, D., and D. Fairhead (1997), Estimates of the effective elastic thickness of the continental lithosphere from Bouguer and free air gravity anomalies, *J. Geophys. Res.*, *102*(B12), 27523–27552, doi:10.1029/97JB02481.

McNutt, M. K., and R. L. Parker (1978), Isostasy in Australia and the evolution of the compensation mechanism, *Science*, *199*(433), 773–775, doi:10.1126/science.199.4330.773.

McQuarrie, N., and D. W. Rodgers (1998), Subsidence of a volcanic basin by flexure and lower crustal flow: The eastern Snake River Plain, Idaho, *Tectonics*, *17*(2), 203–220, doi:10.1029/97TC03762.

Mouthereau, F., A. Watts, and E. Burov (2013), Structure of orogenic belts controlled by lithosphere age, *Nat. Geosci.*, *6*, 785–789, doi:10.1038/ngeo1902.

Nagihara, S., C. Lister, and J. Sclater (1996), Reheating of old oceanic lithosphere: Deductions from observations, *Earth Planet. Sci. Lett.*, *139*(1-2), 91–104, doi:10.1016/0012-821X(96)00010-6.

Obrebski, M., R. M. Allen, F. Pollitz, and S. H. Hung (2011), Lithosphere-asthenosphere interaction beneath the western United States from the joint inversion of body-wave traveltimes and surface-wave phase velocities, *Geophys. J. Int.*, *185*(2), 1003–1021, doi:10.1111/j.1365-246X.2011.04990.x.

Ojeda, G. Y., and D. Whitman (2002), Effect of windowing on lithosphere elastic thickness estimates obtained via the coherence method: Results from northern South America, *J. Geophys. Res.*, *107*(B11), 2275, doi:10.1029/2000JB000114.

Pan American Center for Earth & Environmental Studies 2015, Gravity Database of the US - Office of Research and Sponsored Projects. Available at: http://research.utep.edu/default.aspx?tabid=37229 (accessed 1 October 2015).

Pankow, K. L., M. Stickney, K. D. Koper, and K. M. Whidden (2014), The 2014 Challis, Idaho Earthquake Swarm, in 2014 AGU Fall Meeting, 2014 Dec 15–19, San Francisco, California.

Pardee, J. T. (1926), The Montana earthquake of June 27, 1925, *U.S. Geol. Surv. Prof. Pap.*, *147*, 7–23.

Pardee, J. T. (1950), Late Cenozoic block faulting in western Montana, *Geol. Soc. Am. Bull.*, *61*(4), 359–406, doi:10.1130/0016-7606(1950)61[359:LCBFIW]2.0.CO;2.

Pérez-Gussinyé, M., A. R. Lowry, A. B. Watts, and I. Velicogna (2004), On the recovery of effective elastic thickness using spectral methods: Examples from synthetic data and from the Fennoscandian Shield, *J. Geophys. Res.*, *109*, B10409, doi:10.1029/2003JB002788.

Pérez-Gussinyé, M., and A. B. Watts (2005), The long-term strength of Europe and its implications for plate-forming processes, *Nature*, *436*, 381–384, doi:10.1038/nature03854.

Petersen, M. D., A. D. Frankel, S. C. Harmsen, C. S. Mueller, K. M. Haller, R. L. Wheeler, R. L. Wesson, Y. Zeng, O. S. Boyd, D. M. Perkins, N. Luco, E. H. Field, C. J. Wills, and K. S. Rukstales (2008), Documentation for the 2008 Update of the United States National Seismic Hazard Maps, *U.S. Geol. Surv. Open File Rep., 2008–1128*.

Plouff, D. (1966), Digital terrain corrections based on geographic coordinates (abs.), *Geophysics*., *31*(6), 1208.

Porritt, R. W., R. M. Allen, D. C. Boyarko, M. R. Brudzinski (2011), Investigation of Cascadia segmentation with ambient noise tomography, *Earth Planet. Sci. Lett.*, *309*(1–2), 67–76, doi:10.1016/j.epsl.2011.06.026.

Porritt, R. W., R. M. Allen, and F. F. Pollitz (2014), Seismic imaging east of the Rocky Mountains with USArray, *Earth Planet. Sci. Lett.*, *402*, 16–25, doi:10.1016/j.epsl.2013.10.034.

Pratt, J. H. (1855), On the attraction of the Himalaya mountains, and of the elevated regions beyond them, upon the plumb line in India, *Phil. Trans. R. Soc.*, *145*, 53–100.

Prezzi, C., M. P. I. Llanos, H.-J. Götze, and S. Schmidt 2014, Thermal and geodynamic contributions to the elevation of the Altiplano–Puna plateau, *Phys. Earth Planet. Inter.*, *237*, 51–64, doi:10.1016/j.pepi.2014.10.002.

Putnam, G. R. (1930), Isostatic compensation in relation to geological problems, *J. Geol.*, *38*, 590–599.

Qamar, A., and B. Hawley (1979), Seismic activity near the Three Forks basin, Montana, *Bull. Seism. Soc. Am.*, *69*(6), 1917–1929.

Richins, W. D., J. C. Pechmann, R. B. Smith, C. J. Langer, S. K. Goter, J. E. Zollweg, and J. J. King (1987), The 1983 Borah Peak, Idaho, earthquake and its aftershocks, *Bull. Seism. Soc. Am.*, *77*(3), 694–723.

Ryall, A. (1962), The Hebgen Lake Montana, earthquake of August 17, 1959: *P* waves, *Bull. Seism. Soc. Am.*, *52*(2), 235–271.

Schmandt, B., and E. Humphreys (2010), Complex subduction and small-scale convection revealed by body-wave tomography of the western United States upper mantle, *Earth Planet. Sci. Lett.*, *297*(3–4), 435–445, doi:10.1016/j.epsl.2010.06.047.

Severinghaus, J., and T. Atwater (1990), Cenozoic geometry and thermal state of the subducting slabs beneath western North America, in Basin-Range Extensional Tectonics Near the Latitude of Las Vegas, Nevada, edited by B. P. Wernicke, *Mem. Geol. Soc. Am.*, *176*, 1-22.

Sibson, R. (1981), A brief description of natural neighbor interpolation, in *Interpreting Multivariate Data*, edited by V. Barnett, pp. 21–36, John Wiley, New York.

Simons, F. J., M. T. Zuber, and J. Korenaga (2000), Isostatic response of the Australian lithosphere: Estimation of effective elastic thickness and anisotropy using multitaper spectral analysis, *J. Geophys. Res.*, *105*(B8), 19163–19184, doi:10.1029/2000JB900157.

Smith, J. G. (1965), Fundamental transcurrent faulting in northern Rocky Mountains, *Am. Assoc. Petrol. Geol. Bull*, *49*(9), 1398–1409.

Smith, R. B., and W. J. Arabasz (1991) Seismicity of the Intermountain seismic belt, in D. B. Slemmons, E. R. Engdahl, M. D. Zoback, and D. D. Blackwell, eds., GSA Decade Map Vol. 1, 185–228.

Smith, R. B., and M. L. Sbar (1974), Contemporary tectonics and seismicity of the western United States with emphasis on the Intermountain Seismic Belt, *Geol. Soc. Am. Bull.*, *85*(8), 1205–1218, doi:10.1130/ 0016–7606(1974)85<1205:CTASOT>2.0.CO;2.

Smith, R. B., W. D. Richins, and D. I. Doser (1985), The 1983 Borah Peak, Idaho, earthquake: Regional seismicity, kinematics of faulting, and tectonic mechanism, *U.S. Geol. Surv. Open File Rep.*, *85-290*, 236–263.

Smith, R. B., J. O. D. Byrd, and D. D. Susong (1990), Neotectonics and structural evolution of the Teton fault, in Geologic field tours of western Wyoming and parts of adjacent Idaho, Montana, and Utah edited by S. Roberts, *Goological Survey of Wyoming Public Information Circular*, *29*, 126–138.

Smith, R. B., J. O. D. Byrd, and D. D. Susong (1993), The Teton fault, Wyoming: Seismotectonics, Quaternary history, and earthquake hazards, in Geology of Wyoming edited by A. W. Snoke, J. R. Steidtmann, S. M. Roberts, *Geological Survey of Wyoming Memoir*, *5*, 628–667.

Smith, R. B., M. Jordan, B. Steinberger, C. M. Puskas, J. Farrell, G. P. Waite, S. Husen, W.-L. Chang, and R. O'Connell (2009), Geodynamics of the Yellowstone hotspot and mantle plume: Seismic and GPS imaging, kinematics, and mantle flow, *J. Volcanol. Geotherm. Res.*, *188*(1-3), 26–56, doi:10.1016/j.jvolgeores.2009.08.020.

Sprenke, K. F., and R. M. Breckenridge (1992), Seismic intensities in Idaho, *Idaho Geological Survey Information Circular*, *50*, 36p.

Stevenson, P. R. (1976), Microearthquakes at Flathead Lake, Montana: A study using automatic earthquake processing, *Bull. Seism. Soc. Am.*, *66*(1), 61–80.

Stewart, J. H. (1978), Basin-range structure in western North America, a review. in *Cenozoic Tectonics and Regional Geophysics of the Western Cordillera*, eds. R. B. Smith, G. P. Eaton, *Geol. Soc. Am. Mem. 152*.

Stickney, M. C. (1978), Seismicity and faulting of central western Montana, *Northwest Geology*, *7*, 1–9.

Stickney, M. C. (1980), Seismicity and gravity studies of faulting in the Kalispell valley, northwestern Montana, M.S. thesis, Univ. of Montana, Missoula, Montana, U.S.A.

Stickney, M. C. (1984), P-wave traveltimes and crustal structure of SW Montana from aftershocks of the October 28, 1983 Borah Peak, Idaho, Earthquake, U.S. Geologic Survey, Proceedings of Workshop.

Stickney, M. C., and M. J. Bartholomew (1987), Seismicity and late Quaternary faulting of the northern Basin and Range Province, Montana and Idaho, *Bull. Seism. Soc. Am.*, *77*(5), 1602–1625.

Swan, F. H., III, D. P. Schwartz, and L. S. Cluff (1980), Recurrence of moderate to large magnitude earthquakes produced by surface faulting on the Wasatch fault zone, Utah, *Bull. Seism. Soc. Am.*, *70*(5), 1431–1462.

Tocher, D. (1962), The Hebgen Lake, Montana, earthquake of August 17, 1959, MST, *Bull. Seism. Soc. Am.*, *52*(2), 153–162.

Turcotte, D., and G. Schubert (2002), *Geodynamics*, Cambridge Univ. Press, New York, NY.

Vening Meinesz, F. A. (1931), Une nouvelle method pour la réduction isostatique régionale de l'intensité de la pesanteur, *Bull. Géodésique*, *29*, 33–51.

Walcott, R. I. (1970), Flexural rigidity, thickness, and viscosity of the lithosphere, *J. Geophys. Res.*, *75*(20), 3941–3954, doi:10.1029/JB075i020p03941.

Watts, A. B. (2001), *Isostasy and Flexure of the Lithosphere*, Cambridge Univ. Press, New York, NY.

Watts, A.B., and E. B. Burov (2003), Lithospheric strength and its relationship to the elastic and seismogenic layer thickness. *Earth Planet. Sci. Lett.*, *213*(1-2), 113–131, doi:10.1016/S0012-821X(03)00289-9.

Weidman, R. M. (1965), The Montana lineament, in Geology of the Flint Creek Range, Montana, Billings Geological Society 16th Annual Field Conference Guidebook, 137–143.

Wernicke, B. P., R. L. Christiansen, P. C. England, and L. J. Sonder (1987), Tectonomagmatic evolution of Cenozoic extension in the North American Cordillera, in Continental Extensional Tectonics, edited by M. P. Coward, J. F. Dewey, and P. L. Hancock, Geol. Soc. Spec. Publ. London, 28, 203–221.

Witkind, I. J., J. B. Hadley, and W. H. Nelson (1964), Pre-Tertiary stratigraphy and structure of the Hebgen Lake area, *U.S. Geol. Surv. Prof. Pap.*, *435*, 199–208.

Zollweg, J. E., and W. D. Richins (1985), Later aftershocks of the 1983 Borah Peak, Idaho, earthquake and related activity in central Idaho, *U.S. Geol. Surv. Open File Rep.*, *85-290*, 345–367.

Zuber, M. T., T. D. Bechtel, and D. W. Forsyth (1989), Effective elastic thicknesses of the lithosphere and mechanisms of isostatic compensation in Australia, *J. Geophys. Res.*, *94*(B7), 9353–9367, doi:10.1029/JB094iB07p09353.

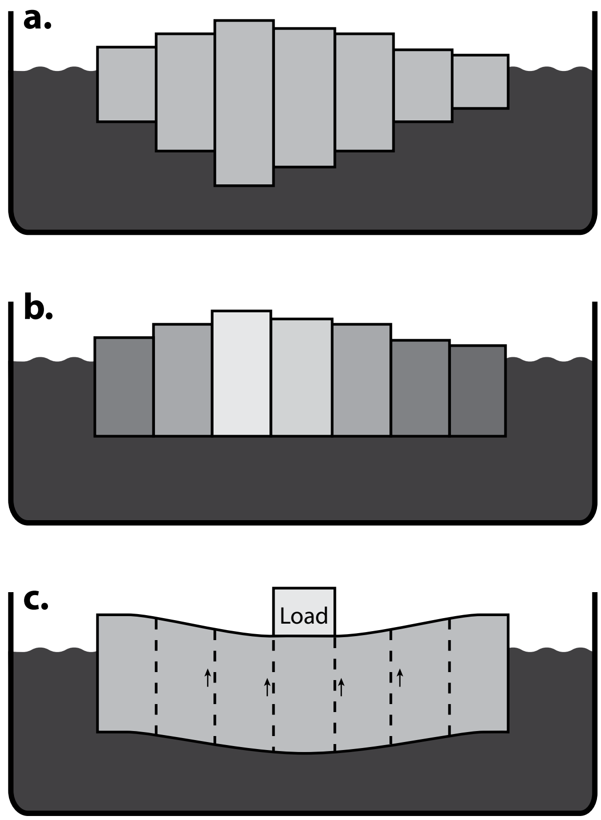

Figure 4.1. Local compensation models by (a) Airy and (b) Pratt (modified from Bowie, 1927), and (c) the regional compensation model. Gray scale indicates density variation of substances. In Airy's model, compensation is achieved by thickening a uniform density crust. Pratt's model assumes a constant compensation depth achieved by lateral changes in crustal density. In the regional compensation model, a loaded column drags down its adjacent columns through vertical shear stress (vertical arrows) [*Gunn*, 1943a] because the columns are mechanically attached to each other.

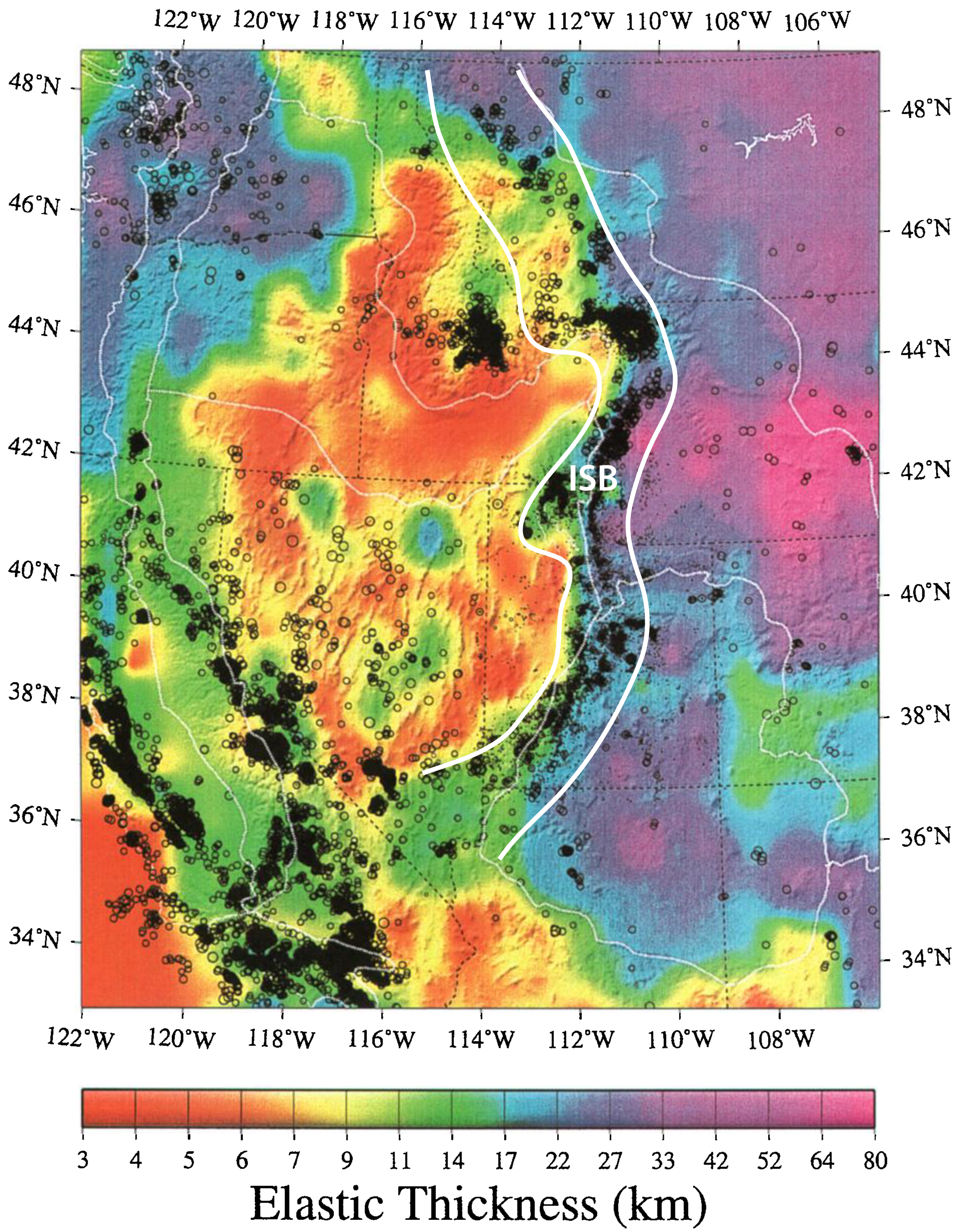

Figure 4.2. Effective elastic thickness T_e in the western U.S. from the Bouguer coherence method [from *Lowry et al.*, 2000]. The Intermountain Seismic Belt (ISB) coincides with an area of high gradient in T_e.

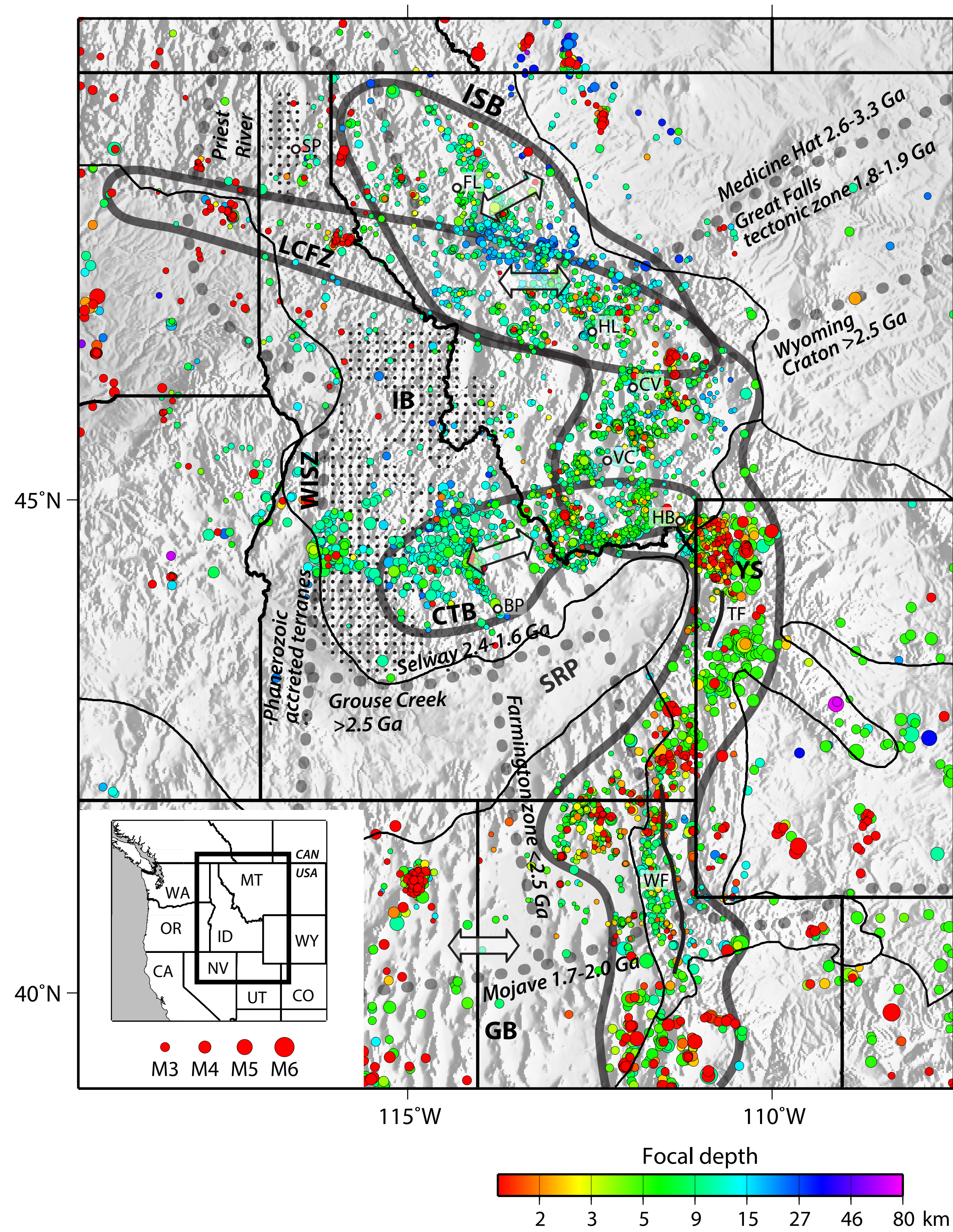
ISB
Priest River
SP
FL
Medicine Hat 2.6-3.3 Ga
Great Falls tectonic zone 1.8-1.9 Ga
LCFZ
HL
Wyoming Craton >2.5 Ga
CV
IB
VC
WISZ
45˚N
HB
YS
CTB
BP
TF
Phanerozoic accreted terranes
Selway 2.4-1.6 Ga
SRP
Grouse Creek >2.5 Ga
Farmington zone <2.5 Ga
WF
Mojave 1.7-2.0 Ga
GB
40˚N
CAN
USA
MT
WA
OR
ID
WY
CA
NV
UT
CO
M3
M4
M5
M6
115˚W
110˚W
Focal depth
2
3
5
9
15
27
46
80 km

Figure 4.3

Figure 4.3. Regional tectonic setting and seismicity. Earthquake epicenters (colored dots; M>1.5; 2000-2013) [M.C. Stickney, personal communication, 2013] are scaled by magnitude and color-coded by focal depth. White dots represent the epicenters of the historical events mentioned in text (FL: Flathead Lake, HL: Helena, CV: Clarkston Valley, VC: Virginia City, HB: Hebgen Lake, BP: Borah Peak). Major seismic zones in the map area are the Intermountain Seismic Belt (ISB), Lewis Clark Fault Zone (LCFZ), and Centennial Tectonic Belt (CTB). Thick dotted lines indicate cratonic boundaries [*Foster et al.*, 2006]. Extension directions indicated by seismicity are shown as white arrows. Thin black lines indicate physiographic provinces [*Fenneman*, 1946]. Annotations are given for the Idaho Batholith (IB; dotted shade), Yellowstone (YS), Teton and Wasatch faults (TF and WF), Snake River Plain (SRP), Western Idaho Suture Zone (WISZ), and the Great Basin section of the Basin and Range province (GB). Inset shows location of the map area.

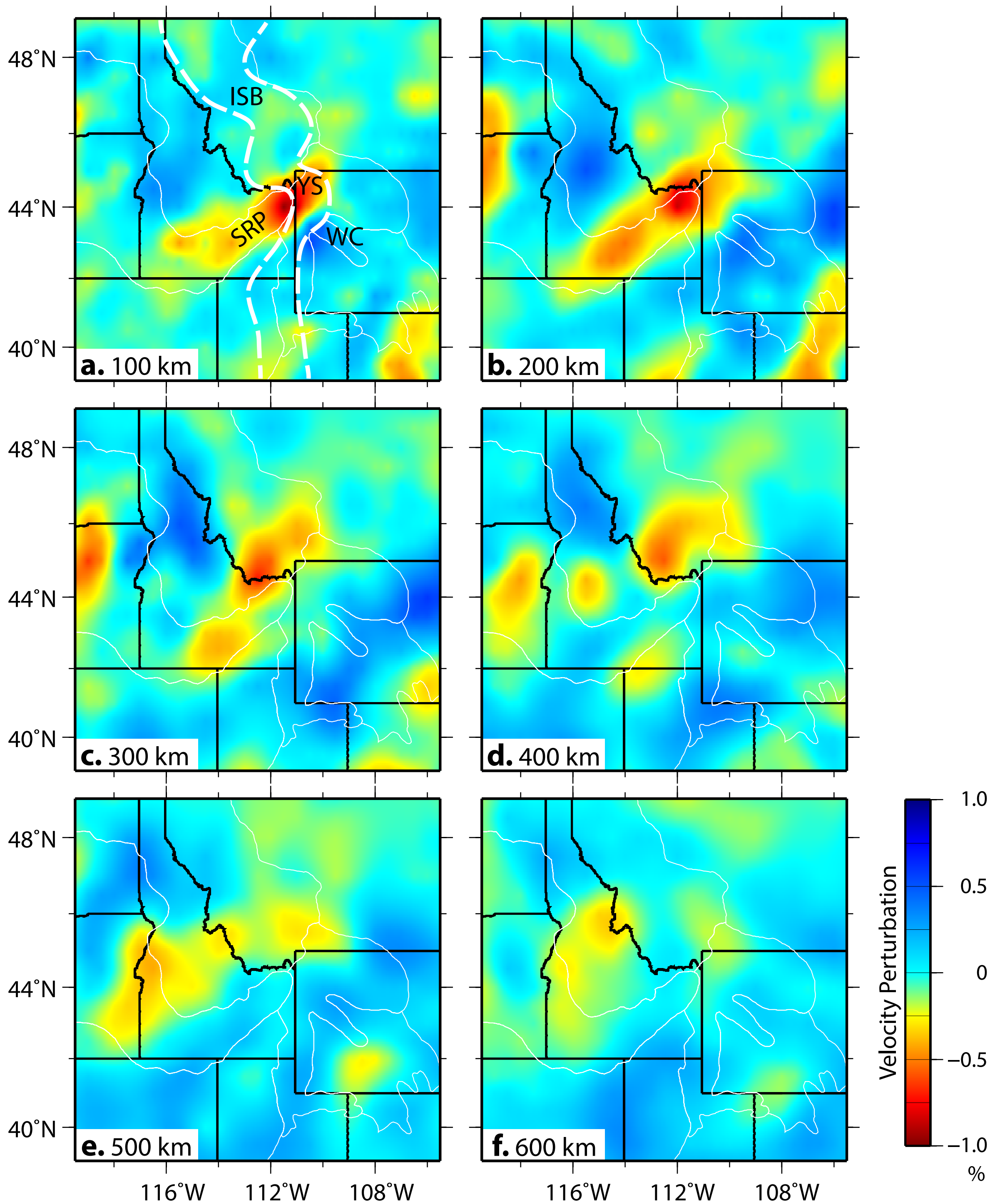

Figure 4.4. *P*-wave velocity perturbation of a seismic tomography model, DNA13 by *Porritt et al.* [2014] for the study area. Depths for maps (a-f) are given in the lower left corner. Thin white lines indicate the physiographic boundaries [*Fenneman*, 1946]. Gray dashed lines bracket the Intermountain Seismic Belt (ISB). YS: Yellowstone. SRP: Snake River Plain. WC: Wyoming craton. A strong negative anomaly lies below Yellowstone and Snake River Plain at up to 200 km depths.

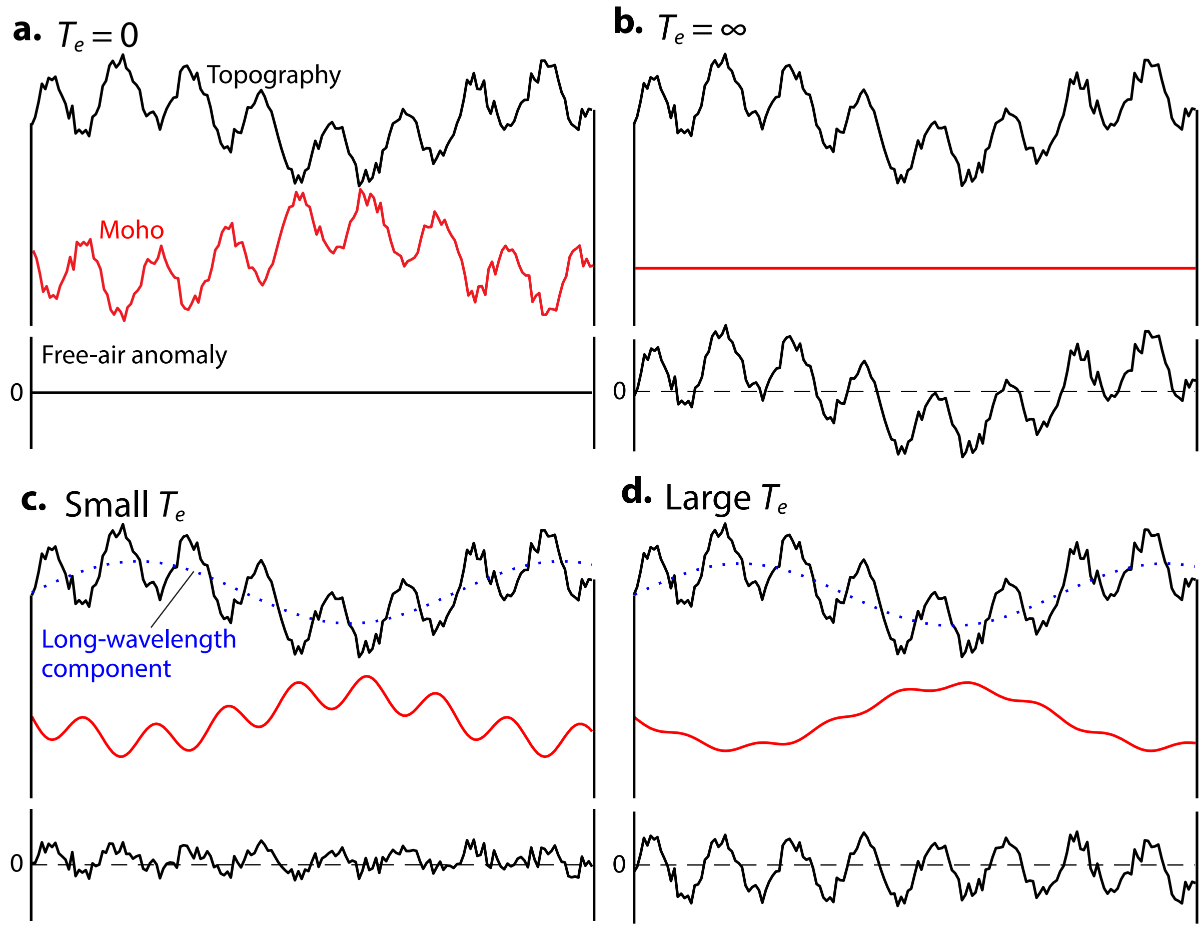

Figure 4.5. Theoretical profiles showing the relationship between surface and Moho topographies and free-air anomaly for (a) $T_e = 0$, (b) $T_e = \infty$, (c) a small T_e, and (d) a large T_e. Black and red lines in the upper plot are surface and Moho topographies, respectively. Blue dotted line is a long-wavelength component of the surface topography.

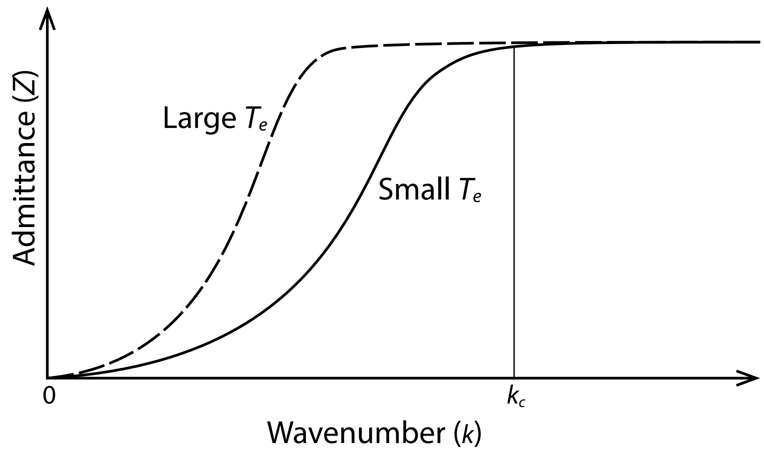

	$k = 0$	$0 < k < k_c$	$k_c < k$
Compensation	local	regional	N/A (no compensation)
Isostatic model	Airy/Pratt	flexural	N/A
Support of loads	fully isostatic		fully elastic
Behavior of crust	no mechanical strength	deflected	rigid

Figure 4.6. Example admittance curves for a small T_e (solid) and a large T_e (dashed). Horizontal line in the center column of the table represents a binary diagram between the two endmembers. Topographic loads of $k > k_c$ are on the full elastic support, causing free-air gravity signals and therefore a high admittance.

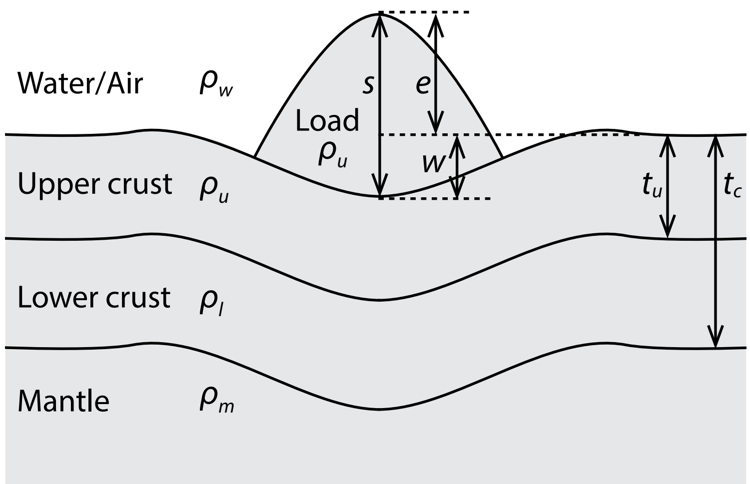

Figure 4.7. Schematic diagram of flexural deflection and the two-layer model from *McKenzie* [2003] to calculate response to surface and internal loading in the method by *McKenzie and Fairhead* [1997]. Thickness of the load s, elevation e, and the amount of deflection w are shown as well as the upper-crust (t_u) and total (t_c) thicknesses.

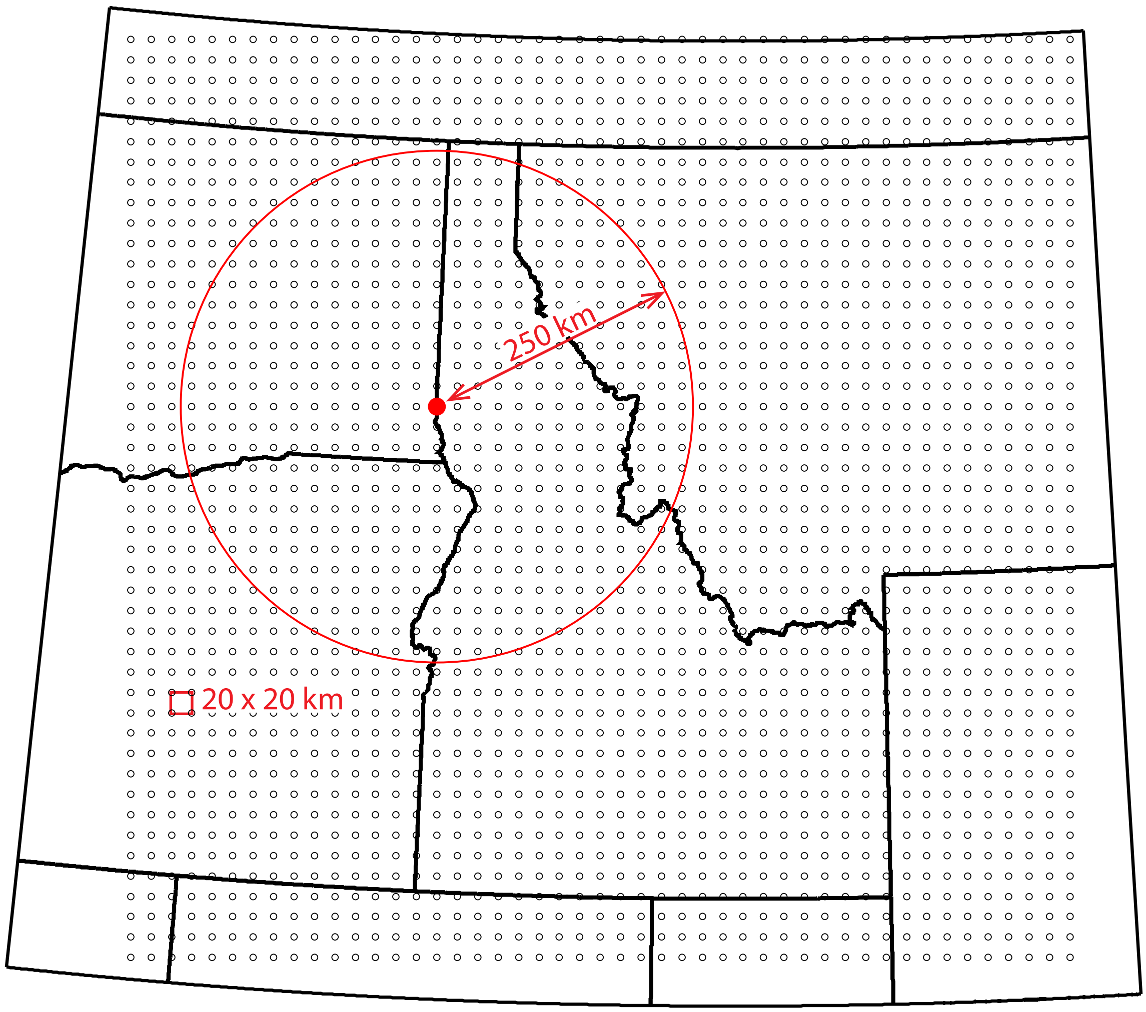

Figure 4.8. Grid points (white dots) of 20 km spacing and the area of a 250 km radius submap centered at a grid point. T_e is estimated for each grid point. The 500 km diameter is sufficient for the spectrum analysis.

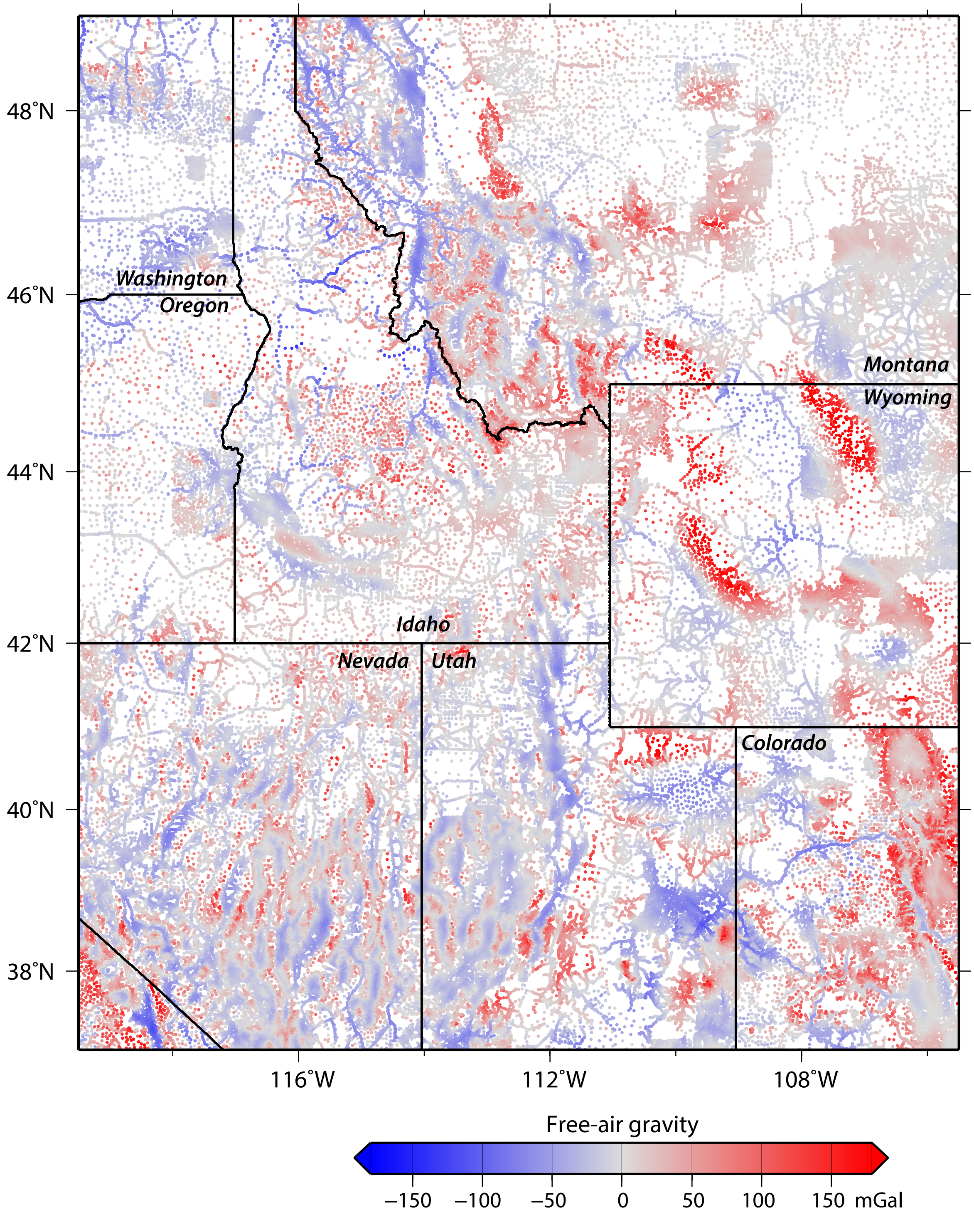

Figure 4.9. Free-air gravity anomaly from *Pan American Center for Earth & Environmental Studies* (PACES) [2015]. Each dot represents a data point. The data are interpolated onto a 5-km grid on the Albers projection, which minimizes distortion in the middle-latitude areas. The color scale is saturated at 180 mGal.

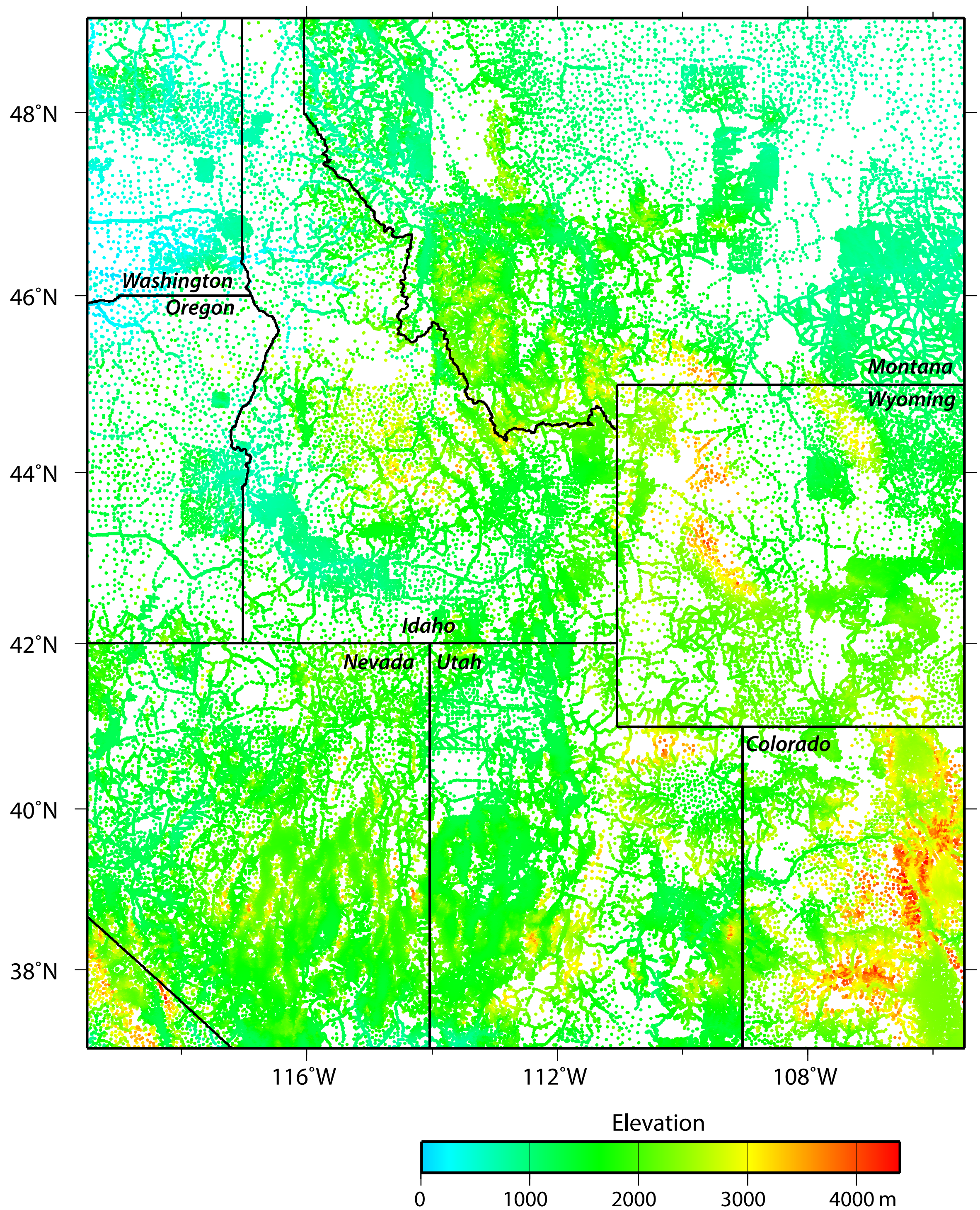

Figure 4.10. Topography data from *Pan American Center for Earth & Environmental Studies* (PACES) [2015]. The data is interpolated in the same way as the gravity data (Figure 4.8).

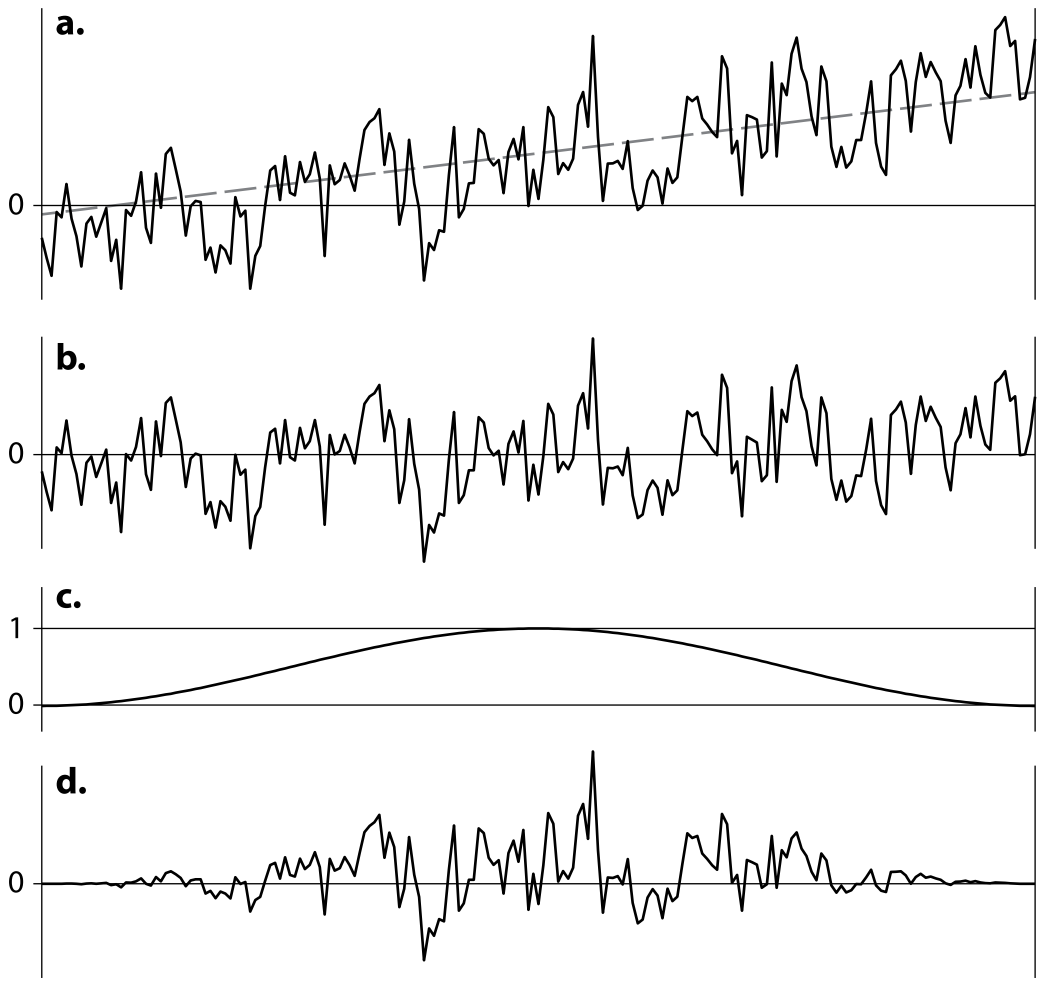

Figure 4.11. Random 1-D data showing the preprocess for the Fourier transform. From (a) raw data, the linear regression (dashed line) is subtracted to remove the DC component and large-wavelength signals, which results in (b). Then, (c) the Hann window function is applied to avoid edge effects. (d) is the result. This process is applied for each submap (Figure 4.10).

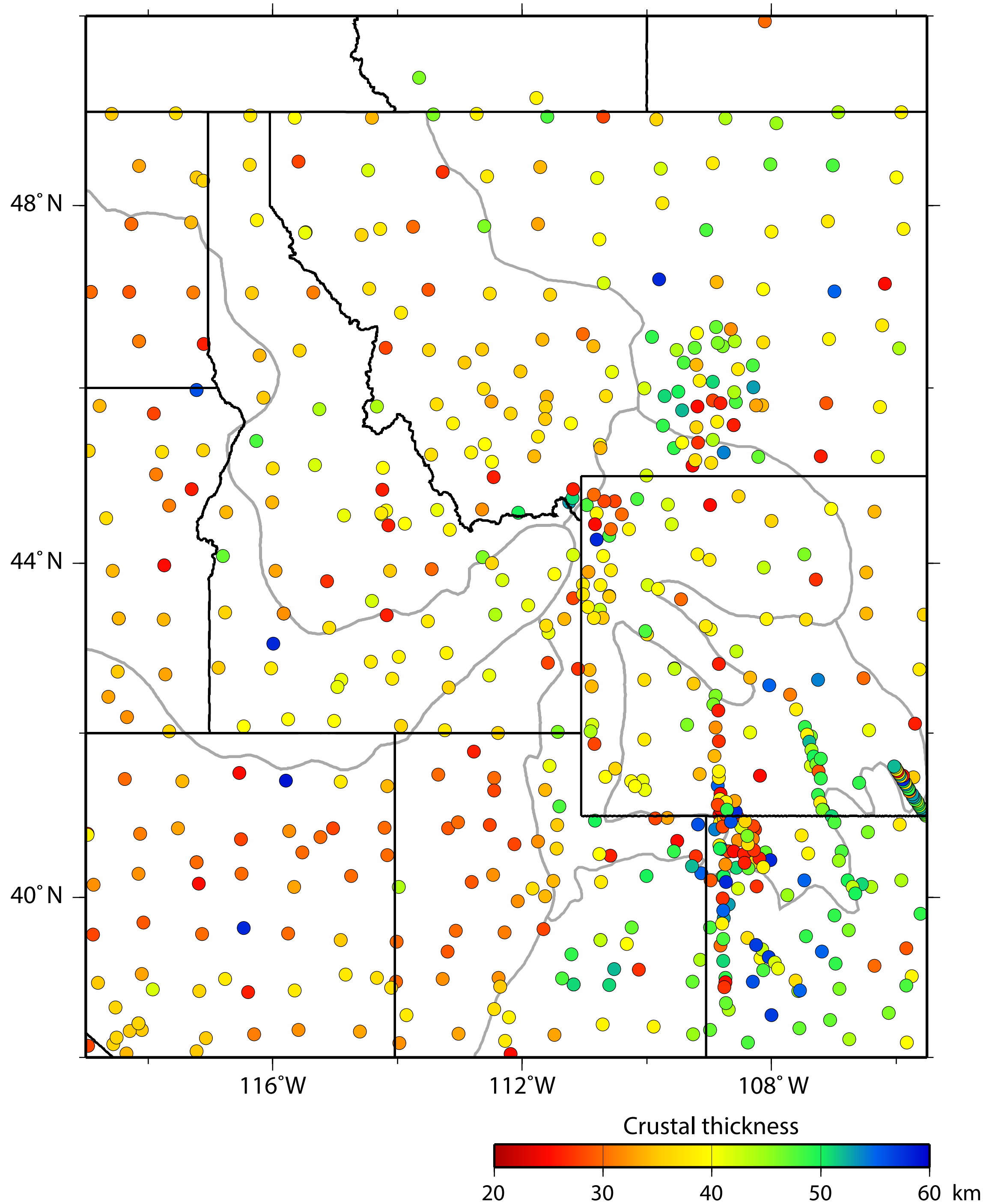

Figure 4.12. Estimates of crustal thickness from the receiver function analysis provided by the Incorporated Research Institutions for Seismology (IRIS) [*IRIS DMC*, 2010; *Crotwell and Owens*, 2005]. Each dot represents a thickness estimate at a station. Gray lines indicate the physiographic boundaries [*Fenneman*, 1946].

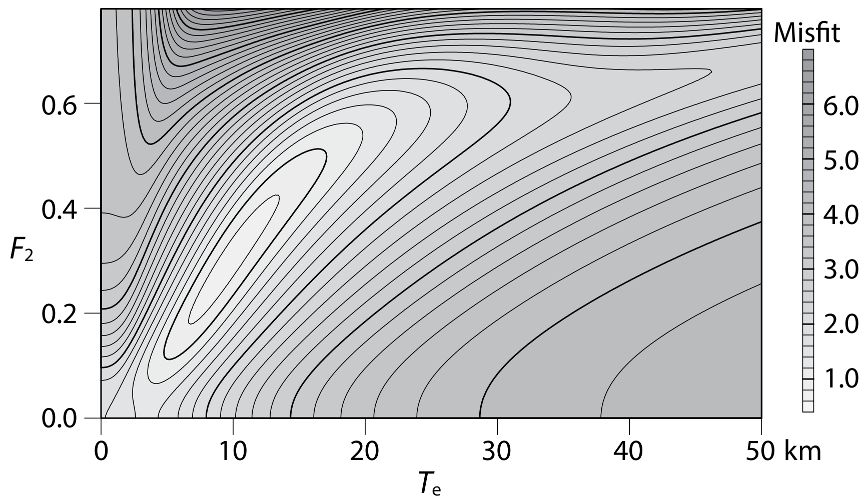

Figure 4.13. Plot of misfit function $H(T_e, F_2)$ from *McKenzie* [2003], showing the global minimum in a "flat-bottomed valley" and no local minimum.

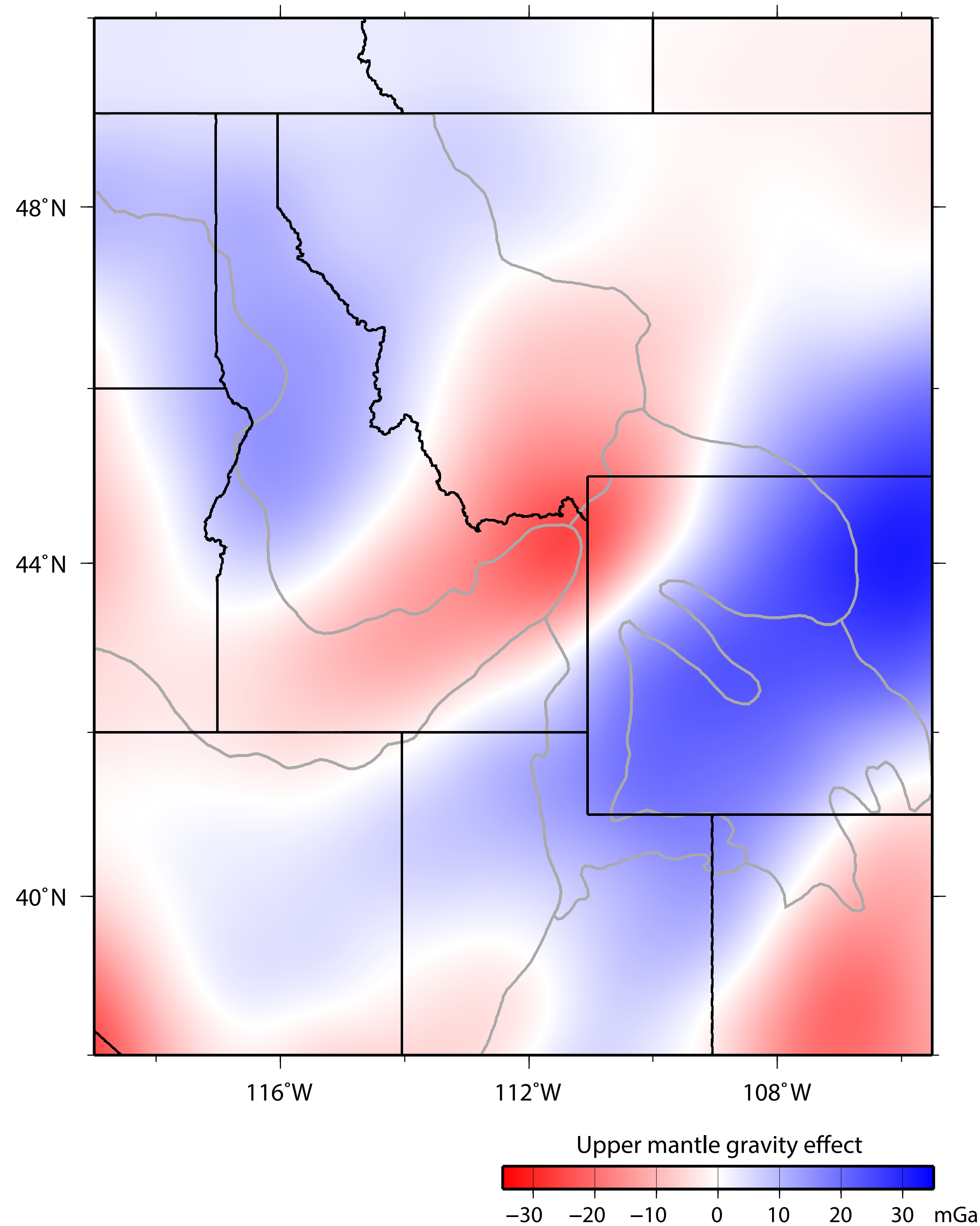

Figure 4.14. Gravity anomaly contribution at the surface from the mantle heterogeneity at 50-600 km depths. Velocity perturbation data of the DNA13 model [*Porritt et al.*, 2014] and the 1-D velocity structure of PREM [*Dziewonski and Anderson,*1981] are used to find the 3-D velocity model, which is then converted to a density model [*Birch*, 1964].

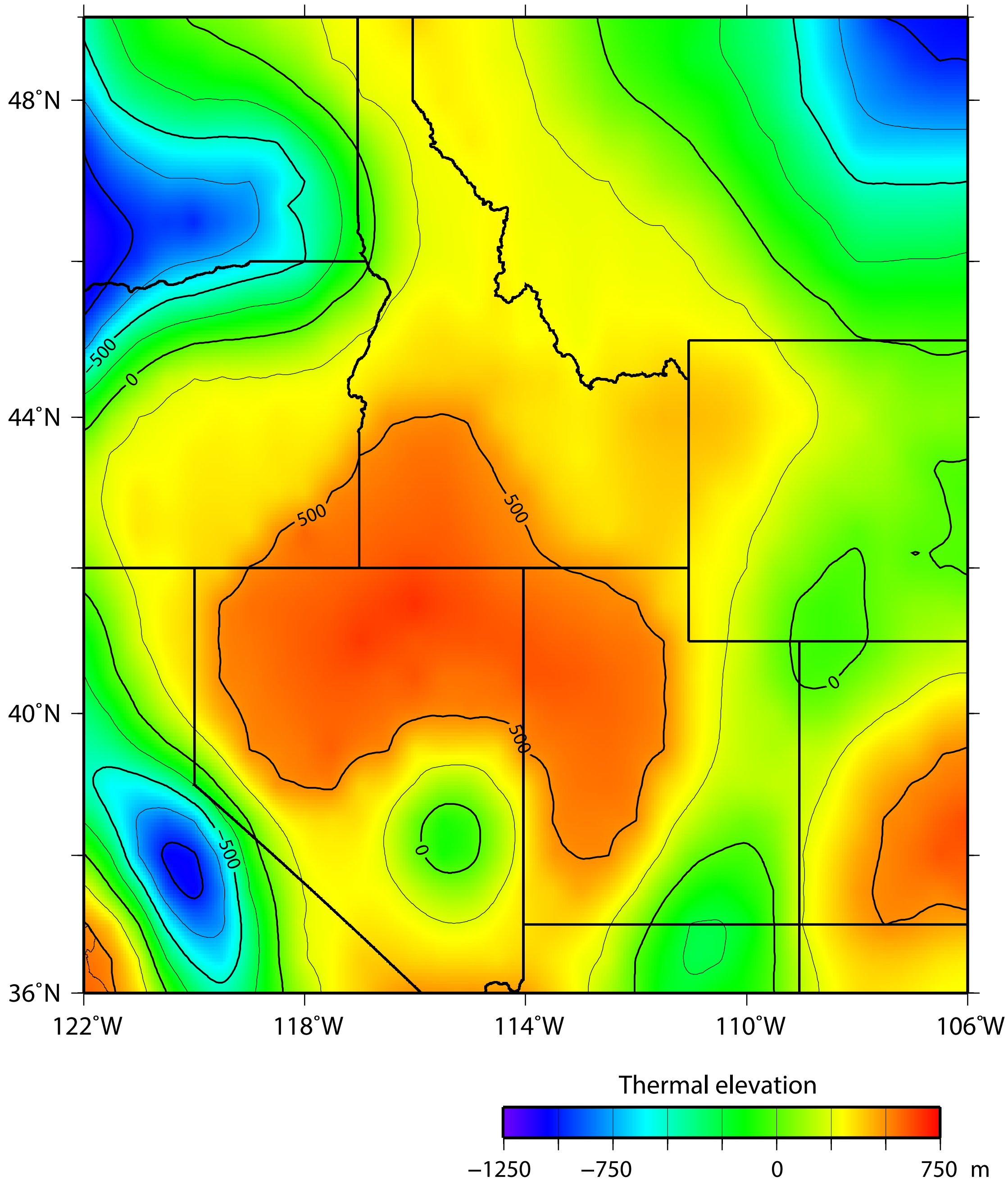

Figure 4.15. Thermal elevation in the study area from heat flow measurements after *Lowry et al.* [2000]. The corrected elevation is given by subtracting the thermal elevation from the raw elevation.

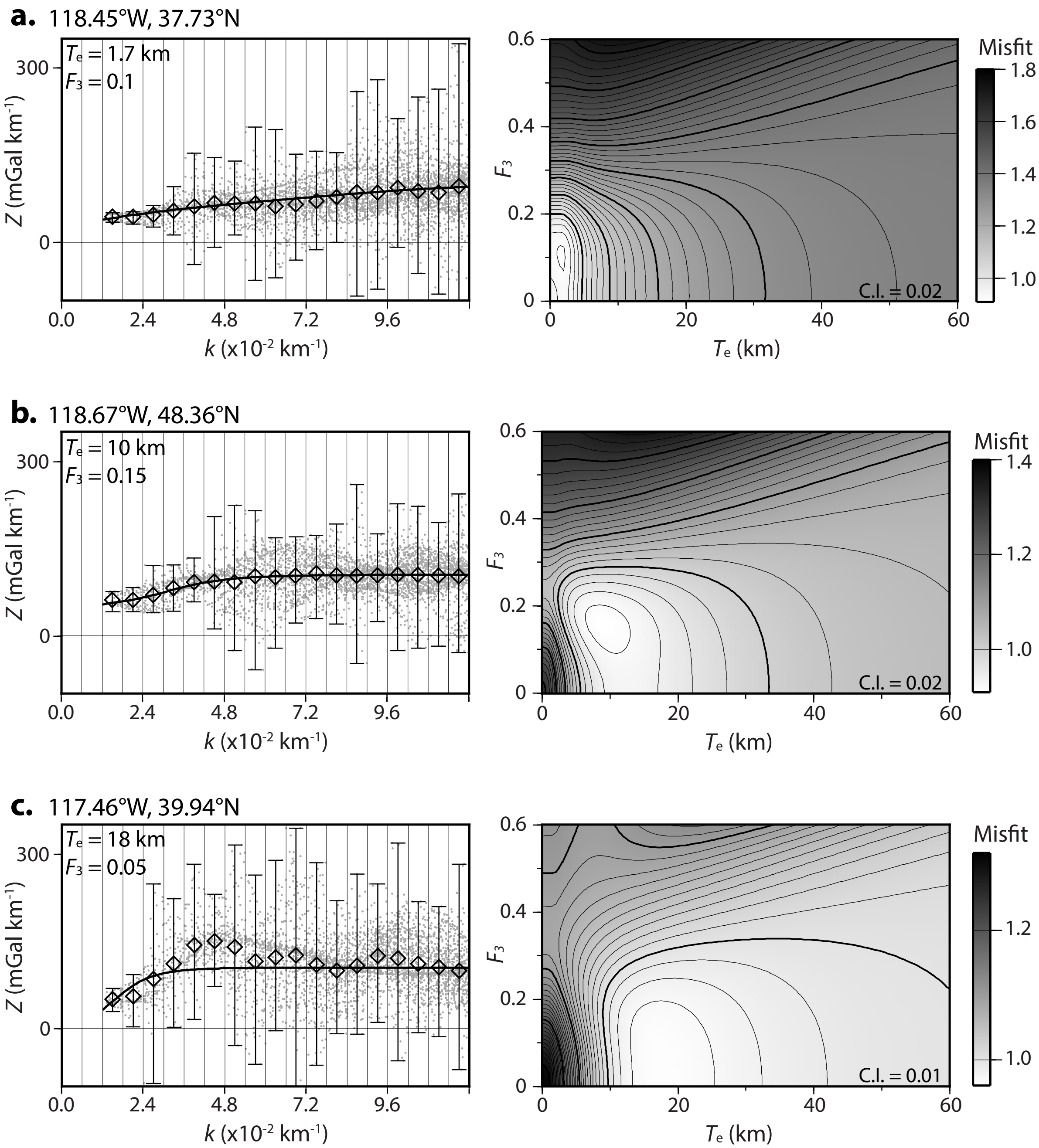

Figure 4.16. Admittance (left) and contoured misfit (right) plots for the best fitting values of T_e and F_3 for selected grid points at (a) 118.45°W, 37.73°N (T_e = 1.7 km), (b) 118.67°W, 48.36°N (T_e = 10 km), and (c) 117.46°W, 39.94°N (T_e = 18 km). Each admittance plot shows observed values (gray dots) and the theoretical best fit curve. Error bar denotes $\pm 1\sigma$ from the median (diamond) for each bin. The range of uncertainty of Te increases as the best fit Te value becomes larger.

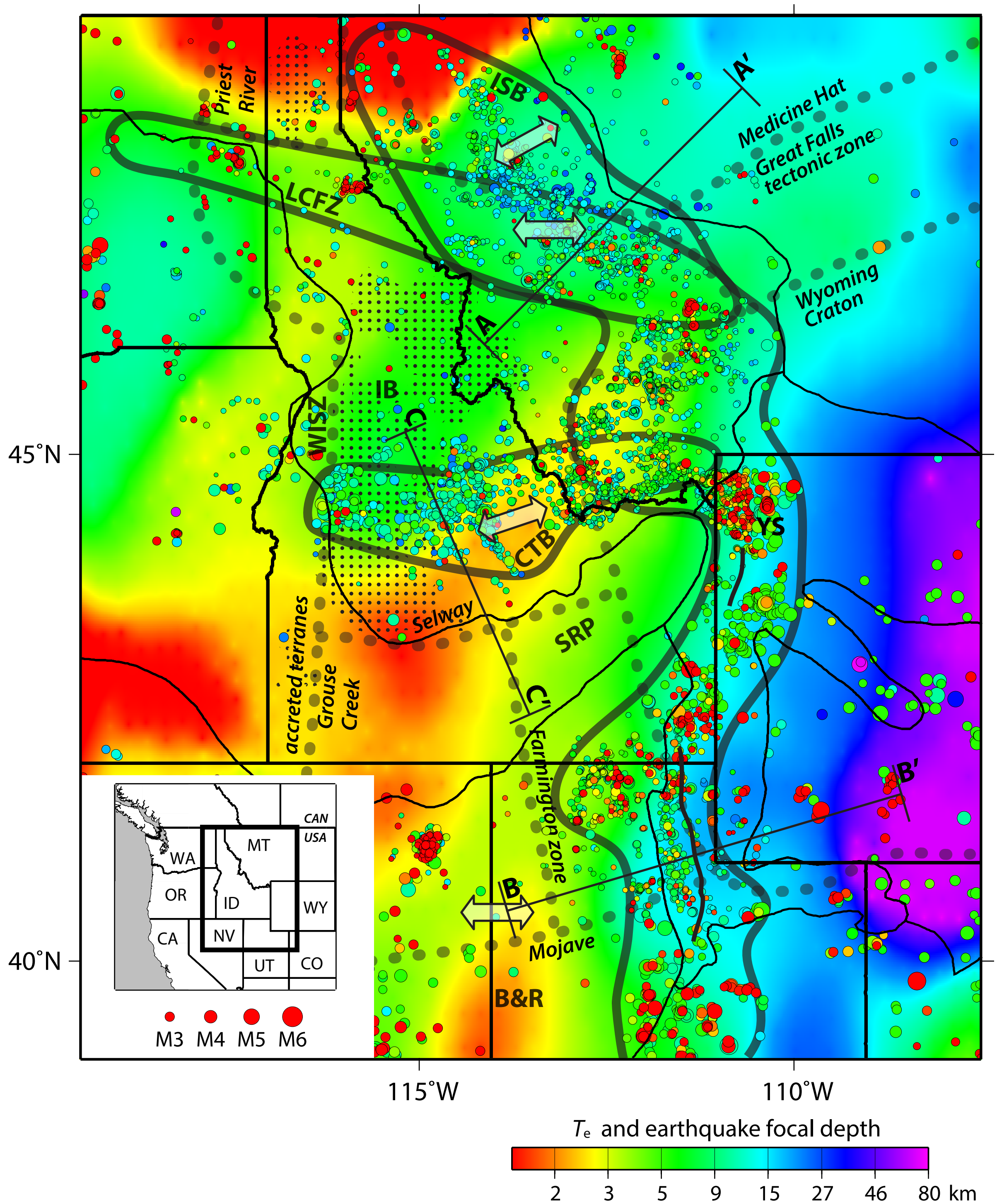

Figure 4.17. The resultant T_e and earthquake epicenters. T_e and the focal depths are in the same color scale for comparison. Black lines A, B, and C indicates the locations of cross sections and width for earthquake profile in Figure 4.23. See Figure 4.6 for explanation.

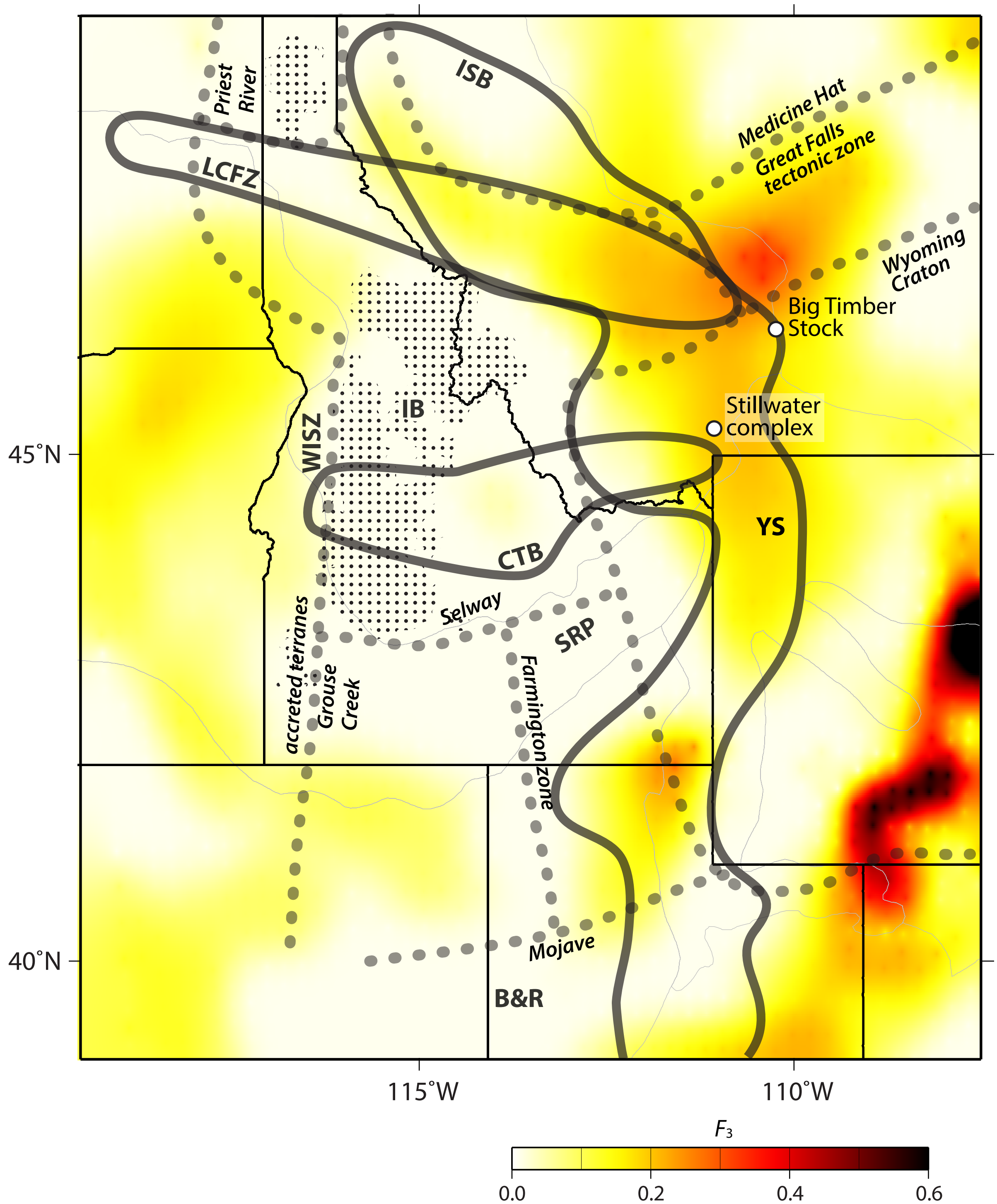

Figure 4.18. Spatial variation of F_3, the fraction of the load at the Moho. F_3 is low (< 0.18) throughout the map area except for western Montana and central Wyoming. The Stillwater igneous complex and the Big Tiimber stock are in southwestern Montana. See Figure 4.6 for explanation.

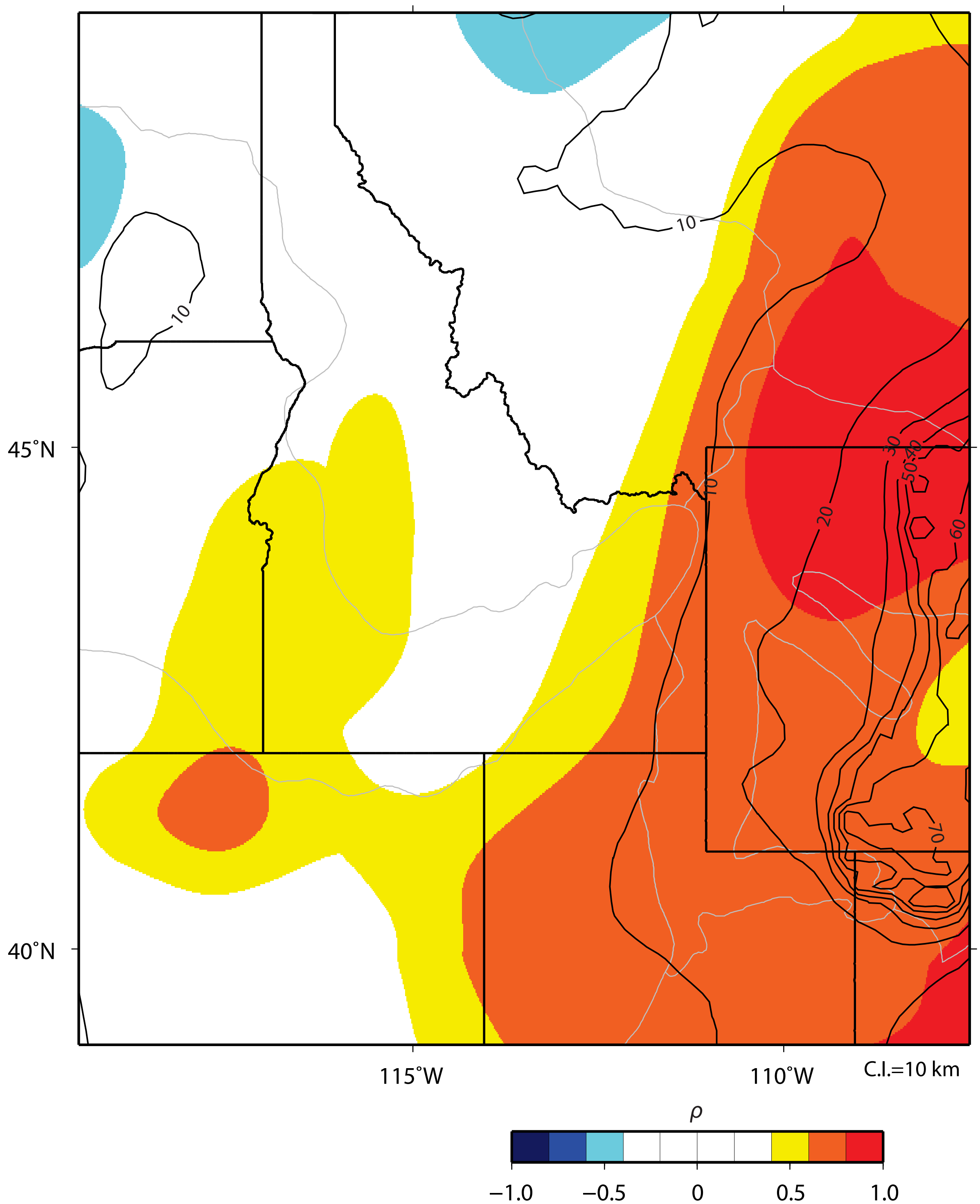

Figure 4.19. Spatial variation in 2-D correlation coefficient ρ between the estimated T_e (contoured) and the mantle gravity effect (figure 4.14). The correlation is relatively strong (>0.6) in the area of large T_e values (i.e., the eastern side of the map area in central Montana, western Wyoming, and northern Utah).

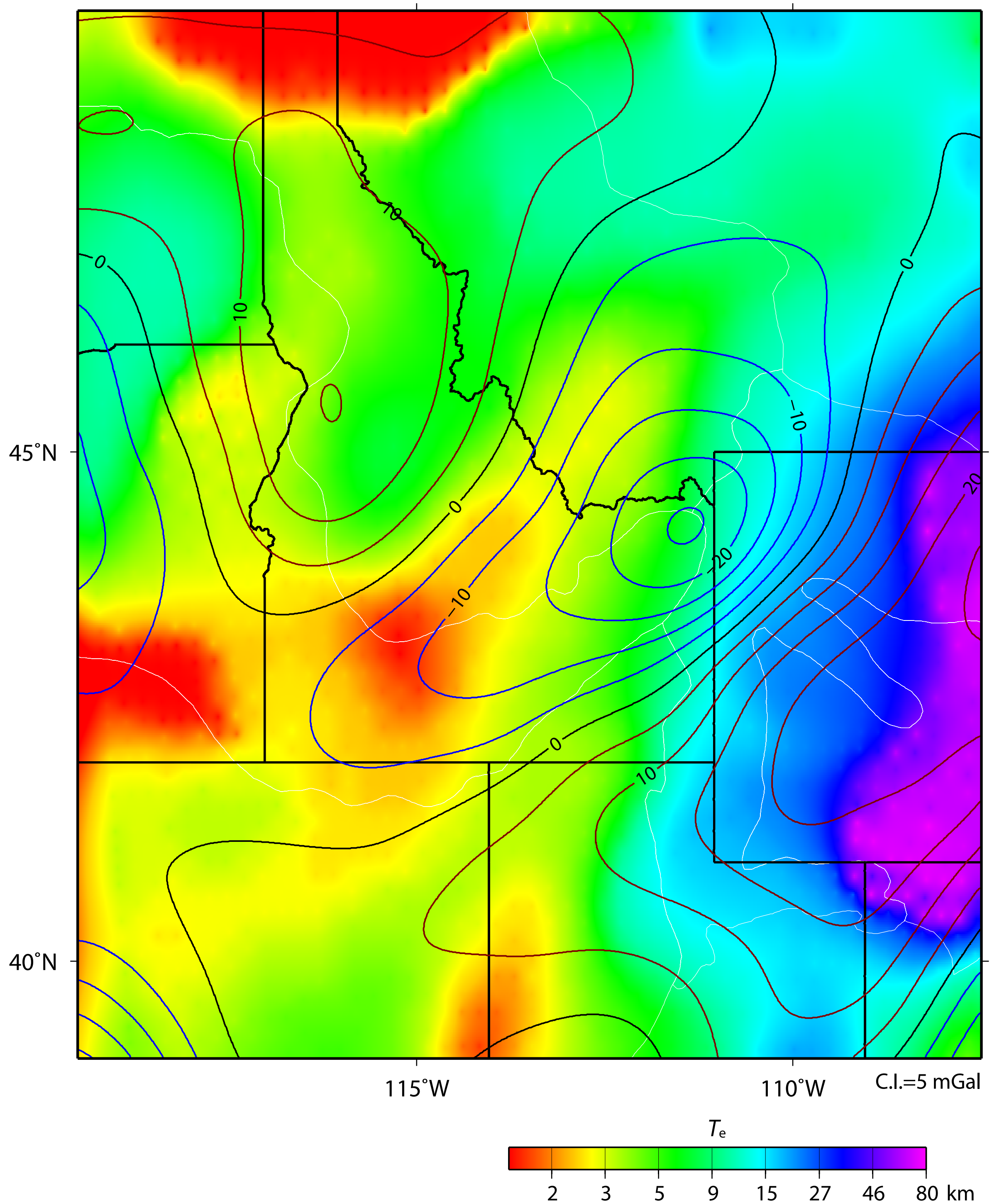

Figure 4.20. T_e map from the corrected free-air anomaly data, which is given by subtracting the mantle gravity contribution from the raw gravity data. The map is nearly identical to the map of the basic model using the raw gravity data. Contour lines are for the gravity anomaly contribution from the upper mantle heterogeneity (Figure 4.14).

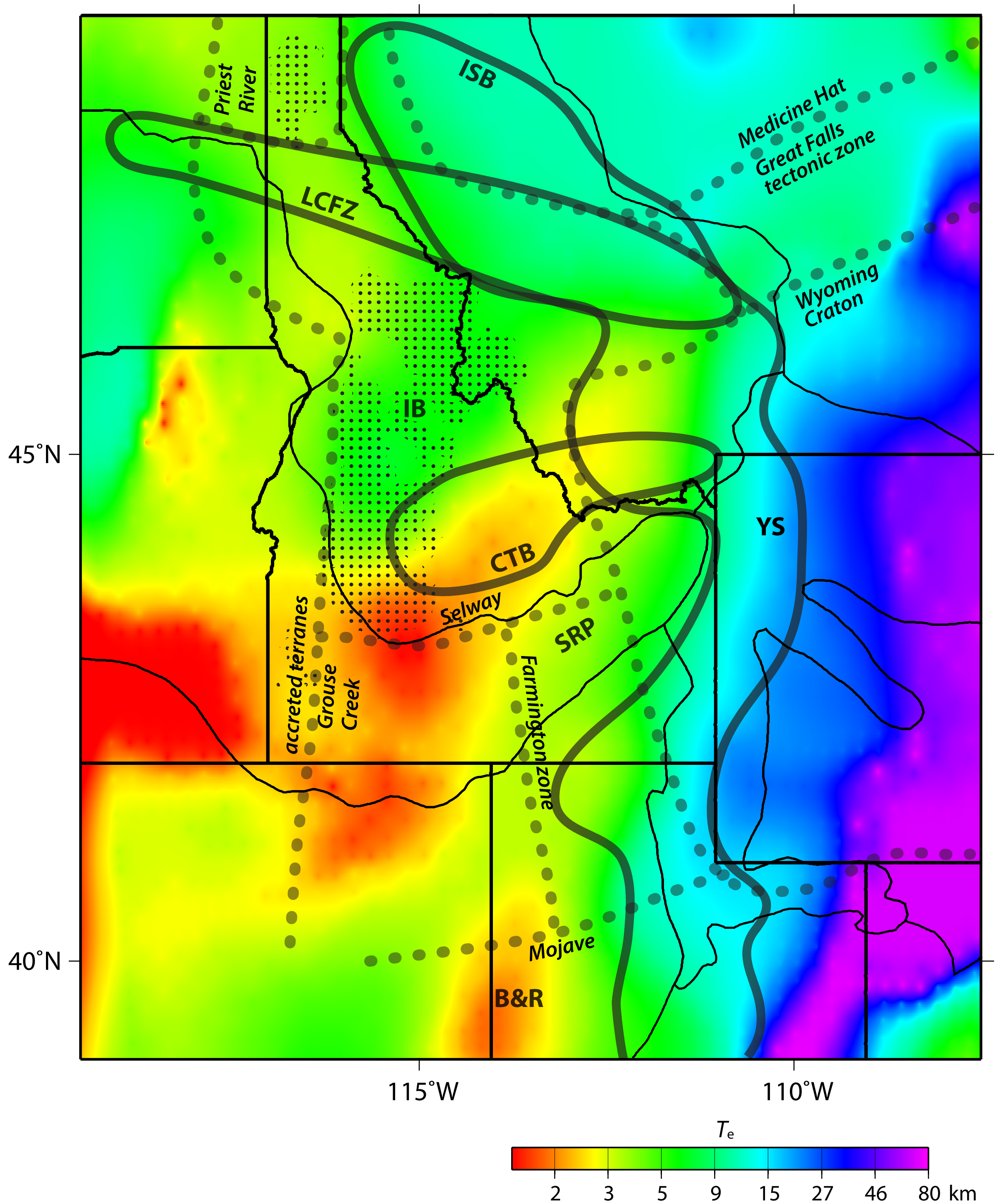

Figure 4.21. T_e map from the elevation data corrected for the thermal elevation (Figure 4.15). The T_e variation is very similar to that of the basic model (Figure 4.17). One notable difference is that the low-T_e zone (~1-2 km) along the northwestern map limit in the basic model (Figure 4.17) does not appear in this map. See Figure 4.6 for explanation.

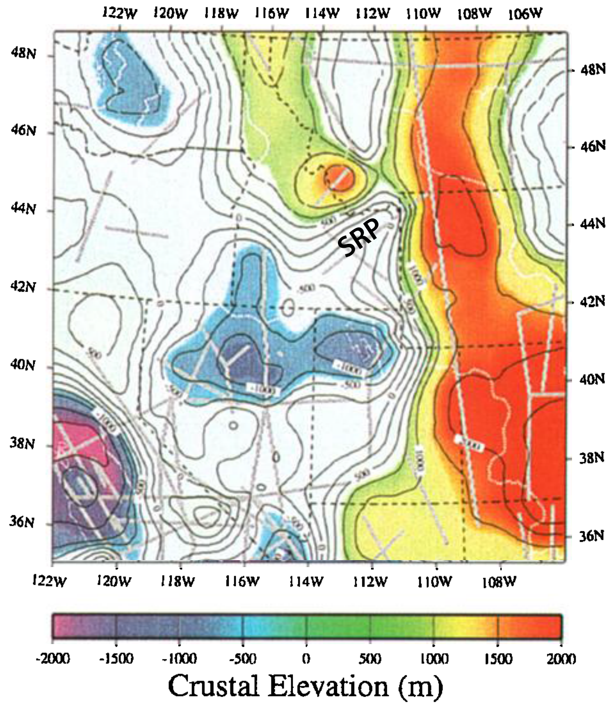

Figure 4.22. Crustal elevation from *Lowry et al.* [2000]. They used a horizontally variable *P*-wave velocity model given from seismic refraction profiles, two of which crisscross the eastern SRP, in order to find crustal elevation.

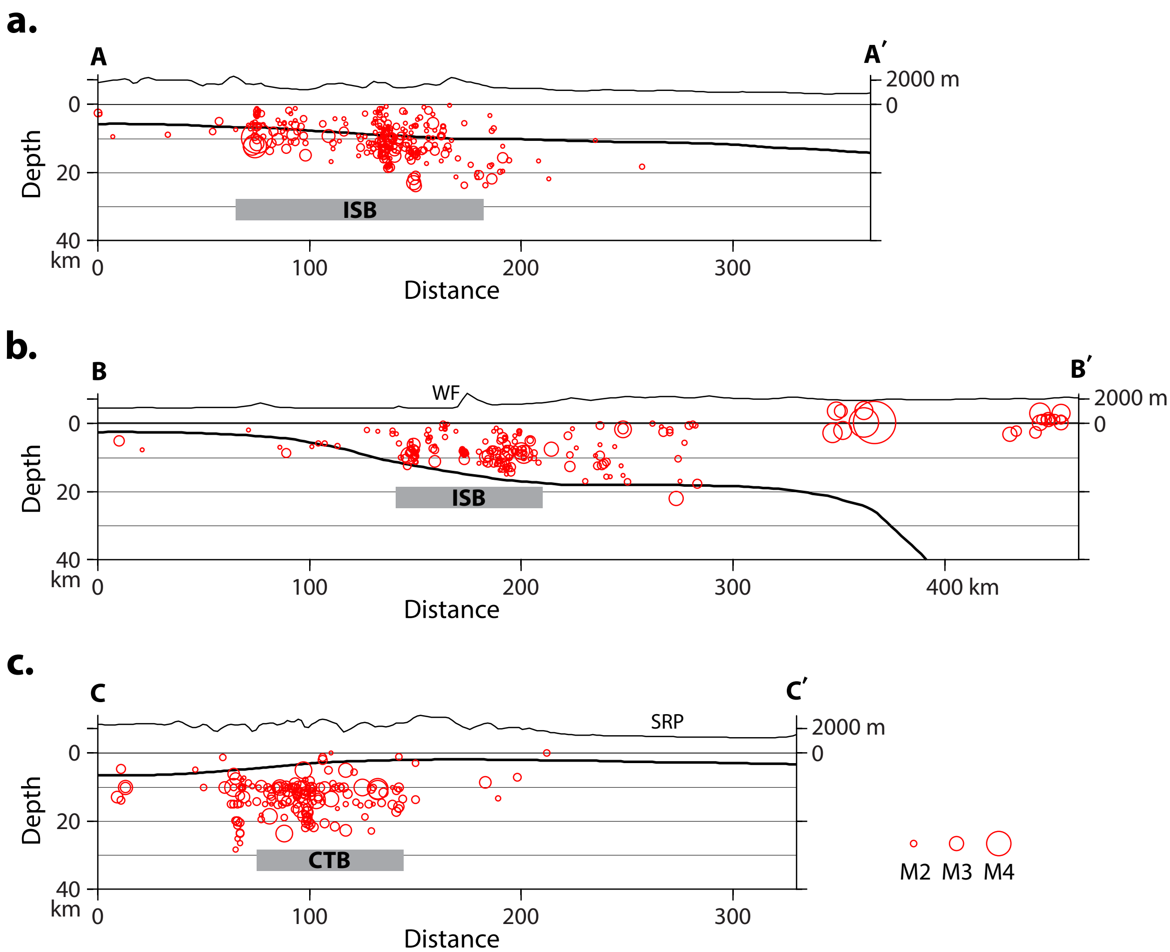

Figure 4.23. Cross sections showing relationships between T_e (thick black lines) and earthquake focal depths (red circles). A-A′ (a) is across the ISB in western Montana, B-B′ (b) across the ISB in northern Utah, and C-C′ (c) across the CTB. See Figure 4.17 for the exact locations. Vertical scale above the sea level (i.e., the surface topography) is exaggerated (×4). ISB: Intermountain Seismic Belt; CTB: Centennial Tectonic Belt; WF: Wasatch Fault; SRP: Snake River Plain. For the northern segment of the ISB (a), T_s is larger than T_e by ~10-15 km while T_e and T_s show the same along-profile increasing trend from west to east. In the southern segment (b), the values and changes in T_e and T_s are strikingly similar to each other.

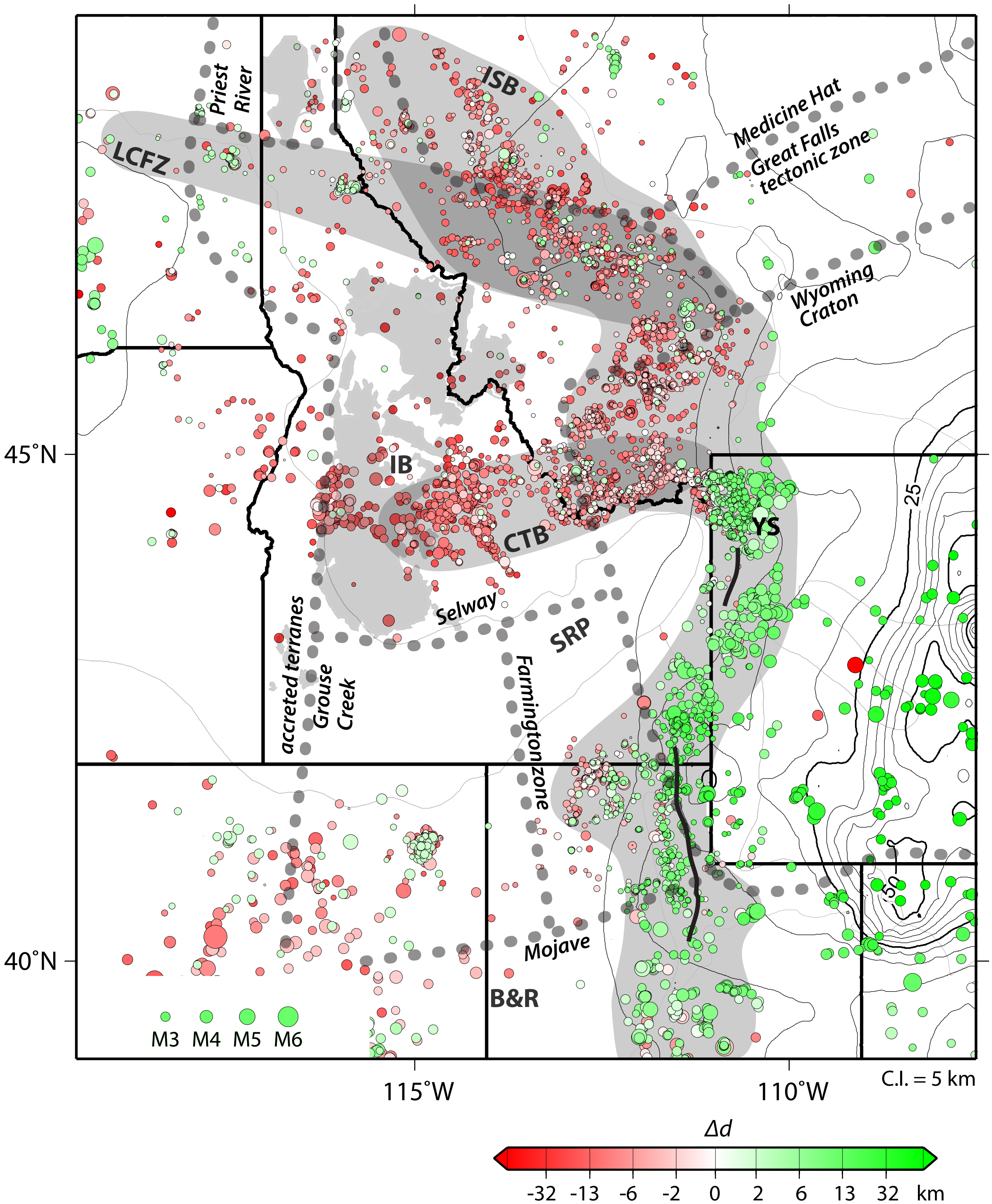

Figure 4.24. Depth difference Δd between T_e and earthquake focal depth z ($\Delta d = T_e - z$) at each epicenter. In the area north of the SRP, the majority of the events occurred at greater depths than T_e while the most events along the ISB south of Yellowstone occurred within the range of T_e. T_e estimate is contoured. See Figure 4.6 for explanation.

APPENDICES

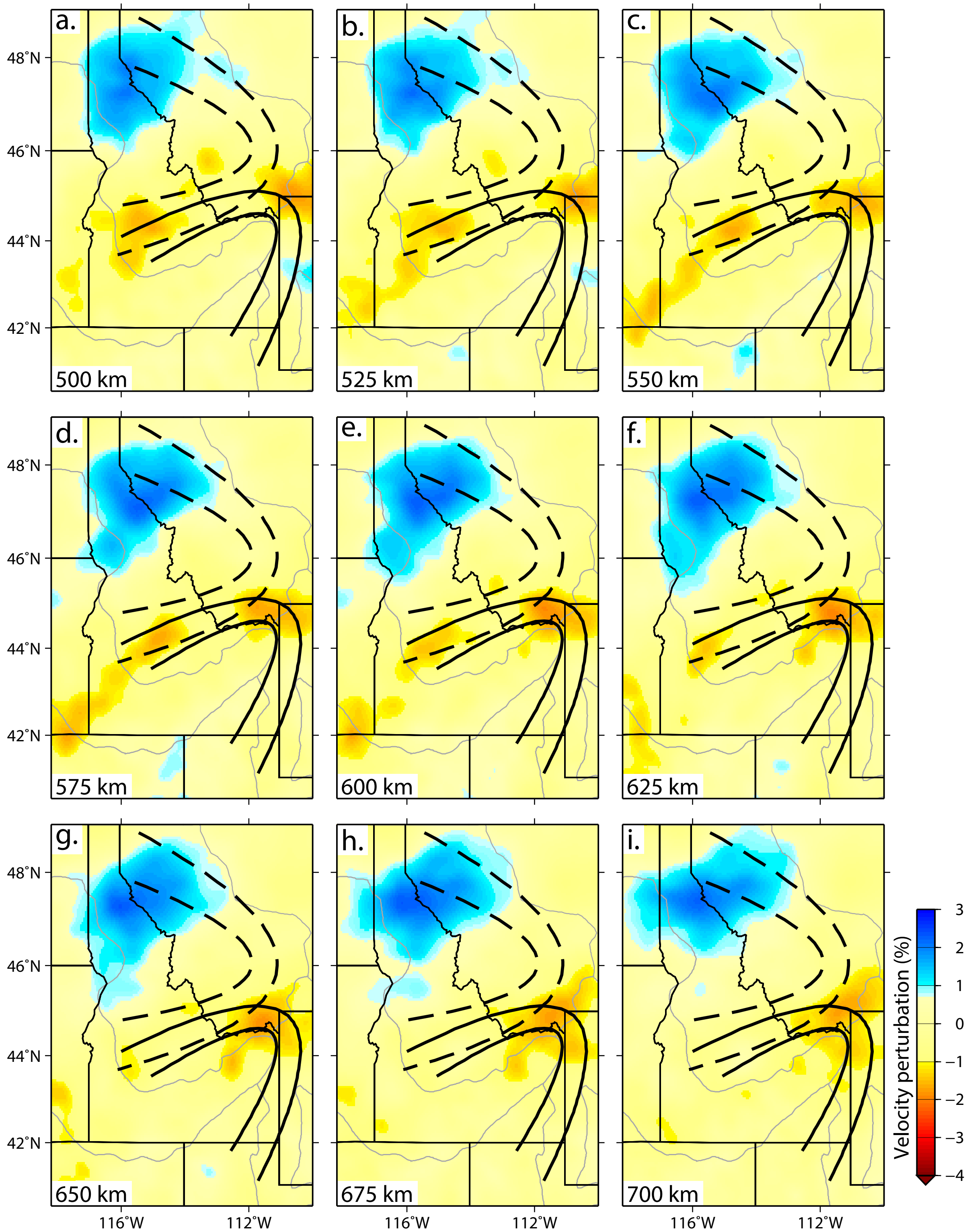

Appendix 1.A. Horizontal sections (≥500 km depths) of the *S*-wave tomography model of *James et al.* [2011]. Depths for (a–i) are given in lower left-hand corner. See Figure 1.2 for explanation.

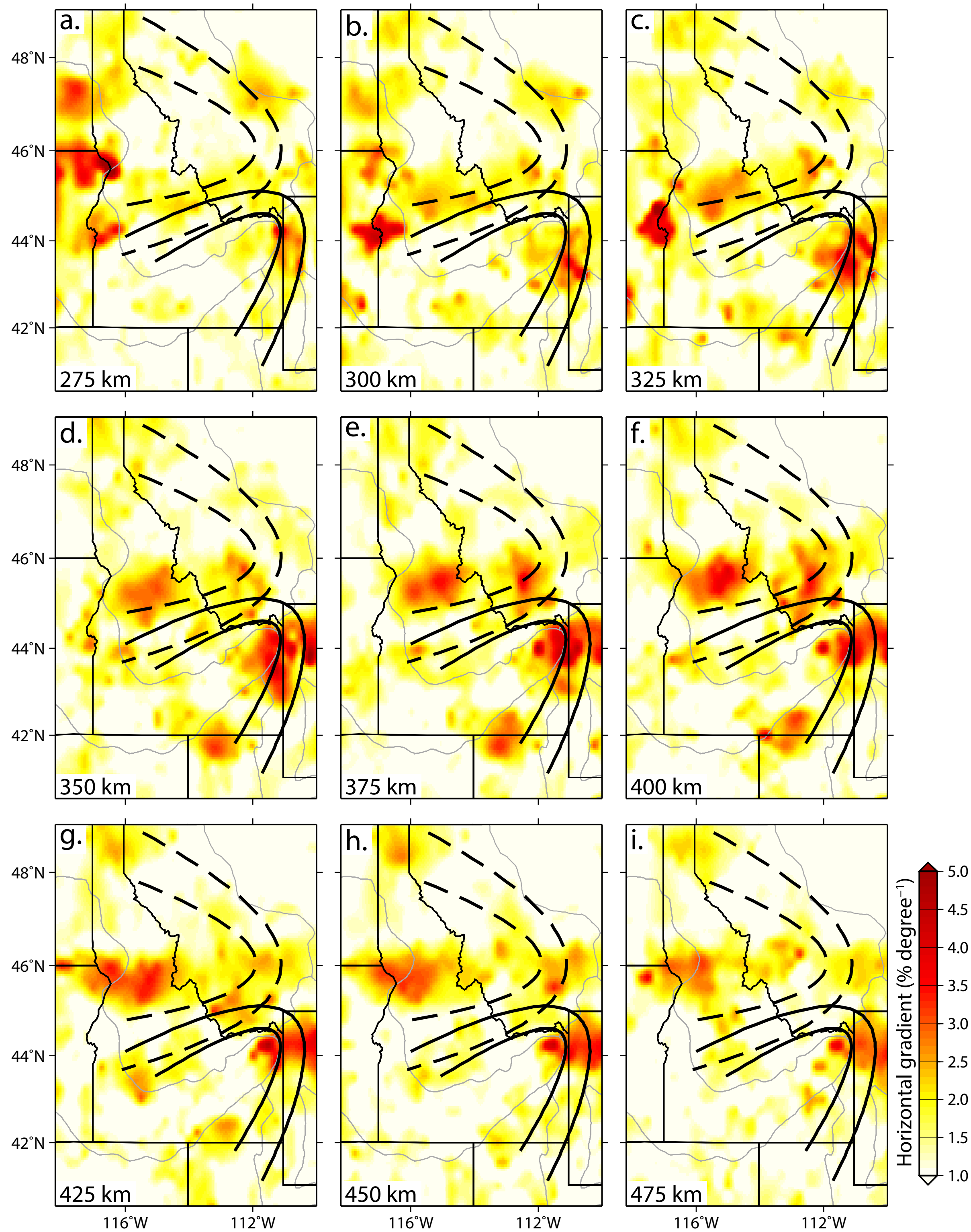

Appendix 1.B. Horizontal gradients (≥275 km depths) of the *S*-wave velocity perturbations from *James et al.* [2011]. Depths for (a–r) are given in lower left-hand corner. See Figure 1.2 for explanation.

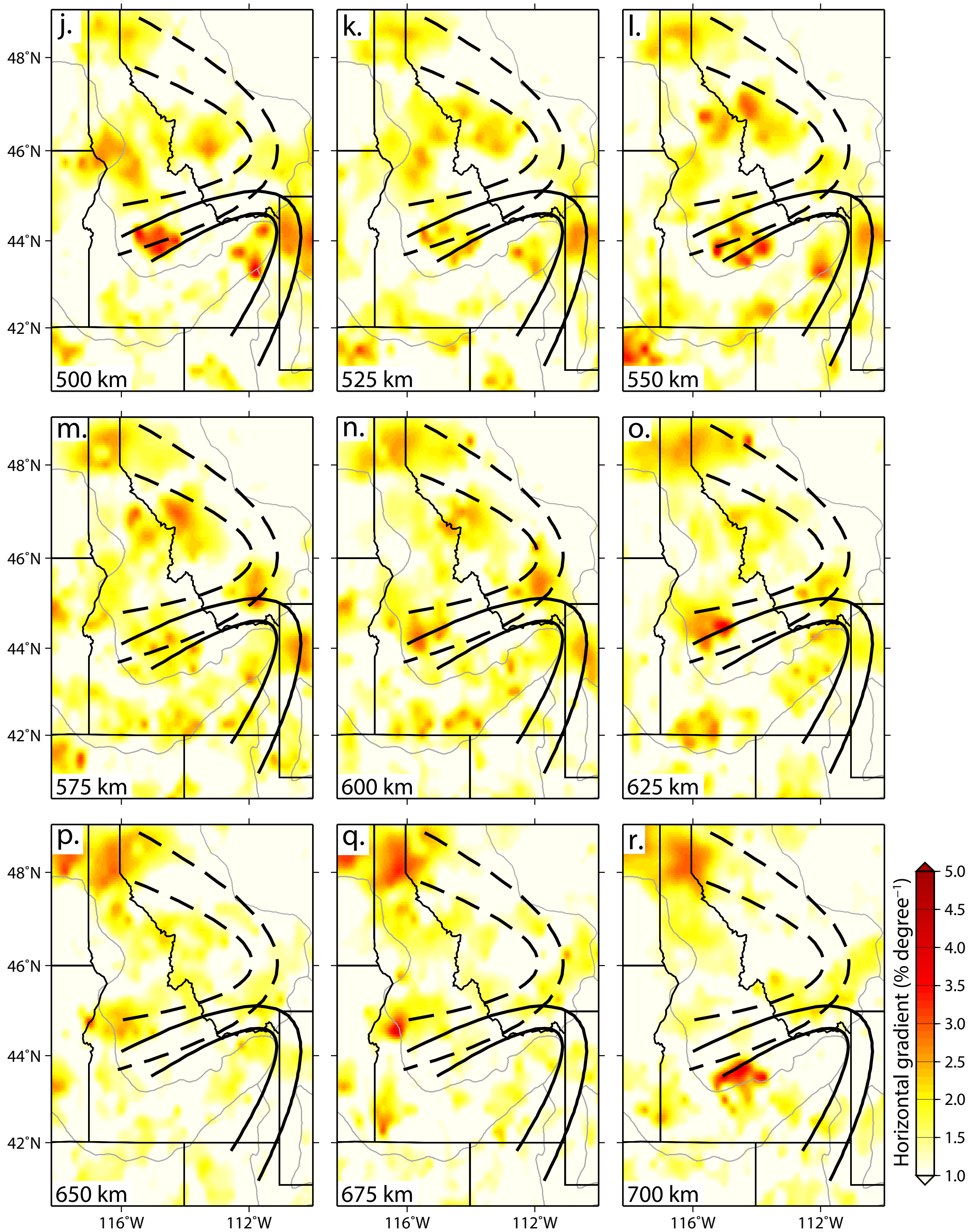

Appendix 1.B. (continued)

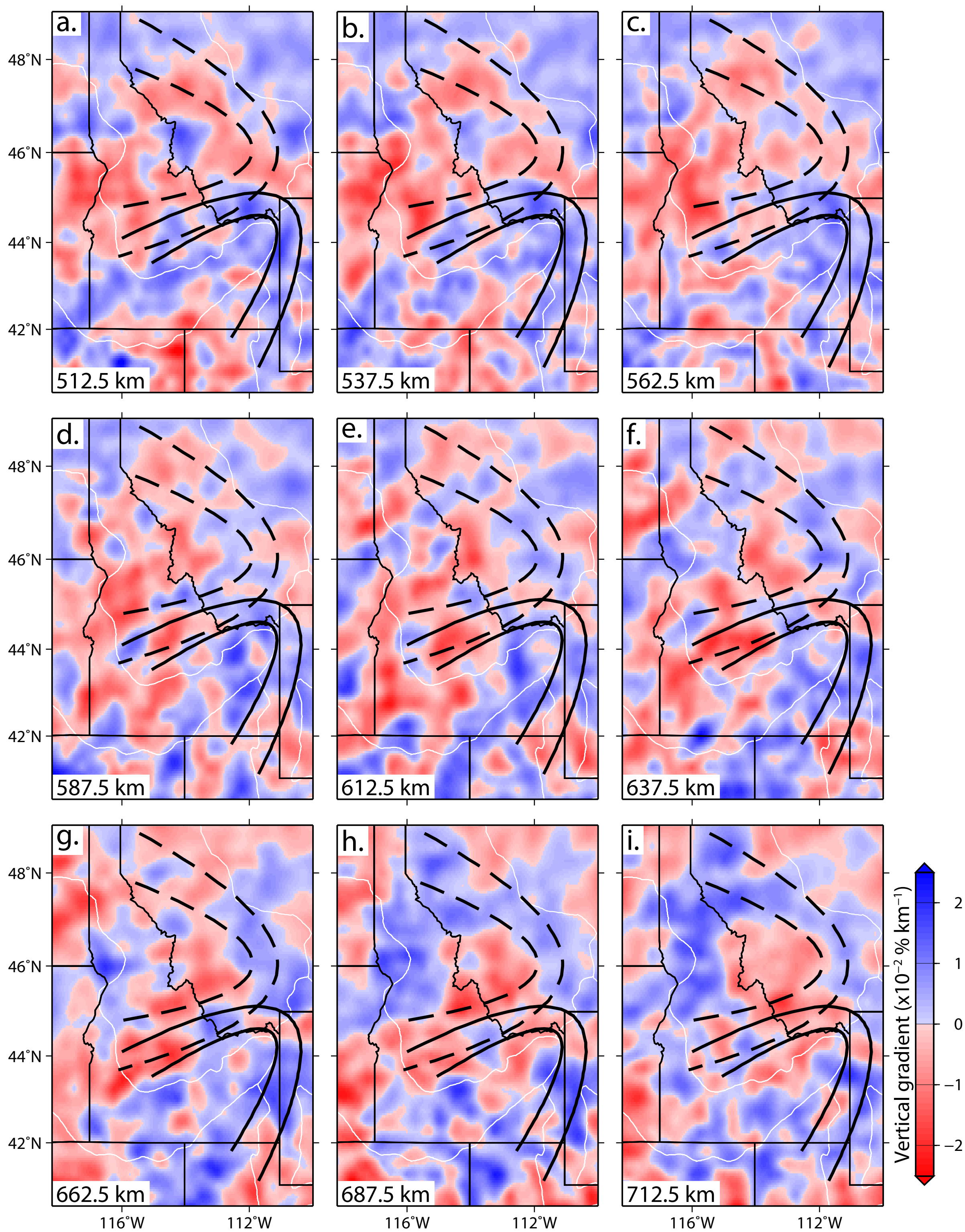

Appendix 1.C. Vertical gradients (>512 km depths) of the *S*-wave velocity perturbations from *James et al.* [2011]. Depths for (a–i) are given in lower left-hand corner. See Figure 1.2 for explanation.

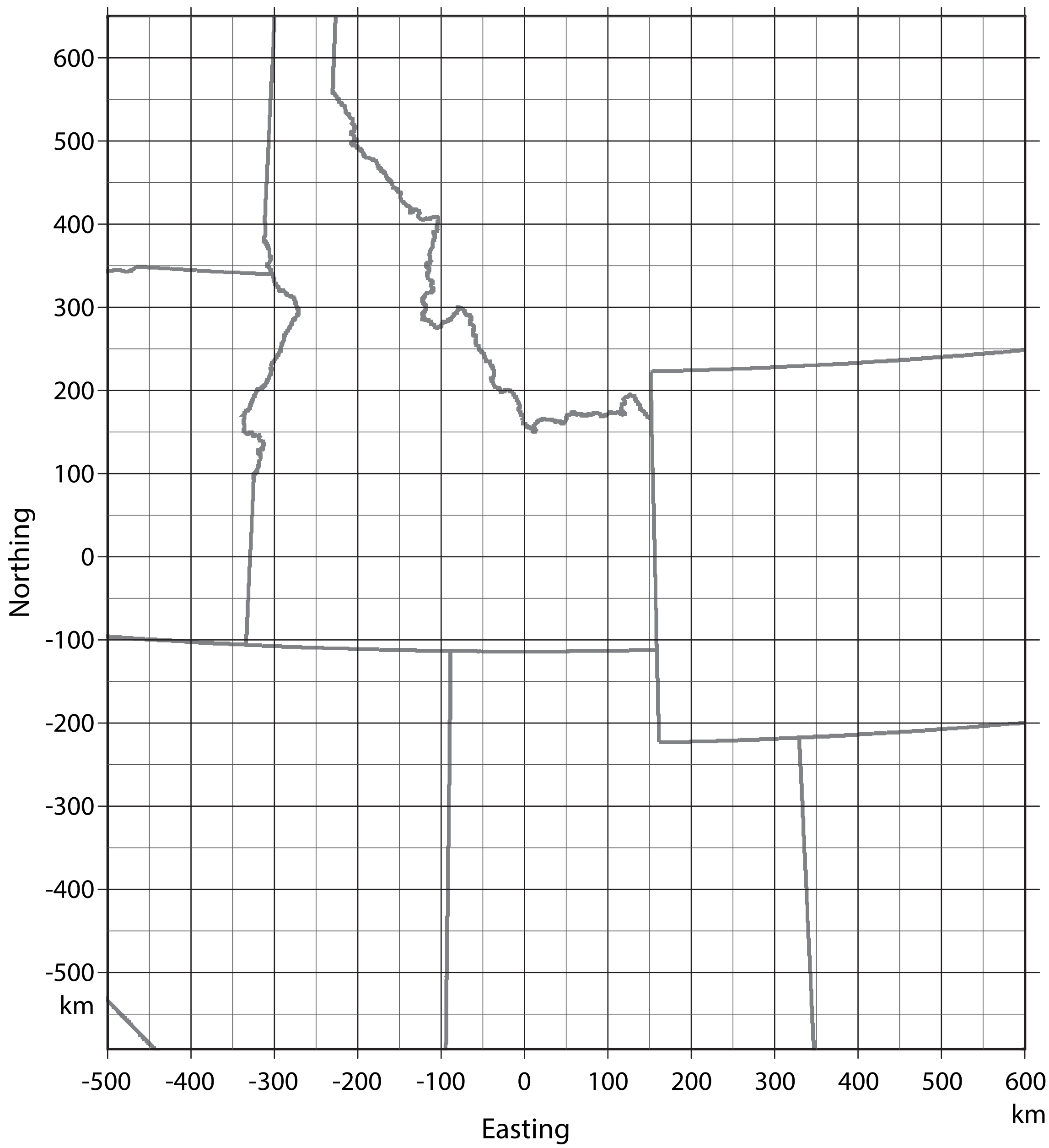

Appendix 4.A. Coordinates for the 20 km grid used for the T_e estimation. The origin is at 113W, 43N.

Appendix 4.B. The best fit T_e, F_3, and misfit H. See Appendix 4.A for location. x and y represent Easting and Northing, respectively. T_e is in km.

x	y	T_e	F_3	H	x	y	T_e	F_3	H	x	y	T_e	F_3	H
-500	650	3.5	0.00	1.380	-500	-370	3.3	0.16	2.691	-480	-130	2.8	0.00	1.504
-500	630	4.0	0.00	1.264	-500	-390	3.8	0.12	2.370	-480	-150	2.8	0.00	1.662
-500	610	4.5	0.00	1.067	-500	-410	3.8	0.12	2.055	-480	-170	2.8	0.00	1.791
-500	590	5.0	0.00	0.864	-500	-430	4.0	0.12	1.815	-480	-190	2.8	0.00	1.921
-500	570	5.5	0.00	0.679	-500	-450	4.0	0.08	1.497	-480	-210	2.8	0.00	2.009
-500	550	6.3	0.00	0.588	-500	-470	4.0	0.08	1.145	-480	-230	2.8	0.00	2.028
-500	530	6.8	0.04	0.674	-500	-490	4.0	0.08	0.866	-480	-250	2.8	0.04	2.120
-500	510	7.5	0.04	0.986	-500	-510	4.0	0.08	0.691	-480	-270	2.5	0.08	2.362
-500	490	8.0	0.08	1.419	-500	-530	4.0	0.08	0.609	-480	-290	2.5	0.12	2.635
-500	470	8.5	0.08	1.872	-500	-550	4.0	0.08	0.578	-480	-310	2.5	0.12	2.888
-500	450	8.8	0.08	2.181	-500	-570	4.0	0.04	0.542	-480	-330	2.8	0.12	3.147
-500	430	9.0	0.08	2.311	-500	-590	4.0	0.04	0.536	-480	-350	2.8	0.16	3.185
-500	410	9.0	0.08	2.269	-480	650	3.5	0.00	1.218	-480	-370	3.0	0.16	3.174
-500	390	9.0	0.08	2.059	-480	630	4.0	0.00	1.115	-480	-390	3.3	0.16	3.032
-500	370	9.0	0.12	1.856	-480	610	4.5	0.00	0.980	-480	-410	3.5	0.12	2.623
-500	350	9.3	0.12	1.700	-480	590	5.0	0.00	0.818	-480	-430	3.5	0.12	2.106
-500	330	9.3	0.12	1.572	-480	570	5.5	0.00	0.688	-480	-450	3.8	0.08	1.760
-500	310	9.5	0.12	1.431	-480	550	6.3	0.00	0.614	-480	-470	3.8	0.08	1.286
-500	290	9.5	0.12	1.289	-480	530	7.0	0.00	0.699	-480	-490	3.8	0.08	0.916
-500	270	9.5	0.12	1.237	-480	510	7.8	0.04	1.034	-480	-510	3.8	0.08	0.715
-500	250	9.8	0.12	1.327	-480	490	8.3	0.08	1.476	-480	-530	3.8	0.08	0.644
-500	230	9.5	0.12	1.490	-480	470	9.0	0.08	1.842	-480	-550	4.0	0.04	0.583
-500	210	9.8	0.08	1.646	-480	450	9.5	0.08	2.026	-480	-570	4.0	0.04	0.527
-500	190	8.8	0.08	1.653	-480	430	9.8	0.08	2.044	-480	-590	4.0	0.04	0.511
-500	170	7.3	0.08	1.624	-480	410	9.8	0.08	1.955	-460	650	3.5	0.00	1.279
-500	150	5.8	0.08	1.460	-480	390	10.0	0.08	1.821	-460	630	4.0	0.00	1.112
-500	130	4.3	0.08	1.232	-480	370	9.8	0.12	1.736	-460	610	4.5	0.00	0.947
-500	110	3.5	0.08	1.147	-480	350	10.0	0.12	1.706	-460	590	5.3	0.00	0.816
-500	90	3.0	0.08	1.063	-480	330	10.0	0.12	1.693	-460	570	5.8	0.04	0.728
-500	70	2.5	0.08	1.076	-480	310	10.0	0.12	1.688	-460	550	6.8	0.00	0.639
-500	50	1.5	0.12	1.441	-480	290	10.0	0.12	1.698	-460	530	7.5	0.00	0.730
-500	30	1.0	0.12	1.914	-480	270	9.8	0.12	1.763	-460	510	8.3	0.00	1.086
-500	10	1.0	0.12	2.212	-480	250	9.5	0.12	1.832	-460	490	9.0	0.04	1.490
-500	-10	1.0	0.08	1.391	-480	230	9.0	0.12	1.801	-460	470	9.5	0.08	1.726
-500	-30	1.3	0.04	1.085	-480	210	8.0	0.12	1.725	-460	450	10.0	0.08	1.754
-500	-50	1.5	0.00	1.082	-480	190	6.8	0.12	1.582	-460	430	10.3	0.08	1.670
-500	-70	1.8	0.00	1.183	-480	170	5.5	0.12	1.423	-460	410	10.3	0.08	1.581
-500	-90	2.3	0.00	1.300	-480	150	4.8	0.08	1.161	-460	390	10.5	0.08	1.577
-500	-110	2.5	0.00	1.479	-480	130	4.0	0.08	0.975	-460	370	10.3	0.12	1.637
-500	-130	2.8	0.00	1.639	-480	110	3.3	0.08	0.982	-460	350	10.3	0.12	1.761
-500	-150	2.8	0.00	1.745	-480	90	2.8	0.08	0.948	-460	330	10.5	0.12	1.915
-500	-170	3.0	0.00	1.831	-480	70	2.3	0.08	0.939	-460	310	10.3	0.12	2.106
-500	-190	3.0	0.00	1.935	-480	50	2.0	0.08	1.339	-460	290	9.3	0.16	2.260
-500	-210	3.0	0.00	2.014	-480	30	1.0	0.12	1.636	-460	270	8.8	0.16	2.434
-500	-230	3.0	0.00	2.053	-480	10	1.0	0.12	2.306	-460	250	7.8	0.16	2.519
-500	-250	2.8	0.08	2.198	-480	-10	1.0	0.08	1.764	-460	230	6.8	0.16	2.419
-500	-270	2.8	0.08	2.453	-480	-30	1.0	0.08	1.336	-460	210	6.5	0.12	2.088
-500	-290	2.5	0.12	2.626	-480	-50	1.5	0.04	1.241	-460	190	5.3	0.12	1.647
-500	-310	2.8	0.12	2.802	-480	-70	1.8	0.00	1.097	-460	170	4.5	0.12	1.248
-500	-330	3.0	0.12	2.944	-480	-90	2.3	0.00	1.144	-460	150	4.0	0.08	0.983
-500	-350	3.0	0.16	2.851	-480	-110	2.5	0.00	1.323	-460	130	3.5	0.08	0.894

Appendix 4.B. (continued)

x	y	T_e	F_3	H	x	y	T_e	F_3	H	x	y	T_e	F_3	H
-460	110	3.0	0.08	1.039	-440	330	9.8	0.16	2.263	-420	550	7.3	0.00	0.960
-460	90	2.8	0.08	1.024	-440	310	9.5	0.16	2.603	-420	530	8.0	0.00	0.981
-460	70	2.3	0.08	0.939	-440	290	8.8	0.16	2.995	-420	510	9.0	0.00	1.269
-460	50	1.8	0.08	1.340	-440	270	7.8	0.16	3.248	-420	490	9.8	0.00	1.437
-460	30	1.0	0.12	2.130	-440	250	6.5	0.16	3.171	-420	470	10.3	0.04	1.342
-460	10	1.0	0.12	3.806	-440	230	4.8	0.16	2.754	-420	450	10.8	0.04	1.155
-460	-10	1.0	0.12	3.233	-440	210	4.0	0.16	2.264	-420	430	10.8	0.08	1.007
-460	-30	1.0	0.12	2.378	-440	190	4.3	0.12	1.744	-420	410	10.8	0.08	1.026
-460	-50	1.3	0.08	1.704	-440	170	3.8	0.12	1.333	-420	390	10.5	0.12	1.299
-460	-70	1.8	0.08	1.520	-440	150	3.5	0.08	1.103	-420	370	10.5	0.12	1.715
-460	-90	2.3	0.04	1.431	-440	130	3.3	0.08	1.035	-420	350	9.8	0.16	2.235
-460	-110	2.5	0.00	1.486	-440	110	3.0	0.08	1.120	-420	330	9.5	0.16	2.726
-460	-130	2.8	0.00	1.507	-440	90	2.8	0.04	1.034	-420	310	8.8	0.16	3.373
-460	-150	2.8	0.00	1.585	-440	70	2.3	0.08	0.911	-420	290	4.5	0.20	3.918
-460	-170	2.8	0.00	1.717	-440	50	1.8	0.08	1.375	-420	270	3.3	0.20	3.694
-460	-190	2.8	0.00	1.821	-440	30	1.0	0.12	2.095	-420	250	2.8	0.20	3.407
-460	-210	2.8	0.00	1.887	-440	10	1.0	0.12	4.496	-420	230	3.5	0.16	2.666
-460	-230	2.8	0.00	1.905	-440	-10	1.0	0.16	5.357	-420	210	3.3	0.16	2.233
-460	-250	2.5	0.04	2.004	-440	-30	1.0	0.12	3.505	-420	190	3.5	0.12	1.746
-460	-270	2.5	0.08	2.241	-440	-50	1.0	0.12	2.471	-420	170	3.3	0.12	1.522
-460	-290	2.3	0.12	2.489	-440	-70	1.8	0.08	2.149	-420	150	3.3	0.08	1.239
-460	-310	2.5	0.12	2.659	-440	-90	2.0	0.08	1.852	-420	130	3.0	0.04	1.189
-460	-330	2.5	0.12	2.909	-440	-110	2.3	0.08	1.788	-420	110	2.8	0.04	1.071
-460	-350	2.5	0.16	3.136	-440	-130	2.8	0.04	1.696	-420	90	2.5	0.04	0.992
-460	-370	2.8	0.16	3.250	-440	-150	2.8	0.00	1.612	-420	70	2.3	0.08	0.952
-460	-390	3.0	0.16	3.375	-440	-170	3.0	0.00	1.617	-420	50	2.0	0.08	1.156
-460	-410	3.0	0.16	3.170	-440	-190	2.8	0.00	1.668	-420	30	1.0	0.12	1.594
-460	-430	3.3	0.12	2.587	-440	-210	2.8	0.00	1.719	-420	10	1.0	0.12	2.890
-460	-450	3.3	0.12	2.047	-440	-230	2.5	0.00	1.763	-420	-10	1.0	0.16	4.594
-460	-470	3.5	0.08	1.581	-440	-250	2.5	0.04	1.888	-420	-30	1.0	0.16	4.371
-460	-490	3.5	0.08	1.087	-440	-270	2.5	0.08	2.095	-420	-50	1.0	0.12	3.278
-460	-510	3.8	0.08	0.798	-440	-290	2.3	0.12	2.338	-420	-70	1.5	0.12	2.540
-460	-530	4.0	0.04	0.653	-440	-310	2.5	0.12	2.325	-420	-90	2.0	0.12	2.322
-460	-550	4.0	0.04	0.560	-440	-330	2.5	0.12	2.455	-420	-110	2.5	0.08	2.159
-460	-570	4.0	0.04	0.522	-440	-350	2.8	0.12	2.705	-420	-130	2.8	0.08	1.989
-460	-590	3.8	0.04	0.509	-440	-370	2.8	0.16	2.908	-420	-150	3.0	0.00	1.702
-440	650	3.0	0.08	1.645	-440	-390	2.8	0.16	3.066	-420	-170	3.0	0.00	1.543
-440	630	3.8	0.08	1.399	-440	-410	3.0	0.16	3.143	-420	-190	3.0	0.00	1.491
-440	610	4.8	0.04	1.139	-440	-430	3.0	0.16	2.880	-420	-210	2.8	0.00	1.481
-440	590	5.5	0.00	0.971	-440	-450	3.3	0.12	2.256	-420	-230	2.8	0.00	1.513
-440	570	6.3	0.00	0.872	-440	-470	3.3	0.12	1.908	-420	-250	2.5	0.04	1.683
-440	550	7.3	0.00	0.787	-440	-490	3.5	0.08	1.420	-420	-270	2.5	0.08	1.868
-440	530	8.0	0.00	0.834	-440	-510	3.5	0.08	1.062	-420	-290	2.5	0.08	2.050
-440	510	8.8	0.00	1.188	-440	-530	3.8	0.04	0.848	-420	-310	2.5	0.12	2.056
-440	490	9.5	0.00	1.505	-440	-550	3.8	0.04	0.692	-420	-330	2.5	0.12	2.034
-440	470	10.3	0.04	1.563	-440	-570	3.8	0.04	0.622	-420	-350	2.8	0.12	2.118
-440	450	10.3	0.08	1.462	-440	-590	3.8	0.00	0.610	-420	-370	3.0	0.12	2.308
-440	430	10.5	0.08	1.315	-420	650	2.3	0.12	2.129	-420	-390	3.0	0.12	2.494
-440	410	10.8	0.08	1.235	-420	630	3.0	0.12	1.942	-420	-410	3.3	0.12	2.631
-440	390	10.3	0.12	1.364	-420	610	4.3	0.08	1.686	-420	-430	3.3	0.12	2.532
-440	370	10.5	0.12	1.594	-420	590	5.5	0.04	1.362	-420	-450	3.3	0.12	2.169
-440	350	10.5	0.12	1.896	-420	570	6.5	0.00	1.102	-420	-470	3.3	0.12	1.900

Appendix 4.B. (continued)

x	y	T_e	F_3	H	x	y	T_e	F_3	H	x	y	T_e	F_3	H
-420	-490	3.5	0.08	1.647	-400	-270	2.5	0.08	1.592	-380	-50	1.0	0.16	3.350
-420	-510	3.5	0.08	1.455	-400	-290	2.5	0.08	1.713	-380	-70	1.3	0.16	3.298
-420	-530	3.5	0.08	1.305	-400	-310	2.5	0.12	1.807	-380	-90	2.3	0.12	2.692
-420	-550	3.5	0.04	1.139	-400	-330	2.8	0.12	1.687	-380	-110	2.5	0.12	2.459
-420	-570	3.5	0.04	1.030	-400	-350	2.8	0.12	1.631	-380	-130	2.8	0.12	2.316
-420	-590	3.5	0.04	0.975	-400	-370	3.0	0.12	1.625	-380	-150	3.0	0.08	1.977
-400	650	1.3	0.12	2.413	-400	-390	3.3	0.12	1.641	-380	-170	3.0	0.04	1.587
-400	630	2.3	0.12	2.364	-400	-410	3.3	0.12	1.700	-380	-190	3.0	0.04	1.303
-400	610	3.3	0.12	2.225	-400	-430	3.5	0.12	1.750	-380	-210	3.0	0.04	1.150
-400	590	4.5	0.08	1.864	-400	-450	3.5	0.12	1.742	-380	-230	2.8	0.08	1.243
-400	570	6.0	0.00	1.422	-400	-470	3.5	0.12	1.719	-380	-250	2.5	0.08	1.267
-400	550	7.0	0.00	1.114	-400	-490	3.5	0.08	1.609	-380	-270	2.5	0.08	1.362
-400	530	7.8	0.00	1.114	-400	-510	3.5	0.08	1.593	-380	-290	2.5	0.08	1.459
-400	510	8.5	0.00	1.331	-400	-530	3.3	0.08	1.638	-380	-310	2.8	0.08	1.524
-400	490	9.5	0.00	1.335	-400	-550	3.3	0.08	1.685	-380	-330	2.8	0.12	1.467
-400	470	10.0	0.04	1.108	-400	-570	3.3	0.08	1.726	-380	-350	3.0	0.12	1.300
-400	450	10.5	0.04	0.875	-400	-590	3.3	0.08	1.706	-380	-370	3.3	0.12	1.177
-400	430	10.5	0.08	0.849	-380	650	1.0	0.12	2.535	-380	-390	3.3	0.12	1.124
-400	410	10.8	0.08	1.095	-380	630	1.3	0.12	2.420	-380	-410	3.8	0.08	1.039
-400	390	10.3	0.12	1.488	-380	610	2.3	0.12	2.319	-380	-430	3.8	0.08	1.169
-400	370	10.3	0.12	2.040	-380	590	3.8	0.08	2.006	-380	-450	3.8	0.08	1.297
-400	350	9.0	0.16	2.634	-380	570	5.3	0.00	1.580	-380	-470	3.8	0.08	1.368
-400	330	8.5	0.16	3.376	-380	550	6.3	0.00	1.299	-380	-490	3.8	0.08	1.487
-400	310	3.8	0.20	3.976	-380	530	7.3	0.00	1.248	-380	-510	3.5	0.08	1.640
-400	290	3.0	0.20	3.839	-380	510	8.0	0.00	1.331	-380	-530	3.3	0.08	1.894
-400	270	2.5	0.20	3.442	-380	490	9.0	0.00	1.196	-380	-550	3.3	0.08	2.176
-400	250	3.3	0.16	3.179	-380	470	9.8	0.00	0.928	-380	-570	3.0	0.12	2.430
-400	230	3.0	0.16	2.350	-380	450	10.3	0.04	0.818	-380	-590	3.0	0.12	2.618
-400	210	3.3	0.12	2.155	-380	430	10.3	0.08	1.007	-360	650	1.0	0.12	2.528
-400	190	3.0	0.12	1.680	-380	410	10.5	0.08	1.376	-360	630	1.0	0.12	2.310
-400	170	3.3	0.08	1.506	-380	390	9.8	0.12	1.834	-360	610	2.3	0.08	2.252
-400	150	3.0	0.08	1.355	-380	370	9.8	0.12	2.435	-360	590	3.0	0.08	2.017
-400	130	3.0	0.04	1.254	-380	350	7.8	0.16	3.087	-360	570	4.5	0.00	1.719
-400	110	2.8	0.00	1.110	-380	330	3.8	0.20	3.719	-360	550	5.5	0.00	1.507
-400	90	2.5	0.04	0.988	-380	310	3.0	0.20	3.725	-360	530	6.5	0.00	1.355
-400	70	2.3	0.04	0.983	-380	290	2.5	0.20	3.432	-360	510	7.3	0.00	1.263
-400	50	2.0	0.08	1.124	-380	270	2.3	0.20	3.129	-360	490	8.3	0.00	1.089
-400	30	1.3	0.12	1.763	-380	250	3.0	0.16	2.579	-360	470	9.0	0.00	0.959
-400	10	1.0	0.12	2.157	-380	230	2.8	0.16	2.131	-360	450	9.5	0.04	1.091
-400	-10	1.0	0.12	3.191	-380	210	3.0	0.12	1.818	-360	430	9.5	0.08	1.374
-400	-30	1.0	0.16	3.709	-380	190	2.8	0.12	1.651	-360	410	9.8	0.08	1.724
-400	-50	1.0	0.16	3.578	-380	170	3.0	0.08	1.436	-360	390	8.8	0.12	2.164
-400	-70	1.8	0.12	2.969	-380	150	3.0	0.04	1.395	-360	370	8.8	0.12	2.726
-400	-90	2.0	0.12	2.514	-380	130	2.8	0.00	1.301	-360	350	6.0	0.16	3.246
-400	-110	2.5	0.12	2.363	-380	110	2.8	0.00	1.142	-360	330	3.0	0.20	3.396
-400	-130	3.0	0.08	2.144	-380	90	2.5	0.00	0.992	-360	310	2.5	0.20	3.162
-400	-150	3.0	0.08	1.892	-380	70	2.3	0.04	0.991	-360	290	2.3	0.20	2.972
-400	-170	3.0	0.00	1.530	-380	50	2.0	0.08	1.158	-360	270	3.0	0.16	2.919
-400	-190	3.0	0.00	1.343	-380	30	2.0	0.08	1.512	-360	250	2.8	0.16	2.102
-400	-210	3.0	0.00	1.238	-380	10	1.3	0.12	2.040	-360	230	3.0	0.12	2.057
-400	-230	2.8	0.04	1.306	-380	-10	1.5	0.12	2.324	-360	210	2.8	0.12	1.620
-400	-250	2.5	0.08	1.486	-380	-30	1.5	0.12	3.110	-360	190	3.0	0.08	1.553

Appendix 4.B. (continued)

x	y	T_e	F_3	H	x	y	T_e	F_3	H	x	y	T_e	F_3	H
-360	170	2.8	0.08	1.419	-340	390	7.5	0.12	2.407	-320	610	1.0	0.12	2.675
-360	150	2.8	0.04	1.383	-340	370	5.5	0.16	2.829	-320	590	1.8	0.12	2.644
-360	130	2.8	0.00	1.310	-340	350	4.5	0.16	3.083	-320	570	2.5	0.12	2.594
-360	110	2.5	0.00	1.172	-340	330	2.8	0.20	3.093	-320	550	3.8	0.08	2.131
-360	90	2.5	0.00	1.035	-340	310	2.3	0.20	2.874	-320	530	4.8	0.04	1.696
-360	70	2.3	0.04	1.035	-340	290	2.3	0.20	3.016	-320	510	5.5	0.04	1.325
-360	50	2.3	0.04	1.175	-340	270	2.8	0.16	2.230	-320	490	6.0	0.04	1.285
-360	30	2.0	0.08	1.321	-340	250	2.5	0.16	2.043	-320	470	6.3	0.08	1.543
-360	10	2.0	0.08	1.593	-340	230	3.0	0.12	1.773	-320	450	6.5	0.08	1.824
-360	-10	2.0	0.08	2.064	-340	210	2.8	0.12	1.605	-320	430	6.8	0.08	2.083
-360	-30	1.8	0.12	2.280	-340	190	3.0	0.08	1.446	-320	410	5.8	0.12	2.277
-360	-50	2.0	0.12	2.981	-340	170	3.0	0.04	1.375	-320	390	5.8	0.12	2.475
-360	-70	1.5	0.16	3.228	-340	150	2.8	0.04	1.326	-320	370	4.0	0.16	2.692
-360	-90	2.5	0.12	2.880	-340	130	2.8	0.00	1.299	-320	350	3.5	0.16	2.670
-360	-110	2.8	0.12	2.517	-340	110	2.5	0.00	1.194	-320	330	3.3	0.16	2.710
-360	-130	2.8	0.12	2.267	-340	90	2.5	0.00	1.131	-320	310	3.0	0.16	2.612
-360	-150	3.0	0.08	1.914	-340	70	2.3	0.00	1.159	-320	290	2.8	0.16	2.263
-360	-170	3.0	0.08	1.588	-340	50	2.3	0.04	1.140	-320	270	2.5	0.16	2.027
-360	-190	3.0	0.04	1.288	-340	30	2.0	0.04	1.206	-320	250	3.0	0.12	2.002
-360	-210	2.8	0.08	1.187	-340	10	2.0	0.08	1.363	-320	230	3.0	0.12	1.649
-360	-230	2.8	0.08	1.147	-340	-10	2.0	0.08	1.492	-320	210	2.8	0.12	1.606
-360	-250	2.5	0.08	1.217	-340	-30	2.3	0.08	1.941	-320	190	3.0	0.08	1.325
-360	-270	2.5	0.08	1.253	-340	-50	2.0	0.12	2.229	-320	170	3.0	0.04	1.225
-360	-290	2.8	0.08	1.372	-340	-70	2.3	0.12	2.783	-320	150	2.8	0.00	1.233
-360	-310	2.8	0.08	1.455	-340	-90	2.5	0.12	2.871	-320	130	2.8	0.00	1.261
-360	-330	3.0	0.08	1.344	-340	-110	2.8	0.12	2.516	-320	110	2.5	0.00	1.234
-360	-350	3.3	0.08	1.131	-340	-130	2.8	0.12	2.170	-320	90	2.5	0.00	1.229
-360	-370	3.5	0.08	0.848	-340	-150	3.0	0.08	1.846	-320	70	2.3	0.00	1.216
-360	-390	3.8	0.08	0.706	-340	-170	3.0	0.08	1.464	-320	50	2.3	0.00	1.189
-360	-410	3.8	0.08	0.710	-340	-190	2.8	0.08	1.145	-320	30	2.0	0.04	1.184
-360	-430	4.0	0.08	0.772	-340	-210	2.8	0.08	1.097	-320	10	2.0	0.04	1.171
-360	-450	4.0	0.08	0.868	-340	-230	2.5	0.08	1.296	-320	-10	2.3	0.04	1.285
-360	-470	4.0	0.08	1.030	-340	-250	2.5	0.08	1.404	-320	-30	2.3	0.08	1.558
-360	-490	3.8	0.08	1.268	-340	-270	2.5	0.08	1.449	-320	-50	2.3	0.08	1.985
-360	-510	3.5	0.08	1.566	-340	-290	2.8	0.08	1.427	-320	-70	2.3	0.12	2.462
-360	-530	3.3	0.12	1.941	-340	-310	3.0	0.08	1.409	-320	-90	2.5	0.12	2.670
-360	-550	3.0	0.12	2.337	-340	-330	3.3	0.08	1.204	-320	-110	2.5	0.12	2.479
-360	-570	2.8	0.12	2.795	-340	-350	3.5	0.08	0.951	-320	-130	2.8	0.12	2.072
-360	-590	2.5	0.12	3.243	-340	-370	3.8	0.08	0.807	-320	-150	3.0	0.08	1.772
-340	650	1.0	0.08	2.278	-340	-390	4.0	0.08	0.742	-320	-170	2.8	0.08	1.293
-340	630	1.0	0.12	2.094	-340	-410	4.0	0.08	0.738	-320	-190	2.8	0.08	1.006
-340	610	1.8	0.08	2.071	-340	-430	4.3	0.04	0.685	-320	-210	2.5	0.08	0.920
-340	590	2.5	0.08	1.931	-340	-450	4.3	0.04	0.726	-320	-230	2.5	0.08	1.227
-340	570	3.5	0.04	1.849	-340	-470	4.3	0.08	0.827	-320	-250	2.5	0.08	1.395
-340	550	4.8	0.00	1.705	-340	-490	4.0	0.08	0.998	-320	-270	2.5	0.08	1.612
-340	530	5.8	0.00	1.482	-340	-510	3.8	0.08	1.327	-320	-290	2.8	0.08	1.586
-340	510	6.5	0.00	1.240	-340	-530	3.5	0.08	1.783	-320	-310	3.0	0.08	1.410
-340	490	7.3	0.00	1.119	-340	-550	2.8	0.12	2.233	-320	-330	3.3	0.08	1.200
-340	470	8.0	0.00	1.245	-340	-570	2.5	0.12	2.770	-320	-350	3.5	0.08	1.055
-340	450	8.5	0.04	1.508	-340	-590	2.3	0.12	3.379	-320	-370	3.8	0.08	1.002
-340	430	8.3	0.08	1.780	-320	650	1.0	0.08	2.344	-320	-390	4.3	0.04	0.916
-340	410	8.5	0.08	2.069	-320	630	1.0	0.12	2.628	-320	-410	4.3	0.04	0.825

Appendix 4.B. (continued)

x	y	T_e	F_3	H
-320	-430	4.5	0.04	0.765
-320	-450	4.5	0.04	0.720
-320	-470	4.5	0.04	0.712
-320	-490	4.3	0.08	0.810
-320	-510	4.0	0.08	1.029
-320	-530	3.5	0.08	1.426
-320	-550	3.0	0.12	1.925
-320	-570	2.5	0.12	2.449
-320	-590	2.0	0.12	3.020
-300	650	1.0	0.12	4.484
-300	630	1.0	0.12	4.279
-300	610	1.0	0.12	3.751
-300	590	1.5	0.12	3.365
-300	570	2.3	0.12	3.117
-300	550	2.8	0.12	2.550
-300	530	3.8	0.08	1.898
-300	510	4.3	0.08	1.381
-300	490	4.5	0.08	1.233
-300	470	4.8	0.08	1.521
-300	450	4.8	0.08	1.824
-300	430	4.0	0.12	2.030
-300	410	4.0	0.12	2.145
-300	390	4.3	0.12	2.272
-300	370	4.0	0.12	2.448
-300	350	3.0	0.16	2.336
-300	330	3.0	0.16	2.193
-300	310	2.8	0.16	2.189
-300	290	2.8	0.16	2.101
-300	270	3.0	0.12	2.159
-300	250	3.0	0.12	1.782
-300	230	3.0	0.12	1.596
-300	210	3.3	0.08	1.440
-300	190	3.3	0.08	1.247
-300	170	3.3	0.04	1.112
-300	150	3.0	0.00	1.159
-300	130	2.8	0.00	1.232
-300	110	2.5	0.00	1.236
-300	90	2.3	0.00	1.240
-300	70	2.3	0.00	1.243
-300	50	2.3	0.00	1.225
-300	30	2.0	0.00	1.209
-300	10	2.3	0.00	1.144
-300	-10	2.3	0.04	1.192
-300	-30	2.3	0.04	1.368
-300	-50	2.3	0.08	1.678
-300	-70	2.5	0.08	2.285
-300	-90	2.3	0.12	2.416
-300	-110	2.5	0.12	2.283
-300	-130	2.5	0.12	1.941
-300	-150	2.5	0.12	1.645
-300	-170	2.8	0.08	1.184
-300	-190	2.5	0.08	0.848

x	y	T_e	F_3	H
-300	-210	2.5	0.08	0.729
-300	-230	2.5	0.08	0.981
-300	-250	2.5	0.08	1.187
-300	-270	2.5	0.08	1.486
-300	-290	2.8	0.08	1.622
-300	-310	3.0	0.08	1.529
-300	-330	3.3	0.08	1.475
-300	-350	3.5	0.04	1.403
-300	-370	4.0	0.04	1.246
-300	-390	4.3	0.04	1.050
-300	-410	4.5	0.04	0.892
-300	-430	4.5	0.04	0.793
-300	-450	4.8	0.04	0.749
-300	-470	4.5	0.04	0.717
-300	-490	4.5	0.04	0.729
-300	-510	4.3	0.08	0.817
-300	-530	3.8	0.08	0.991
-300	-550	3.3	0.08	1.351
-300	-570	2.8	0.08	1.909
-300	-590	2.0	0.12	2.486
-280	650	1.0	0.12	4.800
-280	630	1.0	0.12	4.443
-280	610	1.0	0.12	3.828
-280	590	1.3	0.12	3.357
-280	570	2.0	0.12	2.892
-280	550	3.0	0.08	2.402
-280	530	3.5	0.08	1.854
-280	510	3.8	0.08	1.264
-280	490	4.0	0.08	0.965
-280	470	3.8	0.08	1.228
-280	450	3.8	0.08	1.542
-280	430	3.8	0.08	1.750
-280	410	3.3	0.12	1.934
-280	390	3.5	0.12	2.018
-280	370	3.5	0.12	2.085
-280	350	3.5	0.12	2.201
-280	330	2.8	0.16	2.150
-280	310	2.8	0.16	2.209
-280	290	3.3	0.12	2.110
-280	270	3.3	0.12	1.835
-280	250	3.3	0.12	1.679
-280	230	3.5	0.08	1.567
-280	210	3.5	0.08	1.333
-280	190	3.8	0.04	1.212
-280	170	3.5	0.04	1.072
-280	150	3.3	0.00	1.140
-280	130	3.0	0.00	1.200
-280	110	2.8	0.00	1.222
-280	90	2.3	0.00	1.250
-280	70	2.3	0.04	1.297
-280	50	2.0	0.00	1.192
-280	30	2.0	0.00	1.192

x	y	T_e	F_3	H
-280	10	2.0	0.00	1.165
-280	-10	2.3	0.00	1.159
-280	-30	2.3	0.04	1.280
-280	-50	2.3	0.04	1.520
-280	-70	2.3	0.08	1.837
-280	-90	2.3	0.12	2.226
-280	-110	2.3	0.12	2.084
-280	-130	2.3	0.12	1.770
-280	-150	2.3	0.12	1.550
-280	-170	2.5	0.08	1.148
-280	-190	2.3	0.08	0.867
-280	-210	2.3	0.08	0.711
-280	-230	2.3	0.08	0.811
-280	-250	2.5	0.08	1.043
-280	-270	2.5	0.08	1.325
-280	-290	2.8	0.08	1.516
-280	-310	3.0	0.04	1.620
-280	-330	3.3	0.04	1.676
-280	-350	3.5	0.04	1.644
-280	-370	4.0	0.04	1.467
-280	-390	4.3	0.04	1.239
-280	-410	4.5	0.04	1.034
-280	-430	4.8	0.04	0.870
-280	-450	4.8	0.04	0.757
-280	-470	4.8	0.04	0.697
-280	-490	4.5	0.04	0.693
-280	-510	4.3	0.08	0.739
-280	-530	4.0	0.08	0.803
-280	-550	3.5	0.08	0.929
-280	-570	3.0	0.08	1.246
-280	-590	2.3	0.08	1.821
-260	650	1.0	0.08	3.696
-260	630	1.0	0.08	3.700
-260	610	1.3	0.08	3.704
-260	590	1.3	0.12	3.400
-260	570	2.3	0.08	2.919
-260	550	3.0	0.08	2.250
-260	530	3.3	0.08	1.628
-260	510	3.5	0.08	1.026
-260	490	3.5	0.08	0.689
-260	470	3.5	0.08	0.847
-260	450	3.5	0.08	1.225
-260	430	3.3	0.08	1.480
-260	410	3.5	0.08	1.644
-260	390	3.5	0.08	1.777
-260	370	3.3	0.12	1.870
-260	350	3.3	0.12	1.850
-260	330	3.3	0.12	1.946
-260	310	3.3	0.12	1.931
-260	290	3.3	0.12	1.887
-260	270	3.5	0.12	1.822
-260	250	4.0	0.08	1.677

Appendix 4.B. (continued)

x	y	T_e	F_3	H	$\boldsymbol{x}$	y	T_e	F_3	H	x	y	T_e	F_3	H
-260	230	4.0	0.08	1.481	-240	450	3.3	0.08	0.891	-240	-590	1.5	0.08	1.132
-260	210	4.3	0.08	1.364	-240	430	3.5	0.04	1.191	-220	650	1.0	0.00	3.379
-260	190	4.3	0.04	1.253	-240	410	3.3	0.08	1.380	-220	630	1.0	0.08	3.953
-260	170	4.0	0.04	1.118	-240	390	3.3	0.08	1.529	-220	610	1.0	0.12	4.217
-260	150	3.8	0.00	1.150	-240	370	3.5	0.08	1.618	-220	590	1.5	0.12	4.183
-260	130	3.3	0.00	1.237	-240	350	3.5	0.08	1.680	-220	570	2.0	0.16	3.854
-260	110	2.8	0.00	1.259	-240	330	3.8	0.08	1.770	-220	550	3.0	0.12	3.386
-260	90	2.3	0.00	1.303	-240	310	4.0	0.08	1.847	-220	530	3.5	0.12	2.597
-260	70	2.0	0.04	1.345	-240	290	4.3	0.08	1.820	-220	510	3.8	0.12	1.774
-260	50	2.0	0.00	1.218	-240	270	4.5	0.08	1.705	-220	490	3.8	0.12	1.208
-260	30	2.0	0.00	1.168	-240	250	5.0	0.04	1.577	-220	470	3.8	0.08	0.799
-260	10	2.0	0.00	1.178	-240	230	5.0	0.04	1.454	-220	450	3.5	0.08	0.705
-260	-10	2.0	0.00	1.131	-240	210	5.3	0.00	1.393	-220	430	3.3	0.08	0.955
-260	-30	2.0	0.00	1.158	-240	190	5.0	0.00	1.346	-220	410	3.3	0.08	1.166
-260	-50	2.3	0.04	1.329	-240	170	4.8	0.00	1.233	-220	390	3.5	0.04	1.345
-260	-70	2.3	0.04	1.598	-240	150	4.3	0.00	1.281	-220	370	3.8	0.04	1.453
-260	-90	2.3	0.08	1.764	-240	130	3.8	0.00	1.350	-220	350	4.0	0.04	1.514
-260	-110	2.0	0.12	1.918	-240	110	3.0	0.00	1.397	-220	330	4.3	0.00	1.549
-260	-130	2.0	0.12	1.624	-240	90	2.3	0.00	1.475	-220	310	4.8	0.00	1.578
-260	-150	2.3	0.08	1.498	-240	70	2.0	0.00	1.461	-220	290	5.3	0.00	1.586
-260	-170	2.3	0.08	1.222	-240	50	1.8	0.00	1.330	-220	270	5.5	0.00	1.556
-260	-190	2.3	0.08	1.043	-240	30	1.8	0.00	1.238	-220	250	5.8	0.00	1.484
-260	-210	2.3	0.08	0.949	-240	10	1.8	0.00	1.199	-220	230	6.3	0.00	1.491
-260	-230	2.3	0.08	0.918	-240	-10	2.0	0.00	1.142	-220	210	6.3	0.00	1.545
-260	-250	2.5	0.04	0.943	-240	-30	2.0	0.00	1.100	-220	190	6.0	0.00	1.517
-260	-270	2.8	0.04	1.070	-240	-50	2.0	0.00	1.093	-220	170	5.5	0.00	1.461
-260	-290	3.0	0.00	1.332	-240	-70	2.0	0.04	1.268	-220	150	4.8	0.00	1.424
-260	-310	3.3	0.00	1.570	-240	-90	2.0	0.08	1.407	-220	130	4.0	0.00	1.434
-260	-330	3.5	0.00	1.682	-240	-110	2.3	0.08	1.427	-220	110	3.0	0.00	1.501
-260	-350	3.8	0.00	1.687	-240	-130	2.3	0.08	1.469	-220	90	2.3	0.00	1.616
-260	-370	4.0	0.00	1.586	-240	-150	2.3	0.08	1.467	-220	70	1.8	0.00	1.657
-260	-390	4.3	0.00	1.412	-240	-170	2.3	0.08	1.353	-220	50	1.5	0.00	1.563
-260	-410	4.5	0.04	1.197	-240	-190	2.3	0.08	1.252	-220	30	1.5	0.00	1.425
-260	-430	4.8	0.04	1.015	-240	-210	2.3	0.08	1.184	-220	10	1.5	0.00	1.301
-260	-450	4.8	0.04	0.858	-240	-230	2.5	0.04	1.137	-220	-10	1.8	0.00	1.199
-260	-470	4.8	0.04	0.765	-240	-250	2.5	0.04	1.057	-220	-30	1.8	0.00	1.081
-260	-490	4.5	0.04	0.738	-240	-270	2.8	0.00	1.081	-220	-50	2.0	0.00	0.975
-260	-510	4.5	0.04	0.766	-240	-290	3.3	0.00	1.288	-220	-70	2.0	0.00	1.001
-260	-530	4.0	0.04	0.820	-240	-310	3.5	0.00	1.505	-220	-90	2.0	0.04	1.216
-260	-550	3.5	0.00	0.906	-240	-330	3.8	0.00	1.654	-220	-110	2.0	0.08	1.132
-260	-570	3.0	0.04	0.865	-240	-350	4.0	0.00	1.679	-220	-130	2.0	0.08	1.264
-260	-590	2.3	0.08	0.821	-240	-370	4.3	0.00	1.613	-220	-150	2.0	0.08	1.383
-240	650	1.0	0.00	2.661	-240	-390	4.3	0.00	1.477	-220	-170	2.3	0.08	1.405
-240	630	1.0	0.04	3.113	-240	-410	4.5	0.00	1.291	-220	-190	2.3	0.08	1.345
-240	610	1.0	0.08	3.666	-240	-430	4.5	0.00	1.122	-220	-210	2.3	0.08	1.298
-240	590	1.3	0.12	3.621	-240	-450	4.8	0.00	0.981	-220	-230	2.5	0.04	1.300
-240	570	2.3	0.12	3.148	-240	-470	4.5	0.04	0.887	-220	-250	2.8	0.04	1.233
-240	550	3.0	0.08	2.489	-240	-490	4.5	0.04	0.875	-220	-270	3.0	0.00	1.246
-240	530	3.5	0.08	1.809	-240	-510	4.3	0.04	0.918	-220	-290	3.3	0.00	1.367
-240	510	3.5	0.08	1.128	-240	-530	3.8	0.00	1.001	-220	-310	3.5	0.00	1.531
-240	490	3.5	0.08	0.566	-240	-550	3.3	0.00	1.124	-220	-330	3.8	0.00	1.651
-240	470	3.5	0.08	0.554	-240	-570	2.5	0.04	1.205	-220	-350	4.0	0.00	1.676

Appendix 4.B. (continued)

x	y	T_e	F_3	H	x	y	T_e	F_3	H	x	y	T_e	F_3	H
-220	-370	4.3	0.00	1.623	-200	-150	2.0	0.08	1.267	-180	70	1.5	0.00	1.882
-220	-390	4.3	0.00	1.512	-200	-170	2.3	0.08	1.350	-180	50	1.3	0.00	1.981
-220	-410	4.3	0.00	1.371	-200	-190	2.3	0.08	1.332	-180	30	1.0	0.00	1.933
-220	-430	4.3	0.00	1.213	-200	-210	2.3	0.08	1.332	-180	10	1.0	0.00	1.778
-220	-450	4.3	0.00	1.084	-200	-230	2.5	0.08	1.379	-180	-10	1.3	0.00	1.578
-220	-470	4.3	0.00	1.043	-200	-250	3.0	0.00	1.376	-180	-30	1.5	0.00	1.347
-220	-490	4.0	0.00	1.034	-200	-270	3.0	0.00	1.406	-180	-50	1.5	0.00	1.090
-220	-510	3.8	0.00	1.146	-200	-290	3.3	0.00	1.468	-180	-70	1.8	0.00	0.811
-220	-530	3.0	0.04	1.277	-200	-310	3.5	0.00	1.555	-180	-90	2.0	0.04	0.821
-220	-550	2.3	0.08	1.332	-200	-330	3.8	0.00	1.644	-180	-110	2.0	0.08	0.853
-220	-570	1.5	0.08	1.469	-200	-350	4.0	0.00	1.666	-180	-130	2.0	0.08	0.862
-220	-590	1.0	0.08	2.205	-200	-370	4.0	0.00	1.623	-180	-150	2.0	0.08	1.118
-200	650	1.0	0.04	4.233	-200	-390	4.0	0.00	1.529	-180	-170	2.3	0.08	1.208
-200	630	1.0	0.12	4.499	-200	-410	4.0	0.00	1.396	-180	-190	2.3	0.08	1.237
-200	610	1.0	0.12	4.433	-200	-430	4.0	0.00	1.267	-180	-210	2.5	0.08	1.296
-200	590	1.0	0.16	4.220	-200	-450	4.0	0.00	1.208	-180	-230	2.5	0.08	1.418
-200	570	1.8	0.20	4.082	-200	-470	3.8	0.00	1.235	-180	-250	3.0	0.04	1.443
-200	550	3.0	0.20	3.817	-200	-490	3.5	0.00	1.333	-180	-270	3.3	0.00	1.455
-200	530	4.0	0.16	3.190	-200	-510	3.0	0.00	1.475	-180	-290	3.3	0.00	1.506
-200	510	4.3	0.16	2.404	-200	-530	2.3	0.04	1.535	-180	-310	3.5	0.00	1.550
-200	490	4.3	0.12	1.650	-200	-550	1.5	0.04	1.522	-180	-330	3.5	0.00	1.593
-200	470	4.0	0.12	1.162	-200	-570	1.0	0.04	1.548	-180	-350	3.8	0.00	1.615
-200	450	4.0	0.08	1.014	-200	-590	1.0	0.00	2.098	-180	-370	3.8	0.00	1.616
-200	430	3.8	0.08	0.928	-180	650	1.0	0.04	4.598	-180	-390	3.5	0.00	1.540
-200	410	3.5	0.08	1.086	-180	630	1.0	0.12	4.599	-180	-410	3.5	0.00	1.440
-200	390	3.8	0.04	1.235	-180	610	1.0	0.16	4.472	-180	-430	3.5	0.00	1.355
-200	370	4.0	0.00	1.283	-180	590	1.0	0.20	4.276	-180	-450	3.3	0.00	1.371
-200	350	4.3	0.00	1.360	-180	570	1.8	0.20	4.104	-180	-470	3.0	0.00	1.494
-200	330	4.5	0.00	1.413	-180	550	2.8	0.24	4.033	-180	-490	2.8	0.00	1.656
-200	310	5.0	0.00	1.440	-180	530	4.5	0.20	3.610	-180	-510	2.0	0.04	1.797
-200	290	5.5	0.00	1.448	-180	510	4.8	0.20	2.926	-180	-530	1.5	0.04	1.826
-200	270	6.0	0.00	1.481	-180	490	4.8	0.16	2.042	-180	-550	1.0	0.00	1.863
-200	250	6.5	0.00	1.542	-180	470	4.8	0.12	1.675	-180	-570	1.0	0.00	2.237
-200	230	6.8	0.00	1.629	-180	450	4.3	0.12	1.193	-180	-590	1.0	0.00	3.040
-200	210	6.8	0.00	1.723	-180	430	4.3	0.08	1.065	-160	650	1.0	0.04	4.188
-200	190	6.5	0.00	1.694	-180	410	4.3	0.08	0.984	-160	630	1.0	0.12	4.224
-200	170	6.0	0.00	1.604	-180	390	4.3	0.04	0.977	-160	610	1.0	0.16	4.224
-200	150	5.0	0.00	1.477	-180	370	4.5	0.00	1.003	-160	590	1.0	0.20	4.271
-200	130	4.0	0.00	1.502	-180	350	4.8	0.00	1.145	-160	570	1.5	0.20	4.169
-200	110	3.0	0.00	1.601	-180	330	5.0	0.00	1.244	-160	550	2.3	0.24	4.006
-200	90	2.3	0.00	1.705	-180	310	5.3	0.00	1.311	-160	530	5.0	0.24	3.772
-200	70	1.8	0.00	1.805	-180	290	5.8	0.00	1.351	-160	510	5.5	0.24	3.374
-200	50	1.3	0.00	1.831	-180	270	6.3	0.00	1.398	-160	490	5.3	0.20	2.624
-200	30	1.3	0.00	1.714	-180	250	6.8	0.00	1.512	-160	470	5.3	0.16	2.084
-200	10	1.3	0.00	1.521	-180	230	7.0	0.00	1.629	-160	450	4.8	0.16	1.572
-200	-10	1.5	0.00	1.350	-180	210	6.8	0.00	1.683	-160	430	4.8	0.12	1.032
-200	-30	1.5	0.00	1.193	-180	190	6.5	0.00	1.639	-160	410	4.8	0.08	0.797
-200	-50	1.8	0.00	0.974	-180	170	5.8	0.00	1.534	-160	390	4.8	0.04	0.662
-200	-70	1.8	0.00	0.838	-180	150	4.8	0.00	1.519	-160	370	5.0	0.00	0.745
-200	-90	2.0	0.04	0.921	-180	130	3.5	0.00	1.621	-160	350	5.0	0.00	0.948
-200	-110	2.0	0.08	0.924	-180	110	2.8	0.00	1.687	-160	330	5.3	0.00	1.078
-200	-130	2.0	0.08	0.989	-180	90	2.0	0.04	1.781	-160	310	5.5	0.00	1.186

Appendix 4.B. (continued)

x	y	T_e	F_3	H	x	y	T_e	F_3	H	x	y	T_e	F_3	H
-160	290	5.8	0.00	1.239	-140	510	6.0	0.24	3.494	-140	-530	1.0	0.00	1.825
-160	270	6.3	0.00	1.282	-140	490	6.0	0.24	3.271	-140	-550	1.0	0.00	1.990
-160	250	6.5	0.00	1.381	-140	470	5.8	0.24	2.854	-140	-570	1.0	0.00	2.277
-160	230	6.5	0.00	1.484	-140	450	5.5	0.20	2.093	-140	-590	1.0	0.00	2.538
-160	210	6.5	0.00	1.541	-140	430	5.3	0.16	1.392	-120	650	1.0	0.04	2.853
-160	190	5.8	0.00	1.538	-140	410	5.3	0.12	0.933	-120	630	1.0	0.08	2.801
-160	170	5.0	0.00	1.522	-140	390	5.5	0.04	0.730	-120	610	1.0	0.12	3.135
-160	150	4.0	0.00	1.574	-140	370	5.5	0.00	0.727	-120	590	1.5	0.16	3.453
-160	130	3.0	0.00	1.641	-140	350	5.5	0.00	0.923	-120	570	2.5	0.20	3.852
-160	110	2.5	0.00	1.667	-140	330	5.5	0.00	1.067	-120	550	6.0	0.20	3.677
-160	90	2.0	0.04	1.748	-140	310	5.8	0.00	1.135	-120	530	6.5	0.24	3.488
-160	70	1.5	0.00	1.873	-140	290	5.8	0.00	1.170	-120	510	7.0	0.28	3.262
-160	50	1.3	0.00	2.028	-140	270	6.0	0.00	1.216	-120	490	6.8	0.28	3.185
-160	30	1.3	0.00	2.059	-140	250	6.3	0.00	1.305	-120	470	6.8	0.28	3.086
-160	10	1.3	0.00	1.967	-140	230	6.0	0.00	1.438	-120	450	6.0	0.20	2.479
-160	-10	1.3	0.00	1.788	-140	210	5.5	0.00	1.533	-120	430	5.8	0.16	1.757
-160	-30	1.3	0.00	1.564	-140	190	4.8	0.00	1.606	-120	410	5.8	0.12	1.255
-160	-50	1.5	0.00	1.281	-140	170	3.8	0.04	1.620	-120	390	5.8	0.08	0.953
-160	-70	1.8	0.00	0.986	-140	150	3.0	0.04	1.594	-120	370	5.8	0.00	0.867
-160	-90	2.0	0.04	0.932	-140	130	2.5	0.04	1.567	-120	350	5.8	0.00	1.021
-160	-110	2.0	0.08	0.971	-140	110	2.0	0.04	1.560	-120	330	5.8	0.00	1.140
-160	-130	2.0	0.08	0.964	-140	90	2.0	0.00	1.647	-120	310	5.8	0.00	1.199
-160	-150	2.3	0.08	1.121	-140	70	1.8	0.00	1.856	-120	290	5.8	0.00	1.232
-160	-170	2.3	0.08	1.122	-140	50	1.5	0.00	2.048	-120	270	6.0	0.00	1.294
-160	-190	2.5	0.08	1.124	-140	30	1.5	0.00	2.121	-120	250	5.8	0.00	1.423
-160	-210	2.8	0.08	1.246	-140	10	1.5	0.00	2.094	-120	230	5.3	0.00	1.591
-160	-230	2.8	0.08	1.416	-140	-10	1.5	0.00	1.992	-120	210	4.5	0.04	1.744
-160	-250	3.0	0.04	1.455	-140	-30	1.5	0.00	1.752	-120	190	3.8	0.04	1.812
-160	-270	3.3	0.00	1.477	-140	-50	1.8	0.00	1.514	-120	170	2.8	0.08	1.754
-160	-290	3.3	0.00	1.490	-140	-70	2.0	0.00	1.267	-120	150	2.5	0.04	1.637
-160	-310	3.3	0.00	1.504	-140	-90	2.0	0.04	1.171	-120	130	2.3	0.04	1.488
-160	-330	3.3	0.00	1.530	-140	-110	2.0	0.08	1.192	-120	110	2.0	0.04	1.445
-160	-350	3.3	0.00	1.564	-140	-130	2.3	0.08	1.110	-120	90	2.0	0.00	1.591
-160	-370	3.3	0.00	1.607	-140	-150	2.5	0.08	1.123	-120	70	1.8	0.00	1.887
-160	-390	3.0	0.00	1.576	-140	-170	2.5	0.08	1.046	-120	50	1.8	0.00	2.079
-160	-410	3.0	0.00	1.523	-140	-190	2.8	0.08	1.049	-120	30	1.8	0.00	2.178
-160	-430	2.8	0.00	1.464	-140	-210	2.8	0.08	1.213	-120	10	1.8	0.00	2.180
-160	-450	2.5	0.00	1.522	-140	-230	3.0	0.04	1.400	-120	-10	1.8	0.00	2.118
-160	-470	2.3	0.00	1.655	-140	-250	3.3	0.00	1.454	-120	-30	1.8	0.00	1.950
-160	-490	2.0	0.00	1.796	-140	-270	3.3	0.00	1.498	-120	-50	2.0	0.00	1.747
-160	-510	1.5	0.00	1.853	-140	-290	3.0	0.00	1.520	-120	-70	2.3	0.00	1.510
-160	-530	1.0	0.00	1.914	-140	-310	3.0	0.00	1.484	-120	-90	2.3	0.00	1.328
-160	-550	1.0	0.00	2.061	-140	-330	3.0	0.00	1.495	-120	-110	2.3	0.08	1.303
-160	-570	1.0	0.00	2.492	-140	-350	2.8	0.00	1.534	-120	-130	2.5	0.08	1.144
-160	-590	1.0	0.00	2.986	-140	-370	2.5	0.00	1.606	-120	-150	2.5	0.08	1.017
-140	650	1.0	0.04	2.986	-140	-390	2.5	0.00	1.608	-120	-170	2.8	0.08	0.911
-140	630	1.0	0.08	2.669	-140	-410	2.3	0.00	1.555	-120	-190	2.8	0.08	1.004
-140	610	1.0	0.12	2.877	-140	-430	2.0	0.00	1.479	-120	-210	3.0	0.04	1.211
-140	590	1.0	0.16	3.367	-140	-450	2.0	0.00	1.483	-120	-230	3.0	0.04	1.347
-140	570	1.3	0.20	3.859	-140	-470	1.8	0.00	1.599	-120	-250	3.3	0.00	1.462
-140	550	4.8	0.20	4.208	-140	-490	1.3	0.00	1.714	-120	-270	3.0	0.00	1.560
-140	530	5.8	0.24	3.699	-140	-510	1.0	0.00	1.786	-120	-290	2.8	0.00	1.609

Appendix 4.B. (continued)

x	y	T_e	F_3	H	x	y	T_e	F_3	H	x	y	T_e	F_3	H
-120	-310	2.8	0.00	1.593	-100	-90	2.5	0.00	1.344	-80	130	2.0	0.04	1.419
-120	-330	2.5	0.00	1.583	-100	-110	2.8	0.04	1.167	-80	110	2.0	0.04	1.316
-120	-350	2.3	0.00	1.581	-100	-130	2.8	0.08	1.065	-80	90	2.0	0.00	1.426
-120	-370	2.0	0.00	1.626	-100	-150	2.8	0.08	0.949	-80	70	2.0	0.00	1.741
-120	-390	1.8	0.00	1.646	-100	-170	3.0	0.04	0.957	-80	50	2.3	0.00	2.025
-120	-410	1.8	0.00	1.576	-100	-190	3.0	0.04	0.963	-80	30	2.3	0.00	2.204
-120	-430	1.5	0.00	1.427	-100	-210	3.3	0.00	1.119	-80	10	2.5	0.00	2.294
-120	-450	1.5	0.00	1.321	-100	-230	3.0	0.00	1.329	-80	-10	2.5	0.00	2.293
-120	-470	1.3	0.00	1.354	-100	-250	3.0	0.00	1.521	-80	-30	2.5	0.00	2.126
-120	-490	1.3	0.00	1.459	-100	-270	2.8	0.00	1.674	-80	-50	2.8	0.00	1.910
-120	-510	1.0	0.00	1.577	-100	-290	2.8	0.00	1.763	-80	-70	2.8	0.00	1.593
-120	-530	1.0	0.04	1.685	-100	-310	2.5	0.00	1.780	-80	-90	2.8	0.00	1.291
-120	-550	1.0	0.04	1.789	-100	-330	2.3	0.00	1.756	-80	-110	3.0	0.00	1.024
-120	-570	1.0	0.04	1.860	-100	-350	2.0	0.00	1.724	-80	-130	3.0	0.04	0.877
-120	-590	1.0	0.00	1.906	-100	-370	1.8	0.00	1.733	-80	-150	3.0	0.04	0.884
-100	650	1.0	0.08	2.891	-100	-390	1.5	0.00	1.736	-80	-170	3.0	0.00	0.894
-100	630	1.0	0.12	2.905	-100	-410	1.5	0.00	1.646	-80	-190	3.0	0.00	0.934
-100	610	1.0	0.16	3.263	-100	-430	1.3	0.00	1.450	-80	-210	3.0	0.00	1.104
-100	590	3.0	0.16	3.479	-100	-450	1.3	0.00	1.248	-80	-230	3.0	0.00	1.352
-100	570	6.3	0.16	2.990	-100	-470	1.3	0.00	1.147	-80	-250	2.8	0.00	1.583
-100	550	7.0	0.20	2.667	-100	-490	1.3	0.04	1.208	-80	-270	2.5	0.00	1.744
-100	530	7.5	0.24	2.906	-100	-510	1.3	0.04	1.381	-80	-290	2.3	0.00	1.849
-100	510	7.5	0.24	3.168	-100	-530	1.5	0.04	1.573	-80	-310	2.3	0.00	1.883
-100	490	7.5	0.28	3.239	-100	-550	1.5	0.04	1.686	-80	-330	2.0	0.00	1.875
-100	470	6.8	0.24	3.145	-100	-570	1.3	0.04	1.720	-80	-350	1.8	0.00	1.872
-100	450	6.5	0.20	2.688	-100	-590	1.0	0.04	1.699	-80	-370	1.8	0.00	1.904
-100	430	6.5	0.16	2.138	-80	650	1.0	0.08	2.806	-80	-390	1.5	0.00	1.917
-100	410	6.5	0.12	1.698	-80	630	1.0	0.12	2.939	-80	-410	1.5	0.00	1.842
-100	390	6.3	0.08	1.323	-80	610	1.8	0.16	3.257	-80	-430	1.5	0.00	1.641
-100	370	6.3	0.00	1.120	-80	590	6.3	0.12	2.736	-80	-450	1.5	0.00	1.365
-100	350	6.0	0.00	1.148	-80	570	7.8	0.12	2.101	-80	-470	1.5	0.04	1.113
-100	330	5.8	0.00	1.207	-80	550	8.3	0.16	1.786	-80	-490	1.8	0.04	1.062
-100	310	5.8	0.00	1.294	-80	530	8.3	0.20	2.136	-80	-510	1.8	0.04	1.189
-100	290	5.8	0.00	1.428	-80	510	8.5	0.20	2.460	-80	-530	1.8	0.08	1.366
-100	270	5.8	0.00	1.631	-80	490	7.8	0.24	2.809	-80	-550	1.8	0.08	1.454
-100	250	5.5	0.00	1.839	-80	470	7.3	0.24	2.839	-80	-570	1.5	0.08	1.440
-100	230	4.5	0.04	1.992	-80	450	7.0	0.20	2.554	-80	-590	1.5	0.08	1.382
-100	210	3.5	0.08	2.045	-80	430	7.0	0.16	2.241	-60	650	1.0	0.12	2.775
-100	190	3.0	0.08	1.993	-80	410	7.3	0.12	1.960	-60	630	2.3	0.12	3.091
-100	170	2.5	0.08	1.850	-80	390	7.0	0.08	1.647	-60	610	5.3	0.12	2.768
-100	150	2.0	0.08	1.683	-80	370	6.5	0.04	1.367	-60	590	7.0	0.12	1.999
-100	130	2.0	0.04	1.458	-80	350	6.3	0.00	1.255	-60	570	8.3	0.12	1.486
-100	110	2.0	0.04	1.390	-80	330	6.0	0.00	1.290	-60	550	9.3	0.12	1.496
-100	90	2.0	0.00	1.538	-80	310	5.8	0.00	1.459	-60	530	9.3	0.16	1.775
-100	70	2.0	0.00	1.841	-80	290	5.8	0.04	1.827	-60	510	9.5	0.16	1.958
-100	50	2.0	0.00	2.089	-80	270	5.8	0.00	2.260	-60	490	9.5	0.16	2.117
-100	30	2.0	0.00	2.215	-80	250	4.5	0.08	2.509	-60	470	9.3	0.16	2.223
-100	10	2.0	0.00	2.243	-80	230	3.8	0.08	2.457	-60	450	8.5	0.16	2.169
-100	-10	2.3	0.00	2.213	-80	210	3.3	0.08	2.323	-60	430	7.5	0.16	2.042
-100	-30	2.3	0.00	2.058	-80	190	2.8	0.08	2.171	-60	410	7.8	0.12	1.900
-100	-50	2.3	0.00	1.869	-80	170	2.3	0.08	1.942	-60	390	6.8	0.12	1.740
-100	-70	2.5	0.00	1.615	-80	150	2.0	0.08	1.663	-60	370	6.5	0.08	1.528

Appendix 4.B. (continued)

x	y	T_e	F_3	H
-60	350	5.8	0.08	1.390
-60	330	5.5	0.08	1.457
-60	310	5.5	0.04	1.699
-60	290	5.3	0.04	2.179
-60	270	4.5	0.08	2.775
-60	250	3.5	0.12	2.967
-60	230	3.0	0.12	2.763
-60	210	3.0	0.08	2.504
-60	190	2.5	0.08	2.234
-60	170	2.3	0.08	1.925
-60	150	2.0	0.08	1.577
-60	130	2.0	0.04	1.288
-60	110	2.0	0.04	1.170
-60	90	2.3	0.00	1.280
-60	70	2.3	0.00	1.579
-60	50	2.5	0.00	1.890
-60	30	2.5	0.00	2.151
-60	10	2.8	0.00	2.316
-60	-10	2.8	0.00	2.340
-60	-30	2.8	0.00	2.183
-60	-50	3.0	0.00	1.887
-60	-70	3.0	0.00	1.546
-60	-90	3.0	0.00	1.241
-60	-110	3.0	0.00	1.023
-60	-130	3.0	0.00	0.956
-60	-150	3.3	0.00	1.001
-60	-170	3.0	0.00	0.985
-60	-190	3.0	0.00	1.001
-60	-210	3.0	0.00	1.118
-60	-230	2.8	0.00	1.328
-60	-250	2.5	0.00	1.570
-60	-270	2.3	0.00	1.735
-60	-290	2.3	0.00	1.842
-60	-310	2.0	0.00	1.894
-60	-330	2.0	0.00	1.921
-60	-350	1.8	0.00	1.957
-60	-370	1.8	0.00	1.993
-60	-390	1.8	0.00	2.061
-60	-410	1.8	0.00	2.051
-60	-430	1.8	0.04	1.897
-60	-450	1.8	0.04	1.527
-60	-470	2.0	0.04	1.120
-60	-490	2.0	0.08	0.951
-60	-510	2.0	0.08	0.958
-60	-530	2.3	0.08	1.157
-60	-550	2.3	0.08	1.277
-60	-570	2.3	0.08	1.303
-60	-590	2.0	0.08	1.243
-40	650	1.3	0.12	2.836
-40	630	4.0	0.12	2.939
-40	610	6.3	0.12	2.187
-40	590	7.5	0.12	1.535

x	y	T_e	F_3	H
-40	570	8.5	0.12	1.346
-40	550	9.3	0.12	1.506
-40	530	9.8	0.12	1.685
-40	510	10.0	0.12	1.753
-40	490	10.3	0.12	1.756
-40	470	9.0	0.16	1.741
-40	450	8.5	0.16	1.718
-40	430	9.0	0.12	1.685
-40	410	7.8	0.12	1.631
-40	390	6.8	0.12	1.564
-40	370	5.8	0.12	1.429
-40	350	5.3	0.12	1.352
-40	330	4.5	0.12	1.421
-40	310	4.3	0.12	1.718
-40	290	3.8	0.12	2.247
-40	270	3.5	0.12	2.857
-40	250	3.3	0.12	3.018
-40	230	2.8	0.12	2.740
-40	210	2.8	0.08	2.464
-40	190	2.5	0.08	2.106
-40	170	2.5	0.08	1.738
-40	150	2.3	0.08	1.350
-40	130	2.3	0.04	1.054
-40	110	2.3	0.00	0.943
-40	90	2.5	0.00	1.105
-40	70	2.5	0.00	1.421
-40	50	2.8	0.00	1.764
-40	30	2.8	0.00	2.067
-40	10	3.0	0.00	2.279
-40	-10	3.0	0.00	2.314
-40	-30	3.3	0.00	2.136
-40	-50	3.3	0.00	1.830
-40	-70	3.3	0.00	1.495
-40	-90	3.3	0.00	1.272
-40	-110	3.3	0.00	1.196
-40	-130	3.3	0.00	1.264
-40	-150	3.3	0.00	1.333
-40	-170	3.3	0.00	1.292
-40	-190	3.0	0.00	1.213
-40	-210	3.0	0.00	1.182
-40	-230	2.8	0.00	1.301
-40	-250	2.5	0.00	1.500
-40	-270	2.3	0.00	1.686
-40	-290	2.3	0.00	1.796
-40	-310	2.3	0.00	1.898
-40	-330	2.0	0.00	1.948
-40	-350	2.3	0.00	1.969
-40	-370	2.0	0.00	2.033
-40	-390	2.0	0.00	2.111
-40	-410	2.0	0.00	2.135
-40	-430	2.3	0.00	2.024
-40	-450	2.3	0.04	1.710

x	y	T_e	F_3	H
-40	-470	2.3	0.08	1.311
-40	-490	2.5	0.08	0.875
-40	-510	2.5	0.08	0.863
-40	-530	2.8	0.08	1.107
-40	-550	2.8	0.08	1.325
-40	-570	2.8	0.08	1.457
-40	-590	2.3	0.12	1.433
-20	650	2.8	0.12	2.943
-20	630	5.3	0.12	2.488
-20	610	7.0	0.12	1.719
-20	590	8.0	0.12	1.341
-20	570	8.8	0.12	1.420
-20	550	9.5	0.12	1.632
-20	530	9.8	0.12	1.763
-20	510	10.0	0.12	1.758
-20	490	10.0	0.12	1.654
-20	470	9.8	0.12	1.501
-20	450	9.5	0.12	1.392
-20	430	8.8	0.12	1.357
-20	410	7.8	0.12	1.357
-20	390	6.8	0.12	1.335
-20	370	5.8	0.12	1.278
-20	350	4.8	0.12	1.247
-20	330	4.3	0.12	1.200
-20	310	3.8	0.12	1.238
-20	290	3.3	0.12	1.622
-20	270	3.0	0.12	2.241
-20	250	3.0	0.12	2.507
-20	230	2.8	0.12	2.351
-20	210	2.5	0.12	2.139
-20	190	2.8	0.08	1.824
-20	170	2.5	0.08	1.420
-20	150	2.5	0.08	1.045
-20	130	2.5	0.04	0.829
-20	110	2.5	0.00	0.777
-20	90	2.8	0.00	0.978
-20	70	2.8	0.00	1.305
-20	50	3.0	0.00	1.644
-20	30	3.0	0.00	1.942
-20	10	3.3	0.00	2.159
-20	-10	3.5	0.00	2.205
-20	-30	3.5	0.00	2.047
-20	-50	3.5	0.00	1.770
-20	-70	3.3	0.00	1.487
-20	-90	3.3	0.00	1.390
-20	-110	3.3	0.00	1.479
-20	-130	3.3	0.04	1.614
-20	-150	3.3	0.04	1.706
-20	-170	3.3	0.04	1.662
-20	-190	3.3	0.04	1.511
-20	-210	3.3	0.00	1.346
-20	-230	3.0	0.00	1.296

Appendix 4.B. (continued)

x	y	T_e	F_3	H	x	y	T_e	F_3	H	x	y	T_e	F_3	H
-20	-250	2.8	0.00	1.402	0	-30	3.8	0.00	1.901	20	190	3.0	0.08	1.549
-20	-270	2.8	0.00	1.604	0	-50	3.8	0.00	1.720	20	170	3.0	0.08	1.288
-20	-290	2.5	0.00	1.763	0	-70	3.5	0.00	1.567	20	150	3.0	0.08	0.982
-20	-310	2.5	0.00	1.825	0	-90	3.3	0.04	1.623	20	130	3.3	0.04	0.809
-20	-330	2.5	0.00	1.859	0	-110	3.3	0.08	1.781	20	110	3.3	0.00	0.747
-20	-350	2.5	0.00	1.902	0	-130	3.3	0.08	1.934	20	90	3.3	0.00	0.945
-20	-370	2.5	0.00	1.983	0	-150	3.3	0.08	1.986	20	70	3.5	0.00	1.206
-20	-390	2.5	0.00	2.064	0	-170	3.5	0.08	1.910	20	50	3.8	0.00	1.430
-20	-410	2.5	0.00	2.079	0	-190	3.5	0.08	1.736	20	30	3.8	0.00	1.587
-20	-430	2.5	0.00	2.034	0	-210	3.5	0.08	1.523	20	10	4.0	0.00	1.686
-20	-450	2.8	0.04	1.822	0	-230	3.5	0.04	1.357	20	-10	4.0	0.00	1.731
-20	-470	2.8	0.08	1.453	0	-250	3.5	0.04	1.266	20	-30	4.0	0.00	1.699
-20	-490	3.0	0.08	1.137	0	-270	3.3	0.04	1.396	20	-50	4.0	0.00	1.649
-20	-510	2.8	0.12	1.087	0	-290	3.3	0.00	1.575	20	-70	3.8	0.00	1.693
-20	-530	2.8	0.12	1.117	0	-310	3.3	0.00	1.674	20	-90	3.5	0.08	1.876
-20	-550	2.8	0.12	1.277	0	-330	3.3	0.00	1.721	20	-110	3.5	0.08	2.097
-20	-570	2.8	0.12	1.372	0	-350	3.3	0.00	1.767	20	-130	3.3	0.12	2.178
-20	-590	2.8	0.12	1.393	0	-370	3.0	0.00	1.846	20	-150	3.5	0.12	2.134
0	650	2.8	0.16	2.948	0	-390	3.0	0.00	1.934	20	-170	3.8	0.12	2.002
0	630	6.0	0.12	2.140	0	-410	3.0	0.04	1.965	20	-190	3.8	0.12	1.827
0	610	7.5	0.12	1.460	0	-430	3.0	0.04	1.976	20	-210	4.0	0.12	1.633
0	590	8.5	0.12	1.331	0	-450	3.0	0.08	1.901	20	-230	4.5	0.08	1.492
0	570	9.3	0.12	1.547	0	-470	3.3	0.08	1.758	20	-250	4.5	0.08	1.400
0	550	9.8	0.12	1.762	0	-490	3.3	0.12	1.358	20	-270	4.5	0.08	1.413
0	530	10.0	0.12	1.857	0	-510	3.3	0.12	1.140	20	-290	4.3	0.08	1.494
0	510	10.0	0.12	1.817	0	-530	3.5	0.12	1.205	20	-310	4.3	0.04	1.549
0	490	10.0	0.12	1.673	0	-550	3.5	0.12	1.408	20	-330	4.0	0.00	1.563
0	470	9.8	0.12	1.467	0	-570	3.5	0.12	1.582	20	-350	4.0	0.00	1.593
0	450	9.5	0.12	1.271	0	-590	3.3	0.12	1.701	20	-370	3.8	0.04	1.688
0	430	8.8	0.12	1.168	20	650	4.0	0.16	2.884	20	-390	3.8	0.04	1.802
0	410	8.0	0.12	1.174	20	630	6.8	0.12	1.962	20	-410	3.5	0.08	1.904
0	390	6.0	0.16	1.257	20	610	8.0	0.12	1.410	20	-430	3.5	0.08	2.006
0	370	5.0	0.16	1.245	20	590	8.8	0.12	1.458	20	-450	3.5	0.12	1.980
0	350	4.3	0.16	1.345	20	570	9.5	0.12	1.713	20	-470	3.8	0.12	1.755
0	330	3.8	0.12	1.431	20	550	10.0	0.12	1.910	20	-490	3.8	0.12	1.504
0	310	3.5	0.12	1.351	20	530	10.3	0.12	1.976	20	-510	4.0	0.12	1.352
0	290	3.0	0.12	1.393	20	510	10.3	0.12	1.913	20	-530	3.8	0.16	1.398
0	270	2.8	0.12	1.680	20	490	10.3	0.12	1.752	20	-550	3.8	0.16	1.487
0	250	2.8	0.12	1.893	20	470	10.0	0.12	1.523	20	-570	3.8	0.16	1.591
0	230	2.8	0.12	1.874	20	450	9.8	0.12	1.282	20	-590	3.5	0.16	1.621
0	210	2.5	0.12	1.781	20	430	9.3	0.12	1.147	40	650	5.0	0.16	3.095
0	190	2.8	0.08	1.566	20	410	7.5	0.16	1.058	40	630	7.0	0.16	1.960
0	170	2.8	0.08	1.192	20	390	6.3	0.16	1.200	40	610	8.0	0.16	1.558
0	150	2.8	0.08	0.843	20	370	5.0	0.16	1.282	40	590	9.3	0.12	1.679
0	130	2.8	0.04	0.744	20	350	4.0	0.16	1.604	40	570	10.0	0.12	1.916
0	110	3.0	0.00	0.714	20	330	3.5	0.16	2.046	40	550	10.3	0.12	2.081
0	90	3.0	0.00	0.923	20	310	3.0	0.16	2.346	40	530	10.5	0.12	2.127
0	70	3.0	0.00	1.250	20	290	2.8	0.16	2.357	40	510	10.8	0.12	2.047
0	50	3.3	0.00	1.542	20	270	2.8	0.12	2.127	40	490	10.5	0.12	1.874
0	30	3.3	0.00	1.791	20	250	2.8	0.12	1.903	40	470	9.8	0.16	1.643
0	10	3.5	0.00	1.957	20	230	2.5	0.12	1.707	40	450	9.3	0.16	1.389
0	-10	3.8	0.00	2.005	20	210	2.8	0.12	1.694	40	430	8.8	0.16	1.196

Appendix 4.B. (continued)

x	y	T_e	F_3	H	x	y	T_e	F_3	H	x	y	T_e	F_3	H
40	410	7.0	0.20	1.253	60	630	7.5	0.16	2.072	60	-410	4.8	0.12	1.926
40	390	5.8	0.20	1.611	60	610	8.8	0.16	1.627	60	-430	4.5	0.16	2.096
40	370	4.8	0.20	2.196	60	590	9.5	0.16	1.802	60	-450	4.8	0.16	1.964
40	350	3.8	0.20	2.820	60	570	10.0	0.16	2.062	60	-470	5.0	0.16	1.674
40	330	3.3	0.20	3.345	60	550	10.3	0.16	2.219	60	-490	5.3	0.16	1.314
40	310	2.8	0.20	3.504	60	530	10.5	0.16	2.244	60	-510	5.5	0.16	1.065
40	290	2.8	0.16	3.245	60	510	10.5	0.16	2.155	60	-530	5.8	0.16	1.061
40	270	2.5	0.16	2.666	60	490	10.3	0.16	1.969	60	-550	5.8	0.16	1.224
40	250	2.8	0.12	2.229	60	470	10.3	0.16	1.728	60	-570	5.8	0.16	1.450
40	230	2.8	0.12	1.897	60	450	10.0	0.16	1.531	60	-590	5.5	0.16	1.684
40	210	2.8	0.12	1.865	60	430	8.5	0.20	1.430	80	650	6.0	0.20	4.269
40	190	3.0	0.08	1.809	60	410	7.0	0.24	1.763	80	630	8.3	0.20	2.403
40	170	3.3	0.08	1.576	60	390	5.8	0.24	2.725	80	610	9.5	0.16	1.807
40	150	3.3	0.08	1.282	60	370	4.5	0.24	3.233	80	590	10.0	0.16	1.914
40	130	3.5	0.04	1.050	60	350	4.0	0.28	3.559	80	570	10.5	0.16	2.161
40	110	3.8	0.00	0.897	60	330	3.5	0.28	3.704	80	550	10.8	0.16	2.322
40	90	3.8	0.00	0.979	60	310	3.0	0.24	3.832	80	530	10.8	0.16	2.339
40	70	4.0	0.00	1.168	60	290	2.8	0.20	3.569	80	510	10.8	0.16	2.257
40	50	4.3	0.00	1.313	60	270	2.8	0.16	2.671	80	490	10.8	0.16	2.094
40	30	4.5	0.00	1.399	60	250	2.8	0.12	2.344	80	470	10.8	0.16	1.894
40	10	4.5	0.00	1.429	60	230	3.0	0.12	2.104	80	450	9.8	0.20	1.727
40	-10	4.5	0.00	1.457	60	210	3.0	0.12	2.086	80	430	9.0	0.20	1.857
40	-30	4.5	0.00	1.470	60	190	3.0	0.12	2.069	80	410	7.0	0.24	2.308
40	-50	4.5	0.00	1.536	60	170	3.5	0.08	1.936	80	390	5.8	0.28	2.877
40	-70	4.0	0.08	1.739	60	150	3.5	0.08	1.609	80	370	5.0	0.32	3.299
40	-90	3.8	0.12	1.939	60	130	3.8	0.08	1.350	80	350	4.3	0.32	3.507
40	-110	3.8	0.12	2.071	60	110	4.3	0.00	1.100	80	330	4.0	0.32	3.598
40	-130	3.8	0.12	2.100	60	90	4.5	0.00	1.063	80	310	3.3	0.24	3.659
40	-150	4.0	0.12	2.031	60	70	4.8	0.00	1.171	80	290	3.0	0.20	3.089
40	-170	4.5	0.12	1.926	60	50	5.0	0.00	1.257	80	270	3.0	0.16	2.184
40	-190	5.0	0.12	1.826	60	30	5.3	0.00	1.303	80	250	3.0	0.16	2.099
40	-210	5.5	0.12	1.801	60	10	5.5	0.00	1.310	80	230	3.3	0.12	2.041
40	-230	6.3	0.12	1.848	60	-10	5.5	0.00	1.267	80	210	3.5	0.12	2.125
40	-250	6.8	0.12	1.931	60	-30	5.5	0.00	1.216	80	190	3.5	0.12	2.161
40	-270	7.5	0.08	1.963	60	-50	5.3	0.08	1.304	80	170	3.8	0.12	2.067
40	-290	6.8	0.08	1.922	60	-70	4.8	0.12	1.533	80	150	4.0	0.08	1.832
40	-310	5.8	0.08	1.778	60	-90	4.3	0.16	1.776	80	130	4.3	0.08	1.496
40	-330	5.3	0.04	1.599	60	-110	4.5	0.16	1.820	80	110	5.0	0.00	1.171
40	-350	4.8	0.04	1.501	60	-130	4.8	0.16	1.804	80	90	5.3	0.00	1.107
40	-370	4.5	0.04	1.565	60	-150	5.3	0.16	1.762	80	70	5.5	0.00	1.200
40	-390	4.3	0.08	1.717	60	-170	6.0	0.16	1.782	80	50	6.0	0.00	1.290
40	-410	4.3	0.08	1.931	60	-190	7.0	0.16	1.851	80	30	6.3	0.00	1.360
40	-430	4.0	0.12	2.020	60	-210	9.5	0.12	1.899	80	10	6.5	0.00	1.378
40	-450	4.3	0.12	1.990	60	-230	10.3	0.12	1.866	80	-10	6.8	0.00	1.297
40	-470	4.3	0.16	1.828	60	-250	11.0	0.08	1.896	80	-30	7.0	0.00	1.129
40	-490	4.5	0.16	1.460	60	-270	10.8	0.08	1.907	80	-50	6.8	0.12	1.110
40	-510	4.5	0.16	1.184	60	-290	10.3	0.04	1.893	80	-70	6.5	0.16	1.178
40	-530	4.8	0.16	1.188	60	-310	9.0	0.04	1.773	80	-90	6.0	0.20	1.557
40	-550	4.8	0.16	1.351	60	-330	7.0	0.08	1.578	80	-110	6.0	0.20	1.649
40	-570	4.5	0.16	1.511	60	-350	5.8	0.08	1.435	80	-130	6.5	0.20	1.712
40	-590	4.3	0.16	1.627	60	-370	5.3	0.08	1.476	80	-150	7.5	0.20	1.823
60	650	4.8	0.20	3.521	60	-390	4.8	0.12	1.695	80	-170	9.8	0.16	1.880

Appendix 4.B. (continued)

x	y	T_e	F_3	H	x	y	T_e	F_3	H	x	y	T_e	F_3	H
80	-190	11.3	0.16	1.900	100	30	7.5	0.00	1.571	120	250	5.3	0.16	1.248
80	-210	12.0	0.16	1.950	100	10	7.8	0.00	1.637	120	230	6.0	0.12	1.503
80	-230	12.8	0.12	1.908	100	-10	8.3	0.00	1.609	120	210	6.3	0.12	1.634
80	-250	12.8	0.12	1.858	100	-30	8.8	0.04	1.573	120	190	6.3	0.12	1.736
80	-270	12.5	0.08	1.763	100	-50	9.3	0.12	1.700	120	170	6.3	0.12	1.760
80	-290	11.8	0.08	1.626	100	-70	9.5	0.16	1.793	120	150	6.5	0.12	1.651
80	-310	10.8	0.04	1.466	100	-90	9.5	0.20	2.004	120	130	6.8	0.08	1.482
80	-330	8.8	0.08	1.331	100	-110	9.3	0.24	2.128	120	110	7.0	0.08	1.304
80	-350	7.3	0.08	1.293	100	-130	9.8	0.24	2.233	120	90	7.5	0.00	1.287
80	-370	5.8	0.12	1.384	100	-150	11.5	0.20	2.281	120	70	7.8	0.00	1.449
80	-390	5.5	0.12	1.629	100	-170	13.0	0.20	2.366	120	50	8.5	0.00	1.707
80	-410	5.0	0.16	1.918	100	-190	14.3	0.16	2.408	120	30	9.0	0.00	1.972
80	-430	5.0	0.16	1.989	100	-210	14.3	0.16	2.441	120	10	9.5	0.00	2.157
80	-450	5.3	0.16	1.893	100	-230	14.8	0.12	2.364	120	-10	10.0	0.00	2.251
80	-470	5.5	0.16	1.644	100	-250	14.3	0.12	2.209	120	-30	10.8	0.04	2.404
80	-490	6.0	0.16	1.341	100	-270	14.0	0.08	1.970	120	-50	11.3	0.16	2.702
80	-510	6.5	0.16	1.126	100	-290	13.0	0.08	1.651	120	-70	12.0	0.20	2.895
80	-530	7.0	0.16	1.041	100	-310	11.8	0.08	1.305	120	-90	13.0	0.24	3.076
80	-550	7.0	0.16	1.097	100	-330	10.3	0.08	1.046	120	-110	13.0	0.24	3.074
80	-570	7.3	0.16	1.326	100	-350	8.3	0.12	1.072	120	-130	13.5	0.24	3.066
80	-590	7.3	0.16	1.635	100	-370	7.0	0.12	1.213	120	-150	14.5	0.24	3.135
100	650	8.0	0.24	4.785	100	-390	5.8	0.16	1.518	120	-170	15.8	0.20	3.082
100	630	10.0	0.20	2.720	100	-410	5.8	0.16	1.728	120	-190	16.3	0.16	2.997
100	610	10.3	0.20	2.011	100	-430	5.8	0.16	1.835	120	-210	16.5	0.12	2.929
100	590	10.8	0.16	2.023	100	-450	6.0	0.16	1.821	120	-230	15.8	0.12	2.795
100	570	11.0	0.16	2.228	100	-470	6.3	0.16	1.685	120	-250	15.5	0.08	2.590
100	550	11.0	0.16	2.348	100	-490	7.0	0.16	1.484	120	-270	14.8	0.08	2.297
100	530	11.3	0.16	2.380	100	-510	7.5	0.16	1.312	120	-290	13.8	0.08	1.931
100	510	11.3	0.16	2.325	100	-530	8.0	0.16	1.157	120	-310	12.8	0.08	1.508
100	490	11.3	0.16	2.199	100	-550	8.5	0.16	1.062	120	-330	11.3	0.08	1.093
100	470	10.5	0.20	2.012	100	-570	8.8	0.16	1.162	120	-350	9.5	0.12	0.915
100	450	10.3	0.20	2.007	100	-590	8.8	0.16	1.411	120	-370	8.3	0.12	0.976
100	430	8.5	0.24	2.049	120	650	13.8	0.24	4.434	120	-390	6.8	0.16	1.246
100	410	7.3	0.28	2.671	120	630	13.0	0.20	2.823	120	-410	6.5	0.16	1.472
100	390	6.3	0.32	2.978	120	610	12.3	0.20	2.165	120	-430	6.3	0.16	1.678
100	370	5.3	0.32	3.259	120	590	12.0	0.16	2.130	120	-450	6.5	0.16	1.775
100	350	4.5	0.32	3.387	120	570	11.5	0.16	2.250	120	-470	7.0	0.16	1.757
100	330	4.0	0.28	3.425	120	550	11.3	0.16	2.348	120	-490	7.8	0.16	1.630
100	310	3.5	0.24	3.185	120	530	11.3	0.16	2.337	120	-510	8.8	0.16	1.502
100	290	3.5	0.20	2.086	120	510	11.3	0.16	2.265	120	-530	9.5	0.16	1.380
100	270	3.8	0.16	1.389	120	490	11.5	0.16	2.209	120	-550	10.0	0.16	1.247
100	250	3.8	0.16	1.501	120	470	10.8	0.20	2.073	120	-570	10.3	0.16	1.183
100	230	4.3	0.12	1.778	120	450	9.8	0.24	2.079	120	-590	10.3	0.16	1.225
100	210	4.5	0.12	1.910	120	430	8.8	0.28	2.382	140	650	19.8	0.16	3.191
100	190	4.5	0.12	1.991	120	410	7.3	0.28	2.579	140	630	16.8	0.16	2.561
100	170	4.8	0.12	1.975	120	390	6.0	0.28	2.876	140	610	14.3	0.16	2.139
100	150	4.8	0.12	1.816	120	370	5.3	0.28	2.934	140	590	13.0	0.12	2.039
100	130	5.5	0.08	1.469	120	350	4.8	0.28	2.916	140	570	12.0	0.12	2.068
100	110	6.0	0.00	1.137	120	330	4.3	0.24	2.413	140	550	11.5	0.12	2.126
100	90	6.3	0.00	1.082	120	310	4.5	0.20	1.528	140	530	11.8	0.12	2.174
100	70	6.5	0.00	1.239	120	290	5.0	0.16	1.381	140	510	11.3	0.16	2.169
100	50	7.0	0.00	1.425	120	270	5.0	0.16	0.973	140	490	11.5	0.16	2.145

Appendix 4.B. (continued)

x	y	T_e	F_3	H	x	y	T_e	F_3	H	x	y	T_e	F_3	H
140	470	10.5	0.20	2.045	140	-570	11.3	0.16	1.380	160	-350	12.3	0.08	1.211
140	450	9.5	0.24	2.016	140	-590	11.5	0.16	1.244	160	-370	10.8	0.12	0.904
140	430	8.5	0.24	2.060	160	650	17.5	0.00	2.478	160	-390	9.3	0.16	0.887
140	410	7.5	0.28	2.291	160	630	16.3	0.00	2.230	160	-410	8.8	0.16	1.082
140	390	6.3	0.24	2.276	160	610	14.5	0.00	2.000	160	-430	8.0	0.20	1.423
140	370	5.8	0.24	1.778	160	590	13.0	0.00	1.853	160	-450	8.0	0.20	1.547
140	350	5.5	0.24	1.590	160	570	12.0	0.00	1.870	160	-470	8.8	0.20	1.600
140	330	6.0	0.20	1.395	160	550	11.5	0.08	2.006	160	-490	9.8	0.20	1.657
140	310	6.3	0.20	1.372	160	530	11.5	0.12	2.167	160	-510	11.0	0.20	1.810
140	290	7.0	0.16	0.930	160	510	11.0	0.16	2.213	160	-530	12.3	0.16	1.857
140	270	7.3	0.16	0.973	160	490	11.3	0.16	2.230	160	-550	12.5	0.16	1.760
140	250	8.0	0.12	1.166	160	470	10.3	0.20	2.068	160	-570	12.5	0.16	1.562
140	230	8.3	0.12	1.263	160	450	9.3	0.24	1.973	160	-590	12.5	0.16	1.357
140	210	8.3	0.12	1.407	160	430	8.3	0.24	1.811	180	650	16.5	0.00	2.468
140	190	8.3	0.12	1.548	160	410	7.5	0.24	1.745	180	630	15.3	0.00	2.304
140	170	8.3	0.12	1.636	160	390	7.0	0.24	1.465	180	610	13.8	0.00	2.115
140	150	8.3	0.12	1.622	160	370	6.8	0.24	1.535	180	590	12.8	0.00	1.953
140	130	8.3	0.12	1.559	160	350	7.5	0.20	1.459	180	570	12.0	0.00	1.912
140	110	8.5	0.12	1.560	160	330	7.8	0.20	1.288	180	550	11.5	0.08	2.091
140	90	8.8	0.12	1.700	160	310	8.8	0.16	1.149	180	530	10.8	0.16	2.314
140	70	9.8	0.08	1.941	160	290	9.0	0.16	1.091	180	510	10.8	0.16	2.376
140	50	10.5	0.08	2.284	160	270	9.8	0.12	1.180	180	490	10.0	0.20	2.327
140	30	11.5	0.04	2.632	160	250	9.8	0.12	1.257	180	470	9.8	0.20	2.190
140	10	12.0	0.00	2.891	160	230	9.8	0.12	1.372	180	450	9.0	0.24	1.962
140	-10	12.3	0.00	3.023	160	210	10.0	0.12	1.496	180	430	8.3	0.24	1.902
140	-30	12.5	0.00	3.150	160	190	10.0	0.12	1.632	180	410	8.0	0.24	1.831
140	-50	13.5	0.12	3.404	160	170	10.3	0.12	1.732	180	390	7.8	0.24	1.581
140	-70	14.0	0.20	3.556	160	150	10.3	0.12	1.768	180	370	8.5	0.20	1.770
140	-90	14.5	0.20	3.501	160	130	10.5	0.12	1.774	180	350	9.0	0.20	1.497
140	-110	15.3	0.20	3.411	160	110	10.8	0.12	1.880	180	330	9.3	0.20	1.583
140	-130	15.8	0.20	3.340	160	90	11.5	0.12	2.151	180	310	10.0	0.16	1.406
140	-150	16.5	0.20	3.464	160	70	12.3	0.12	2.538	180	290	10.8	0.12	1.466
140	-170	17.5	0.16	3.420	160	50	13.3	0.12	2.979	180	270	11.0	0.12	1.497
140	-190	17.8	0.12	3.284	160	30	14.3	0.08	3.341	180	250	11.0	0.12	1.595
140	-210	16.8	0.12	3.202	160	10	14.8	0.04	3.552	180	230	11.3	0.12	1.684
140	-230	16.8	0.08	3.075	160	-10	14.5	0.00	3.631	180	210	11.5	0.12	1.770
140	-250	16.0	0.08	2.859	160	-30	14.5	0.00	3.670	180	190	11.8	0.12	1.859
140	-270	15.5	0.04	2.581	160	-50	14.8	0.08	3.748	180	170	12.0	0.12	1.929
140	-290	14.8	0.04	2.234	160	-70	15.3	0.12	3.753	180	150	12.3	0.12	1.977
140	-310	13.8	0.04	1.796	160	-90	15.8	0.12	3.605	180	130	12.8	0.12	2.047
140	-330	12.3	0.08	1.343	160	-110	16.8	0.12	3.530	180	110	13.5	0.12	2.272
140	-350	11.3	0.08	0.973	160	-130	17.8	0.12	3.479	180	90	14.3	0.12	2.643
140	-370	9.5	0.12	0.843	160	-150	17.3	0.16	3.484	180	70	15.3	0.12	3.086
140	-390	8.0	0.16	1.018	160	-170	18.3	0.12	3.499	180	50	16.0	0.12	3.510
140	-410	7.5	0.16	1.231	160	-190	17.5	0.12	3.427	180	30	16.5	0.12	3.818
140	-430	7.3	0.16	1.545	160	-210	17.5	0.08	3.339	180	10	17.0	0.08	3.980
140	-450	7.0	0.20	1.725	160	-230	17.0	0.08	3.251	180	-10	17.0	0.04	4.052
140	-470	7.5	0.20	1.718	160	-250	16.5	0.08	3.092	180	-30	16.5	0.04	4.057
140	-490	8.5	0.20	1.676	160	-270	16.0	0.04	2.835	180	-50	16.0	0.00	3.987
140	-510	10.0	0.16	1.691	160	-290	15.3	0.04	2.480	180	-70	16.0	0.00	3.879
140	-530	10.8	0.16	1.642	160	-310	14.3	0.04	2.059	180	-90	17.0	0.00	3.820
140	-550	11.3	0.16	1.528	160	-330	13.0	0.08	1.624	180	-110	18.0	0.00	3.767

Appendix 4.B. (continued)

x	y	T_e	F_3	H	x	y	T_e	F_3	H	x	y	T_e	F_3	H
180	-130	18.8	0.08	3.730	200	90	16.0	0.12	2.957	220	310	11.8	0.16	2.034
180	-150	18.5	0.12	3.666	200	70	17.0	0.12	3.403	220	290	12.8	0.12	2.032
180	-170	19.0	0.08	3.608	200	50	17.8	0.12	3.803	220	270	13.0	0.12	2.065
180	-190	18.0	0.08	3.510	200	30	18.3	0.12	4.102	220	250	13.3	0.12	2.132
180	-210	17.8	0.04	3.436	200	10	19.0	0.08	4.264	220	230	13.8	0.12	2.195
180	-230	17.5	0.04	3.394	200	-10	18.8	0.08	4.355	220	210	14.0	0.12	2.263
180	-250	16.8	0.08	3.273	200	-30	18.5	0.04	4.366	220	190	14.5	0.12	2.325
180	-270	16.3	0.08	3.029	200	-50	17.5	0.00	4.248	220	170	15.0	0.12	2.368
180	-290	15.3	0.08	2.678	200	-70	16.5	0.00	4.074	220	150	15.3	0.12	2.413
180	-310	14.8	0.04	2.272	200	-90	17.3	0.00	4.036	220	130	15.8	0.12	2.531
180	-330	13.8	0.08	1.858	200	-110	18.5	0.00	4.004	220	110	16.3	0.12	2.784
180	-350	13.3	0.08	1.454	200	-130	19.8	0.00	3.990	220	90	17.0	0.12	3.140
180	-370	12.0	0.12	1.098	200	-150	20.0	0.04	3.881	220	70	17.8	0.12	3.540
180	-390	10.8	0.16	0.903	200	-170	19.0	0.08	3.757	220	50	19.0	0.08	3.919
180	-410	10.5	0.16	0.991	200	-190	18.8	0.04	3.643	220	30	20.0	0.08	4.244
180	-430	9.8	0.20	1.167	200	-210	18.0	0.04	3.550	220	10	20.3	0.08	4.443
180	-450	10.0	0.20	1.378	200	-230	17.8	0.04	3.488	220	-10	20.3	0.08	4.576
180	-470	11.0	0.20	1.483	200	-250	17.0	0.08	3.382	220	-30	20.3	0.04	4.618
180	-490	11.8	0.20	1.646	200	-270	16.5	0.08	3.169	220	-50	19.3	0.00	4.511
180	-510	12.5	0.20	1.897	200	-290	15.8	0.08	2.833	220	-70	18.0	0.00	4.327
180	-530	13.8	0.16	1.962	200	-310	15.0	0.08	2.441	220	-90	18.0	0.00	4.258
180	-550	13.8	0.16	1.836	200	-330	14.5	0.08	2.046	220	-110	19.3	0.00	4.253
180	-570	13.3	0.16	1.618	200	-350	13.5	0.12	1.667	220	-130	20.8	0.00	4.295
180	-590	13.8	0.12	1.363	200	-370	13.3	0.12	1.310	220	-150	21.0	0.00	4.136
200	650	16.5	0.00	2.535	200	-390	12.3	0.16	1.024	220	-170	20.3	0.00	3.928
200	630	15.3	0.00	2.427	200	-410	12.5	0.16	0.974	220	-190	19.3	0.04	3.792
200	610	13.8	0.00	2.245	200	-430	12.0	0.20	1.117	220	-210	18.5	0.04	3.678
200	590	12.8	0.00	2.106	200	-450	12.5	0.20	1.265	220	-230	17.8	0.04	3.567
200	570	11.8	0.08	2.071	200	-470	13.3	0.20	1.429	220	-250	17.0	0.08	3.450
200	550	11.0	0.12	2.223	200	-490	14.8	0.16	1.677	220	-270	16.8	0.08	3.276
200	530	10.5	0.16	2.419	200	-510	14.8	0.16	1.923	220	-290	16.3	0.08	2.975
200	510	9.8	0.20	2.493	200	-530	14.8	0.16	1.990	220	-310	15.5	0.08	2.600
200	490	9.5	0.20	2.436	200	-550	15.0	0.12	1.831	220	-330	14.8	0.12	2.233
200	470	9.3	0.24	2.349	200	-570	14.3	0.12	1.554	220	-350	14.5	0.12	1.868
200	450	8.8	0.24	2.057	200	-590	13.8	0.12	1.349	220	-370	14.5	0.12	1.533
200	430	8.3	0.24	2.058	220	650	17.0	0.00	2.625	220	-390	14.0	0.16	1.254
200	410	8.3	0.24	1.948	220	630	15.3	0.00	2.501	220	-410	14.5	0.16	1.128
200	390	8.5	0.24	1.781	220	610	14.0	0.00	2.350	220	-430	15.5	0.16	1.221
200	370	9.5	0.20	1.675	220	590	12.5	0.08	2.226	220	-450	16.0	0.16	1.330
200	350	10.0	0.20	1.701	220	570	11.5	0.08	2.178	220	-470	16.3	0.16	1.535
200	330	10.8	0.16	1.715	220	550	10.5	0.16	2.332	220	-490	16.3	0.16	1.845
200	310	11.0	0.16	1.737	220	530	10.0	0.20	2.537	220	-510	16.5	0.12	2.062
200	290	11.8	0.12	1.762	220	510	9.5	0.20	2.542	220	-530	15.8	0.12	1.997
200	270	12.0	0.12	1.810	220	490	9.3	0.20	2.536	220	-550	15.0	0.12	1.754
200	250	12.3	0.12	1.885	220	470	8.8	0.24	2.404	220	-570	14.8	0.08	1.499
200	230	12.5	0.12	1.967	220	450	8.5	0.24	2.282	220	-590	14.0	0.08	1.351
200	210	12.8	0.12	2.040	220	430	8.3	0.24	2.174	240	650	17.5	0.00	2.736
200	190	13.3	0.12	2.099	220	410	8.5	0.24	1.925	240	630	15.3	0.00	2.526
200	170	13.5	0.12	2.155	220	390	9.3	0.24	1.895	240	610	13.8	0.00	2.327
200	150	14.0	0.12	2.208	220	370	10.3	0.20	1.784	240	590	12.5	0.04	2.200
200	130	14.5	0.12	2.313	220	350	11.3	0.16	1.943	240	570	11.5	0.08	2.205
200	110	15.0	0.12	2.571	220	330	11.5	0.16	1.963	240	550	10.3	0.16	2.402

Appendix 4.B. (continued)

x	y	T_e	F_3	H	x	y	T_e	F_3	H	x	y	T_e	F_3	H
240	530	9.8	0.20	2.608	240	-510	17.3	0.08	2.203	260	-290	17.3	0.12	3.303
240	510	9.3	0.20	2.603	240	-530	16.3	0.08	2.054	260	-310	16.5	0.12	2.933
240	490	9.0	0.24	2.641	240	-550	15.3	0.08	1.773	260	-330	16.3	0.12	2.592
240	470	8.5	0.24	2.504	240	-570	14.8	0.04	1.546	260	-350	16.5	0.12	2.307
240	450	8.3	0.24	2.407	240	-590	14.0	0.00	1.460	260	-370	16.0	0.16	2.081
240	430	8.3	0.24	2.019	260	650	16.5	0.12	2.957	260	-390	16.5	0.16	1.961
240	410	9.0	0.24	1.781	260	630	15.0	0.08	2.670	260	-410	17.3	0.16	1.959
240	390	10.3	0.20	1.819	260	610	13.5	0.04	2.412	260	-430	19.3	0.12	1.988
240	370	11.0	0.20	1.937	260	590	12.0	0.08	2.239	260	-450	19.3	0.12	2.062
240	350	12.0	0.16	2.080	260	570	11.0	0.12	2.285	260	-470	19.0	0.12	2.246
240	330	12.3	0.16	2.211	260	550	10.3	0.20	2.621	260	-490	19.3	0.04	2.362
240	310	13.3	0.12	2.284	260	530	9.8	0.20	2.761	260	-510	17.8	0.04	2.325
240	290	13.8	0.12	2.288	260	510	9.3	0.20	2.770	260	-530	16.5	0.04	2.137
240	270	14.0	0.12	2.313	260	490	8.8	0.24	2.691	260	-550	15.8	0.00	1.892
240	250	14.5	0.12	2.351	260	470	8.5	0.24	2.495	260	-570	14.8	0.00	1.715
240	230	15.5	0.08	2.389	260	450	8.3	0.24	2.229	260	-590	13.5	0.00	1.656
240	210	15.8	0.08	2.452	260	430	8.5	0.24	1.800	280	650	14.5	0.20	3.262
240	190	16.3	0.08	2.507	260	410	9.5	0.24	1.772	280	630	13.8	0.16	2.943
240	170	16.8	0.08	2.544	260	390	10.8	0.20	1.739	280	610	13.0	0.12	2.621
240	150	17.0	0.08	2.587	260	370	12.0	0.16	2.041	280	590	12.0	0.08	2.332
240	130	17.5	0.08	2.707	260	350	12.5	0.16	2.251	280	570	11.0	0.12	2.332
240	110	18.0	0.08	2.972	260	330	13.0	0.16	2.422	280	550	10.3	0.20	2.727
240	90	18.5	0.08	3.315	260	310	13.5	0.16	2.517	280	530	10.0	0.24	2.915
240	70	18.8	0.08	3.661	260	290	14.8	0.12	2.536	280	510	9.5	0.24	2.804
240	50	19.5	0.04	3.974	260	270	15.3	0.12	2.548	280	490	9.0	0.24	2.689
240	30	20.3	0.04	4.283	260	250	16.3	0.08	2.582	280	470	8.5	0.24	2.434
240	10	21.3	0.04	4.538	260	230	16.8	0.08	2.604	280	450	8.3	0.24	2.084
240	-10	21.8	0.04	4.718	260	210	17.0	0.08	2.644	280	430	9.3	0.20	1.655
240	-30	22.0	0.00	4.811	260	190	17.5	0.08	2.691	280	410	10.3	0.20	1.316
240	-50	21.0	0.00	4.758	260	170	18.0	0.08	2.725	280	390	11.8	0.16	1.762
240	-70	19.5	0.00	4.609	260	150	18.3	0.08	2.766	280	370	12.3	0.16	2.072
240	-90	19.3	0.00	4.519	260	130	18.8	0.08	2.894	280	350	13.0	0.16	2.374
240	-110	20.3	0.00	4.511	260	110	19.5	0.08	3.176	280	330	13.5	0.16	2.592
240	-130	22.3	0.00	4.614	260	90	20.0	0.08	3.546	280	310	15.0	0.12	2.730
240	-150	22.3	0.00	4.406	260	70	20.5	0.04	3.876	280	290	15.8	0.12	2.786
240	-170	21.3	0.00	4.140	260	50	20.8	0.00	4.131	280	270	16.5	0.12	2.808
240	-190	20.5	0.00	3.974	260	30	21.0	0.00	4.360	280	250	17.8	0.08	2.822
240	-210	19.3	0.04	3.815	260	10	21.5	0.00	4.594	280	230	18.5	0.04	2.831
240	-230	18.0	0.08	3.674	260	-10	22.5	0.00	4.825	280	210	18.8	0.00	2.838
240	-250	17.5	0.08	3.529	260	-30	23.0	0.00	4.962	280	190	19.3	0.00	2.865
240	-270	17.3	0.08	3.368	260	-50	22.3	0.00	4.966	280	170	19.5	0.00	2.896
240	-290	16.3	0.12	3.126	260	-70	21.5	0.00	4.900	280	150	20.0	0.00	2.950
240	-310	15.8	0.12	2.775	260	-90	21.0	0.00	4.842	280	130	20.8	0.00	3.094
240	-330	15.5	0.12	2.428	260	-110	22.3	0.00	4.901	280	110	21.3	0.00	3.392
240	-350	15.8	0.12	2.106	260	-130	24.8	0.00	5.053	280	90	22.0	0.00	3.765
240	-370	15.3	0.16	1.816	260	-150	24.5	0.00	4.829	280	70	22.3	0.00	4.107
240	-390	15.5	0.16	1.600	260	-170	23.5	0.00	4.502	280	50	22.5	0.00	4.368
240	-410	16.3	0.16	1.520	260	-190	22.5	0.00	4.291	280	30	22.5	0.00	4.557
240	-430	17.3	0.16	1.531	260	-210	20.8	0.08	4.090	280	10	22.5	0.00	4.716
240	-450	17.5	0.16	1.641	260	-230	19.5	0.08	3.884	280	-10	23.3	0.00	4.932
240	-470	18.8	0.12	1.896	260	-250	18.0	0.12	3.708	280	-30	24.0	0.00	5.102
240	-490	17.8	0.12	2.118	260	-270	17.5	0.12	3.540	280	-50	23.8	0.00	5.165

Appendix 4.B. (continued)

x	y	T_e	F_3	H	x	y	T_e	F_3	H	x	y	T_e	F_3	H
280	-70	23.3	0.00	5.164	300	150	21.5	0.00	3.199	320	370	14.0	0.08	2.280
280	-90	23.0	0.00	5.183	300	130	22.0	0.00	3.333	320	350	14.8	0.08	2.642
280	-110	24.8	0.00	5.382	300	110	22.8	0.00	3.619	320	330	15.5	0.12	2.929
280	-130	27.8	0.00	5.624	300	90	23.3	0.00	3.992	320	310	17.0	0.12	3.161
280	-150	28.5	0.00	5.477	300	70	24.0	0.00	4.342	320	290	18.5	0.12	3.360
280	-170	27.5	0.00	5.088	300	50	24.3	0.00	4.608	320	270	20.0	0.12	3.514
280	-190	26.8	0.04	4.821	300	30	24.5	0.00	4.808	320	250	22.3	0.00	3.571
280	-210	24.0	0.12	4.562	300	10	24.3	0.00	4.949	320	230	22.8	0.00	3.583
280	-230	20.8	0.16	4.282	300	-10	24.8	0.00	5.098	320	210	22.8	0.00	3.556
280	-250	19.3	0.16	4.033	300	-30	25.3	0.00	5.256	320	190	23.0	0.00	3.541
280	-270	18.3	0.16	3.793	300	-50	25.3	0.00	5.355	320	170	23.3	0.00	3.552
280	-290	17.3	0.16	3.457	300	-70	24.8	0.00	5.397	320	150	23.5	0.00	3.604
280	-310	16.3	0.16	3.052	300	-90	25.0	0.00	5.510	320	130	24.0	0.00	3.718
280	-330	15.8	0.16	2.695	300	-110	28.3	0.00	5.922	320	110	24.5	0.00	3.951
280	-350	16.8	0.12	2.434	300	-130	34.0	0.00	6.515	320	90	25.0	0.00	4.274
280	-370	17.0	0.12	2.266	300	-150	36.0	0.00	6.465	320	70	25.8	0.00	4.609
280	-390	17.5	0.12	2.215	300	-170	36.8	0.00	6.172	320	50	26.3	0.00	4.888
280	-410	18.3	0.12	2.257	300	-190	35.8	0.00	5.747	320	30	26.8	0.00	5.105
280	-430	19.0	0.12	2.309	300	-210	31.0	0.16	5.316	320	10	26.8	0.00	5.244
280	-450	19.5	0.12	2.389	300	-230	24.5	0.20	4.859	320	-10	26.5	0.00	5.340
280	-470	20.0	0.08	2.494	300	-250	21.3	0.20	4.447	320	-30	26.8	0.00	5.451
280	-490	19.5	0.00	2.510	300	-270	19.3	0.20	4.064	320	-50	26.8	0.00	5.557
280	-510	18.0	0.00	2.397	300	-290	18.5	0.16	3.627	320	-70	26.8	0.00	5.657
280	-530	16.8	0.00	2.189	300	-310	16.8	0.16	3.165	320	-90	28.0	0.00	5.873
280	-550	15.5	0.00	1.971	300	-330	15.8	0.16	2.757	320	-110	39.8	0.00	6.848
280	-570	14.5	0.00	1.847	300	-350	16.3	0.12	2.481	320	-130	9.5	0.60	8.316
280	-590	12.5	0.00	1.780	300	-370	16.5	0.12	2.357	320	-150	9.5	0.60	8.424
300	650	14.0	0.24	3.429	300	-390	17.0	0.12	2.367	320	-170	75.0	0.00	7.894
300	630	13.3	0.20	3.082	300	-410	17.8	0.12	2.413	320	-190	73.8	0.00	7.278
300	610	12.8	0.16	2.797	300	-430	18.3	0.12	2.451	320	-210	50.5	0.00	6.416
300	590	12.3	0.12	2.478	300	-450	18.5	0.12	2.492	320	-230	31.0	0.24	5.585
300	570	11.3	0.12	2.347	300	-470	19.3	0.08	2.532	320	-250	25.3	0.20	4.864
300	550	10.5	0.20	2.608	300	-490	18.8	0.00	2.473	320	-270	21.0	0.20	4.264
300	530	10.0	0.20	2.862	300	-510	17.3	0.00	2.321	320	-290	18.5	0.20	3.729
300	510	9.5	0.20	2.783	300	-530	16.3	0.00	2.120	320	-310	17.3	0.16	3.212
300	490	9.3	0.20	2.569	300	-550	14.8	0.00	1.922	320	-330	15.8	0.16	2.744
300	470	9.0	0.20	2.226	300	-570	13.3	0.00	1.803	320	-350	15.5	0.12	2.475
300	450	9.0	0.20	1.819	300	-590	11.0	0.00	1.762	320	-370	15.3	0.12	2.394
300	430	9.5	0.20	1.326	320	650	13.3	0.24	3.369	320	-390	15.5	0.12	2.412
300	410	11.3	0.16	1.295	320	630	12.8	0.20	3.020	320	-410	16.3	0.12	2.425
300	390	12.0	0.16	1.727	320	610	12.8	0.16	2.797	320	-430	16.5	0.12	2.414
300	370	13.3	0.12	2.152	320	590	12.3	0.16	2.498	320	-450	16.8	0.12	2.411
300	350	14.0	0.12	2.485	320	570	11.5	0.16	2.318	320	-470	17.3	0.08	2.364
300	330	14.8	0.12	2.744	320	550	10.8	0.16	2.321	320	-490	16.8	0.04	2.233
300	310	16.0	0.12	2.932	320	530	10.3	0.20	2.527	320	-510	16.0	0.00	2.066
300	290	17.3	0.12	3.054	320	510	10.0	0.20	2.549	320	-530	14.8	0.04	1.887
300	270	18.0	0.12	3.125	320	490	9.5	0.20	2.296	320	-550	13.0	0.08	1.765
300	250	19.3	0.08	3.137	320	470	10.0	0.16	1.959	320	-570	11.0	0.08	1.725
300	230	20.3	0.00	3.120	320	450	10.3	0.16	1.648	320	-590	9.5	0.00	1.684
300	210	20.3	0.00	3.105	320	430	10.8	0.16	1.235	340	650	12.8	0.24	3.080
300	190	20.5	0.00	3.113	320	410	12.3	0.12	1.238	340	630	12.8	0.20	2.799
300	170	21.0	0.00	3.143	320	390	12.8	0.12	1.804	340	610	12.8	0.20	2.605

Appendix 4.B. (continued)

x	y	T_e	F_3	H
340	590	12.8	0.16	2.365
340	570	12.0	0.16	2.171
340	550	11.5	0.16	2.106
340	530	11.0	0.16	2.169
340	510	10.8	0.16	2.199
340	490	10.5	0.16	1.954
340	470	10.8	0.12	1.662
340	450	11.0	0.12	1.517
340	430	11.8	0.12	1.246
340	410	13.0	0.08	1.336
340	390	13.8	0.04	1.978
340	370	14.5	0.04	2.493
340	350	15.8	0.04	2.870
340	330	17.0	0.08	3.173
340	310	18.8	0.08	3.437
340	290	20.8	0.08	3.676
340	270	23.3	0.04	3.925
340	250	25.8	0.00	4.151
340	230	26.8	0.00	4.269
340	210	28.0	0.00	4.367
340	190	27.8	0.00	4.322
340	170	27.5	0.00	4.280
340	150	27.5	0.00	4.273
340	130	27.5	0.00	4.312
340	110	27.5	0.00	4.445
340	90	27.8	0.00	4.677
340	70	28.0	0.00	4.954
340	50	28.8	0.00	5.216
340	30	29.5	0.00	5.445
340	10	30.0	0.00	5.609
340	-10	29.8	0.00	5.700
340	-30	29.8	0.00	5.785
340	-50	30.3	0.00	5.897
340	-70	31.0	0.00	6.040
340	-90	36.0	0.00	6.395
340	-110	9.5	0.60	7.586
340	-130	10.0	0.60	9.279
340	-150	10.3	0.60	10.033
340	-170	10.0	0.60	9.406
340	-190	75.0	0.52	8.319
340	-210	65.8	0.00	7.136
340	-230	43.0	0.00	6.132
340	-250	29.3	0.20	5.260
340	-270	23.5	0.20	4.541
340	-290	21.3	0.16	3.845
340	-310	18.0	0.16	3.140
340	-330	15.8	0.16	2.588
340	-350	14.8	0.12	2.358
340	-370	13.8	0.12	2.357
340	-390	13.5	0.12	2.378
340	-410	13.8	0.12	2.355
340	-430	14.3	0.12	2.304
340	-450	14.3	0.12	2.218
340	-470	14.5	0.08	2.084
340	-490	13.8	0.08	1.912
340	-510	13.0	0.08	1.750
340	-530	12.0	0.08	1.657
340	-550	10.5	0.08	1.602
340	-570	9.3	0.04	1.555
340	-590	8.0	0.00	1.509
360	650	11.8	0.20	2.375
360	630	12.5	0.20	2.183
360	610	13.0	0.16	2.121
360	590	13.0	0.16	2.082
360	570	13.5	0.12	1.986
360	550	13.0	0.12	1.866
360	530	12.5	0.12	1.879
360	510	12.3	0.12	1.934
360	490	11.5	0.12	1.788
360	470	11.8	0.00	1.543
360	450	12.0	0.00	1.476
360	430	12.8	0.04	1.378
360	410	13.8	0.00	1.588
360	390	14.3	0.00	2.243
360	370	15.3	0.00	2.777
360	350	16.5	0.00	3.146
360	330	18.5	0.00	3.462
360	310	20.8	0.04	3.792
360	290	23.0	0.00	4.072
360	270	26.0	0.00	4.405
360	250	30.0	0.00	4.832
360	230	34.5	0.00	5.247
360	210	37.3	0.00	5.490
360	190	39.0	0.00	5.635
360	170	38.0	0.00	5.561
360	150	36.0	0.00	5.392
360	130	34.3	0.00	5.255
360	110	33.0	0.00	5.220
360	90	32.5	0.00	5.327
360	70	32.0	0.00	5.481
360	50	32.3	0.00	5.664
360	30	33.0	0.00	5.870
360	10	33.8	0.00	6.057
360	-10	34.3	0.00	6.177
360	-30	35.3	0.00	6.277
360	-50	36.8	0.00	6.375
360	-70	39.8	0.00	6.518
360	-90	64.5	0.00	6.934
360	-110	10.0	0.60	7.873
360	-130	10.3	0.60	9.378
360	-150	11.0	0.60	11.118
360	-170	11.3	0.60	10.746
360	-190	11.3	0.60	9.105
360	-210	75.0	0.00	7.658
360	-230	46.5	0.00	6.512
360	-250	35.8	0.00	5.575
360	-270	27.8	0.16	4.794
360	-290	23.0	0.16	3.928
360	-310	19.5	0.16	3.085
360	-330	16.5	0.16	2.455
360	-350	14.8	0.12	2.209
360	-370	13.0	0.12	2.217
360	-390	12.0	0.12	2.277
360	-410	11.8	0.12	2.283
360	-430	11.8	0.12	2.205
360	-450	12.0	0.08	2.073
360	-470	11.8	0.08	1.876
360	-490	11.0	0.08	1.679
360	-510	10.0	0.08	1.530
360	-530	9.3	0.08	1.424
360	-550	8.5	0.04	1.353
360	-570	7.8	0.00	1.306
360	-590	7.0	0.00	1.294
380	650	10.3	0.20	1.954
380	630	12.0	0.16	1.767
380	610	12.8	0.16	1.765
380	590	14.3	0.12	1.848
380	570	14.8	0.12	1.832
380	550	14.5	0.12	1.769
380	530	14.5	0.08	1.758
380	510	13.5	0.08	1.805
380	490	12.8	0.04	1.757
380	470	12.3	0.00	1.655
380	450	12.3	0.00	1.604
380	430	13.3	0.00	1.645
380	410	14.3	0.00	1.995
380	390	15.3	0.00	2.627
380	370	16.3	0.00	3.128
380	350	17.8	0.00	3.474
380	330	19.8	0.00	3.793
380	310	22.3	0.00	4.147
380	290	24.8	0.00	4.458
380	270	28.0	0.00	4.844
380	250	33.3	0.00	5.414
380	230	43.3	0.00	6.152
380	210	63.5	0.00	6.799
380	190	75.0	0.00	7.118
380	170	8.5	0.60	7.159
380	150	74.8	0.00	7.052
380	130	56.3	0.00	6.754
380	110	48.5	0.00	6.504
380	90	43.5	0.00	6.341
380	70	40.0	0.00	6.268
380	50	38.0	0.00	6.280
380	30	37.8	0.00	6.384
380	10	38.5	0.00	6.540

Appendix 4.B. (continued)

x	y	T_e	F_3	H	x	y	T_e	F_3	H	x	y	T_e	F_3	H
380	-10	40.0	0.00	6.689	400	210	9.0	0.60	7.564	420	430	15.3	0.00	2.385
380	-30	42.8	0.00	6.796	400	190	8.8	0.60	7.833	420	410	16.8	0.00	2.969
380	-50	48.5	0.00	6.907	400	170	8.8	0.60	7.998	420	390	18.3	0.00	3.520
380	-70	64.5	0.00	7.044	400	150	8.8	0.60	8.061	420	370	20.0	0.00	4.016
380	-90	10.0	0.60	7.374	400	130	8.8	0.60	7.989	420	350	21.5	0.00	4.340
380	-110	10.5	0.60	8.121	400	110	8.5	0.60	7.704	420	330	23.8	0.00	4.641
380	-130	11.0	0.60	9.405	400	90	8.3	0.60	7.362	420	310	26.8	0.00	5.032
380	-150	12.3	0.60	11.384	400	70	8.3	0.60	7.175	420	290	30.3	0.00	5.461
380	-170	12.8	0.60	11.848	400	50	49.3	0.00	7.055	420	270	36.5	0.00	6.184
380	-190	12.5	0.60	9.846	400	30	47.0	0.00	7.037	420	250	9.3	0.60	7.294
380	-210	75.0	0.40	8.311	400	10	47.5	0.00	7.135	420	230	9.3	0.60	7.899
380	-230	55.0	0.00	7.003	400	-10	51.0	0.00	7.261	420	210	9.0	0.60	8.195
380	-250	40.0	0.00	5.977	400	-30	9.0	0.60	7.302	420	190	9.0	0.60	8.532
380	-270	33.0	0.00	5.070	400	-50	9.5	0.60	7.394	420	170	9.0	0.60	8.793
380	-290	25.8	0.16	4.109	400	-70	10.0	0.60	7.510	420	150	9.0	0.60	8.908
380	-310	21.5	0.16	3.158	400	-90	10.5	0.60	7.780	420	130	9.0	0.60	8.873
380	-330	17.8	0.16	2.401	400	-110	11.3	0.60	8.256	420	110	9.0	0.60	8.602
380	-350	14.5	0.16	2.039	400	-130	11.3	0.60	8.850	420	90	9.0	0.60	8.099
380	-370	12.8	0.12	2.053	400	-150	12.0	0.60	9.672	420	70	9.0	0.60	7.659
380	-390	11.3	0.12	2.115	400	-170	12.8	0.60	10.158	420	50	9.0	0.60	7.478
380	-410	10.5	0.12	2.143	400	-190	12.5	0.60	9.381	420	30	9.0	0.60	7.455
380	-430	10.0	0.08	2.063	400	-210	12.3	0.60	8.480	420	10	9.3	0.60	7.554
380	-450	9.8	0.08	1.877	400	-230	75.0	0.00	7.301	420	-10	9.8	0.60	7.579
380	-470	9.3	0.04	1.624	400	-250	46.5	0.00	6.288	420	-30	9.8	0.60	7.540
380	-490	8.5	0.00	1.413	400	-270	36.8	0.00	5.350	420	-50	10.3	0.60	7.631
380	-510	7.8	0.04	1.306	400	-290	29.3	0.12	4.313	420	-70	10.8	0.60	7.772
380	-530	7.3	0.04	1.260	400	-310	23.0	0.16	3.287	420	-90	10.8	0.60	7.894
380	-550	6.8	0.04	1.225	400	-330	17.5	0.20	2.375	420	-110	11.3	0.60	7.970
380	-570	6.5	0.04	1.215	400	-350	14.3	0.16	1.885	420	-130	11.5	0.60	7.819
380	-590	6.3	0.00	1.219	400	-370	11.8	0.16	1.851	420	-150	12.0	0.60	7.809
400	650	7.3	0.20	2.475	400	-390	10.3	0.12	1.928	420	-170	12.5	0.60	7.906
400	630	10.8	0.16	2.029	400	-410	9.0	0.12	1.908	420	-190	12.3	0.60	7.813
400	610	11.8	0.16	1.794	400	-430	8.3	0.08	1.776	420	-210	12.3	0.60	7.592
400	590	14.3	0.12	1.852	400	-450	7.5	0.04	1.555	420	-230	75.0	0.00	7.117
400	570	15.8	0.12	1.941	400	-470	6.8	0.00	1.321	420	-250	56.3	0.00	6.406
400	550	16.3	0.12	1.933	400	-490	6.3	0.00	1.215	420	-270	39.8	0.00	5.481
400	530	16.5	0.08	1.878	400	-510	6.0	0.00	1.220	420	-290	30.3	0.08	4.337
400	510	15.5	0.04	1.908	400	-530	5.8	0.00	1.242	420	-310	22.0	0.16	3.150
400	490	13.8	0.00	1.833	400	-550	5.8	0.00	1.238	420	-330	15.5	0.20	2.242
400	470	12.8	0.00	1.786	400	-570	5.8	0.00	1.258	420	-350	12.5	0.16	1.831
400	450	13.0	0.00	1.769	400	-590	5.8	0.00	1.304	420	-370	10.0	0.16	1.769
400	430	14.0	0.00	2.001	420	650	4.5	0.24	2.874	420	-390	8.5	0.12	1.757
400	410	15.3	0.00	2.486	420	630	7.3	0.20	2.531	420	-410	6.8	0.12	1.639
400	390	16.5	0.00	3.052	420	610	10.8	0.16	2.155	420	-430	6.0	0.08	1.463
400	370	17.8	0.00	3.546	420	590	13.5	0.12	2.008	420	-450	5.3	0.04	1.289
400	350	19.3	0.00	3.868	420	570	16.0	0.12	2.089	420	-470	5.0	0.00	1.187
400	330	21.3	0.00	4.180	420	550	18.5	0.08	2.186	420	-490	4.8	0.00	1.214
400	310	24.0	0.00	4.553	420	530	18.8	0.04	2.241	420	-510	4.8	0.00	1.262
400	290	27.0	0.00	4.916	420	510	17.5	0.00	2.213	420	-530	5.0	0.00	1.289
400	270	31.3	0.00	5.425	420	490	14.8	0.00	2.065	420	-550	5.0	0.00	1.288
400	250	39.3	0.00	6.188	420	470	13.8	0.00	1.958	420	-570	5.3	0.00	1.306
400	230	57.8	0.00	7.076	420	450	14.3	0.00	1.973	420	-590	5.5	0.00	1.368

Appendix 4.B. (continued)

x	y	T_e	F_3	H	x	y	T_e	F_3	H	x	y	T_e	F_3	H
440	650	4.5	0.24	2.860	440	-390	6.5	0.12	1.533	460	-170	12.0	0.60	6.186
440	630	5.3	0.24	2.816	440	-410	5.5	0.08	1.387	460	-190	63.0	0.00	6.179
440	610	8.3	0.20	2.523	440	-430	4.8	0.00	1.292	460	-210	63.5	0.00	6.217
440	590	11.8	0.16	2.258	440	-450	4.3	0.00	1.274	460	-230	57.5	0.00	6.154
440	570	15.5	0.12	2.242	440	-470	4.3	0.00	1.318	460	-250	43.8	0.00	5.730
440	550	19.5	0.04	2.425	440	-490	4.0	0.00	1.359	460	-270	33.0	0.00	4.853
440	530	21.0	0.00	2.685	440	-510	4.3	0.00	1.374	460	-290	23.8	0.12	3.631
440	510	20.3	0.00	2.779	440	-530	4.3	0.00	1.346	460	-310	16.0	0.16	2.420
440	490	17.3	0.00	2.595	440	-550	4.5	0.00	1.326	460	-330	11.3	0.12	1.814
440	470	15.5	0.00	2.399	440	-570	5.0	0.00	1.330	460	-350	8.8	0.12	1.633
440	450	16.3	0.00	2.375	440	-590	5.3	0.00	1.396	460	-370	7.3	0.08	1.522
440	430	18.0	0.00	2.800	460	650	4.8	0.24	3.001	460	-390	5.8	0.04	1.371
440	410	19.8	0.00	3.502	460	630	5.8	0.24	2.831	460	-410	4.8	0.00	1.282
440	390	21.8	0.00	4.150	460	610	7.8	0.20	2.660	460	-430	4.0	0.00	1.371
440	370	23.3	0.00	4.614	460	590	11.8	0.16	2.533	460	-450	3.8	0.00	1.489
440	350	24.8	0.00	4.914	460	570	15.5	0.12	2.536	460	-470	3.5	0.00	1.550
440	330	27.3	0.00	5.212	460	550	19.8	0.00	2.678	460	-490	3.5	0.00	1.560
440	310	30.8	0.00	5.637	460	530	23.0	0.00	3.072	460	-510	3.8	0.00	1.495
440	290	35.5	0.00	6.175	460	510	24.8	0.00	3.407	460	-530	3.8	0.00	1.388
440	270	9.3	0.60	7.161	460	490	22.0	0.00	3.336	460	-550	4.3	0.00	1.290
440	250	9.5	0.60	8.217	460	470	19.8	0.00	3.164	460	-570	4.8	0.00	1.264
440	230	9.5	0.60	9.227	460	450	20.3	0.00	3.096	460	-590	5.0	0.00	1.339
440	210	9.3	0.60	9.337	460	430	22.3	0.00	3.382	480	650	5.5	0.28	3.062
440	190	9.3	0.60	9.287	460	410	24.3	0.00	4.091	480	630	6.8	0.24	3.036
440	170	9.3	0.60	9.415	460	390	26.0	0.00	4.847	480	610	9.0	0.20	2.892
440	150	9.3	0.60	9.565	460	370	27.8	0.00	5.352	480	590	12.5	0.16	2.781
440	130	9.3	0.60	9.474	460	350	29.8	0.00	5.637	480	570	16.3	0.12	2.811
440	110	9.3	0.60	9.124	460	330	33.0	0.00	5.940	480	550	20.5	0.00	2.951
440	90	9.3	0.60	8.571	460	310	39.0	0.00	6.460	480	530	25.0	0.00	3.387
440	70	9.3	0.60	8.091	460	290	9.3	0.60	7.131	480	510	29.8	0.00	3.856
440	50	9.8	0.60	7.828	460	270	9.5	0.60	7.982	480	490	30.5	0.00	3.974
440	30	10.3	0.60	7.754	460	250	9.5	0.60	9.615	480	470	28.0	0.00	3.903
440	10	10.0	0.60	7.744	460	230	9.8	0.60	10.850	480	450	26.0	0.00	3.720
440	-10	10.5	0.60	7.721	460	210	9.5	0.60	10.815	480	430	26.8	0.00	3.780
440	-30	10.5	0.60	7.633	460	190	9.5	0.60	10.475	480	410	29.0	0.00	4.460
440	-50	10.5	0.60	7.621	460	170	9.3	0.60	9.810	480	390	31.3	0.00	5.450
440	-70	10.8	0.60	7.710	460	150	9.5	0.60	9.872	480	370	33.8	0.00	6.084
440	-90	10.8	0.60	7.602	460	130	9.5	0.60	9.722	480	350	37.3	0.00	6.413
440	-110	11.0	0.60	7.298	460	110	9.8	0.60	9.263	480	330	43.0	0.00	6.733
440	-130	11.5	0.60	6.931	460	90	9.8	0.60	8.719	480	310	9.3	0.60	7.203
440	-150	12.0	0.60	6.761	460	70	10.3	0.60	8.450	480	290	9.0	0.60	7.648
440	-170	12.3	0.60	6.709	460	50	10.8	0.60	8.245	480	270	9.5	0.60	8.850
440	-190	12.0	0.60	6.729	460	30	11.3	0.60	8.036	480	250	9.8	0.60	10.727
440	-210	12.0	0.60	6.790	460	10	10.8	0.60	7.968	480	230	10.0	0.60	11.405
440	-230	75.0	0.00	6.697	460	-10	10.8	0.60	7.904	480	210	9.8	0.60	11.153
440	-250	56.8	0.00	6.199	460	-30	10.8	0.60	7.700	480	190	9.3	0.60	11.087
440	-270	37.8	0.00	5.294	460	-50	11.0	0.60	7.619	480	170	9.3	0.60	10.724
440	-290	27.8	0.08	4.075	460	-70	10.8	0.60	7.452	480	150	9.5	0.60	10.020
440	-310	19.0	0.16	2.766	460	-90	11.3	0.60	7.074	480	130	10.0	0.60	9.746
440	-330	13.3	0.16	1.997	460	-110	11.0	0.60	6.710	480	110	10.0	0.60	9.420
440	-350	10.3	0.16	1.770	460	-130	53.5	0.00	6.433	480	90	10.3	0.60	9.211
440	-370	8.3	0.12	1.643	460	-150	55.8	0.00	6.260	480	70	10.5	0.60	9.021

Appendix 4.B. (continued)

x	y	T_e	F_3	H
480	50	11.0	0.60	8.755
480	30	11.5	0.60	8.525
480	10	11.8	0.60	8.468
480	-10	11.5	0.60	8.267
480	-30	11.3	0.60	8.037
480	-50	11.0	0.60	7.729
480	-70	11.3	0.60	7.272
480	-90	11.0	0.60	6.743
480	-110	52.5	0.00	6.358
480	-130	51.0	0.00	6.115
480	-150	51.5	0.00	5.954
480	-170	51.0	0.00	5.830
480	-190	48.8	0.00	5.735
480	-210	45.0	0.00	5.669
480	-230	39.8	0.00	5.519
480	-250	33.8	0.00	5.048
480	-270	27.5	0.00	4.115
480	-290	19.8	0.12	2.975
480	-310	14.0	0.12	2.122
480	-330	9.8	0.12	1.727
480	-350	7.8	0.08	1.624
480	-370	6.5	0.04	1.518
480	-390	5.3	0.00	1.363
480	-410	4.3	0.00	1.339
480	-430	3.8	0.00	1.510
480	-450	3.5	0.00	1.685
480	-470	3.3	0.00	1.735
480	-490	3.3	0.00	1.655
480	-510	3.3	0.00	1.512
480	-530	3.5	0.00	1.334
480	-550	4.0	0.00	1.172
480	-570	4.5	0.00	1.108
480	-590	4.8	0.00	1.173
500	650	6.5	0.28	3.265
500	630	8.5	0.24	3.285
500	610	11.5	0.20	3.064
500	590	14.0	0.16	2.938
500	570	17.5	0.12	3.004
500	550	23.3	0.00	3.262
500	530	29.0	0.00	3.729
500	510	36.8	0.00	4.084
500	490	15.8	0.60	4.058
500	470	15.8	0.60	4.108
500	450	32.0	0.00	3.963
500	430	31.0	0.00	3.871
500	410	34.5	0.00	4.382
500	390	39.8	0.00	5.884
500	370	45.0	0.00	6.844
500	350	50.8	0.00	7.068
500	330	9.3	0.60	7.242
500	310	9.5	0.60	7.598
500	290	9.3	0.60	8.114

x	y	T_e	F_3	H
500	270	9.3	0.60	9.054
500	250	9.3	0.60	10.553
500	230	9.5	0.60	11.394
500	210	9.3	0.60	11.329
500	190	9.3	0.60	11.406
500	170	9.3	0.60	11.090
500	150	9.3	0.60	10.717
500	130	10.0	0.60	10.607
500	110	10.0	0.60	10.144
500	90	11.0	0.60	10.254
500	70	11.5	0.60	10.180
500	50	12.0	0.60	9.912
500	30	12.3	0.60	9.415
500	10	12.3	0.60	9.140
500	-10	11.5	0.60	8.926
500	-30	11.3	0.60	8.552
500	-50	11.0	0.60	7.873
500	-70	11.5	0.60	7.160
500	-90	75.0	0.00	6.556
500	-110	62.3	0.00	6.132
500	-130	56.8	0.00	5.877
500	-150	53.3	0.00	5.702
500	-170	49.3	0.00	5.526
500	-190	44.5	0.00	5.368
500	-210	39.0	0.00	5.201
500	-230	33.0	0.00	4.880
500	-250	26.3	0.12	4.162
500	-270	19.8	0.16	3.193
500	-290	14.5	0.16	2.380
500	-310	10.3	0.16	1.948
500	-330	8.0	0.12	1.790
500	-350	6.8	0.08	1.717
500	-370	5.8	0.04	1.591
500	-390	5.0	0.00	1.444
500	-410	4.0	0.00	1.419
500	-430	3.5	0.00	1.593
500	-450	3.3	0.00	1.777
500	-470	3.0	0.00	1.821
500	-490	3.0	0.00	1.670
500	-510	3.0	0.00	1.448
500	-530	3.3	0.00	1.209
500	-550	3.8	0.00	1.012
500	-570	4.3	0.00	0.923
500	-590	4.8	0.00	0.980
520	650	8.0	0.32	3.558
520	630	9.8	0.28	3.491
520	610	12.0	0.24	3.396
520	590	16.0	0.20	3.395
520	570	21.0	0.16	3.424
520	550	27.5	0.00	3.590
520	530	36.3	0.00	4.001
520	510	16.5	0.60	3.934

x	y	T_e	F_3	H
520	490	16.8	0.60	3.875
520	470	16.8	0.60	3.843
520	450	6.8	0.40	4.048
520	430	38.8	0.00	4.025
520	410	44.5	0.00	4.238
520	390	62.3	0.00	6.048
520	370	75.0	0.00	7.703
520	350	9.5	0.60	7.419
520	330	9.5	0.60	7.420
520	310	9.3	0.60	7.703
520	290	9.0	0.60	8.125
520	270	9.0	0.60	8.819
520	250	9.0	0.60	9.874
520	230	9.0	0.60	10.972
520	210	9.0	0.60	11.489
520	190	9.3	0.60	11.782
520	170	9.5	0.60	11.250
520	150	9.5	0.60	10.179
520	130	9.8	0.60	9.367
520	110	11.0	0.60	9.481
520	90	11.8	0.60	9.872
520	70	12.3	0.60	10.484
520	50	13.0	0.60	11.246
520	30	13.3	0.60	11.131
520	10	13.3	0.60	10.419
520	-10	13.0	0.60	9.891
520	-30	11.8	0.60	8.938
520	-50	11.3	0.60	7.840
520	-70	11.0	0.60	6.994
520	-90	11.5	0.60	6.450
520	-110	75.0	0.00	6.066
520	-130	72.5	0.00	5.793
520	-150	58.3	0.00	5.590
520	-170	49.3	0.00	5.365
520	-190	42.0	0.00	5.118
520	-210	34.0	0.12	4.793
520	-230	23.5	0.20	4.215
520	-250	17.5	0.20	3.372
520	-270	14.0	0.16	2.671
520	-290	10.5	0.16	2.222
520	-310	8.5	0.12	2.016
520	-330	7.0	0.12	1.895
520	-350	6.3	0.08	1.786
520	-370	5.5	0.04	1.654
520	-390	4.8	0.00	1.499
520	-410	4.0	0.00	1.446
520	-430	3.5	0.00	1.581
520	-450	3.0	0.00	1.731
520	-470	2.8	0.00	1.745
520	-490	2.8	0.00	1.576
520	-510	3.0	0.00	1.305
520	-530	3.3	0.00	1.034

Appendix 4.B. (continued)

x	y	T_e	F_3	H	x	y	T_e	F_3	H	x	y	T_e	F_3	H
520	-550	3.5	0.00	0.843	540	-330	7.0	0.12	1.806	560	-110	11.3	0.60	6.409
520	-570	4.0	0.00	0.786	540	-350	6.3	0.08	1.725	560	-130	75.0	0.44	6.181
520	-590	4.5	0.00	0.860	540	-370	5.5	0.08	1.617	560	-150	75.0	0.00	5.897
540	650	12.0	0.36	3.946	540	-390	4.8	0.04	1.474	560	-170	54.8	0.00	5.530
540	630	12.3	0.32	3.975	540	-410	4.0	0.00	1.404	560	-190	35.3	0.24	5.020
540	610	13.0	0.32	3.952	540	-430	3.5	0.00	1.460	560	-210	22.8	0.24	4.279
540	590	14.3	0.32	4.013	540	-450	3.0	0.00	1.551	560	-230	16.3	0.24	3.425
540	570	32.0	0.28	4.062	540	-470	3.0	0.00	1.524	560	-250	13.0	0.20	2.685
540	550	42.5	0.00	4.066	540	-490	2.8	0.00	1.350	560	-270	10.5	0.20	2.245
540	530	8.0	0.44	4.162	540	-510	3.0	0.00	1.084	560	-290	9.3	0.16	1.939
540	510	16.8	0.60	3.802	540	-530	3.3	0.00	0.881	560	-310	8.3	0.12	1.809
540	490	17.0	0.60	3.801	540	-550	3.5	0.00	0.784	560	-330	7.0	0.12	1.703
540	470	17.0	0.60	3.729	540	-570	4.0	0.00	0.791	560	-350	6.5	0.08	1.642
540	450	17.0	0.60	3.793	540	-590	4.5	0.00	0.828	560	-370	5.8	0.08	1.521
540	430	6.8	0.36	3.974	560	650	40.3	0.56	4.440	560	-390	4.8	0.08	1.391
540	410	75.0	0.00	4.220	560	630	51.0	0.60	4.487	560	-410	4.3	0.04	1.318
540	390	75.0	0.52	5.461	560	610	55.3	0.60	4.475	560	-430	3.8	0.04	1.295
540	370	75.0	0.56	8.437	560	590	24.8	0.44	4.471	560	-450	3.3	0.04	1.274
540	350	9.5	0.60	7.662	560	570	70.0	0.60	4.504	560	-470	3.3	0.00	1.186
540	330	9.5	0.60	7.407	560	550	9.0	0.44	4.257	560	-490	3.0	0.00	1.038
540	310	9.3	0.60	7.627	560	530	16.5	0.60	3.815	560	-510	3.3	0.00	0.927
540	290	9.0	0.60	7.994	560	510	16.8	0.60	3.716	560	-530	3.3	0.00	0.923
540	270	8.5	0.60	8.505	560	490	16.8	0.60	3.686	560	-550	3.8	0.00	0.954
540	250	8.5	0.60	9.306	560	470	17.0	0.60	3.624	560	-570	4.0	0.00	0.946
540	230	9.0	0.60	10.544	560	450	17.0	0.60	3.594	560	-590	4.5	0.00	0.929
540	210	9.3	0.60	11.453	560	430	7.5	0.44	3.809	580	650	13.3	0.60	5.572
540	190	9.3	0.60	11.958	560	410	7.5	0.40	4.127	580	630	27.5	0.56	5.632
540	170	9.3	0.60	11.372	560	390	75.0	0.60	5.319	580	610	34.0	0.56	5.377
540	150	9.5	0.60	10.118	560	370	74.3	0.60	8.373	580	590	28.5	0.52	5.150
540	130	10.5	0.60	9.161	560	350	9.5	0.60	8.185	580	570	13.0	0.52	4.672
540	110	11.5	0.60	8.494	560	330	9.8	0.60	7.494	580	550	15.8	0.60	3.846
540	90	12.3	0.60	8.237	560	310	9.5	0.60	7.583	580	530	16.0	0.60	3.584
540	70	13.3	0.60	8.933	560	290	9.3	0.60	8.018	580	510	16.3	0.60	3.608
540	50	13.3	0.60	10.403	560	270	9.0	0.60	8.617	580	490	16.5	0.60	3.620
540	30	14.3	0.60	12.295	560	250	9.0	0.60	9.399	580	470	16.8	0.60	3.547
540	10	13.5	0.60	11.834	560	230	9.3	0.60	10.508	580	450	16.8	0.60	3.477
540	-10	13.0	0.60	10.574	560	210	9.0	0.60	11.423	580	430	16.3	0.60	3.504
540	-30	12.5	0.60	9.028	560	190	9.5	0.60	12.039	580	410	13.3	0.56	3.898
540	-50	12.0	0.60	7.780	560	170	9.3	0.60	11.219	580	390	11.8	0.56	5.118
540	-70	11.0	0.60	6.967	560	150	10.0	0.60	10.153	580	370	9.5	0.60	8.191
540	-90	11.5	0.60	6.512	560	130	11.0	0.60	9.173	580	350	9.5	0.60	9.444
540	-110	75.0	0.44	6.185	560	110	11.5	0.60	8.320	580	330	9.8	0.60	7.929
540	-130	75.0	0.00	5.900	560	90	12.8	0.60	8.043	580	310	9.5	0.60	7.668
540	-150	68.5	0.00	5.664	560	70	13.5	0.60	8.488	580	290	9.3	0.60	8.117
540	-170	51.0	0.00	5.377	560	50	14.8	0.60	10.117	580	270	9.5	0.60	9.015
540	-190	40.8	0.00	5.021	560	30	14.3	0.60	12.124	580	250	9.5	0.60	9.988
540	-210	25.0	0.24	4.503	560	10	13.5	0.60	12.578	580	230	9.3	0.60	10.826
540	-230	19.3	0.20	3.748	560	-10	13.0	0.60	11.058	580	210	9.3	0.60	11.804
540	-250	14.3	0.20	2.943	560	-30	12.5	0.60	9.136	580	190	9.5	0.60	12.037
540	-270	11.8	0.16	2.409	560	-50	12.3	0.60	7.916	580	170	10.0	0.60	11.037
540	-290	9.5	0.16	2.071	560	-70	12.3	0.60	7.208	580	150	10.0	0.60	9.423
540	-310	8.0	0.12	1.920	560	-90	12.0	0.60	6.762	580	130	11.3	0.60	8.714

Appendix 4.B. (continued)

x	y	T_e	F_3	H	x	y	T_e	F_3	H	x	y	T_e	F_3	H
580	110	12.0	0.60	8.066	580	-570	4.3	0.00	1.121	600	10	13.5	0.60	13.735
580	90	13.3	0.60	7.761	580	-590	4.5	0.00	1.080	600	-10	13.0	0.60	12.072
580	70	14.5	0.60	8.323	600	650	14.5	0.60	6.822	600	-30	12.8	0.60	10.502
580	50	15.0	0.60	10.040	600	630	13.8	0.60	7.065	600	-50	12.8	0.60	9.324
580	30	14.3	0.60	12.338	600	610	13.3	0.60	6.535	600	-70	13.0	0.60	8.614
580	10	13.5	0.60	13.245	600	590	13.5	0.60	5.534	600	-90	12.5	0.60	8.117
580	-10	13.0	0.60	11.371	600	570	14.3	0.60	4.231	600	-110	12.3	0.60	7.818
580	-30	12.8	0.60	9.510	600	550	15.3	0.60	3.528	600	-130	12.0	0.60	7.548
580	-50	12.5	0.60	8.342	600	530	15.8	0.60	3.510	600	-150	75.0	0.60	7.178
580	-70	12.3	0.60	7.663	600	510	16.0	0.60	3.544	600	-170	75.0	0.24	6.513
580	-90	12.3	0.60	7.223	600	490	16.3	0.60	3.497	600	-190	53.5	0.00	5.525
580	-110	11.5	0.60	6.886	600	470	16.5	0.60	3.420	600	-210	22.8	0.28	4.248
580	-130	11.3	0.60	6.665	600	450	16.5	0.60	3.313	600	-230	16.3	0.24	3.225
580	-150	75.0	0.44	6.359	600	430	15.8	0.60	3.257	600	-250	12.5	0.24	2.572
580	-170	67.5	0.00	5.877	600	410	14.5	0.60	3.588	600	-270	11.0	0.20	2.114
580	-190	35.3	0.28	5.174	600	390	12.8	0.60	5.013	600	-290	10.0	0.16	1.883
580	-210	21.5	0.28	4.190	600	370	10.0	0.60	8.853	600	-310	8.8	0.16	1.736
580	-230	15.8	0.24	3.244	600	350	9.3	0.60	11.075	600	-330	8.3	0.12	1.630
580	-250	12.8	0.20	2.567	600	330	9.5	0.60	9.315	600	-350	7.3	0.12	1.536
580	-270	10.5	0.20	2.151	600	310	9.5	0.60	8.208	600	-370	6.5	0.12	1.445
580	-290	9.5	0.16	1.882	600	290	9.5	0.60	8.654	600	-390	5.8	0.08	1.308
580	-310	8.3	0.16	1.765	600	270	9.5	0.60	9.979	600	-410	5.3	0.08	1.126
580	-330	7.5	0.12	1.640	600	250	9.8	0.60	11.715	600	-430	4.5	0.08	0.926
580	-350	6.8	0.12	1.574	600	230	9.5	0.60	12.698	600	-450	4.3	0.08	0.761
580	-370	6.0	0.08	1.466	600	210	9.3	0.60	12.475	600	-470	4.3	0.08	0.704
580	-390	5.3	0.08	1.320	600	190	10.3	0.60	11.519	600	-490	4.3	0.08	0.775
580	-410	4.5	0.08	1.190	600	170	10.3	0.60	9.827	600	-510	4.3	0.08	0.926
580	-430	4.0	0.08	1.084	600	150	10.8	0.60	8.628	600	-530	4.5	0.04	1.036
580	-450	3.8	0.08	0.989	600	130	11.3	0.60	8.023	600	-550	4.8	0.00	1.112
580	-470	3.5	0.04	0.911	600	110	12.5	0.60	7.809	600	-570	5.0	0.00	1.128
580	-490	3.5	0.04	0.853	600	90	13.5	0.60	7.626	600	-590	5.0	0.00	1.078
580	-510	3.5	0.04	0.914	600	70	14.5	0.60	8.388	600	330	9.5	0.60	9.315
580	-530	3.8	0.00	1.008	600	50	15.0	0.60	10.290	600	310	9.5	0.60	8.208
580	-550	4.0	0.00	1.092	600	30	14.3	0.60	13.202	600	290	9.5	0.60	8.654